SAPIENZA
UNIVERSITÀ DI ROMA

DOTTORATO DI RICERCA IN ENERGIA E AMBIENTE
PhD Program in ENERGY and ENVIRONMENT

XXXVI° Cycle

Development of a System Magneto-Thermal-Hydraulics Code for the Modelling of Nuclear Fusion Reactors

PhD Thesis

Scuola di Dottorato in Scienze e Tecnologie per l'Innovazione Industriale
Facoltà di Ingegneria Civile e Industriale
Dipartimento di Ingegneria Astronautica, Elettrica ed Energetica

Lorenzo Melchiorri

Advisor
Dr. Alessandro Tassone

Co-Advisor
Prof. Gianfranco Caruso

A.A. 2022-2023

Abstract

This doctoral research focuses on the critical problem of modeling and understanding Magnetohydrodynamic (MHD) phenomena in the Liquid Metal Breeding Blankets (BB) within magnetic confinement fusion reactors. Conventional analytical and numerical methodologies have proven to be inadequate for capturing the complex interactions and phenomena inherent to the extreme conditions present in fusion environments. To address this lacuna, the study presents the development, Verification and Validation (V&V) of a novel Systems Thermal-Hydraulic (SYS-TH) computational tool, named RELAP5 Development for MagnetoHydroDynamics (REDMaHD).

The foundation for REDMaHD is the well-regarded RELAP5/Mod 3.3 code, which has been widely validated for thermo-fluid-dynamic assessments of fission reactors. Adapting this code for fusion applications has led to a software platform with comprehensive capabilities, including the computation of distributed MHD pressure losses in various channel configurations and the evaluation of localized MHD pressure drops due to factors like bends, cross-sectional changes, and electrical conductivity discontinuities in the walls. The tool is also designed to work with fusion-relevant liquid metals, such as the lead-lithium eutectic alloy (PbLi) and sodium-potassium (NaK), further expanding its applicability.

An extensive V&V procedure was conducted to establish the reliability and accuracy of REDMaHD. This involved not only the validation of individual subroutines but also the comparison of the code output against existing numerical simulations and empirical data from three Test Blanket Modules (TBMs) including the LLCB, HCLL, and WCLL. The validation process has shown that REDMaHD predictions deviate only minimally, by approximately 1% to 10%, when compared to these benchmark results, thus confirming its fidelity in simulating key electromagnetic effects relevant to fusion reactor design.

Although REDMaHD has proven to be an advanced and dependable tool, it is important to note the existing limitations. The code currently lacks specialized modules for certain electromagnetic coupling phenomena and three-dimensional MHD losses, which impacts its ability to predict mass flow distributions in multi-channel configurations. The study outlines the future work needed to resolve these issues, including the integration of additional modules that can handle the newly identified requirements.

By providing an advanced numerical tool with verified capabilities, this thesis significantly contributes to ongoing research efforts in fusion technology, offering a robust computational platform for tackling a wide range of engineering challenges in the design and operational analysis of future fusion reactors.

Keywords: Magnetohydrodynamics, Systems Thermal-Hydraulic, Liquid Metal Breeding Blanket, Fusion Reactors, Code Development

Contents

List of Figures

List of Tables

Acronyms

BB Breeding Blanket

CAE Computer-Aided engineering

CFD Computational Fluid Dynamics

FPP Fusion Power Plant

HTC Heat Transfer Coefficient

LM Liquid Metal

MHD Magnetohydrodynamics

NPP Nuclear Power Plant

OHD Ordinary hydrodynamics

REDMaHD RELAP5 Development for MagnetoHydroDynamics

SYS-TH Thermal-Hydraulics System

TBM Test Blanket Module

WCLL Water Cooled Lithium Lead

Part I

Introduction

Chapter 1

Objective of the Ph.D. project and outline

1.1 Motivation and scope of the project

The exponential increase in global energy demand underscores the necessity for sustainable solutions, particularly as industrial, transportation, and electronic sectors expand. Given the environmental drawbacks of fossil fuel-based power generation, nuclear fusion emerges as a compelling alternative, offering benefits such as a programmable energy source with low carbon dioxide emissions, abundant and geographically widespread fuel, minimal production of long-lived radioactive waste, and inherently safe operation.

Although rich in potential, magnetic-confinement fusion technology remains in a nascent stage of development. The forthcoming ITER experimental reactor, aims to investigate the physics of burning plasmas and provide an first-of-a-kind test bed for the development of engineering solutions that will then further validated in DEMO. This latter reactor, for which the pre-conceptual phase was concluded in 2020, serves as both a technological demonstrator, aspiring to contribute fusion-generated electricity to the grid by mid-century, and as a qualifying facility for reactor technologies.

Computer-Aided Engineering (CAE) codes are instrumental in contemporary engineering pursuits, and the nuclear fusion sector is no exception. The specialized conditions within fusion reactors necessitate multifaceted analyses that conventional codes, originally designed for fission applications, struggle to provide. This doctoral research is geared towards filling this technological gap by contributing to the development of a Thermal-Hydraulics System (SYS-TH) software that can expediently facilitate fusion reactor design, by advancing the state of the art on the topic of reduced order models for the simulation of multiphysical effects in Liquid Metal (LM) coolants.

LMs are advantageous due to their superior thermal characteristics and their potential role as fuel breeders. Yet, their electrical conductivity introduces challenges; when they flow under the influence of the magnetic fields that confines the reactor plasma, complex Magnetohydrodynamics (MHD) effects arise within the fluid domain, caused by Lorentz forces. These effects include, but are not limited to, elevated pressure drops, suppression of heat transfer, and alterations in mass transport mechanisms. The complex interplay of electromagnetic fields, fluid dynamics, and heat and mass transport is challenging to simulate but the goal of designing an effective fusion reactor mandates an exhaustive understanding of these MHD phenomena during both steady-state and transient operations. Presently, achieving this level of detail is challenging due to limitations in existing analytical and numerical methodologies.

Despite sustained efforts by the fusion research community to advance MHD numerical techniques and software capabilities, a comprehensive code capable of simulating all MHD phenomena at all the scales relevant for LM system and components remains elusive. If local scale analyses are accessible through Computational Fluid Dynamics (CFD) tools like ANSYS-CFX, ANSYS-FLUENT, and OpenFOAM, even if at exorbitant computational cost, mesoscale and system scale analyses remain challenging to perform due to the limitations (or even lack thereof) MHD models in conventional SYS-TH codes such as RELAP and TRACE. Existing models have only rudimentary MHD correlations that are primarily applicable to linear geometries and do not support more complex configurations like junctions and manifolds.

The development of a reliable SYS-TH code capable of modeling MHD phenomena at a higher degree of fidelity is essential, especially since various elements of fusion reactors can be accurately represented using such a simplified approach. This is undoubtedly a challenging task, yet the current scientific literature offers a plethora of works that can inform the establishment of appropriate models and correlations for system-level analyses.

The overarching objective of this PhD research is to lay the groundwork for the development of software capable of analyzing all phenomena crucial for reactor design at the required system-level scale. Specifically, the numerical tool will incorporate MHD effects, along with other non-MHD phenomena that are critical for the design of fusion facilities.

The foundation for the development of the software discussed in this research has been established on the basis of the RELAP5/Mod 3.3 code. This code has been specifically engineered for the thermo-fluid-dynamic assessments of fission reactors and is regarded as the *gold standard* in that domain. Given its highly validated nature for fission applications, it was a natural candidate for adaptation to address fusion reactor requirements. Consequently, this led to the conception of RELAP5 Development for MagnetoHydroDynamics (REDMaHD), the subject of this thesis.

To the best of the Author understanding, REDMaHD stands as the most comprehensively validated MHD system code with the broadest range of capabilities. Specifically, it is equipped to tackle multiple features pertinent to blanket design:

- Computation of distributed MHD pressure losses in circular/rectangular channels.
- Evaluation of local MHD pressure drops in bending pipes.
- Evaluation of local MHD pressure drops due to variations in duct cross-sectional areas.
- Evaluation of local MHD pressure drops induced by discontinuities in wall electrical conductivity.
- Basic evaluation of forced convection MHD heat transfer coefficient in circular/rectangular channels.
- Dealing with fusion-relevant liquid metals such as sodium-potassium and lithium-lead.
- Upgraded models for nucleate boiling and film condensation for water in vertical tubes to improve modeling of passive safety systems.

In the rest of this document, it is discussed the development, implementation, validation and verification of these models and, ultimately, their applications for the purpose of advancing the development of LM systems and components for fusion reactors.

1.2 Thesis outline

The initial part (Part I) of this thesis elucidates the foundational theoretical and technical elements essential for comprehending the research context.

Chapter 2 offers a detailed examination of nuclear fusion as an energy alternative, highlighting its potential and global efforts to exploit it. Key international projects, notably ITER and EU-DEMO reactors, are touched upon, underscoring advancements in magnetic confinement fusion. The significance of Breeding Blanket (BB) systems in fusion, especially the Water Cooled Lithium Lead (WCLL) BB, is articulated, with a nod to the design of the DCLL BB and the ITER Test Blanket Module (TBM) program.

Chapter 3 introduces the foundational principles of MHD. Core theories of incompressible MHD, including the formulations of governing equations, are elucidated. Subsequent sections explore into a description of basic phenomenology using examples from practical applications, delving into confined flows and pressure drop scenarios. The chapter culminates with a discussion on the role of electromagnetic coupling in LM flows.

Part II of the document is designed to describe foundational notions pertaining to the numerical methodology adopted by SYS-TH codes and, more in general, software included in CAE platforms.

Within Chapter 4, an encompassing discourse on SYS-TH code utilization, optimal practices, and application domains is provided. Noteworthy attention is given to RELAP5, which forms the core structure of the REDMaHD package. Furthermore, an introductory exposition of certain CFD tools is presented, considering their anticipated paramount role in upcoming numerical MHD evaluations.

Chapter 5 delves into the articulation and construction of REDMaHD. This chapter elucidates the approach to model integration and delineates the necessary variables added to the foundational code repository.

Part III encompasses the results from the validation and verification (V&V) campaign, essential for asserting the reliability of the code.

Chapter 6 is dedicated to the discussion of the derived MHD pressure drop models that address both distributed and local pressure drops. Chapter 7, the most pivotal verification cases are showcased, demonstrating the software accurate execution of the designated models, ensuring the absence of programming discrepancies. Chapter 8 reports the actual validation of REDMaHD, utilizing high-quality experimental and numerical data gathered by full-scale simulations and experimental campaigns performed on mockups of BB concepts. Chapter 9 discusses the conceptualization of the forced convection heat transfer model. A current state-of-the-art overview related to MHD convection numerical models is presented, and a preliminary validation of the formulated model is presented.

At last, Part IV focuses on the discussions related to the activities undertaken to support the design of fusion and fission reactor components.

In Chapter 10, parametric studies concerning MHD induced pressure drops in the prevailing layout of the WCLL TBM are detailed, encompassing both the box structure and the associated liquid metal system. A more extensive analysis has been conducted on the MHD effect within the entire WCLL blanket segment, comparing the reference design with an alternative configuration. Chapter 11 addresses the adaptations integrated into REDMaHD to manage complex two-phase heat transfer regimes pertinent to fission reactor safety components.

Chapter 2

Nuclear Fusion Reactor Technology

2.1 Fusion Energy overview

In a profound sense, the quality of human life hinges upon effectively addressing the escalating energy demands. To meet the world future energy needs, investment in environmentally compatible energy options is imperative. However, energy sources that are associated to significant carbon dioxide emissions, for several compelling reasons, prove to be unsustainable and precarious:

- The combustion of fossil fuels exerts a measurable impact on the Earth atmosphere, potentially triggering significant climate shifts.
- Considerably more valuable applications of these resources, such as in the chemical and pharmaceutical sectors, agriculture, steel and hydrogen production, remain underutilized.
- Fossil fuel reservoirs are finite and, despite the possibility of resources still unknown, are going to be inevitably depleted over a timescale of, considering coal as a reference, at most a few centuries [34].

The remedy to the complex conundrum of energy and climate challenges necessitates the adoption of a multifaceted approach that entails the successful execution of several strategies: the enhancement of energy efficiency, the development of efficient and cost-effective carbon capture and storage technology, embracing renewable energy sources (to varying extents across different countries depending on their possibility, energetic demands, and population size), exploring other emission-free energy sources like nuclear fission and fusion, etc [34]. Among emission-free energy sources, those with the potential to substantially contribute to sustained energy production are renewable energies, nuclear fission, and nuclear fusion. While renewable energy sources that have a still significant potential for growth, like wind and solar, provide an attractive option to cater to the ever-growing energy demand, their intermittent nature calls for energy storage, which in turn diminishes their efficiency. Moreover, they are characterized by a low energy density compared with fossil fuels and, as such, tend to require an increased consumption of mineral resources and structural materials per unit of produced energy [35].

Turning to nuclear fission, apprehensions center around waste management, operational safety, and nuclear proliferation. However, the complete abandonment of nuclear power without a viable replacement could lead to an increased dependence on fossil fuels [3].

Although nuclear fusion remains a less mature contender, it presents a series of distinctive advantages, primarily rooted in its peculiar technological features. Fusion draws from geographically widespread and nearly limitless fuel resources, and it boasts inherent safety with minimal long-term radioactive waste. Fusion power plants hold the promise of providing substantial and programmable emission-free electricity production.

The merits of fusion manifest in three fundamental aspects [36]:

1. **Fuel**: It harnesses abundant, non-radioactive fuels like deuterium and lithium, thereby mitigating significant ecological repercussions.

2. **Safety**: Fusion reactors are inherently safe from a nuclear perspective since they do not rely on a chain reaction, thus nullifying the risk of runaway power production for the reactor integrity, operate with a limited inventory of radioactive isotopes (themselves of reduced radiotoxicity compared with fission products), and of nuclear fuel.

3. **Environment**: Fusion energy production does not generate radioactive waste

that requires disposal for geological timescales. Challenges arise primarily from tritium and reactor material activation, yet innovative designs hold the potential to mitigate these concerns.

The development of fusion energy was started in military laboratories after World War II as an offshot of the reaserch on atomic weapons. In 1958, at the second International Conference on the Peaceful Applications of Nuclear Energy, the veil of secrecy was lifted from nuclear fusion research [4, 36]. This initiated a longstanding tradition, facilitated by the International Atomic Energy Agency (IAEA), of periodic dissemination of fusion advancements through a sequence of conferences and academic publications. The field witnessed its first pivotal advancement in 1968 when Russian researchers introduced the tokamak, a magnetic confinement apparatus adept at sustaining high-temperature nuclear fuel. Since then, tokamak-based fusion research has become the cornerstone of mainstream fusion development, culminating in the construction of large-scale machines like the Joint European Torus (JET) in Culham, UK and the Tokamak Fusion Test Reactor (TFTR) at Princeton Plasma Physics Laboratory, USA, in the early 1980s [4, 36].

A subsequent milestone was reached in the 1990s, as both JET and TFTR empirically demonstrated the generation of fusion energy using a tritium-deuterium mix, both isotopes of hydrogen. The successes chalked up by the tokamak concept led, in 1986, to an international accord among the European Union, USA, the Soviet Union, and Japan to collaboratively design an experimental fusion reactor. Up until about 1997, the advancement of tokamak-based fusion technology experienced significant progress. However, since then, its development has largely plateaued as the field anticipates the launch of the next generation of machines [4, 36].

In 2006, the fusion landscape underwent another transformation with the induction of China, India, and South Korea, culminating in a collective resolution to build an international thermonuclear fusion experimental reactor, called ITER, from the Latin word "the way". With operations slated to commence in mid-2020 and full-scale 500 MW power output expected by mid-2030, the focus of fusion research is gradually shifting from a science-centric endeavor to a more industrial and technologically-driven initiative. Private sector enthusiasm has also been on the rise, as evidenced by around two dozen companies currently participating in fusion ventures. Among these, General Fusion, partially financed by Jeff Bezos, aims to inaugurate a prototype plant by 2024, while Commonwealth Fusion Systems, supported by Bill Gates, targets net energy yield by 2025. If forthcoming R&D outcomes in fusion align with current expectations, fusion energy stands to fulfill increasingly stringent energy quality standards, mandating that energy production be not only economical but also environmentally and socially responsible [4].

2.2 ITER and EU-DEMO reactors

The path to achieving commercial fusion power is punctuated by major milestones, chiefly ITER and demonstration reactors like the EU-DEMO. The former, ITER, is an international initiative that has the primary goal of demonstrating the feasibility of a burning plasma. It aims to produce several hundred megawatts of fusion power, and serves as the main focus for European fusion research resources in the initial stages of the road-map [37]. This significant initiative has already propelled advancements in key technologies for primary components and auxiliary systems, while also establishing fusion safety credentials.

Achieving ITER full potential, particularly in demonstrating a positive fusion gain, will require a concerted effort from scientists and engineers until the early 2040s. During this phase, the initiative will also focus on rigorous testing and validation of technological enhancements such as breeding blanket modules, plasma heating systems, and measurement and control techniques.

On the other hand, the EU-DEMO is designed to serve as the next significant step in the European fusion programme following and gaining from the successful operation of ITER. DEMO is intended to bridge the gap between experimental and commercial fusion power plants. Specifically, it aims to be the first fusion reactor to sustainably generate electricity, showcasing the viability of tritium breeding and waste management technologies. It will integrate comprehensive scientific and technological demonstrations, thus propelling fusion science into the realm of practical energy production.

Both projects play crucial roles; ITER is an experimental machine designed for exploring unknown plasma physics regimes and aims to prove the feasibility of generating more thermal energy than consumed, with its primary technological focus being on LTS magnets and control systems. On the other hand, EU-DEMO is tasked with demonstrating the production of net electrical energy and establishing the fuel cycle, centering primarily on technological objectives. The strategies and goals set forth are in alignment with the ITER Organization proposed approach, and they collectively serve to prepare for the long-term success of the European DEMO and subsequent commercial fusion energy production [37].

Summarizing, EU-DEMO overarching objectives encompass:

- Demonstrating continuous power production within the bounds of the specified availability, with an aim to contribute electricity to the grid.
- Achieving self-sufficiency in fusion fuel, specifically tritium.
- Validating technologies in an environment representative of a nuclear fusion reactor, aiming to achieve technology readiness levels 7 or 8.
- Establishing a foundation to evaluate the practicality and economic viability of a fusion power plant.

2.3 Nuclear Fusion

Nuclear binding energy is linked to the mass defect Δm through Einstein equation $E = \Delta mc^2$, signifying that a nucleus weighs less than the sum of its individual nucleons. If the binding energy per nucleon of the resulting nucleus, formed by the fusion of lighter elements, surpasses that of the initial nuclei, the nuclear reaction will result in a net energy gain (see the sketch in Figure 2.1). The binding energy per nucleon peaks at ^{56}Fe and, as a result, a net energy release is observed for fusion of lighter elements than ^{56}Fe, whereas the opposite holds true for the fission of elements heavier than ^{56}Fe [2].

Fusion, as observed in stars like the Sun, involves reactions such as, for instance, the proton-proton chain and carbon-nitrogen-oxygen cycle. These reactions, although effective for power production in stars, are not suitable for terrestrial applications since they require extremely long time-scales and unfeasible large quantity of reactant mass. In contrast, the high temperature generated by precursor fission

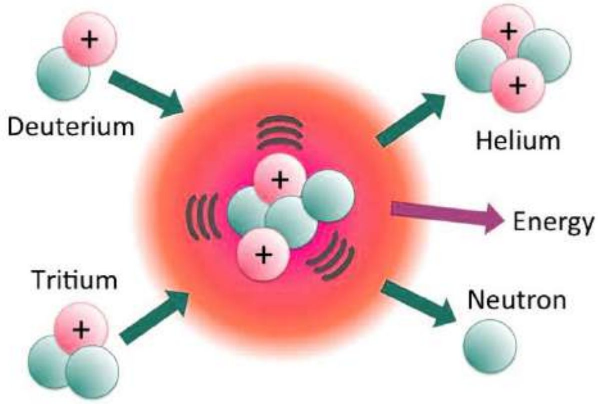

Figure 2.1: Fusion Process: When a deuterium nucleus, consisting of a proton and a neutron, combines with a tritium nucleus, which has a proton and two neutrons, they undergo fusion. This results in the formation of a helium nucleus, with two protons and two neutrons, and a highly energetic free neutron [1].

detonations triggers rapid, uncontrolled fusion in hydrogen bombs. Controlled fusion lies between these extremes [2]. Fusion necessitates high particle velocities to counteract the electrostatic repulsion between protons, allowing them to enter the range of the strong nuclear forcean inherently short-range force binding nucleons within a nucleus.

Plasma, a highly ionized and electrically neutral gas, enables the attainment of high particle energies. By supplying sufficient energy to the plasma, its temperature increases, enabling particles to reach fusion-relevant energies. This leads to thermonuclear fusion, a process characterized by temperatures of approximately $1 \cdot 10^8$ K, far surpassing solar core temperatures. Achieving this temperature is a considerable milestone but, in order to produce a significant quantity of fusion energy, this condition must be also satisfied over a considerable time duration, that is to say that the plasma must be confined by an appropriate confinement scheme. While the elevate fuel mass presents in starts makes feasible to use gravity as plasma confinement (gravitational confinement), on Earth, confinement must be obtained through other mans. Through common approaches involve the use of magnetic and electric fields (magnetic confinement) to manipulate the electrically charged particles composing the plasma or, conversely, the use of the inertia of the collapsing fuel pellets under the irradiation by focused electromagnetic radiation (inertial confinement) [2, 3].

Assessing fusion technology progress involves the gain factor Q, representing the ratio of thermal energy generated by the plasma to external thermal energy input. Two relevant milestones are associated to this parameter in the development of fusion energy: breakeven ($Q = 1$), when the thermal power generated matches the input required to sustain the thermonuclear reaction, and a burning plasma ($Q \gg 1$), where the energy contained in the electrically charged fusion products is sufficient, once deposited in the plasma, to sustain the reaction. A value of Q exceeding 30 to 50 is typically required for a Fusion Power Plant (Fusion Power Plant (FPP)) to account for thermodynamic cycle efficiency (between 30% and 50%) and the need for auxiliary heating [38].

First-generation FPPs are likely to exploit the fusion reaction between deuterium and tritium, called D-T reaction (also ref to Figure 2.1). They are both isotopes of hydrogen (D = ^{2}H, T = ^{3}H). The D-T reaction is deemed the most accessible for power production due to its highest collision cross-section compared to other reactions (e.g., D-D, D-^{3}He) and, besides, the occurrence of this peak at the lowest temperature. This reaction produces an α particle (^{3}He nucleus), accounting for around 20% of the released energy, and a highly energetic neutron as shown in Equation (2.1). Fusion reactions exhibit exceptionally high energy density, with its mass-to-energy conversion ratio outpaced only by antimatter annihilation [2, 3].

$$D + T \rightarrow \alpha(3.5 \text{ MeV}) + n(14.1 \text{ MeV}) \tag{2.1}$$

The α particle, being electrically charged, is effectively retained within the plasma and contributes to maintaining its temperature. In contrast, the energetic neutrons are challenging to confine, escaping into the surrounding fusion chamber materials. These materials become hardened, brittle, and radioactive due to the activation process. This phenomenon limits the operational lifespan of components adjacent to the plasma [2]. However, these neutrons are crucial for extracting power from the plasma, as their energy can be efficiently harvested by slowing them down in a material encircling the plasma chamber. This material is subsequently cooled to transfer power externally.

Fusion fuel is globally accessible, ensuring energy security for all nations. Unlike fossil fuels, fusion fuels have an equal distribution, eliminating resource disparities. Proliferation risks are negligible, as pure fusion reactor operation does not yield fissile materials essential for nuclear weapons production. Any attempt to modify the reactor for such purposes would be detectable by qualified inspectors [36].

Deuterium can be extracted from ordinary water using conventional techniques, while tritium, an unstable isotope, decays into helium via beta emission with a half-life of approximately 12.3 years. Consequently, tritium is not naturally occurring [2]:

$$T \rightarrow^{3} \mathrm{He} + \beta + 18.7 \text{ keV} \tag{2.2}$$

Tritium is bred from lithium, through neutron capture reactions:

$$^{6}\mathrm{Li} + n \rightarrow^{4} \mathrm{He}(2.05 \text{ MeV}) + T(2.73 \text{ MeV}) \tag{2.3}$$

$$^{7}\mathrm{Li} + n \rightarrow^{4} \mathrm{He} + T + n - 2.47 \text{ MeV} \tag{2.4}$$

Neutrons generated by the D-T fusion reaction are used to breed tritium by bombarding a blanket loaded with lithium around the plasma chamber. Due to the less efficient neutron economy compared to fission, a neutron multiplier like beryllium or lead is employed to supplement the reactor neutron balance. The in-situ produced tritium must not only fulfill the reactor needs but also generate a surplus for future reactors within a reasonable time frame (5 years), while staying within safety regulations. To achieve this, the Tritium Breeding Ratio (TBR), the ratio between tritium generated and used by the reactor, needs to be between 1.05 and 1.15 [39].

Fusion inherently ensures safety. At any given time, the amount of fuel in the reaction chamber sustains the reaction for only a brief period, unlike fission power plants storing years' worth of fuel. Unlike fission, fusion does not rely on neutron multiplication, eliminating runaway reactions. Even in the absence of active cooling, the low residual heating prevents reactor structure meltdown [36].

Environmental pollution is minimized. Basic fusion fuels, deuterium and lithium, along with their direct product helium, are non-radioactive, atmospheric-friendly, and environmentally benign. The absence of ecological, geophysical, and land-use concerns sets fusion apart from other energy sources like biomass, hydro-power, and solar energy [36].

Limited radioactive waste issues characterize fusion. Unlike fission, fusion products lack radioactivity, which is beneficial. However, the radioactive inventory includes tritium and activated reactor materials, necessitating meticulous management to ensure public and personnel safety. The activated materials have high melting points, and their low decay heat negates the need for active cooling during decommissioning, transport, or disposal. While FPPs generate a volume of activated materials comparable to that of fission reactors, the qualitative difference lies in significantly reduced long-term radio toxicity. Clever material selection can minimize induced radioactivity, focusing on short-lived isotopes. Developing low activation materials, like vanadium alloys or silicon carbides, holds promise for post-reactor shutdown recycling after approximately 100 yearsan essential strategy [4]. This waste shouldn't mandate geological-time isolation, alleviating future-generation concerns.

Tritium, a weak beta emitter, entails negligible external exposure risk. Internal exposure poses the primary threat, as tritium can replace ordinary hydrogen in water and various hydrocarbons. This substitution could potentially contaminate the food chain if released into the atmosphere. The tritium cycle remains internally closed, with the FPP holding a total tritium inventory of a few kilograms, where approximately 200 grams might be released in case of an accident [38]. Tritium ability to diffuse through high-temperature materials may necessitate the adoption of special permeation barriers and detritiation of contaminated materials to limit its environmental discharge during normal operation.

2.4 Magnetic confinement technology

Magnetic confinement leverages the Lorentz force, $F_L = q\mathbf{v}\times\mathbf{B}$, exerted on a charged particle with electric charge q traversing a magnetic field $\mathbf{B}$ with velocity $\mathbf{v}$. As illustrated in Figure 2.2, the particle velocity component perpendicular to the magnetic field, $v_\perp$, incites a circular trajectory, while its parallel component $v_\parallel$ propels the particle along the magnetic field lines. The resultant motion is a helical gyration that effectively constrains the charged particle within the confines of the field lines [2].

This behavior demonstrates the capability of a consistent magnetic field to restrict transverse motion of plasma particles while permitting longitudinal movement

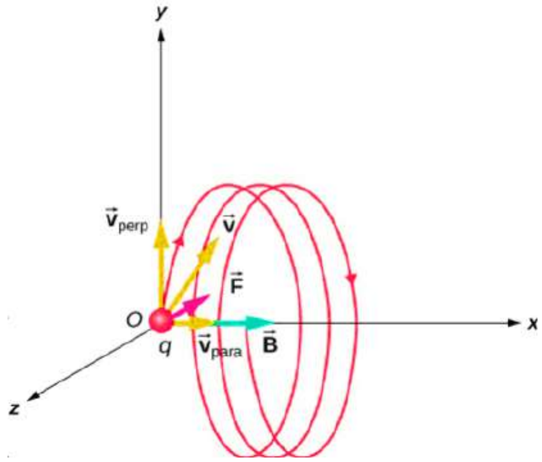

Figure 2.2: A charged particle, whose velocity vector is not aligned with the magnetic field, exhibits a helical trajectory [2].

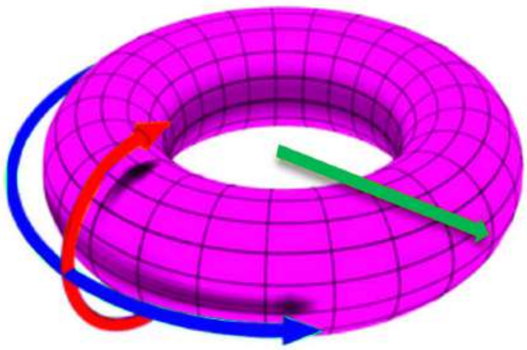

Figure 2.3: A diagram depicting the poloidal direction (red),the toroidal direction (blue) and the radial direction (green).

along the field lines. Various magnetic confinement configurations have been explored, but the tokamak geometry, depicted in Figure 2.4, has proven to be the most efficacious. It is essential to introduce a plasma-based coordinate system that will be used throughout this thesis. Figure Figure 2.3 schematically illustrates the torus geometry. The toroidal direction is the longer path around the torus (indicated by the blue arrow); the poloidal direction is the shorter path around the torus (indicated by the red arrow). The third direction, perpendicular to the magnetic surfaces, is referred to as the "radial direction" (indicated by the green arrow).

The tokamak technology thus employs a series of toroidal field coils to create a closed magnetic loop, mitigating particle losses due to field variations. To counteract drift induced by variations in magnetic strength across the chamber cross-section,

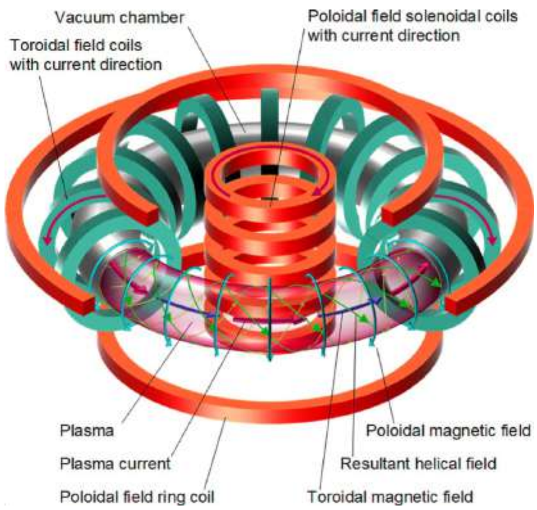

Figure 2.4: Magnetic confinement of plasma in a Tokamak [3].

a toroidal electric current is applied through the plasma to produce an opposing poloidal magnetic field [2].

The ensuing magnetic topology is a helical field, spiraling infinitely around the toroidal loop, with nested, closed magnetic flux surfaces. Although this magnetic confinement remains susceptible to radial hoop forces, the employment of poloidal field ring coils achieves radial equilibrium and stabilizes the plasma. In such a configuration, cross-field particle movement is predominantly restricted to collisional or turbulent processes, enhancing thermal insulation between the hot plasma core and the colder peripheral regions [2, 3].

To sustain the plasma current in tokamaks, inductive methods centered around a solenoid in the torus core have traditionally been employed. However, this method is intrinsically limited by the available magnetic flux swing on the coil used to induce the electrical current. Depending on the machine design, the plasma discharge may range between a few ms to a few s [40]. Longer plasma discharges, likely to be desired in power producing reactors, must rely on the the utilization of non-inductive methods to drive the toroidal current, such as the injection of high-energy neutral particles or radiofrequency waves. This is very challenging to achieve due to the actual low efficiency of non-inductive current drives and the large magnitude of the current envisioned for DEMO-class reactors [40]. To lessen this requirement, a significant portion of the plasma current in these reactors is expected to be a self-induced bootstrap current, which is generated by trapped-passing particle collisions in a radial pressure gradient [2, 3]. The stability of a plasma scenario with a large bootstrap current fraction ($> 60\%$) and a non-inductive current drive sustaining the discharge for a sufficient time to achieve a quasi-steady-state operation is still topic of active research [40].

Various techniques, both inductive and non-inductive, are employed to heat the plasma to fusion-relevant temperatures. However, conventional Joule heating methods encounter limitations due to the inverse correlation between plasma resistivity and temperature [2, 3]. Notably, innovations like D-shaped plasma configurations have been found to optimize the plasma pressure-to-magnetic field pressure ratio, or plasma beta, thereby enhancing plasma confinement [2].

In the first generation of tokamaks, the boundary of the plasma was defined by a physical material limiter that was in contact with the plasma. This limiter existed beyond what is known as the Last Closed Magnetic Flux Surface (LCMFS) or, more commonly, the Separatrix. The region located outside this Separatrix is termed the Scrape Off Layer (SOL), where particles that escape the confined plasma region collide with a target. One drawback of this design was the considerable ingress of impurities into the plasma, mainly due to erosion caused by the bombardment of particles. This influx of impurities led to substantial radiation losses, hampering the efficiency of the system and severely limiting the possible time for a plasma pulse.

To circumvent this issue, a more refined approach involves altering the magnetic field lines at the plasma edge so that they intersect a designated target. In this configuration, the Separatrix is twisted over itself to define one (or more) X-point, at which two magnetic field lines intersect, also called a null, since it is a location in which the poloidal field is zero. Located below this X-point is the divertor, a component designed to bear most of the thermal load generated by the particles. Strong pumping mechanisms in the divertor region enable the prevention of impurities from re-entering the plasma. Moreover, the divertor proves highly effective in the removal of helium ash from the plasma core, which is required to maintain the fusion power production close to nominal value during long discharges to prevent the decrease of reaction rate due to impurity displacement [2, 3]. Figure 2.5 illustrates the two different plasma edge configurations.

However, the plasma is not without its susceptibilities. When certain operational parameters, such as plasma density and current density, are exceeded, the

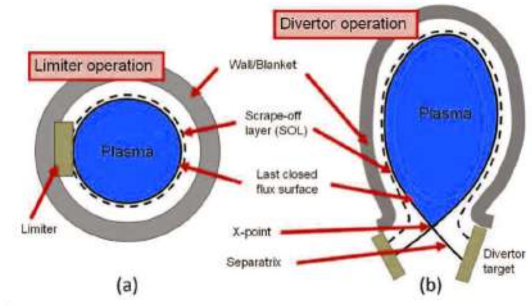

Figure 2.5: Edge of plasma in the limiter (a) and diverted (b) configuration [4].

plasma becomes prone to a variety of instabilities. Near or beyond these thresholds, the plasma can abruptly expand towards the containment walls, thereby losing its confined state. This leads to the occurrence of violent transient events, the most significant and damaging being plasma disruptions. Such disruptions pose a risk to the structural integrity of the machine, causing extensive wear and tear on the plasma chamber walls while also inducing large currents and electromagnetic forces on adjacent components [2].

Figure 2.6 presents a prototypical cross-section of a fusion reactor, identifying its major components [3]:

1. **Breeding Blanket (Breeding Blanket (BB))**: This is the principal in-vessel component that collects the majority of neutrons emitted from the plasma. It occupies about 85% of the total wall surface and plays a pivotal role in the reactor fuel cycle. It not only breeds tritium but also captures the thermal energy from the neutrons and transfers it to a cooling agent for electricity generation. It also serves the fundamental function of radiation shield for the other components behind it.

2. **Divertor**: This component accounts for the remaining 15% of the plasma-exposed wall. It is responsible for defining the plasma edge and bears a significant portion of the thermal load. It is instrumental in the removal of helium ash and other impurities, which are then evacuated by a vacuum pumping system.

3. **Vacuum Vessel (VV)**: This component encloses both the plasma chamber and all in-vessel components, providing mechanical support. It serves as the

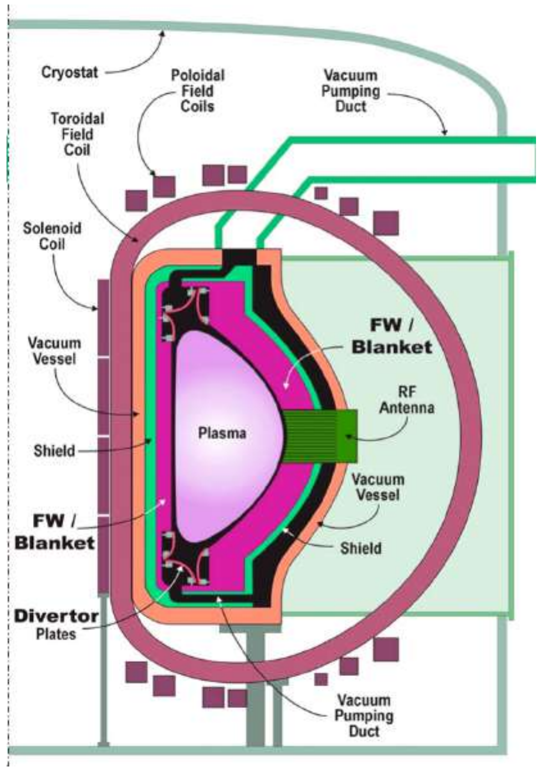

Figure 2.6: Prototypical section of a fusion reactor based on the ITER configuration [5]. The acronym FW stands for 'First Wall', and RF stands for 'Radio Frequency'.

outer boundary of the reactor thermonuclear core and functions as the first containment barrier against the release of radioactive materials.

4. **Magnet**: This assembly provides the magnetic field necessary for plasma confinement and consists of toroidal field coils, poloidal field ring coils, and a central solenoid. Due to the large energy requirements, low-temperature superconducting materials like NbTi and Nb_3Sn are used. These materials need to be cooled with liquid helium to achieve superconductivity.

5. **Cryostat**: This structure encloses all the aforementioned components and establishes an ultra-cold environment, critical for the operation of the superconducting magnets.

Additional components include the Heating and Current Drive (H&CD) system, which supplies the required energy to the plasma and sustains the plasma current. Furthermore, a tritium handling facility is utilized for extracting, purifying, and storing tritium, thereby ensuring a sustainable fuel cycle.

As highlighted earlier, a major drawback of tokamak-based reactors that employ inductive methods to generate plasma current is their inherently pulsed operation. For instance, the EU-DEMO is designed to operate with a power pulse duration of approximately 2 hours, followed by a 10-minute pause, also known as a dwell period [4]. This intermittent operational mode poses challenges for the turbo-generator system and exacerbates wear and tear on structural components due to frequent mechanical and thermal cycling. Unlike tokamaks, stellarators offer an advantage in this context as they can operate in a steady-state regime.

To mitigate the challenges arising from the pulsed nature of tokamak operation, several solutions have been put forth. The most promising among these involves the use of an intermediate heat exchanger featuring molten salt, termed the Energy Storage System (ESS). This system stores a portion of the energy generated during the power pulse and can subsequently supply this stored energy to the turbine during the dwell periods, thus smoothing out the operational cycles [4].

2.5 Breeding Blanket system

The BB is a critical component that needs to fulfill three very different functions. As such, its design exhibits considerable challenges since it requires a careful selection of materials, fabrication techniques, and cooling methods to achieve all of its goals [39]. This design must take into account multiple factors including neutronics, thermomechanics, electromechanics, thermohydraulics, fluid dynamics, magnetohydrodynamics (MHD), radiation, and safety considerations. The primary function of a BB is tritium breeding, and each design must therefore achieve a positive neutron balancetaking into account neutron production in the plasma, neutron leakage from the blanket, and neutron absorption by elements other than lithium; beside the natural decay of this radioactive material.

For the DT reaction, which yields only a single neutron, neutron multiplication is a non-negotiable requirement to define the tritium breeding strategy. Moreover, to optimize performance, natural lithiumwhich consists of 92.5% ^{7}Li and 7.5% ^{6}Liis often enriched in ^{6}Li, which has a higher neutron capture cross-section compared with ^{7}Li. This enriched lithium is then combined with a neutron multiplier, with beryllium (Be) generally used for solid breeders and lead (Pb) for liquid ones. Enrichment levels of 50% to 70% for solid breeders and approximately 90% for liquid PbLi breeders are common [4].

The classification of BBs into solid and liquid types, depending on the phase of the breeder, has direct implications on their operational requirements, notably tritium extraction methods. In solid BB, tritium is generally removed through a separate carrier fluid, most often helium, via gas purging within the VV, while in liquid BB, the breeder can double as a tritium carrier and can be circulated outside of the reactor and into the tritium extraction units. This means that solid breeders must remain in the reactor for the entire BB lifespan, making it difficult to control the breeder composition, an important requirement to mitigate degradation in performance due to ^{6}Li depletion or geometry modifications and to control the inventory of impurities. Instead, liquid BB can conveniently adjust the breeder composition in-line [4].

In solid BB, lithium is commonly encapsulated in ceramic compounds, typically in the form of small pebbles or blocks. A common BB configuration is the one where the breeder is arranged in "beds" that are alternated with layers containing beryllium and cooling plates. For liquid BBs, the breeder material is either pure lithium or, more commonly, a eutectic alloy of PbLi, with a 15.8% atomic weight in Li, that remains liquid above 235°C [41]. PbLi is often preferred to pure lithium due to its lower reactivity with air, water, and concrete, although PbLi has disadvantages including higher rates of corrosion and the generation of hazardous activation products. Additionally, liquid breeders offer the unique advantage of serving dual roles as both tritium carriers and coolants in advanced blanket concepts [4]. Concerning the thermal management of the reactor, taking as reference the EU-DEMO reactor, three principal sources of heat must be acknowledged [4, 42]:

- Volumetric heat load generated by neutron capture reactions with lithium or other materials (steel, tungsten, etc.), which constitutes the main thermal load within the blanket. The heat load decays exponentially with the distance from the plasma-facing surface, starting from peak power densities around 25 MW/m^3 at the first wall/breeding zone interface.
- Surface heat load stemming from the plasma radiative and transport losses. The main contributors here are synchrotron and Bremsstrahlung radiation, imposing a surface load on the First Wall ranging from 0.25 MW/m^2 to 2 MW/m^2 depending on the position.
- Interactions with the Scrape-Off Layer (SOL) particles.

Given that the blanket is responsible for capturing over 82% of the reactor thermal energy output, the choice of primary coolant and its operational parameters are of pivotal importance [4]. To optimize electricity generation while minimizing production costs, the selected coolant should function at elevated temperatures (ideally above 300°C), while simultaneously being material-compatible under both standard and incidental conditions.

Several coolants have been evaluated [4]:

- Water is highly effective as a coolant in its liquid phase, yet its operational temperature ceiling around 335°C when accounting for evaporation is limiting. However, significant experience has been gained under these conditions from fission power plants, particularly Pressurized Water Reactors (PWRs) operating at 155 bar. Although supercritical water could potentially be employed, its application in fusion technologies has been marginal due to severe corrosion issues with steel. Furthermore, it has poor compatibility with typical fusion materials such as lithium, lead, beryllium, and tungsten, and introduces complexities into the neutron economy and radiological evaluations. Tritium contamination via isotopic exchange is also a concern, requiring costly decontamination procedures.

- Helium can sustain very high temperatures and is broadly compatible with reactor materials. However, its thermal conductivity is poor, necessitating elevated pressure (8 to 10 MPa) and flow rates (up to 80 m/s) to achieve sufficient heat transfer, albeit at the expense of considerable pressure losses and increased pumping power. Although helium poses minimal neutron interaction issues, its voluminous requirements complicate the shielding of in-vessel components within the Breeding Zone. Additionally, helium embrittlement considerations cannot be ignored. Supercritical carbon dioxide is considered a backup option due to considerable less maturity compared with helium.

- Liquid Metals (LMs), typically in the form of Li or PbLi alloys, may integrate the functions of coolant, tritium carrier and breeder, thereby optimizing the neutron economy for tritium production and, ideally, reducing the machine complexity. While they possess excellent thermal attributes, their usage introduces challenges in tritium extraction and control. LMs are affected by MHD interactions, which can notably hinder the benefits, particularly in heat removal from the First Wall where elevated fluid velocities are essential. Additional challenges include the corrosive interaction of Li or PbLi with steels, embrittlement, and their hazardous reactivity with air, water, and steam under accidental conditions. Given their solid state at room temperature and pressure, measures must be implemented to prevent solidification during normal or unplanned operational scenarios.

- Molten salts, such as $LiFBeF_2$ (FLiBe) or $LiFNaFBeF_2$ (FLiNaBe), share the same advantages of LM in terms of reactor design. Their low electrical conductivity makes them less susceptible to MHD effects. However, they are disadvantaged by their poor thermal conductivity, high kinematic viscosity, and most critically, their chemical instability under electric fields (electrolysis) or radiation (radiolysis), potentially leading to the formation of corrosive compounds like hydrofluoric acid.

Structural materials within the blanket must not only be compatible with the breeder and the coolant but must also exhibit high resistance to neutron-induced damage, minimal neutron absorption, and robust thermomechanical properties. In the EU-DEMO reactor, Reduced Activation Ferritic-Martensitic (RAFM) steel, specifically EUROFER, will be used for in-vessel components. It has an operational temperature range between 350 to 550°C, limited at the lower end by ductile-to-brittle transitions under irradiation and at the upper end by creep strength degradation. Conversely, austenitic steels like AISI 316L produce long-lived radioisotopes under irradiation by fusion neutrons and are not considered for in-vessel applications, whereas they can be adopted for VV and other components shielded by the BB [4, 43].

The European blanket program, initiated in the 1970s, contributed to international projects such as the International Tokamak Reactor (INTOR) and Next European Torus (NET). Between 1994 and 2000, contemporary blanket designs were developed under the DEMONET initiative, resulting in two primary concepts: the Helium-Cooled Pebble Bed (HCPB) and the Water-Cooled Lithium Lead (WCLL). Budget constraints in 2004 led to a converged blanket design compatible with both solid and liquid breeders, making helium the only suitable coolant. Subsequently, updated versions of HCPB and a new Helium-Cooled Lithium Lead (HCLL) became the European reference for both DEMO and ITER.

Post-2011, following the establishment of the Roadmap by EFDA, fusion activities resumed. The pre-conceptual design phase led by the EUROfusion Consortium Work Package Breeding Blanket (WPBB) since 2014 considered four BB concepts: HCPB, HCLL, WCLL, and the Dual Coolant Lead Lithium (DCLL). However, persistent technological gaps and an increasing recognition of the BB integral role in the reactor overall system demand further research and development. In 2017, a critical reassessment of the blanket choices for testing in ITER Test Blanket Module (TBM) was conducted, significantly influencing the allocation of development resources for design. HCPB and WCLL) concepts were chosen for the TBM. Consequently, the bulk of the WPBB resources have been channeled ever since towards these two options. Research and development activities is still continuing on DCLL and HCLL since both concepts have attractive features that make them suitable for deployment in First-Of-A-Kind and 1st generation FPP after qualification in EU-DEMO [44–56].

In subsequent sections, the WCLL and DCLL concepts are examined in greater detail to highlight the main features of the two more widespread liquid metal BB systems.

2.6 WCLL-BB

The most recent design iteration of the Water-Cooled Lithium Lead WCLL concept, as of 2018, is founded on the EU DEMO2017 baseline [43]. The development has been spearheaded by ENEA and associated third parties since 2014.

The WCLL utilizes an independent loop architecture, separating the breeder from the coolant, which closely mimics the parameters used in Pressurized Water Reactors (PWR), where the coolant is operated at around 155 bar in a temperature range 290řC - 325řC. This design limits MHD phenomena in the breeder by allowing it to flow at reduced velocities. A dedicated loop for the breeder captures and transfers tritium to an external extraction system, operating at much lower pressures and flow rates than the cooling loop. While this configuration potentially permits tritium contamination of the coolant, the slow flow and low solubility of tritium in PbLi may result in tritium accumulation, necessitating periodic coolant replacement once safety thresholds are surpassed [4].

In the current EU DEMO schema, the plant architecture features a variation of the Vertical Maintenance System (VMS) [57], segmented into 16 toroidal sectors, each covering an approximate 22.5° toroidal arc, and vertically divided into five sections: two InBoard (IB) and three OutBoard (OB) segments [4, 54] (see Figure 2.7). This segmentation results in a total of 32 IB segments and 48 OB segments, the latter of which are further categorized based on their size. These segments adopt a Single Module System (SMS), consisting of breeding modules that create a unified monolithic structure, colloquially referred to as a "banana".

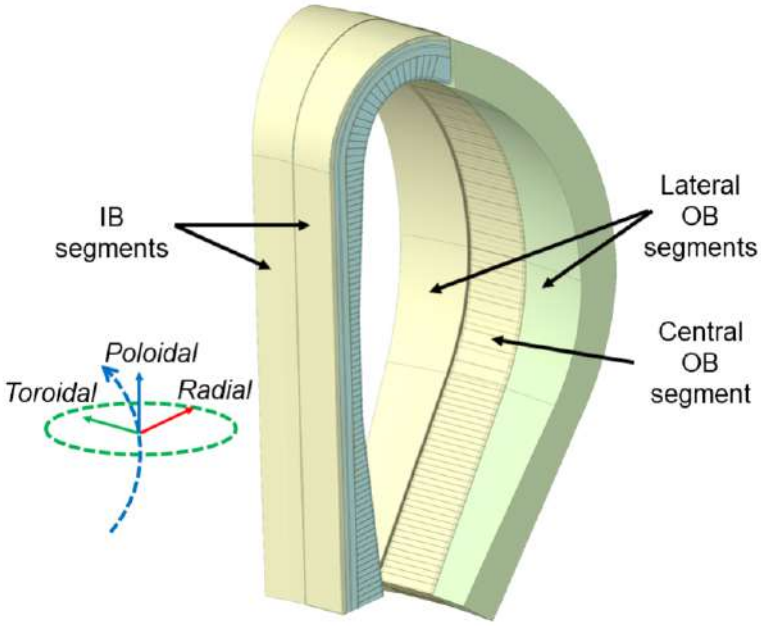

Figure 2.7: WCLL2018 blanket sector layout. Detail of the toroidal-poloidal-radial reference system [6].

2.6.1 Architecture

The WCLL architecture can be categorized into three functional domains: the structural elements, the cooling system, and the Breeding Zone (BZ) [54, 58].

The structural elements, fabricated from EUROFER, can be subdivided into an external framework, delineating the blanket periphery, and an internal structure that outlines the breeding chamber. The internal assembly is girded by Stiffening Plates (SPs) as shown in Figure 2.8. It consists of five poloidal-radial SPs extending vertically across the segment and approximately 120 toroidal-radial SPs anchored to the First Wall (FW) and the backplate, partitioning the segment horizontally into numerous elementary breeding cells. Thin baffle plates, devoid of mechanical functionality, are inserted between the toroidal-radial SPs to delineate the inlet and outlet pathways for PbLi. The external assembly comprises the FW and the Back Supporting Structure (BSS), serving as anchors for the breeding cells and subsequently attached to the VV. The FW is a 25 mm-thick plate demarcating the boundary between the plasma chamber and BB, overlaid with a 2 mm tungsten layer designed to endure a maximum heat flux of 1 MW/m^2 under normal conditions [58].

The cooling apparatus encompasses two separate subsystems, dedicated to the

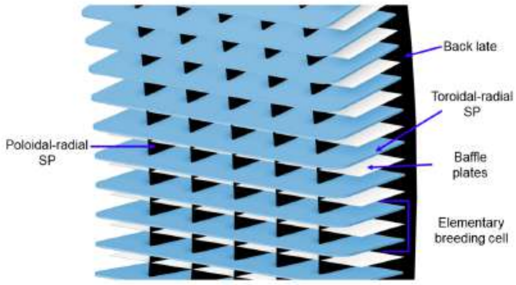

Figure 2.8: WCLL2018 OB internal structural elements. The back plate and the poloidal-radial SPs are black, the toroidal-radial SPs dark grey and the baffle plates light grey [6].

cooling of BZ and FW, composed by manifolds and pipes in which the water is circulated (see Figure 2.9). The FW is cooled via square channels, each with a side length of 7 mm, embedded within the structural material and extending horizontally. Coolant flow in adjacent channels, set apart by a 13.5 mm pitch, is counter-directed. The breeder cooling is facilitated by tubes immersed in PbLi which are double-walled to minimize the risk of rupture and subsequent coolant-breeder interaction. The coolant velocity is capped at 7 m/s to mitigate irradiation-induced corrosion and erosion. Multiple tube configurations are viable within the BZ, aiming for symmetrical temperature distribution in the breeder while minimizing the structural material to avoid compromising tritium breeding efficiency. Manifolds, housed in cavities within the BSS, fuel both cooling systems, while toroidal collectors serve as intermediaries between the manifolds and connection pipes [58].

The BZ consists of approximately 120 elementary cells. These cells feature a modular geometry, as the one depicted in Figure 2.9, that is ideally consistent throughout the vertical span of the segment. Minor modifications are introduced to adapt to the variations in segment width.

2.7 BZ and PbLi piping network

The PbLi loop system has been designed to circulate the fluid throughout the blanket at a designated operational temperature of roughly $328°C$. The entire volume of liquid metal, which approximates to about $1000\,m^3$, is segmented into six individual loops. These loops can be broadly categorized into two distinct sections: the ex-vessel loop and the in-vessel loop.

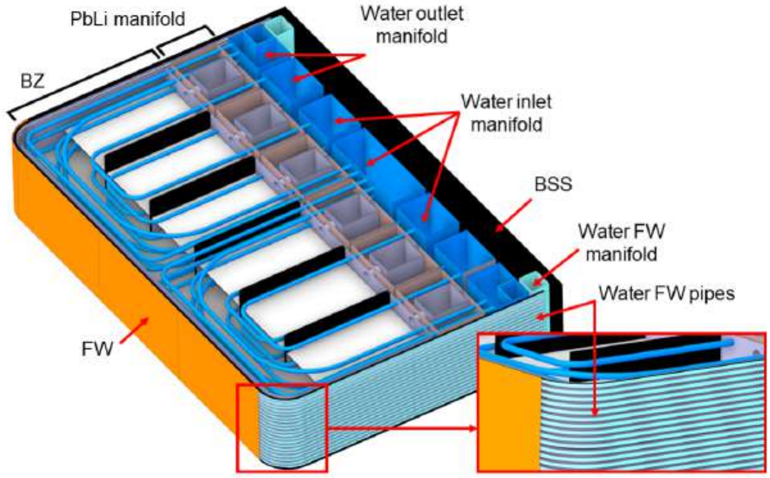

Figure 2.9: WCLL2018 OB elementary cell. The BSS and the poloidal-radial SP are black, the toroidal-radial SP dark grey, the baffle plates light grey, the FW orange, the water manifold and pipes are blue and the FW manifold and pipes are cyan. Lateral FW plates removed for clarity [6].

The ex-vessel loop is a composite of multiple components and is often referred as the Tritium Extraction and Removal System (TER): a charge tank, a storage tank, an expansion tank, a safety tank, a pumping assembly, a heat exchanger, a purification system, and the Tritium Extraction Unit (TEU). Mechanical pumps are utilized for the purpose of circulating the PbLi, primarily because they offer superior efficiency compared to electromagnetic or permanent magnet pumps. Two rings, one above and one below the reactor, are tasked with conveying and retrieving the breeder from the pipes connecting the TER to the single BB sectors; the interface between ex-vessel and in-vessel loop [54].

Contrastingly, the in-vessel loop is an intricate array of various interconnected elements, that can be described as follows:

- **Feeding Pipe (FP)**: This component is responsible for supplying each blanket segment with fresh PbLi that originates from the ex-vessel loop. The pipe typically traverses through the VV lower port.
- **Bottom Collector (BC)**: Positioned at the lower extremity of the blanket, it functions to collect PbLi from the FP and direct it towards the PbLi manifold.
- **PbLi Manifold**: Located in an intermediary position between the water

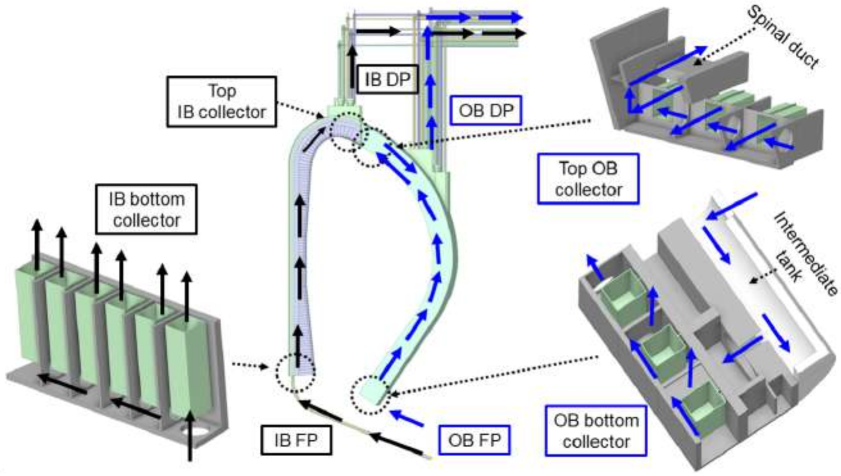

Figure 2.10: WCLL2018 In-Vessel PbLi Circulation. The PbLi trajectory is denoted by continuous arrows: black for the Inboard (IB) and blue for the Outboard (OB). Detailed views of the structural and flow patterns for the bottom collector of the IB and half OB, as well as the top collector for half OB [6].

coolant manifold and the Breeding Zone (BZ), this manifold is charged with the task of both disseminating and retrieving PbLi amongst the vertically arranged breeding cells.

- **Breeding Zone**: Within this zone, the PbLi predominantly flows in radial orientations along horizontal planes, and does so at an approximate speed of $0.2\,mm/s$ [58].
- **Top Collector (TC)**: This is situated at the uppermost region of the blanket. It serves to guide the PbLi flow from the manifold to the Draining Pipe (DP).
- **Draining Pipe (DP)**: This component achieves the final step in the loop by withdrawing tritium-enriched PbLi from the blanket and channeling it back into the ex-vessel loop.

Additional specifics concerning the architectural and functional nuances of the Bottom and Top Collectors, especially as they pertain to InBoard (IB) and OutBoard (OB) segments, as well as the precise routing and affixing details for the DP, can be consulted in [54] and are visually represented in Figure 2.10.

2.8 DCLL

The DCLL represents a prospective BB configuration that is designed to operate at elevated temperatures ($T \approx 700°C$), thereby achieving thermal efficiencies exceeding 40%. In this model, the PbLi serves dual roles: as a tritium breeder and as the primary coolant responsible for extracting the heat deposited by neutrons. The role of eliminating the surface heat flux and cooling the First Wall is allocated to high-pressure helium, typically maintained at 8 MPa. Various DCLL designs have been put forward by European, American and Chinese scientists [7, 8, 59–61].

The focus in this work is on the European design, which is based on its latest iteration [7]. The blanket consists of 16 identical toroidal sectors, each subdivided into three OB zones and two IB zones. Contrary to the WCLL design, DCLL configurations until 2017 utilized a Multi Module Segment (MMS) architecture where each segment is made up of 8 modules. Every module is affixed to a common BSS, constructed from EUROFER like all structural components. The BSS serves not just mechanical functions but also acts as a manifold for both PbLi and helium. Specifically, two large, rectangular PbLi channels along with four helium channels are incorporated into the BSS in the poloidal direction, as depicted in Figure 2.11 [7]. Recent investigations have been conducted to transition to a Single Module System (SMS) arrangement.

The PbLi coolant primarily flows in the poloidal direction via eight parallel channels arranged along the toroidal axis. A 2-mm tungsten layer covers the FW, which is cooled by helium channels. The BZ features two types of channels: front channels adjacent to the FW, which handle higher thermal flux, and rear channels positioned further from the plasma. The PbLi circulates upward in the front channels, makes a U-turn at the module top, and then flows downward in the rear channels, entering through a collector that divides into these channels [7].

A pivotal element in this design is the Flow Channel Inserts (FCIs), which are alumina-based layers purposed for mitigating MHD effects and thermally isolating the EUROFER from the hot PbLi coolant. Despite the low LM velocity ($\approx 1\,\text{cm/s}$), the electrical conductivity of steel-based structural materials would adversely impact the blanket performance due to substantial pressure losses and induced mechanical stress. Both naked alumina and steel-alumina-steel sandwich layers may serve as

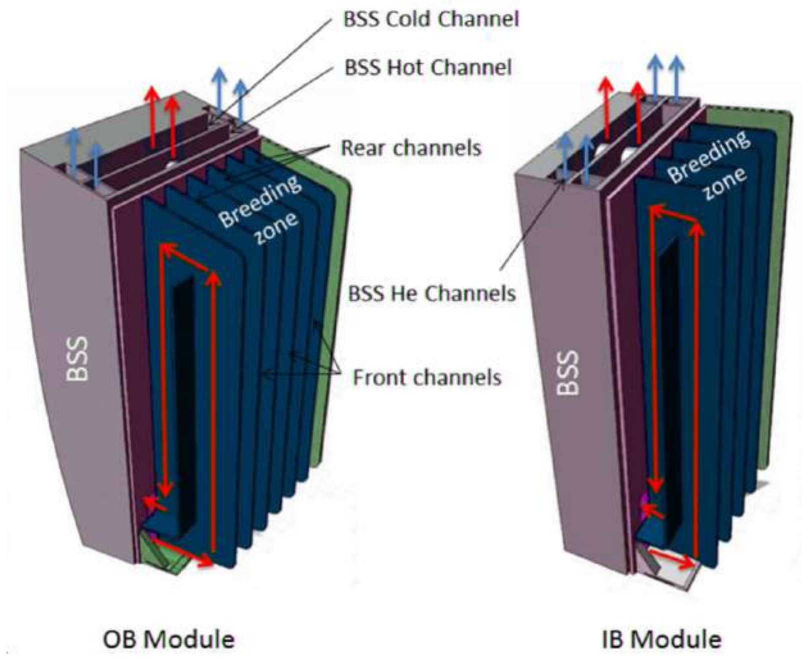

Figure 2.11: OB equatorial module on the left and IB equatorial module on the right. PbLi flows are shown in red and the He one in blue [7].

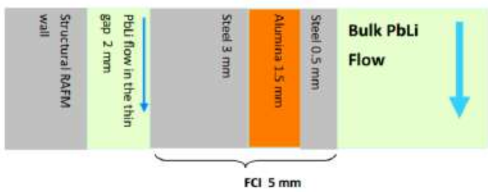

Figure 2.12: Structure of a typical sandwich-type FCI [8].

electrical insulators, with the latter option favoured. These FCIs define two flow regions within the PbLi channels: a bulk flow region and a gap flow region. The layer configuration impacts the rate of flow partitioning between these two regions (see Figure 2.12). For a naked alumina layer, the gap flow remains almost stagnant, but it significantly decreases the PbLi coolant performance despite a minimal pressure drop in the bulk flow. In contrast, sandwich-type FCIs enable significant gap flow, which improves heat removal capabilities at the expense of an increased pressure drop due to amplified MHD effects [7].

2.9 The TBM program

In the framework of this thesis, it is deemed useful to present the Test Blanket Module program in more detail, since TBM-related calculations have been performed by the author.

A Tritium Breeding Blanket (TBB) is indispensable for a demonstration power reactor (DEMO), which is the next phase following ITER. While ITER itself does not require a TBB, as it obtains tritium from external sources, tritium breeding modules are among ITER stated objectives. This endeavor is encapsulated within the "ITER Test Blanket Module (TBM) Program", a vital initiative for the fusion development plans of all seven ITER Members (IMs) [9]. As of 2018, the ITER TBM Program has seen significant advancements, both organizationally and technically. A specialized TBM project team was established. Moreover, the Test Blanket Systems (TBSs) are now configured in two Equatorial Ports, allowing for the operation of four TBSs, as opposed to the original three ports and six TBSs. This modification alleviates spatial and integration challenges within the Tokamak Complex but limits the number of concurrently operating TBSs to four, even if the potential to test six different TBSs throughout ITER lifespan is in principle retained [9, 53].

The TBSs selected for initial testing in ITER are under consideration, with options including two water-cooled and two helium-cooled systems. These could potentially utilize lithium-ceramic pebbles or a lithium-lead alloy as breeders. These TBSs are slated to commence operations during ITER final non-nuclear phase, with the possibility of other TBS types being introduced in later nuclear phases. Progress has been made in designing the infrastructure needed for these four TBSs, including elements such as port plugs, common port cell components, and maintenance tools and equipment [9]. The TBS connection pipes system is in its final development stage, as these components must be installed prior to achieving First Plasma. Unlike other ITER components, which are designed based solely on ITER-specific criteria, the functional characteristics of the TBSs are informed by the operational conditions anticipated for a DEMO-TBB system. Additionally, the integration and safety considerations for TBSs take into account that ITER is classified as a French Nuclear Facility under the designation INB-174.

Each TBS operates independently, with two distinct TBSs sharing a common

Port Plug (PP) and Port Cell (PC) area within each of the two equatorial ports (see Figure 2.13). In-vessel components of the TBSs are referred to as Test Blanket Modules (TBM), each paired with a TBM-shield to form a TBM-Set. These TBM-Sets are mounted in a water-cooled steel frame, creating a TBM PP. If a TBM-Set is unavailable, a Dummy TBM will take its place. Operations for TBSs are planned to commence during the non-nuclear phase "Pre-Fusion Power Operation-2" (PFPO-2) and will continue through the high-duty D-T phase, which involves long pulses and sustained operations.

The testing approach includes the iterative replacement and modification of TBM components to adapt to ITER operational requirements [9]. The TBM replacement strategy involves full TBM PP replacement during major shutdowns, known as "Long Term Maintenance" periods. Off-line refurbishment takes place in the Hot Cell, necessitating the availability of additional frames. These frames must be Remote-Handling (RH) compatible, imposing constraints on their design. Pre-installation leak tests for each TBM PP are conducted in the ITER Port Plug Test Facility. TBS components are situated partly in PCs behind the bio-shield and elsewhere in the tokamak complex. These components are mounted in a self-sustaining structure known as the Ancillary Equipment Unit, and connected to a structure referred to as the Pipe Forest (PF) [9].

Associated subsystems of each TBS may include:

- Primary Cooling System, either Helium or pressurized water.
- Coolant Purification System.
- Tritium Extraction System.
- Pb16Li system, also serving as a Tritium carrier.
- Tritium Accountancy System.
- Instrumentation & Control System.
- Neutron Activation System for local neutron flux measurement.

Each TBS sub-system shares similarities with its counterpart in another TBS, and some may serve multiple functions, such as coolant and breeder.

In an earlier phase of the TBM programme, six TBM designs had passed the IO Conceptual Design Review. They are listed below including the country that proposed them:

- Helium-Cooled Lithium Lead (HCLL) - EU
- Helium-Cooled Pebble-Bed (HCPB) - EU
- Water-Cooled Ceramic Breeder (WCCB) - Japan
- Helium-Cooled Ceramic Reflector (HCCR) - Korea
- Helium-Cooled Ceramic Breeder (HCCB) - China
- Lithium-Lead Ceramic Breeder (LLCB) - India

Three additional TBM designs were later included to the list:

- Water-Cooled Lithium Lead (WCLL) - EU
- Dual-Coolant Lithium Lead (DCLL) - US
- Helium-Cooled Solid Breeder (HCSB) - India

These additions share safety characteristics with the initial six, making them compatible for the program. In Table 2.1 are collected the main features of the nine systems.

An ongoing assessment aims to select the four TBSs to be operated in the final non-nuclear phase of ITER, known as PFPO-2, starting in 2032. The chosen TBSs, termed the "Initial Configuration (InCo)," must be delivered by the end of 2029 and secure design approval by 2025. Each InCo TBS will require four cooling pipes in the TBM vertical shafts, as all proposed systems employ a single coolant. The Initial Configuration (InCo) will likely comprise six TBSs: WCLL, WCCB, HCPB, HCCR, HCCB, and the newly developed HCSB. Design modifications are anticipated if shared development occurs between multiple Implementing Members.

2.10 Summary

This chapter provided an overview of the principles of nuclear fusion and the associated reactor technologies, emphasizing European research initiatives in magnetic-

Table 2.1: Main Characteristics of the TBMs and main operating parameters of the associated TBSs [9].

TBM Type	Main Characteristics
Water-Cooled Lithium Lead (WCLL) TBM, proposed by EU [30]	EUROFER97 Steel (structure), Pb16Li (multiplier/breeder) Coolant: H2O at 15.5 MPa, 280/325°C; T-removal gas: Helium + 0.1 %H2 at 0.4 MPa
Helium-Cooled Pebble-Bed (HCPB) TBM, proposed by EU [62]	EUROFER97 Steel (structure), Be pebbles (multiplier); Li4SiO4 or Li2TiO3 pebbles (breeder) Coolant: He at 8 MPa, 300/500°C Purge gas: Helium + 0.1 %H2 at 0.4 MPa
Water-Cooled Ceramic Breeder (WCCB) TBM, proposed by Japan [63, 64]	F82H Steel (structure), Be pebbles (multiplier), Li2TiO3 pebbles (breeder) Coolant: H2O at 15.5 MPa, 280/325°C Purge gas: He + 0.1 %H2 at 0.1 MPa
Lithium-Lead Ceramic Breeder (LLCB) TBS, proposed by India [65]	IN-RAFM Steel (structure), Pb16Li (multiplier), Pb16Li & Li2TiO3 pebbles (breeders) Coolants: He (8 MPa, 300/340°C) & Pb16Li (1.2 MPa, 300/460°C) Purge gas: Helium + 0.1 %H2 at 0.12–0.15 MPa
Dual-Coolant Lithium-Lead (DCLL) TBM, proposed by US [66]	RAFM Steel (structure), Pb16Li (multiplier and coolant); Coolant: He (8 MPa, 300/tbd°C) & Pb16Li (1.2 MPa, 300/tbd°C) T-removal gas: Helium + 0.1 %H2 at 0.4 MPa
Helium-Cooled Ceramic Breeder (HCCB) TBM, proposed by China [67]	RAFM Steel (structure), Be pebbles (multiplier), Li4SiO4 pebbles (breeder); Coolant: Helium at 8 MPa, 300/500°C Purge gas: He + 0.1 %H2 at 0.3 MPa
Helium-Cooled Lithium Lead (HCLL) TBM, proposed by EU [68]	EUROFER97 Steel (structure), Pb-16Li (multiplier/breeder); Coolant: Helium at 8 MPa, 300/500°C T-removal gas: Helium + 0.1 %H2 at 0.4 MPa
Helium-Cooled Solid Breeder (HCSB), proposed by India [69]	IN-RAFM Steel (structure), Be-pebbles (multiplier), Li2TiO3 pebbles (breeder); Coolant: He at 8 MPa, 300/500°C Purge gas: He + 0.1 %H2 at 0.12–0.15 MPa

confinement technology. The Water-Cooled Lead Lithium (WCLL) blanket is particularly noted due to its significance in the dissertation case studies. Even with six decades of intensive research and numerous advancements in plasma confinement, no fusion reactor has yet managed to sustain a burning plasma that yields net energy

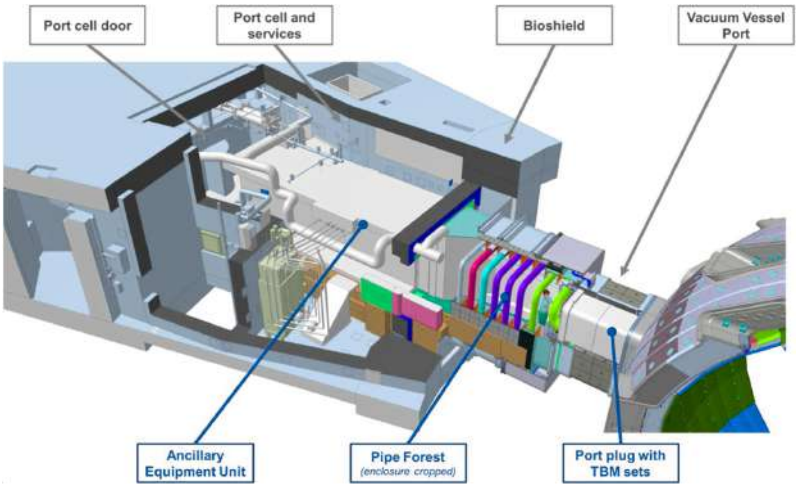

Figure 2.13: View of the 3D model of the main TBM Port Cell components [9].

for extended periods. The ITER project is set to achieve this milestone by 2035. The EUROfusion Consortium is at the forefront of European R&D, focusing on the next step, DEMO, anticipated to demonstrate the feasibility of a Fusion Power Plant (FPP) for electricity production by 2050. Realizing a closed fuel cycle, particularly the onsite synthesis and handling of tritium, is crucial for the success of DEMO. In this context, the evolution of a Breeding Blanket (BB) is essential. As part of the Test Blanket Module (TBM) program, ITER will assess various blanket designs. A number of BB projects propose the use of liquid metals (LMs) as primary coolants due to their superior thermal properties. Nonetheless, their interaction with the reactor magnetic confinement presents challenges that need meticulous attention. The subsequent chapter delves into the magnetohydrodynamics that characterizes these phenomena.

Chapter 3

Magnetohydrodynamics fundamentals

3.1 Introduction

Magnetohydrodynamics is a subfield of fluid dynamics focused on the behavior of electrically conductive fluids in the presence of magnetic fields. The motion of electric charges in the fluid creates a complex, non-linear interplay between fluid velocity and electromagnetic fields. This necessitates the coupling of Navier-Stokes and Maxwell equations to form a unified set of governing equations. Initial research in this area can be traced back to Julius Hartmann's 1937 studies on what is now known as the electromagnetic conduction pump [70, 71]. However, the term "magnetohydrodynamics" was first coined in the work of Hannes Alfvén in 1942 [72], for which he received the Nobel Prize in Physics in 1970. The 1950s marked a period of rapid advancement in diverse scientific and technological disciplines including geomagnetism, astrophysics, plasma physics, liquid metal technology, and nuclear fusion [73].

This chapter aims to provide a concise overview of MHD flows in incompressible fluids like liquid metals, focusing on phenomena pertinent to fusion reactor technology. The primary reference for this chapter is [74], while a comprehensive historical review of MHD is available in [73]. For in-depth discussions on fluid dynamics and electromagnetic considerations, the reader is referred to [75] and [76], respectively.

3.2 Incompressible MHD

In the context of LM-MHD, several classical assumptions can be employed to simplify the derivation of the governing equations. Specifically, the fluid is considered to be:

- Continuous, allowing the neglect of molecular structure and motions at macroscopic scales.
- Homogeneous and isotropic, implying that physical properties are uniform and mechanical properties are invariant with respect to direction.
- Newtonian, such that the the local rates of deformation due to viscous stresses are proportional to the fluid velocity gradients.
- Incompressible, with a density that is independent of the pressure field.
- Characterized by temperature-independent material properties.

The Lorentz force captures the influence of an electric field $\mathbf{E}$ and a magnetic field $\mathbf{B}$ on the electric charge density ρ_e within a conductive fluid particle.

$$\mathbf{F}_L = \rho_e \mathbf{E} + \mathbf{j} \times \mathbf{B} \tag{3.1}$$

The first term, often referred to as the Coulomb force, represents the electrostatic component, whereas the second term is the magnetic component acting on the electric current density $\mathbf{j}$. Incorporating $\mathbf{F}_L$ as a source term in the momentum equation and Joule dissipation $\mathbf{j}^2/\sigma$ in the energy equation, the continuity, Navier-Stokes, and energy equations take the form:

$$\nabla \cdot \mathbf{u} = 0 \tag{3.2}$$

$$\rho \left[\frac{\partial \mathbf{u}}{\partial t} + (\mathbf{u} \cdot \nabla)\mathbf{u} \right] = -\nabla p + \rho \nu \nabla^2 \mathbf{u} + \mathbf{F}_L + \mathbf{S}_M \tag{3.3}$$

$$\rho c_p \left[\frac{\partial T}{\partial t} + (\mathbf{u} \cdot \nabla) T \right] = \kappa \nabla^2 T + \frac{\mathbf{j}^2}{\sigma} + S_E \tag{3.4}$$

Here, $\mathbf{u}$, t, p, and T denote velocity, time, pressure, and temperature, respectively. The symbols ρ, ν, c_p, and κ represent density, kinematic viscosity, specific heat capacity, and thermal conductivity, respectively. $\mathbf{S}_M$ and S_E are the source terms for momentum and energy.

Equation 3.2 outlines the conservation of mass for an incompressible fluid. Equation 3.3 covers the conservation of linear momentum, balancing temporal and convective terms against surface forces and volumetric forces such as electromagnetic and gravitational forces. Equation 3.4 represents the conservation of thermal energy, taking into account conductive, advective, and Joule dissipation terms, as well as other non-electromagnetic sources like chemical or nuclear reactions.

$$\nabla \cdot \mathbf{E} = \frac{q}{\epsilon} \tag{3.5}$$

$$\nabla \cdot \mathbf{B} = 0 \tag{3.6}$$

$$\nabla \times \mathbf{E} = -\frac{\partial \mathbf{B}}{\partial t} \tag{3.7}$$

$$\nabla \times \mathbf{B} = \mu_m \left(\mathbf{j} + \epsilon \frac{\partial \mathbf{E}}{\partial t} \right) \tag{3.8}$$

$$\mathbf{j} = \sigma \left(\mathbf{E} + \mathbf{u} \times \mathbf{B} \right) \tag{3.9}$$

In these equations, ϵ and μ_m denote the electric permittivity and magnetic permeability, respectively. Equations 3.5 and 3.6 articulate Gauss's laws for electric and magnetic fields, indicating the role of charge density and the solenoidality of the magnetic field. Equations 3.7 and 3.8 elaborate on Faraday's and Ampère's laws, describing the electromagnetic induction phenomenon. Equation 3.9 is valid under specific assumptions, such as the negligible velocity of charge carriers relative to the fluid velocity and the absence of thermoelectric voltage sources.

If the low frequency approximation is enforced, the displacement current term $\frac{\partial \mathbf{E}}{\partial t}$ can be neglected, simplifying Equation 3.8 to:

$$\nabla \times \mathbf{B} = \mu_m \mathbf{j} \tag{3.10}$$

Applying the divergence operator to Equation (3.10) and using the identity $\nabla \cdot$

$(\nabla \times \mathbf{B}) = 0$, the current density continuity equation is derived:

$$\nabla \cdot \mathbf{j} = 0 \tag{3.11}$$

For liquid metals, further simplifications can be applied. The quasi-neutral approximation is particularly useful, allowing the electric charge density to be neglected:

$$\frac{|q\mathbf{E}|}{|\rho(\mathbf{u} \cdot \nabla)\mathbf{u}|} \approx \frac{\epsilon \mathbf{B}^2}{\rho} \ll 1 \tag{3.12}$$

With this approximation, the Lorentz force simplifies to:

$$\mathbf{F_L} = \mathbf{j} \times \mathbf{B} \tag{3.13}$$

Combining Equations 3.2, 3.3, 3.4, 3.7, 3.9, and 3.10, we obtain a closed system of 14 scalar equations with 14 variables: p, T, and the three components each of $\mathbf{u}$, $\mathbf{E}$, $\mathbf{B}$, and $\mathbf{j}$. The inclusion of Equation 3.6 ensures the solenoidality of $\mathbf{B}$ and $\mathbf{j}$.

3.2.1 Induction formulation

In cases where isothermal conditions prevail, it is often advantageous to reduce the complexity of the problem by employing only the magnetic field $\mathbf{B}$ as the fundamental electromagnetic variable in Equation 3.3. This leads to the magnetic induction formulation of the MHD governing equation. By substituting the Lorentz force in Equation 3.13 using Ampere's law (Equation 3.8), we obtain:

$$\mathbf{F_L} = \frac{1}{\mu_m} \left(-\nabla \frac{\mathbf{B}^2}{2} + \nabla \cdot (\mathbf{BB}) \right) \tag{3.14}$$

where $\nabla \left(\frac{\mathbf{B}^2}{2} \right)$ is termed the magnetic pressure.

Upon applying the curl operator to Ohm's law (Equation 3.9), and substituting $\mathbf{E}$ and $\mathbf{j}$ from Faraday's and Ampere's laws, we obtain the magnetic induction equation:

$$\frac{\partial \mathbf{B}}{\partial t} + (\mathbf{u} \cdot \nabla)\mathbf{B} = \frac{1}{\mu_m \sigma} \nabla^2 \mathbf{B} + (\mathbf{B} \cdot \nabla)\mathbf{u} \tag{3.15}$$

This equation describes the temporal evolution of $\mathbf{B}$, accounting for advection, diffusion, and field production due to mechanical stretching by the velocity field.

The quantity $\frac{1}{\mu_m \sigma}$ serves as the magnetic diffusivity.

Subsequently, the governing equations reduce to:

$$\nabla \cdot \mathbf{u} = 0 \tag{3.16}$$

$$\rho \left(\frac{\partial \mathbf{u}}{\partial t} + (\mathbf{u} \cdot \nabla)\mathbf{u} \right) = -\nabla p + \rho \nu \nabla^2 \mathbf{u} + \frac{1}{\mu_m} \left(-\nabla \frac{\mathbf{B}^2}{2} + \nabla \cdot (\mathbf{BB}) \right) + \mathbf{S_M} \tag{3.17}$$

$$\rho c_p \left(\frac{\partial T}{\partial t} + (\mathbf{u} \cdot \nabla)T \right) = \kappa \nabla^2 T + \frac{1}{\sigma} |\nabla \times \mathbf{B}|^2 + \mathbf{S_E} \tag{3.18}$$

$$\frac{\partial \mathbf{B}}{\partial t} + (\mathbf{u} \cdot \nabla)\mathbf{B} = \frac{1}{\mu_m \sigma} \nabla^2 \mathbf{B} + (\mathbf{B} \cdot \nabla)\mathbf{u} \tag{3.19}$$

Thus, the final system comprises 8 scalar equations for 8 variables ($\mathbf{u}$, p, $\mathbf{B}$, and T) in the general case, and reduces to a 7x7 system for the isothermal case. Therefore in MHD scenarios, the magnetic field and velocity field are intrinsically interconnected through a bi-directional and non-linear coupling mechanism. This connection is evident in both the momentum and magnetic induction equations, where variables $\mathbf{B}$ and $\mathbf{u}$ coexist. Additionally, electric currents $\mathbf{j}$ are generated due to the relative motion between the conducting fluid and the magnetic field. These currents subsequently induce a self-generated magnetic field $\mathbf{b}$, as dictated by Ampere's law. Thus, the overall magnetic field $\mathbf{B}$ can be expressed as:

$$\mathbf{B} = \mathbf{B}_0 + \mathbf{b} \tag{3.18}$$

Here, $\mathbf{B}_0$ represents the externally applied magnetic field.

3.3 Dimensionless parameters

It is a common practice in scientific research to compare the magnitudes of terms in governing equations to gain insights into the dominant phenomena under specific conditions. A helpful way to achieve this is by rendering the equations in dimensionless form, which enables us to identify the relevant non-dimensional parameters. These parameters can reveal which terms may be neglected for simplification.

For the magnetic induction equation (Equation 3.15), we choose the following scales to non-dimensionalize the variables:

- Length scale L

- Velocity scale u_0
- Magnetic field scale B_0

The variables are then re-scaled as:

$$\nabla \rightarrow \frac{\nabla}{L} \tag{3.20}$$

$$\mathbf{u} \rightarrow \mathbf{u}u_0 \tag{3.21}$$

$$t \rightarrow \nabla \frac{t}{u_0} \tag{3.22}$$

$$\mathbf{B} \rightarrow \mathbf{B}B_0 \tag{3.23}$$

Substituting these into Equation 3.15, we arrive at the dimensionless magnetic induction equation:

$$\frac{\partial \mathbf{B}}{\partial t} + (\mathbf{u} \cdot \nabla)\mathbf{B} = \frac{1}{\mathrm{R}_m}\nabla^2\mathbf{B} + (\mathbf{B} \cdot \nabla)\mathbf{u} \tag{3.24}$$

Here, R_m is the magnetic Reynolds number defined as:

$$\mathrm{R}_m = \mu_m \sigma u_0 L \tag{3.25}$$

This dimensionless form of the magnetic induction equation allows us to understand the relative importance of the terms, thereby guiding us in making reasonable approximations for specific scenarios.

The Magnetic Reynolds number R_m gauges the balance between magnetic field advection and diffusion. For $\mathrm{R}_m \ll 1$, diffusion dominates, causing the magnetic field to smooth out any perturbations induced by fluid motion. In contrast, when $\mathrm{R}_m \gg 1$, the transport of the magnetic field is mainly due to fluid convection, enabling phenomena such as magnetic self-excitation. This is prevalent in dynamo problems and cosmic phenomena where R_m ranges from 10^4 to 10^{10} [77]. In liquid metal magnetohydrodynamics flows, R_m usually lies around 10^{-2} or lower due to relatively small values of u_0 and L.

Continuing with the same scales as in Equation 3.24, we introduce additional scale transformations as follows:

$$p \to p\rho u_0^2 \tag{3.26}$$

$$\mathbf{j} \to \mathbf{j}\sigma u_0 B_0 \tag{3.27}$$

$$\mathbf{S}_M \to \mathbf{S}_M \frac{u_0^2}{L} \tag{3.28}$$

With these transformations, the momentum equation (Equation (3.17)) can be rearranged into:

$$\frac{\partial \mathbf{u}}{\partial t} + (\mathbf{u} \cdot \nabla)\mathbf{u} = -\nabla p + \frac{1}{\mathrm{Re}}\nabla^2 \mathbf{u} + \frac{\mathrm{N}}{\mathrm{R}_m}\left(-\nabla \frac{\mathbf{B}^2}{2} + \nabla \cdot (\mathbf{BB})\right) + \mathbf{S}_M \tag{3.29}$$

Here, $\mathrm{Re} = \frac{u_0 L}{\nu}$ is the classic Reynolds number and $\mathrm{N} = \frac{\sigma B_0^2 L}{\rho u_0}$ is the interaction parameter, sometimes referred to as the Stuart number.

The Reynolds number quantifies the ratio of inertial to viscous forces and is a key parameter for determining the flow regime. For instance, the transition from laminar to turbulent flow in a circular pipe occurs at $\mathrm{Re} \approx 2300$. In the context of fusion reactors with LM flow, typical Reynolds numbers vary between 10^4 and 10^5.

The interaction parameter N signifies the balance between electromagnetic and inertial forces. When $\mathrm{N} \ll 1$, traditional hydrodynamic phenomena dominate; conversely, for $\mathrm{N} \to \infty$, the flow becomes inertialess and turbulence structures are suppressed [10].

This interaction parameter also serves to characterize the magnetic field impact on turbulence. It represents the ratio of the large-eddy turnover time $\frac{L}{u_0}$ to the magnetic damping time $\frac{\rho}{\sigma B_0^2}$, quantifying the rate at which the magnetic field dissipates kinetic energy through the Joule effect [10, 74].

In fluid dynamics, a boundary layer develops when fluid flows over a solid surface, transitioning from the free-stream velocity to the no-slip boundary condition at the surface. In ordinary flow, the boundary layer thickness δ is approximately $\frac{L}{\sqrt{\mathrm{Re}}}$. However, in MHD flows, the boundary layer is governed by the balance between electromagnetic and viscous forces. This balance is captured by the Hartmann number, defined as:

$$\mathrm{Ha} = \sqrt{\mathrm{N} \cdot \mathrm{Re}} = \frac{LB_0\sqrt{\sigma}}{\sqrt{\rho\nu}} \tag{3.30}$$

The Hartmann number quantifies the intensity of the magnetic field and is crucial for assessing how an MHD system deviates from a purely hydrodynamic one. For $\mathrm{Ha} \gg 1$, the flow can be approximated as inviscid, with viscous effects confined to thin boundary layers near the walls. In fusion reactors with LM flows, typical Hartmann numbers are on the order of 10^4.

Subsequently, by applying the same scaling factors in Equation 3.24, we introduce further transformations for the temperature and source term in the energy equation as:

$$T \to T\Delta T_0 \tag{3.31}$$

$$SE \to SE\frac{\rho c_p u_0 \Delta T_0}{L} \tag{3.32}$$

The dimensionless form of the energy equation thus becomes:

$$\frac{\partial T}{\partial t} + (\mathbf{u} \cdot \nabla)T = \frac{1}{\mathrm{Pe}}\nabla^2 T + \mathrm{EcN}\mathbf{j}^2 + SE \tag{3.33}$$

Here, $\mathrm{Pe} = \frac{\rho c_p u_0 L}{\kappa}$ is the Péclet number, discussed in the the following, and $\mathrm{Ec} = \frac{u_0^2}{c_p \Delta T_0}$ is the Eckert number. The latter quantifies the ratio between kinetic energy and enthalpy in the system. The term EcN describes the ratio of energy dissipated due to Joule heating to the accumulated enthalpy [74].

For other equations, the dimensionless form is not presented as they remain nearly identical to their dimensional counterparts.

3.4 Inductionless formulation

In preceding sections, the magnetic Reynolds number $\mathrm{Re}_m = \mu_m \sigma L u_0$ and the self-induced magnetic field $\mathbf{b}$ generated by the fluid motion through $\mathbf{B}_0$ were introduced. It was established that for $\mathrm{Re}_m \ll 1$, the coupling between fluid velocity and the magnetic field is notably weakened. In a uniform external field $\mathbf{B}_0$, the total magnetic field $\mathbf{B} = \mathbf{B}_0 + \mathbf{b}$ has non-zero spatial derivatives only due to the induced component. Thus, it can be expressed as:

$$|\nabla \times \mathbf{B}| = |\nabla \times \mathbf{b}| \approx \frac{b}{L} \approx \mu_m j \tag{3.34}$$

A subsequent analysis of Ohm's law indicates that both terms on the right-hand side are of similar magnitude, leading to the following approximation:

$$|\mathbf{j}| \approx \sigma[E + u_0 B_0] \lesssim \sigma u_0 B_0 \Rightarrow b \lesssim \mu_m \sigma L u_0 B_0 \approx \mathrm{Re}_m B_0 \Rightarrow \frac{b}{B_0} \approx \mathrm{Re}_m \tag{3.35}$$

For LM-MHD flows, $\mathrm{Re}_m \ll 1$ is typically observed, legitimizing the low-Re_m approximation, where $\mathbf{b} = 0$ and $\mathbf{B} = B_0$, fixed as boundary and initial conditions. Under a uniform and stationary $\mathbf{B}_0$, the equations simplify through the inductionless approximation. Given that the electric field is irrotational, it can be expressed as $E = -\nabla\phi$, turning Ohm's law into:

$$\mathbf{j} = \sigma(-\nabla\phi + \mathbf{u} \times \mathbf{B}_0) \tag{3.36}$$

By incorporating charge conservation, the Poisson equation for electric potential follows:

$$\nabla^2\phi = \nabla \cdot (\mathbf{u} \times \mathbf{B}_0) \tag{3.37}$$

This approach, known as the electric potential formulation or ϕ-formulation, is especially advantageous in numerical analyses of LM-MHD flows, as solving the scalar Poisson equation is computationally less demanding than solving the vector magnetic induction equation.

To render the governing equations dimensionless, we employ the scaling parameters from Section 3.3, introducing an additional electric potential scale and a slightly different one for the pressure:

$$p \rightarrow p\sigma u_0 B_0^2 L \tag{3.38}$$

$$\phi \rightarrow \phi u_0 B_0 L \tag{3.39}$$

The resulting dimensionless governing MHD equations for the inductionless approximation are:

$$\nabla \cdot \mathbf{u} = 0 \tag{3.40}$$

$$\frac{1}{\mathrm{N}}\left(\frac{\partial \mathbf{u}}{\partial t} + (\mathbf{u}\cdot\nabla)\mathbf{u}\right) = -\nabla p + \frac{1}{\mathrm{Ha}^2}\nabla^2\mathbf{u} + \mathbf{j}\times\mathbf{B}_0 \tag{3.41}$$

$$\nabla^2\phi = \nabla\cdot(\mathbf{u}\times\mathbf{B}_0) \tag{3.42}$$

$$\mathbf{j} = \sigma(-\nabla\phi + \mathbf{u}\times\mathbf{B}_0) \tag{3.43}$$

A limitation of these simplified equations is the absence of the $\nabla \cdot \mathbf{B} = 0$ condition, therefore the charge conservation is not explicitly required, potentially leading to unphysical current fields in numerical schemes where the Lorentz force is implemented in a non-conservative manner.

3.5 Magneto-convection

Turning our attention to a non-isothermal and induction-free MHD flow, temperature is incorporated as an additional variable, necessitating the derivation of an equation that accounts for the energy balance within the fluid to complete the set of governing equations. In this context, the Lorentz Force is not the sole body force at play in the momentum equation; it becomes essential to take into account buoyancy forces that emerge from density gradients within the fluid. In formulating the energy balance, both the effects of expansion or contraction work are disregarded, owing to the incompressible nature of the fluid. Furthermore, we apply the Boussinesq approximation to omit the temperature dependence of the density, except in the buoyant body force term where the density is presumed to be a linear function of temperature.

In light of these considerations, the equation representing the energy balance in a given fluid volume can be expressed as

$$\rho c_p\left[\frac{\partial T}{\partial t} + (\mathbf{u}\cdot\nabla)\,T\right] = \kappa\nabla^2 T + \frac{1}{\sigma}J^2 + \Phi + Q \tag{3.44}$$

In this equation, c_p is the specific heat capacity and κ is the thermal conductivity. The terms in Equation (3.44) are interpreted as follows: the rate of change of temperature relies on the balance between incoming and outgoing heat fluxes, including both advective (second term on the left-hand side) and conductive (first term on the right-hand side) contributions, Joule dissipation (second term on the right-hand side), viscous dissipation (Φ), and volumetric heat generation from chemical or nuclear reactions (Q). In the context of liquid-metal MHD flows within fusion reactor blankets, both Joule and viscous dissipation terms are often insignificant relative to the others, simplifying the equation to:

$$\frac{\partial T}{\partial t} + (\mathbf{u} \cdot \nabla)T = \alpha_t \nabla^2 T + Q \tag{3.45}$$

where $\alpha_t = \frac{\kappa}{\rho c_p}$ is the thermal diffusivity.

Turning now to the momentum equation, the density in the buoyancy term can be expressed as a linear function of the temperature:

$$\rho = \rho_0(1 - \beta_0(T - T_0)) \tag{3.46}$$

Here β_0 represents the thermal expansion coefficient. By incorporating the buoyancy body force term $F_B = \rho g$ into as $\mathbf{S}_M$ Equation (3.3) and employing the Boussinesq approximation, the modified momentum equation becomes:

$$\frac{\partial \mathbf{u}}{\partial t} + (\mathbf{u} \cdot \nabla)\mathbf{u} = -\frac{1}{\rho_0}\nabla p_d + \nu \nabla^2 \mathbf{u} + \frac{1}{\rho_0}\mathbf{J} \times \mathbf{B} - \beta_0 g(T - T_0) \tag{3.47}$$

Here, p_d is the dynamic pressure, obtained by subtracting the hydrostatic term from the total pressure. Therefore, the set of equations governing magneto-convection comprises:

$$\nabla \cdot \mathbf{u} = 0 \tag{3.48}$$

$$\frac{\partial \mathbf{u}}{\partial t} + (\mathbf{u} \cdot \nabla)\mathbf{u} = -\frac{1}{\rho_0}\nabla p_d + \nu \nabla^2 \mathbf{u} + \frac{1}{\rho_0}\mathbf{J} \times \mathbf{B} - \beta_0 g(T - T_0) \tag{3.49}$$

$$\nabla^2 \phi = \nabla \cdot (\mathbf{u} \times \mathbf{B}) \tag{3.50}$$

$$\mathbf{J} = \sigma(-\nabla\phi + \mathbf{u} \times \mathbf{B}) \tag{3.51}$$

$$\frac{\partial T}{\partial t} + (\mathbf{u} \cdot \nabla)T = \alpha_t \nabla^2 T + Q \tag{3.52}$$

3.5.1 Additional nondimensional parameters

The dimensionless equations governing magneto-convection can be formulated by extending the scaling methodology delineated in Section 3.3, incorporating an additional term for the characteristic temperature difference ΔT_0. This allows us to normalize the temperature $T - T_0$ and establish $Q_0 = \rho c_p u L_0 \Delta T_0$. In the context of a magneto-convection flow, the characteristic velocity u_0 may be calculated assuming that the main force balance is between Lorentz and buoyancy forces, leading to the expression:

$$u_0 = \frac{\rho_0 \beta_0 g \Delta T_0}{\sigma B_0^2} \tag{3.53}$$

In light of these considerations, the dimensionless equations for magneto-convection manifest as:

$$\frac{Ha^2}{\mathrm{Pr}} \left[\frac{\partial \mathbf{u}}{\partial t} + (\mathbf{u} \cdot \nabla)\mathbf{u} \right] = -\nabla p + \frac{1}{Ha^2} \nabla^2 \mathbf{u} + \mathbf{j} \times \mathbf{B} - gT \tag{3.54}$$

$$\mathrm{Pr} \left[\frac{\partial T}{\partial t} + (\mathbf{u} \cdot \nabla)T \right] = \nabla^2 T + Q \tag{3.55}$$

Here, the dimensionless forms of Equations (3.48), (3.50) and (3.51) are not reiterated as they remain essentially unaltered. This formulation involves three dimensionless groups: the Grashof number Gr, the Hartmann number Ha, and the Prandtl number Pr.

Grashof Number

The Grashof number, denoted as Gr, is formulated as:

$$\mathrm{Gr} = \frac{g\beta \Delta T L^3}{\nu^2} \tag{3.56}$$

This dimensionless quantity is traditionally attributed to Franz Grashof. It serves to quantify the relative importance of buoyancy to viscous forces, acting as a counterpart to the Reynolds number within the realm of free convection flows. In scenarios involving mixed convection, the Richardson number $\mathrm{Ri} = \frac{\mathrm{Gr}}{\mathrm{Re}^2}$ is utilized to assess whether the influence of forced or natural convection can be disregarded. Specifically, forced convection becomes negligible when $\mathrm{Gr}/\mathrm{Re}^2 \gg 1$, and natural convection can be ignored when $\mathrm{Gr}/\mathrm{Re}^2 \ll 1$.

Prandtl Number

The Prandtl number, denoted as Pr, is mathematically defined as:

$$\mathrm{Pr} = \frac{\nu}{\alpha_t} \tag{3.57}$$

Attributed to Ludwig Prandtl, this dimensionless parameter quantifies the relative balance between momentum and thermal diffusivity. When $\mathrm{Pr} \gg 1$, momentum diffusivity prevails, thereby significantly affecting heat transfer through convective mechanisms. This condition results in a temperature boundary layer that is thinner than its velocity counterpart, which is commonly observed in highly viscous and poor thermal conductors, such as engine oils. On the opposite end, for $\mathrm{Pr} \ll 1$, thermal diffusivity dominates, making the velocity boundary layer thinner relative to the temperature one. This is characteristic of fluids like liquid metals that have low viscosity but high thermal conductivity. Importantly, the Prandtl number is independent of the geometrical aspects of the problem and it is function only of fluid properties.

Péclet Number

Traditionally, the Péclet number, denoted as Pe, quantifies the relative influence of advective to diffusive transport rates across various phenomena. In the context of thermo-hydraulics, it is given by:

$$\mathrm{Pe} = \mathrm{Re} \cdot \mathrm{Pr} \tag{3.58}$$

By utilizing the identity $\mathrm{Re} = \frac{\mathrm{Gr}}{\mathrm{Ha}^2}$, the Péclet number for magneto-convective flows can be reformulated as:

$$\mathrm{Pe} = \frac{\mathrm{Gr} \cdot \mathrm{Pr}}{\mathrm{Ha}^2} \tag{3.59}$$

Here, $\mathrm{Gr} \cdot \mathrm{Pr}$ is recognized as the Rayleigh number, Ra. This particular definition of the Péclet number serves to gauge the impact of inertial effects in Equation (3.55). Specifically, when $\mathrm{Pe} \ll 1$, the flow can be considered as nearly inertia-less in terms of energy balance.

Nusselt Number

The Nusselt number, although not explicitly appearing in the system of dimensionless equations, serves as a pivotal parameter for governing heat transfer mechanisms and will be utilized in the present thesis. Denoted as Nu, it represents the effectiveness of convective heat transfer relative to conductive heat transfer. Mathematically, it is expressed as:

$$\mathrm{Nu} = \frac{hL}{k} \tag{3.60}$$

where h is the convective heat transfer coefficient, L is the characteristic length, and k is the thermal conductivity of the fluid.

In terms of other dimensionless numbers, the Nusselt number is often related to the Reynolds and Prandtl numbers, particularly for forced convection flows:

$$\mathrm{Nu} = C \cdot \mathrm{Re}^m \cdot \mathrm{Pr}^n \tag{3.61}$$

where C, m, and n are constants that depend on the flow configuration and boundary conditions. For natural convection, the Nusselt number is often correlated with the Rayleigh number Ra:

$$\mathrm{Nu} = f(\mathrm{Ra}) \tag{3.62}$$

or, more explicitly,

$$\mathrm{Nu} = C \cdot \mathrm{Ra}^m \tag{3.63}$$

where f is some function, and C and m are empirical or theoretically derived constants.

3.6 Common boundary conditions

Equipped with an identical count of equations and unknowns, the governing equations for MHD constitute a mathematically complete set of partial differential equations (PDEs). These can be resolved given appropriate Initial Conditions (ICs) and Boundary Conditions (BCs). In the context of MHD, these conditions are classified into kinematic, thermal, and electromagnetic categories. ICs stipulate the state of all variables at the outset within the problem domain. Conversely, BCs are established at an arbitrary interface outlining the fluid domain under study [74].

In many engineering scenarios where fluid is enclosed within a bounded domain with rigid walls, the kinematic boundary condition can be described by the no-slip condition:

$$\mathbf{u} = 0 \text{ at walls} \tag{3.64}$$

For free surface problems devoid of thermocapillary effects, kinematic boundary conditions necessitate a balance of normal stress against surface tension, resulting in no tangential stress τ at the free surface:

$$\tau = 0 \text{ at free surfaces} \tag{3.65}$$

BCs for inlet/outlet configurations need to be explicitly defined to account for fluid movement into or out of the domain. Generally, a uniform velocity at the inlet and zero relative pressure at the outlet are used, although variations are possible [78].

Concerning heat transfer at solid-fluid interfaces, a common approach involves ensuring the continuity of heat flux, described by a conductive relation:

$$(\kappa \nabla T - \kappa_w \nabla T_w) \cdot \mathbf{n} = 0 \tag{3.66}$$

where the subscripts w serves to refer to solid domain parameters (wall).

With respect to electromagnetic boundary conditions, the more employed configurations for are[74]:

$$E_{t1} = E_{t2}, \quad B_{t1}\mu_{m1} = B_{t2}\mu_{m2}, \quad j_{n1} = j_{n2} \tag{3.67}$$

where the subscripts t and n signify the components of the field that are tangential and normal to the interface between material 1 and 2, respectively. Depending on the MHD formulation adopted, specific conditions on the primary electromagnetic variable are enforced. For insulating walls, $j_n = 0$ which can be expressed in terms of the electric potential ϕ as:

$$\mathbf{n} \cdot \nabla\phi = \frac{\partial \phi}{\partial n} = 0 \text{ (zero flux condition)} \tag{3.68}$$

For a perfectly conducting wall, the potential becomes homogeneous and all currents are assumed to cross the boundary surface. The wall potential can be arbitrarily set to zero [74]:

$$\phi = 0 \text{ (ground condition)} \tag{3.69}$$

For walls with finite conductivity, solving the Poisson equation for the electric potential is essential in both the fluid and solid domains. However, for thin walls ($t_w \ll L$), the equation can be simplified to:

$$j_n = -\frac{\partial \phi}{\partial n} = \nabla_{tang} \cdot (c_w \nabla_{tang} \phi_w) \tag{3.70}$$

Here c_w stands for the wall conductance ratio, that would be defined in the next section. ∇_{tang} is the two-dimensional operator in the tangential direction, whereas ϕ_w is the is the wall potential. In general, continuity of electric potential and the normal component of current must always be observed [74]:

$$\phi = \phi_w, \quad j_n = j_{n,w} \tag{3.71}$$

3.7 Basic phenomenology

3.7.1 Overview of confined flows

In this section, we embark on a qualitative analysis of the core magneto-hydrodynamic processes, specifically focusing on MHD flow in scenarios where heat exchange is absent. This serves to elucidate the alterations introduced to the features of the flow by the inclusion of the Lorentz force in the momentum Equation (3.29). More details on heat exchange phenomena under MHD conditions are postponed to Chapter 9.

Imagine a laminar flow that is fully developed and consists of an electrically conductive fluid. This flow is contained within a channel having a rectangular cross-section and infinite length in the stream-wise direction, as illustrated in Figure 3.1. A constant pressure gradient propels the fluid, characterized by a uni-directional velocity $\mathbf{u}_0 = (u_x, 0, 0)$, through a homogeneous magnetic field $\mathbf{B}_0 = (0, B_y, 0)$. The fluid, essentially a moving conductor, interacts with the magnetic field, consequently generating an electric current $\mathbf{j}$. In a 2D context like the one under consideration, this current is restricted to the cross-section. Free electrons, the electric charges in a liquid metal, are propelled by the magnetic force ($\sigma\mathbf{u} \times \mathbf{B}_0$) towards the wall parallel to $\mathbf{B}_0$, as indicated by $\oplus$ in Figure 3.1. This leads to a charge separation, creating a static electric field E that counteracts further separation. The outcome is a current field $\mathbf{j}$ and an electric field $\mathbf{E}$ that abide by Ohms law, Equation (3.9), i.e., $\mathbf{j} = \sigma[\mathbf{E} + (\mathbf{u} \times \mathbf{B}_0)]$ [74].

As elucidated in Section 3.2, the current field is solenoidal and forms loops within the cross-section, circulating near (and within, if conductive) the walls, as represented in the Figure 3.1. Walls on which the magnetic field has a non-zero normal component are termed Hartmann walls, while those in alignment with the field are referred to as side or Shercliff walls. The induced current reciprocally interacts with the magnetic field, causing the appearance of a volumetric Lorentz force in the fluid, $\mathbf{F}_L = \mathbf{j} \times \mathbf{B}_0$. Depending on the relative orientations of the current and the magnetic field, $\mathbf{F}_L$ interacts in various ways with the pressure gradient. Thus, for the case of a strong magnetic field $\mathrm{Ha} \gg 1$, the channel can be divided into three distinct zones [74]:

- The core: Located at the channel center, the primary forces at play here are the pressure gradient and a Lorentz force acting against it, thereby creating a retarding effect. In scenarios where Ha $\gg 1$, $\mathbf{F}_L$ contributes to a pressure drop considerably larger than the one caused by viscosity.

- Hartmann layers (HLs): Situated adjacent to the Hartmann walls, in these layers the Lorentz force changes its direction, thereby supporting the pressure gradient.

- Side layers (SLs): Also known as Shercliff layers, these are attached to the side walls and are minimally influenced by the Lorentz force, which generally interacts with the velocity field in a way that strongly depends on the conductivity ratio between the boundary layer and the wall.

Subsequent to the modification of the fluid macroscopic attributes, MHD phenomena also have a bearing on its microscopic behavior, suppressing turbulent velocity fluctuations [10]. The flow regimes in low-Rm are depicted in Figure 3.2, where line "C" symbolizes the Reynolds number for the transition from hydrodynamic laminar to turbulent flow, equivalent to Re = 2000 ($N = \mathrm{Ha}^2/\mathrm{Re}$). The regime to the left of this line signifies classical laminar flow (low Re), while the area above and to the right of line "A" represents electromagnetically laminarized flow. Both axial and transverse magnetic fields influence the turbulence structures by breaking up large vortexes into smaller, damped ones [79, 80]. This leads to an anisotropic behavior termed as quasi two-dimensional (Q2D) state.

3.7.2 Flow in Rectangular Channels

Magnetohydrodynamic flow within rectangular channels has been extensively analyzed. This is particularly relevant as ducts with rectangular geometries are often utilized for the circulation of liquid metal in the fusion reactor blankets. As elucidated earlier, the spatial distribution of Lorentz forces on the channel cross-section is inherently non-uniform owing to the unique pathways of the electric currents, thereby affecting the flow velocity distribution.

The electric current paths are substantially influenced by the electrical properties of the channel walls. In a conductive channel, a considerable fraction of the currents preferentially close through the walls. This acts as a parallel electrical resistance

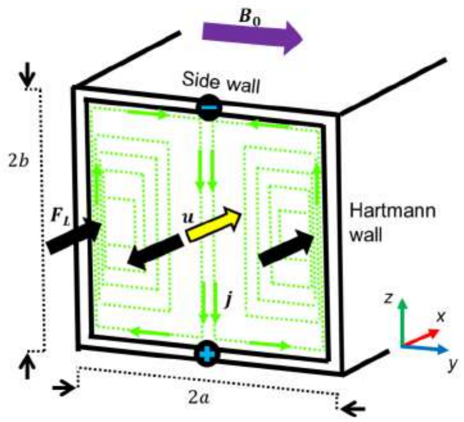

Figure 3.1: Sketch of the MHD phenomenology in an perfectly electrical insulated channel [6].

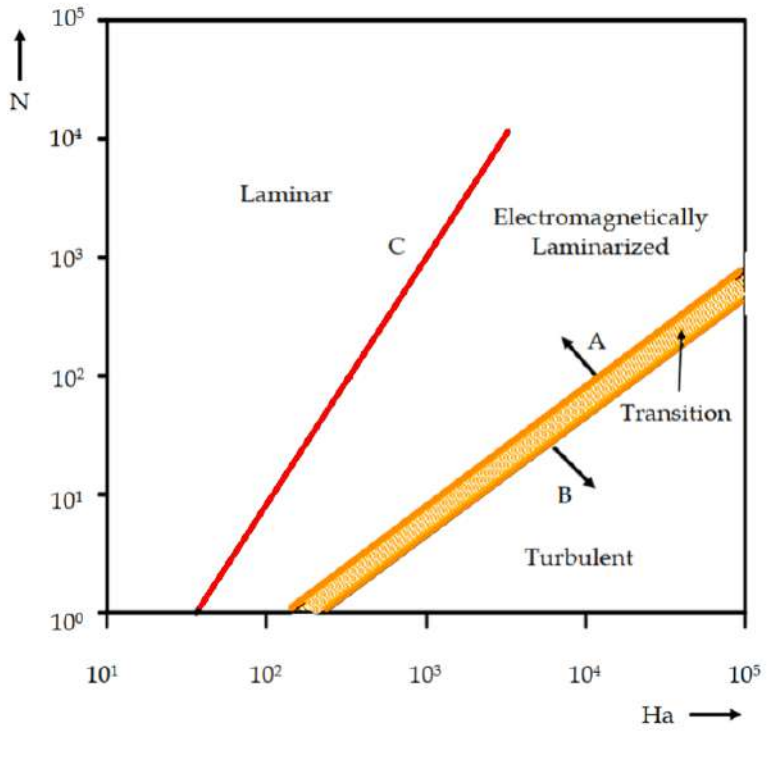

Figure 3.2: Flow regimes at low-Rm [10, 11].

to the currents within the fluid boundary layer, leading to an enhanced magnitude of both the Lorentz forces and the resultant pressure drop. On the other hand, for insulated walls, the currents are restricted to complete their paths exclusively through the Hartmann Layers (HL), resulting in a high series resistance that limits the overall magnitude of the currents.

To quantitatively describe the relative impacts of the fluid and wall conductivity, the wall conductance ratio c_w is introduced. For a rectangular channel, this is formulated as:

$$c_w = \frac{\sigma_w t_w}{\sigma L_c} \tag{3.72}$$

In Equation 3.72, σ_w and t_w are the wall electrical conductivity and thickness, respectively, while σ and L_c denote the fluid electrical conductivity and characteristic flow length. The characteristic length is often selected as the half-width in the direction of the magnetic field for a rectangular channel. For a comprehensive discussion on how this parameter influences flow characteristics, readers are directed to Ref. [74].

Hartmann Flow

While not a channel flow in the strictest sense, it is instructive to commence this discussion with the seminal contributions of Julius Hartmann [70, 71]. Hartmann was the pioneer in both theoretical and experimental investigations of LMs MHD flows, thereby setting the groundwork for subsequent analyses. Figure 3.3a delineates the problem geometry: a flow between two plates presumed to have infinite extension along the z-axis, with an electrically conducting fluid exhibiting unidirectional flow ($\mathbf{u} = u_x$) under the influence of an external magnetic field ($\mathbf{B}_0 = B_{0y}$) normal to both the flow and the duct walls.

The governing equations delineated in Section 3.2 yield the following relationships for the velocity profile [13]:

$$u(y) = \hat{u}\left[1 - \frac{\cosh(\mathrm{Ha}\,y)}{\cosh(\mathrm{Ha})}\right] \tag{3.73}$$

$$\hat{u} = \frac{1}{\mathrm{Ha}}\frac{c_w + 1}{c_w\mathrm{Ha} + \tanh(\mathrm{Ha})} \tag{3.74}$$

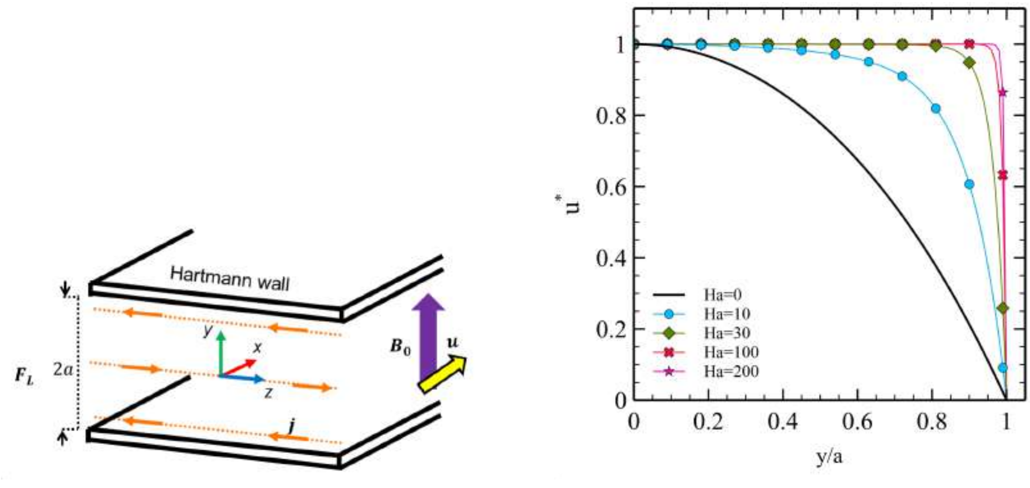

(a) **(b)**

Figure 3.3: (a) Problem geometry based on Hartmann investigations and (b) Illustration of the velocity profiles normalized by $\hat{u}$.

Here, $\hat{u}$ represents the characteristic velocity magnitude. Figure 3.3b illustrates the velocity profiles normalized by $\hat{u}$, thus rendering them independent of c_w. As previously stated, an increase in Ha corresponds to a diminished velocity, a flatter velocity profile in the core, and the emergence of a very thin boundary layer adjacent to the Hartmann walls, known as the Hartmann layer.

In the limiting cases of Ha $\to 0$, Equation 3.73 reverts to the Hagen-Poiseuille profile known for classical hydrodynamics [75]. For Ha $\to \infty$, it yields the following [74]:

$$\lim_{\mathrm{Ha}\to\infty} u(y) = u_c \left[1 - \exp\left(\mathrm{Ha}(|y| - 1)\right)\right] \tag{3.75}$$

$$u_c \to \frac{1}{\mathrm{Ha}} \frac{c_w + 1}{c_w \mathrm{Ha} + 1} \tag{3.76}$$

$$\delta_{HL} \sim \frac{1}{\mathrm{Ha}} \tag{3.77}$$

These expressions illustrate that at high Hartmann numbers, the channel flow can be represented as a core region characterized by a uniform velocity distribution, $u(y) \approx u_c$, and by a sharp velocity gradient, caused by the exponential correction term, occurring close to the Hartmann walls and representing the velocity distribution in the Hartmann layer, which thickness is estimated by δ_{HL}.

Shercliff Flow

Shercliff was the first to analyze the fluid motion in a rectangular channel characterized by perfectly insulating walls [81]. Shercliff derived the analytical expressions for both velocity and the induced magnetic field under these circumstances. Since the walls are insulating, the electric currents induced in the core are constrained to close their paths through the viscous Hartmann layer, as depicted in Figure 3.4a. The velocity profile near the Hartmann layer is identical to the one discussed earlier and illustrated in Figure Figure 3.1. On the other hand, the velocity profile near the side wall is shown in Figure 3.4b. It is evident that the side layer exhibits a greater thickness compared to the Hartmann layer for the same Ha. Specifically, the thickness of the side layer (δ_{SL}) is governed by the relationship:

$$\delta_{\mathrm{SL}} \sim \frac{1}{\sqrt{\mathrm{Ha}}} \tag{3.78}$$

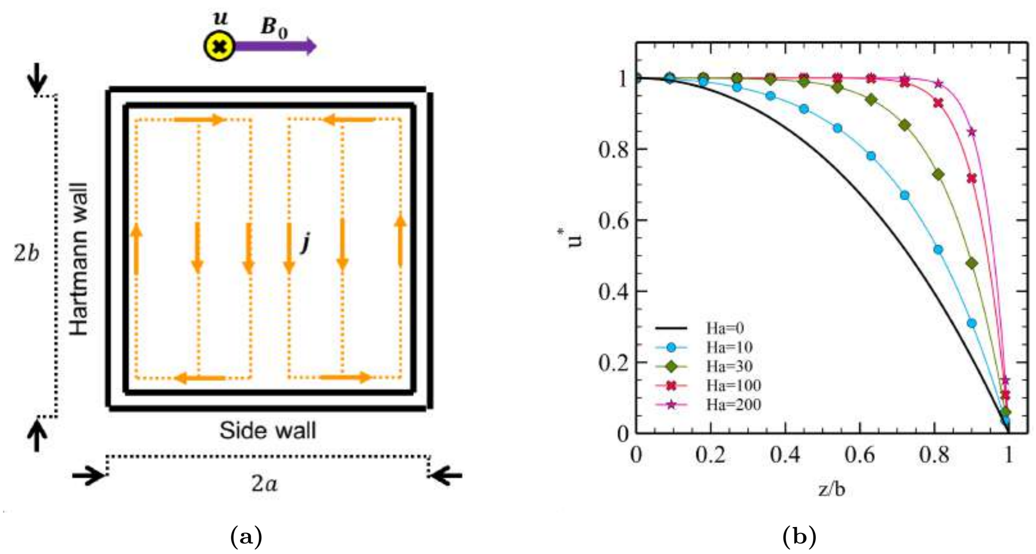

(a) (b)

Figure 3.4: (a) Problem geometry and main parameters (vectors) and (b) and velocity profiles across the side walls (b). Here, the velocity in scaled with the one at the channel centre ($u^* = u/u_0$) [6].

Chang-Lundgren-Uflyand (CLU) Flow

For channels featuring perfectly conductive walls ($c_w \to \infty$), this case was initially studied by Uflyand [82] and Chang and Lundgren [13]. Given the infinite electric conductivity of the walls, the induced currents close their paths exclusively through both the channel walls, which can be conceptualized as an electrical resistance in parallel, as shown in Figure 3.5a. Such a configuration amplifies the current density within the channel and modifies the pathways of the currents. This alteration leads to a novel phenomenon at the side walls, where the velocity locally exceeds that in the core of the channel ($\frac{u}{u_c} \approx 1.25$). This local velocity overshoot arises from the alignment of the current vectors $\mathbf{j}$ with the magnetic field $\mathbf{B}_0$ upon entering the walls, thereby locally minimizing the Lorentz force.

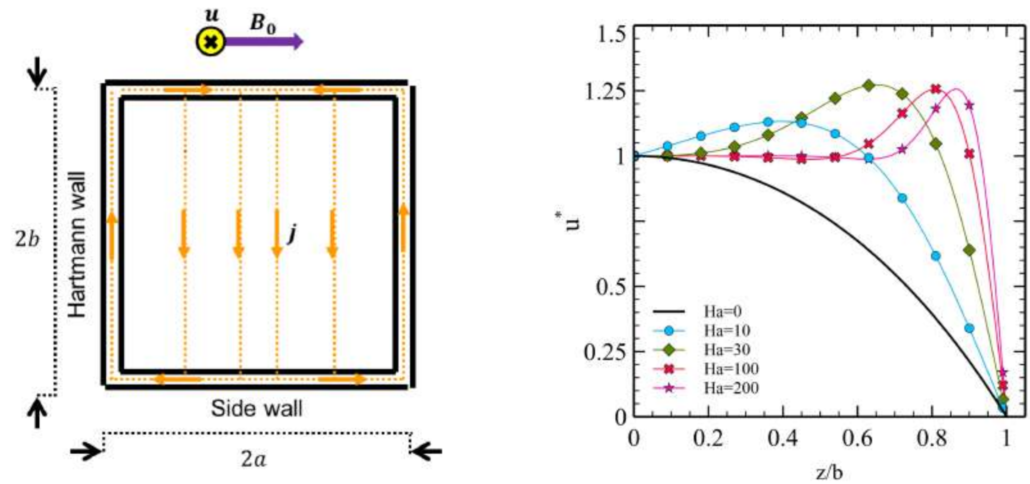

(a) **(b)**

Figure 3.5: Sketch of the CLU geometry case ($c_w = \infty$) with currents paths (a) and velocity profiles across the side wall (b). Here, the velocity in scaled with the one at the channel centre ($u^* = u/u_0$)

Hunt Flow

A situation worth considering is one where the Hartmann walls are perfectly conductive ($c_{wH} = \infty$) and the side walls are completely insulating ($c_{wS} = 0$). This case was initially scrutinized by Hunt [83]. The high conductivity of the Hartmann walls leads to a surge in current density, thereby significantly enhancing the braking effect of the Lorentz force in the central region of the channel. As depicted in Figure 3.6a, the electric currents complete their circuits within the Hartmann walls and the Side Layers (SLs). In this configuration, the currents curve to align themselves with the magnetic field $\mathbf{B}$, which locally mitigates the Lorentz force. Consequently, the majority of the flow is channeled into intense jets, resulting in an M-shaped velocity profile near the side walls, as shown in Figure 3.6b. The potential for reverse flow in the vicinity of the SLs is also notable. The peak jet velocity follows the equation:

$$\frac{u_{\max}}{u_0} \approx \sqrt{\frac{\mathrm{Ha}}{2}} \tag{3.79}$$

as referenced in [74]. The magnitude of these jets is further amplified if the side walls have low conductivity. An inflection point segregates the jets from the SLs, serving as a precursor for instabilities within the SLs, as empirically documented by Burr [84]. For the mirror case where $c_{wH} = 0$ and $c_{wS} = \infty$, the velocity profile (not depicted here) aligns closely with the Shercliff scenario [85]. This is because the currents are constrained to circulate through the HLs, substantially elevating the net electrical resistance across the current paths.

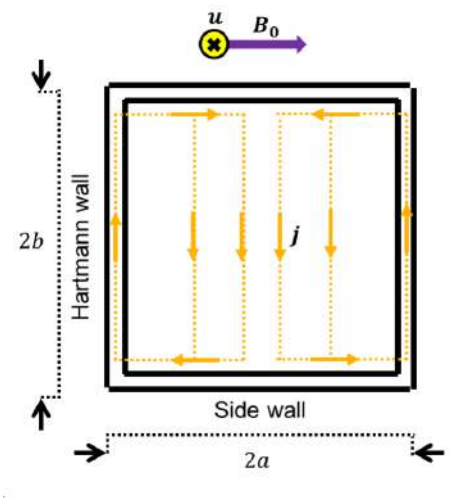

(a)

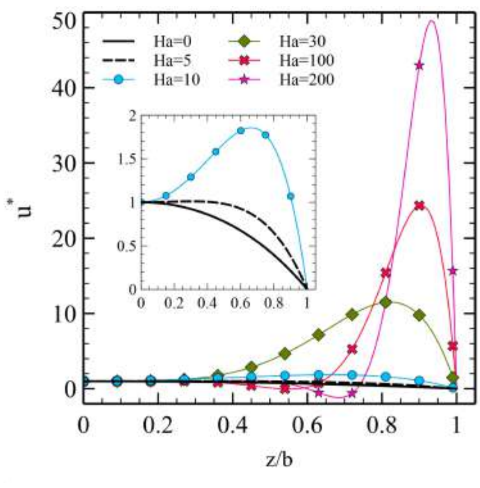

(b)

Figure 3.6: Sketch of the Hunt geometry case ($c_{wH} = \infty, c_{wS} = 0$) with currents paths (a) and velocity profiles across the side wall (b). Here, the velocity in scaled with the one at the channel centre ($u^* = u/u_0$).

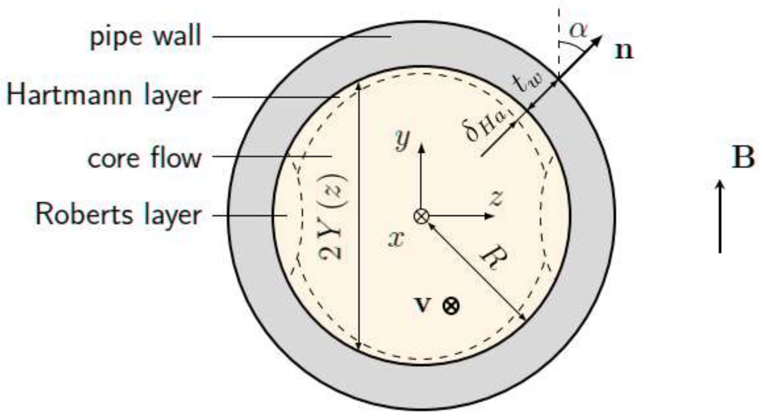

Figure 3.7: Geometrical features and flow domains of steady-state, fully developed MHD flow within a cylindrical conduit for high values of Ha [12].

3.7.3 Flow in circular pipes

Analyzing fully developed MHD flows within circular pipes, as depicted in Figure 3.7, introduces a slightly different scenario.

The flow domain highlighted in blue can be partitioned into several subdomains. The fluid adheres to the wall, causing the velocity to vanish at that boundary. Hartmann layers develop along the upper and lower boundaries, areas where the magnetic field **B** has a significant normal component relative to the wall. The variable thickness of these viscous boundary layers as a function of angle α is governed by the wall-normal component of **B**, and is calculated as

$$\delta_{\mathrm{Ha}} = \frac{1}{\cos(\alpha) \cdot \mathrm{Ha}} \tag{3.80}$$

as proposed by Shercliff in 1962 [86]. The typical length scale is the inner pipe radius r.

When $\alpha \to \pm\frac{\pi}{2}$, where the normal component of **B** becomes minimal, singular layers known as Roberts layers emerge. These layers have been extensively studied by Roberts in 1967, and their geometrical dimensions scale as $\mathrm{Ha}^{-\frac{1}{3}} \times \mathrm{Ha}^{-\frac{2}{3}}$ in y and z directions respectively [87].

Figure 3.8 presents various properties such as electric potential distributions, current streamlines **j**, and velocity profiles for both insulating ($c_w = 0$) and highly conductive pipe walls ($c_w = 1$). In both cases, the internal electric potential within

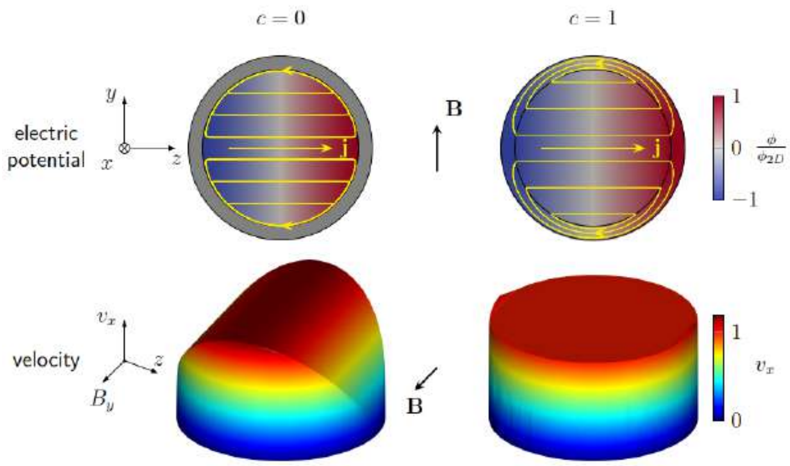

Figure 3.8: Steady-state, fully-developed MHD flow with Ha = 1000 in a cylindrical conduit. The figures depict the electric potential and velocity profiles for an insulating (c_w = 0, left) and highly conductive (c_w = 1, right) pipe wall. Electric current flow is denoted by green streamlines [12].

the fluid increases along z, aligned with the induced electric field $\mathbf{v} \times \mathbf{B}$, and remains invariant along the y-axis along magnetic field lines.

Regarding current streamlines, for insulating walls, they are confined to flow within the narrow Hartmann layers, serving as the bottleneck for electric current circulation. When the wall conductance $c_w > 0$, currents have the liberty to also traverse the solid domain, causing a distribution in wall potential.

Velocity profiles, shown in the lower section of Figure 3.8, reveal a consistent core velocity v_c along $\mathbf{B}$ within the core for both types of wall conductance. These profiles experience a precipitous decline to zero through the Hartmann layers. A distinct core velocity profile appears along the z-axis, depending on wall conductivity. The asymptotic theory proposes a solution for $u_c(z)$ as:

$$u_c(z) \approx (1 + c)\frac{Y}{1 + c \cdot \mathrm{Ha} \cdot Y}, \tag{3.81}$$

based on work by Chang & Lundgren in 1961 [13]. Here Y is the function that describes the shape of the walls. The solution holds for Ha $\gg$ 1 and hinges on the parameter $c_w \cdot$ Ha, which influences the tendency of electric currents to complete their circuits. This impact is further elucidated in Figure 3.9. In the case of perfect insulators (c_w = 0), an ellipsoidal profile is observed, whereas a uniform profile manifests with increasing $c_w \cdot$ Ha values. The asymptotic solution, however, does

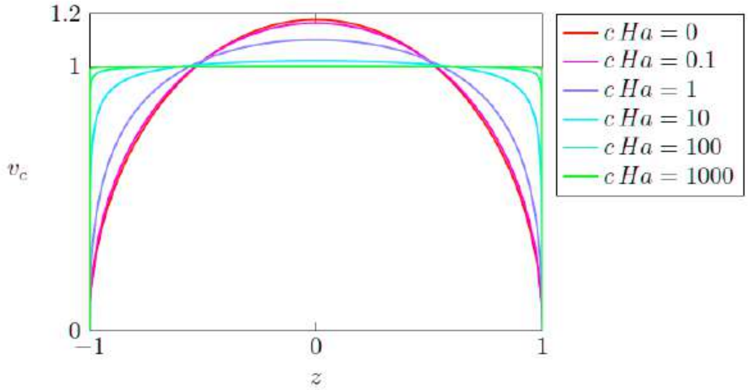

Figure 3.9: Velocity distributions along the plane $y = 0$ based on the asymptotic solution provided by [13] for $\mathrm{Ha} \gg 1$. The core flow velocity becomes homogeneous when the wall exhibits greater conductivity than the Hartmann layer, specifically when $c_w \cdot \mathrm{Ha} \gg 1$ [12].

not account for the emergence of small side jets when $c_w \cdot \mathrm{Ha} \gg 1$, as exemplified for $c_w = 1$ in Figure 3.8 on the right.

3.8 Pressure drop correlations

The significance of the Lorentz force cannot be overstated when considering the pressure drop, a critical parameter in the design of a liquid metal blanket. The arguments presented herein are of significant importance as they lay the foundation for the subsequent code development, which will be elaborated upon in forthcoming sections of this thesis (Chapter 5,Chapter 6.

For an MHD flow driven by pressure in a rectangular duct, illustrated in Figure 3.1, viscous forces are localized to thin boundary layers owing to $\mathrm{Ha} \gg 1$ and $\mathrm{N} \gg 1$. Consequently, the pressure loss is predominantly due to the Lorentz force, or the electromagnetic drag in the core of the channel. This drag can be categorized into two parts as follows:

$$\Delta p \approx \Delta p_{\mathrm{MHD}} = \Delta p_{\mathrm{2D}} + \Delta p_{\mathrm{3D}} \tag{3.82}$$

The term Δp_{2D} refers to the two-dimensional pressure loss, which occurs under fully developed flow conditions. This is the MHD counterpart to hydrodynamic frictional losses. Because there is no velocity gradient along the direction of the flow and the magnetic field $\mathbf{B}$ is perpendicular to the velocity $\mathbf{u}$, electric currents $\mathbf{j}$ are confined to the channel cross-section. These currents are responsible for transforming mechanical energy into thermal energy via Joule heating.

The $\Delta p_{3\mathrm{D}}$ term is the three-dimensional pressure loss component, encountered in flows that possess a velocity gradient along the stream-wise direction or in the presence of non-uniform electromagnetic conditions. These could be sharp gradients in magnetic fields, wall conductivity discontinuities, bends, expansions, contractions, or cross-sectional variations. Here, currents are not restricted to the cross-section but extend in the direction of the flow, thereby inducing additional electromagnetic drag. These kinds of pressure losses serve as the MHD equivalent of concentrated hydrodynamic losses.

3.8.1 2D Pressure Drop

Building on the Hartmann flow discussion from Section 3.7.2 and utilizing the velocity distribution outlined in Equations (3.73) and (3.74), the scaled pressure gradient $K = \Delta p/(u_0 \rho \nu / L_\mathrm{c}^2)$ can be calculated. This has been thoroughly detailed in reference [74]. Given that u_0 and L_c are the average velocity and characteristic length of the channel, K can be defined as:

$$K = \frac{1}{\hat{u}(c_w)} \left(1 - \frac{1}{\mathrm{Ha} \tanh(\mathrm{Ha})} \right) \tag{3.83}$$

The gradient of pressure is governed by Ha and c_w, via the characteristic velocity $\hat{u}$, as depicted in Figure 3.10.

For low Ha, the flow is essentially hydrodynamic and independent of c_w. In the case of high Ha, Equation (3.83) simplifies to $K \approx 1/\hat{u}$, with limiting behaviors $K \to \mathrm{Ha}$ when $c_w \ll 1/\mathrm{Ha}$ and $K \to c_w/(c_w + 1)$ when $c_w \gg 1/\mathrm{Ha}$. This reflects the significant escalation of pressure losses when conductive channels are present, thereby justifying the necessity for electrical insulation of PbLi channels in the blanket, particularly where $\mathrm{Ha} \approx 10^4$, using Flow Channel Inserts or operating at low PbLi velocities, as elaborated in Section 2.8. For an electrically insulated rectangular channel, as outlined in Figure 3.4 and for constant Re, the pressure gradient linearly depends on Ha as stated in [79]:

$$\frac{\partial p}{\partial x} = k_{p,\mathrm{ins}} \frac{\rho u_0^2}{2a} \tag{3.84}$$

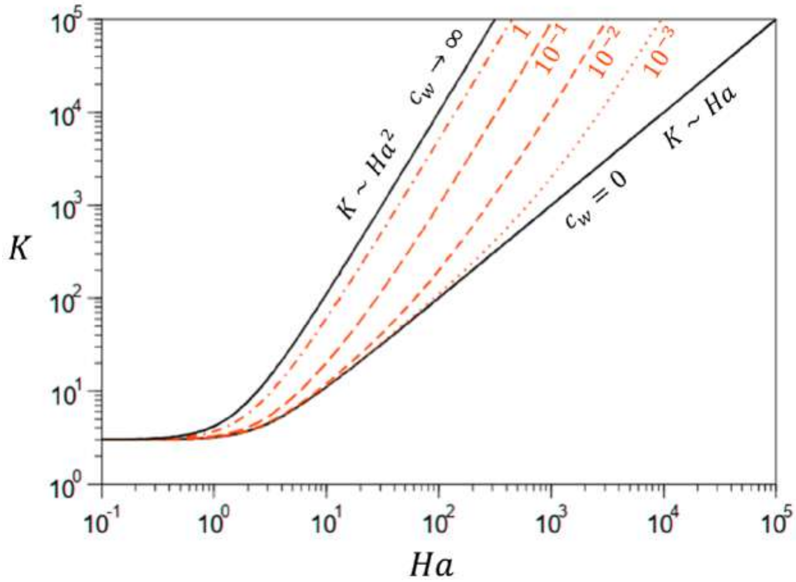

Figure 3.10: Dimensionless MHD pressure gradient in relation to the Hartmann number H and the wall conductance ratio c_w[6].

$$k_{p,\text{ins}} = 2\frac{\text{Ha}}{\text{Re}}\left(1 - \frac{0.852}{(b/a)\sqrt{\text{Ha}} - 1/\text{Ha}}\right)^{-1} \tag{3.85}$$

Here, $k_{p,\text{ins}}$ is the coefficient of pressure drop for an insulated channel. Three components contribute to the pressure drop as seen in the brackets of Equation (3.85): the core flow, the side layers, and the Hartmann layers. The channel aspect ratio b/a also plays a role; channels with long Hartmann walls ($b/a \gg 1$) experience the maximum pressure gradient, while shorter Hartmann walls result in reduced pressure gradients, thereby highlighting the significant influence of the Hartmann layer in generating electromagnetic drag.

In contrast, for a conductive channel as illustrated in Figure 3.6, the pressure gradient exhibits a quadratic dependence on B_0 intensity as per [79]:

$$\frac{\partial p}{\partial x} = k_{p,\text{cond}}\sigma u_0 B_0^2 \tag{3.86}$$

$$k_{p,\text{cond}} = \frac{c_w}{1 + c_w + a/(3b)} \tag{3.87}$$

The coefficient $k_{p,\text{cond}}$ is specifically applicable to a rectangular channel characterized by lateral wall length $2a$ and Hartmann wall length $2b$ as cited in [88]. A comprehensive relation for $k_{p,\mathrm{cond}}$ has been put forth by Tillack et al. in [89]:

$$k_{p,\mathrm{cond}} = \frac{\mathrm{P}_H}{1 + a\mathrm{P}_H/(3bc_{wS^*})} \tag{3.88}$$

$$\mathrm{P}_H = \frac{c_w + 1/\mathrm{Ha}}{c_{wH} + 1} \tag{3.89}$$

$$c_{wS^*} = c_{wS} + \sqrt{1/\mathrm{Ha}} \tag{3.90}$$

where c_{wS} and c_{wH} are the conductance ratios for the side walls and Hartmann walls, respectively.

The special case where $c_{wS} = 0$ and $c_{wH} \to \infty$ (as discussed in Section 3.7.2) represents an intermediate scenario with pressure losses that are higher than a perfectly insulated channel but lower than a channel with fully conductive walls ($c_{wS} = c_{wH} \to \infty$). In the context of the channel flow representation in Figure 3.10, this case lies between the two boundary curves.

For channels with non-uniform conductance ratios on the walls, the pressure gradient must be determined either through different correlations or via numerical simulations, as this case is considerably less explored in the literature compared to the other cases. To the best of the Author knowledge, the only correlations that have been developed for this situation are by Hua et al. in [90], which focuses on channels with uniform c_{wH} and non-uniform c_{wS}, and the recent theoretical work by Tao et al. in [91], which addresses channels with asymmetrical walls of arbitrary conductivity.

3.8.2 3D Pressure Drop

The assessment of the 3D pressure term is considerably more intricate, largely hinging on both the geometry and flow parameters. In general terms, the 3D pressure drop can be decomposed into three constituent terms as given by [29]:

$$\Delta p_{3D} = \Delta p_\infty + \Delta p_v + \Delta p_i \tag{3.91}$$

Here, Δp_∞ denotes the inertialess or inviscid term, for which the condition $\Delta p_{3D} \approx \Delta p_\infty$ holds true under the assumptions $\mathrm{Ha} \gg 1$ and $\mathrm{N} \gg 1$. The terms Δp_v and Δp_i signify the viscous and inertial contributions, respectively, that need to be incorporated if the 3D flow exhibits localized viscous or inertial behavior [29]. Commonly, isolating the contributions of 2D and 3D currents to the pressure drop is challenging. Consequently, the 3D pressure drop is generally expressed via a local MHD resistance coefficient ζ, which is a function not only of N and Ha, but also of the problem geometry and the orientation of the magnetic field [92]:

$$\Delta p_{3D} = \zeta \frac{1}{2} \rho u_0^2 \tag{3.92}$$

$$\zeta = k\mathrm{N} = k \frac{\sigma B_0^2 L_{3D}}{\rho u_0} \tag{3.93}$$

In the above equations, L_{3D} is the characteristic length scale specific to the 3D flow, while k is a constant coefficient and N is the local interaction parameter. One of the pivotal considerations is the determination of the k coefficient, whose value generally lies within the range $0 < k \leq 2$ and is highly sensitive to the specific flow parameters under study. A more detailed discussion about local MHD losses is postponed to Chapter 6.

3.9 Coupling

The phenomenon of coupling holds significant importance in the design of the BB. Essentially, it involves the transfer of what are commonly known as leakage currents between adjacent channels that are separated by a non-insulated wall. This specific subject was initially investigated by Madarame et al., as documented in their seminal work [93]. Consequently, the phenomenon is frequently referred to as the "Madarame effect". The study conducts a numerical analysis on the MHD pressure drop occurring in the second-wall orifice, which serves as a connection between the first-wall cooling channel and the header in self-cooled LM blankets. Despite the second wall thickness being low, the orifice experiences a substantial pressure drop, primarily due to the effects of leakage currents. When those currents escape and do not have to traverse through the thin walls, the electrical resistivity of the current path may be diminished, leading to elevated current intensities and consequently, a significant increase in the pressure drop. The issue of leakage currents was subsequently encapsulated by Zhang et al. in their study [14]. In this work, simpler channel configurations were numerically examined, providing valuable insights into the fundamental mechanisms of the phenomenon.

Four distinct configurations of coupled MHD square duct flows have been examined to determine MHD pressure drop and velocity distribution characteristics. In the first (1) and second scenarios (2), the coupled rectangular ducts are aligned in the direction of the external magnetic field, meaning they share a Hartmann wall. The flow is co-current in the first case and counter-current in the second. In the third (3) and fourth (4) configurations, the coupling duct extends perpendicular to the external magnetic field, meaning the ducts are linked through a side wall. In these scenarios, the flow directions is the same in the third case and opposite in the fourth. Computational results outline the velocity profiles and induced electrical current distributions in the cross-sections of the coupled ducts for these four distinct scenarios. These results reveal the varying influences of the external magnetic field on the flow patterns, as indicated in Figure 3.11 where only more representative cases are collected.

The authors then compared the pressure losses outcomes with a standard square stand-alone duct, as depicted in Figure 3.12 for a fusion-relevant conductance ratio (Equation (3.87) is the reference formulation for those cases). They find that the MHD pressure drop for (1) is comparable with a single duct, whereas the result for (3) and (4) are slightly above. In contrast, the pressure drops in (2) significantly exceed that of a standard duct. It is also observed that the MHD pressure gradients across the four configurations diminish as wall conductance ratios increase, provided other conditions remain constant.

The increasing complexity of phenomena related to MHD pressure losses becomes more pronounced as the number of coupled channels rises. Consequently, the Madarame effect assumes significant importance in the engineering design of a BB, which is expected to incorporate multiple liquid metal channels with several shared walls. So far, only a scarce number of researchers, such as Bluck et al. [94] and Bühler et al. [95], have attempted to develop numerical models adept at elucidating the effects of leakage currents at the component-level scale. The significant influence of the coupling on the results of the REDMaHD validation procedure will be elaborated in Chapter 8.

3.10 Summary

In this chapter, the governing equations for pressure-driven MHD incompressible flow are presented. Both the magnetic induction formulation, where the magnetic field is the primary electromagnetic variable, and the ϕ-formulation, centered on the electric potential, have been derived and explored. The chapter highlights the essential dimensionless groups affecting the flow and presents appropriate kinematic, electromagnetic, and thermal boundary conditions. We delved into the primary MHD phenomena, focusing on the Lorentz force decelerating effect and its implications on velocity distributions, including the Hartmann layer formation on walls perpendicular to the magnetic field. Discussions extended to the characteristics of flows in rectangular channels and thin-film flows in chutes, encompassing cases with varying wall conductivity. Notable channel flow models such as the Shercliff, Uflyand and Hunt. Emphasis was placed on correlations determining the pressure gradient, incorporating the consideration of three-dimensional losses. While the chapter did not extensively cover the MHD impact on turbulence and mass transfer crucial for tritium and corrosion, other phenomena as magneto-convection and Madarame effect are brielfy presented due to their importance for the BB design.

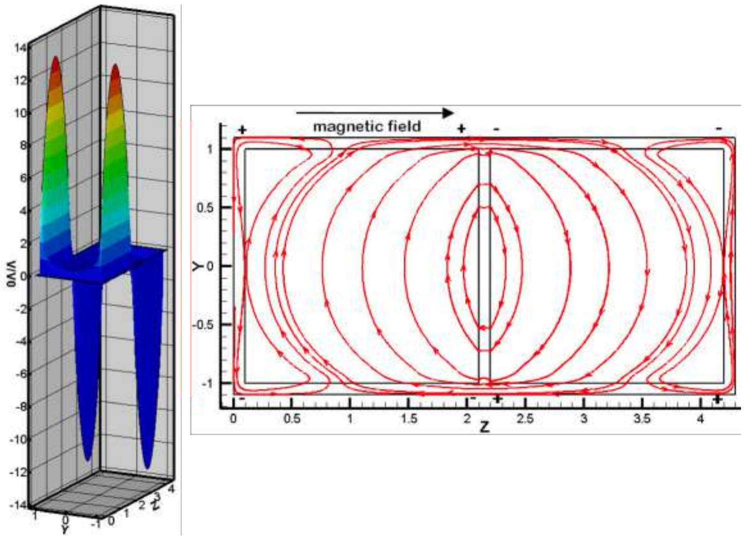

(a)

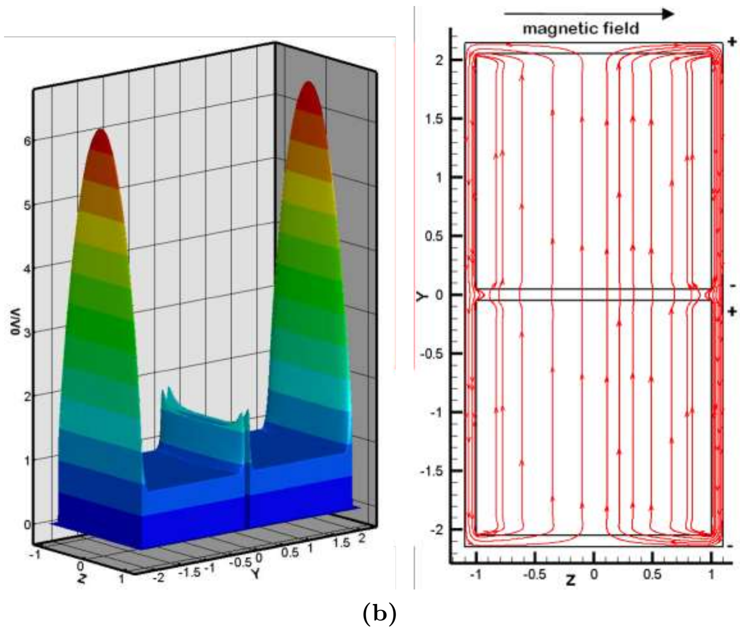

(b)

Figure 3.11: a) Velocity and induced electrical current profiles in the cross-sectional area of the coupled ducts for Scenario 2, under the conditions Ha = 1000 and $c_w = 0.1$. b) Same condition for Scenario 3 [14].

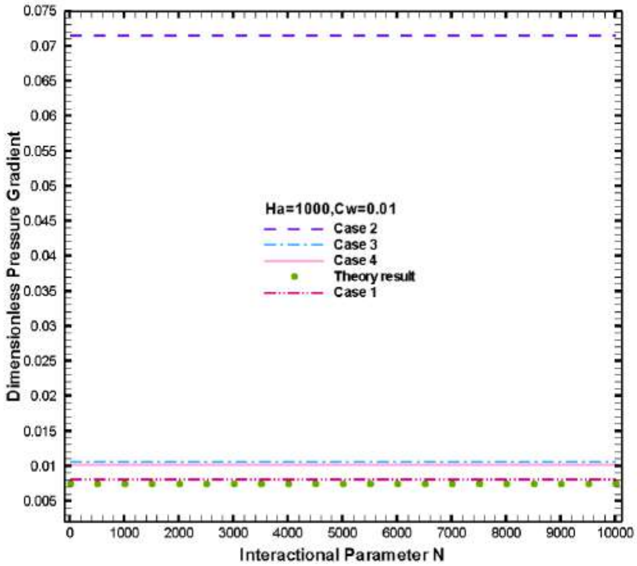

Figure 3.12: MHD pressure gradients in the four distinct coupled configurations are compared with a single, standard MHD duct flow, under conditions where Ha = 1000 and $c_w = 0.01$ [14].

Part II

Numerical tools

Chapter 4

Computer aided-engineering

In the advancement of nuclear fusion technology, the role of Computer-Aided engineering (CAE) codes is incontrovertible. Although several codes were originally developed to meet the specifications of fission-based reactors, they have found limited success in adequately modeling the complex interactions and phenomena that are inherent in fusion environments.

Typically, when investigating MHD effects at the blanket scale, analysts commonly employ semi-analytical methods. These are often supported by a combination of empirical and semi-empirical correlations, along with data gathered from direct numerical simulations [32, 58, 96]. While this approach has some effectiveness, it is also marred by extensive computational time, limited flexibility, and constraints on the attainable spatial and temporal resolutions.

Several computational fluid dynamics (CFD) software packages, such as ANSYS-CFX, ANSYS-FLUENT, and OpenFOAM, do offer specialized MHD modules [92]. However, a fully mature code for simulating all the MHD phenomena within the blanket system is still not in existence despite the efforts of the fusion community; and even further away is the goal to integrate it as a module in a CAE multiphysics platform. These CFD tools are also not feasible for full-scale reactor analysis due to their computational cost. On the other hand, Best-Estimate Systems Thermal-Hydraulic (BE SYS-TH) codes have the potential to provide an efficient means for simulating the thermal-hydraulic network within the blanket, but they currently fall short on MHD capabilities [97].

BE SYS-TH codes are essential for analyzing the thermal-hydraulic phenomena in complicated nuclear systems and are primarily developed for examining incidental or accidental transients, but they are also applicable for operational transient and steady-state situations [97]. To solve the physics of such complicated scenarios, these SYS-TH tools utilize simplified 0-D or 1-D models that are formulated based on extensive experimental data. These codes have become the reference tools for the licensing processes of fission-based nuclear power plants [98]. RELAP5 is an illustrative example of such SYS-TH codes. Initially conceived for light water reactor applications, it has been extended in recent years to handle other types of fluids such as liquid metals [99].

This Ph.D. work is aimed at introducing the first phase of the creation of a robust and comprehensive SYS-TH numerical tool capable of addressing all key MHD phenomena occurring in a liquid metal breeding blanket, from pressure loss to mass transport issues. It is crucial to note that, at this preliminary stage, the focus will be on MHD features that have a direct impact on the standard operation of the reactor and where existing knowledge is sufficient for the module implementation.

4.1 Thermal-hydraulic System codes

System Thermal-Hydraulic codes serve as an essential computational resource in the realm of deterministic safety analysis (DSA) and probabilistic safety analysis (PSA) for fission nuclear reactor safety technology. These codes are particularly significant as they offer a comprehensive simulation environment that encapsulates the entire reactor, modeling the interactions both within circuits and among various components. Their scope is inherently multiphysical, capturing a range of phenomena that include thermal-hydraulic modules for fluid flows and heat transfers, solid domain conduction heat transfer, fuel thermomechanics, neutron kinetics diffusion equations, models for pumps and turbines incorporating equations for shaft rotation speed predictions, and control protocols that govern regulatory and protection systems like SCRAM, valve operations, and safety injections. Furthermore, these codes extend their utility to model auxiliary systems such as residual heat removal, volumetric and chemical control, and emergency core cooling systems, either as dedicated modules or boundary conditions [100].

The codes are versatile enough to simulate a myriad of accident scenarios, from ruptures in primary, secondary, and auxiliary circuits to more complex cases like station black-outs and loss of heat sinks. Point kinetics models, often zero-dimensional, are embedded in these codes to handle the neutron flux in the reactor core, but more intricate three-dimensional neutron kinetics models can be incorporated.

Concerning design basis accidents (DBAs) and some scenarios that go beyond DBAs up to the onset of loss of core geometric integrity, SYS-TH codes are capable until additional, severe accident-specific models become indispensable. Integration with such severe accident codes or modules is often available.

In terms of their applicability, these codes can handle a variety of reactor types such as light water reactors, heavy-water reactors, and liquid metal reactors, whereas applications for fusion reactors, besides being scarcer and less documented in the literature, are also still struggling with numerical models far from being comprehensive of the specific phenomena of these devices. SYS-TH codes are equipped to simulate various flow states and regimes, covering a wide spectrum of pressures, temperatures, and velocities. They include the capability to model all heat transfer regimes between heating or cooling walls and single- or two-phase flows, as well as specific models for phenomena like two-phase critical flow and counter-current flow limitations.

To achieve a stationary state in plant or integral tests, tools within these codes are designed to assimilate a limited set of measured data like temperature, power, and pressure. The code should also integrate fuel modeling capabilities, including fuel deformation and failure metrics and oxidation with hydrogen production. Furthermore, SYS-TH codes come with the feature to model installed logics in the nuclear power plant, irrespective of their relevance from a safety or licensing perspective, which is vital for calculating realistic system performance.

Requirements and domain of simulation

In addressing the multifaceted challenges associated with DBAs, SYS-TH codes are envisioned as multiscale, multiphysics computational frameworks. Formally, the simulation domain of these codes is conceptualized as the ensemble of multiphysical phenomena expected to manifest in a Nuclear Power Plant (NPP) during both operational and DBA conditions.

To meet these requirements, SYS-TH codes draw upon a myriad of scientific disciplines. These include thermal-hydraulics for modeling parts where fluids are present and capable of exchanging mass, momentum, and energy; gases like nitrogen, hydrogen, air, and fission products that may be transported by steam or dissolved in water; boron and non-volatile fission products; heat conduction in solid structures; neutron physics; chemistry limited to zirconium-water reactions; fuel performance; mechanics, such as the inertial behavior of rotors or flapper movement in check valves; and instrumentation and control systems, which manage the overall and subsystem-level functionalities within an NPP.

The spatial resolution in SYS-TH codes varies depending on the reactor component and situation. Typically, the codes employ zero-dimensional or lumped-parameter models for components with low velocities like pressurizers and steam generator domes. One-dimensional models are often used for components with a predominant flow direction like pipes and core assemblies, while two- and three-dimensional models are reserved for components with intricate velocity fields, such as those found in pressure vessels.

However, some phenomena and disciplines are outside the standard purview of SYS-TH codes and are often modeled using specialized tools that can be coupled to SYS-TH codes. These include the mechanical loads on structures, advanced 3-D neutron kinetics tools, CFD codes for detailed spatial resolution in regions requiring turbulent mixing, subchannel modeling of core assemblies, and complex containment thermal hydraulics models [98].

The development and validation of SYS-TH codes to confidently simulate all components and phenomena relevant to DBAs have been an extensive endeavor, taking decades to reach maturity. Documentation of the dominant phenomena in each component, for all reactor designs and considered DBA scenarios, has been outlined in code validation matrices by international organizations [101].

Fundamentals characteristics

SYS-TH codes are characterized by three main attributes: they function as best-estimate codes, safety codes, and industrial codes. In the realm of best-estimate codes, the objective is to model with high reliability all dominant processes within the domain of simulation. Unlike the so-called "conservative codes" that merely predict an upper or lower safety-bound for figures of merit, best-estimate codes aim for an accurate representation of physical reality. The transition from the first generation of system codes, used in the licensing of initial PWRs and Boiling Water Reactors (BWRs), to second-generation best-estimate codes like TRAC, RELAP5, ATHLET, and CATHARE, presented a monumental scientific challenge. These advanced codes necessitated the identification and high-fidelity modeling of all phenomena across all transients, requiring extensive databases and advancements in measurement techniques. Additionally, these codes had to utilize thermal-hydraulic models that were not just more complex but also amenable to experimental validation. The selected two-fluid six-equation model fulfilled this role, as it allowed the modeling of both mechanical and thermal non-equilibrium conditions [100].

When it comes to safety, several essential attributes must be met. These encompass the development under strict Quality Assurance (QA) procedures, comprehensive documentation, and verification and validation protocols. **Verification** is a process aimed at confirming the software correctness and the numerical accuracy of the solution it provides for a specific physical model, defined by a set of equations. This process includes tracking code errors, evaluating numerical discrepancies based on node size and time step, and ensuring code portability across various platforms and compilers. **Validation** is a separate process that focuses on corroborating the accuracy of the physical model. This is done by comparing computational simulations with experimental data, either by the code developers in what is termed as developmental assessment, or by the code users in an independent assessment. User Guidelines are also an integral part of those codes, advising on the appropriate nodalization, input deck configuration, and other parameters that can affect the simulation, thereby minimizing the "user effect" on the results.

From an industrial perspective, the primary requirements of such codes include robustness, precise QA procedures during development and maintenance, and efficient computational performance. This is particularly important when SYS-TH codes are employed in plant simulators for operator training, where real-time calculations of transients requiring operator actions are imperative [98].

Nodalization

As extensively discussed, SYS-TH codes play an indispensable role in modeling the thermal-hydraulic physical systems, alongside other interconnected systems like the cooling circuits in nuclear reactors or in test facilities. These codes function by solving a set of equations that describe the system thermal-hydraulics. While a general method is usually sufficient for simulating most system components, specialized components with unique geometries often require specific thermal-hydraulic models. Additionally, SYS-TH codes are designed to couple thermal-hydraulic systems with non-thermal-hydraulic ones.

Given the complexity of the reactors and the diverse physical processes at play, SYS-TH codes employ a simplified model of the reactor. Specifically, the fluid domain is divided into a series of meshes or "control volumes", wherein balance equations are established. This division effectively transforms the original system, which is described by partial differential equations, into a discretized form governed by ordinary differential equations (ODEs), thereby reducing its state space to finite dimensions. This meticulous process is commonly known as "nodalization", and encompasses a variety of modeling choices that have a profound impact on the simulation predictive accuracy [98].

Critical decisions in nodalization include the choice of dimensions for modeling various components, the types and numbers of meshes in each component, and the options for simulating a wide range of elements like pumps, turbines, valves, safety systems, and neutron kinetics. Moreover, nodalization accounts for specialized subsystems like separators in BWRs or Steam Generators in PWRs. It also includes a range of additional factors such as pressure loss coefficients, heat loss models, and the incorporation of extra transport equations for variables like boron concentration, non-condensable gases, or radioactive elements. Furthermore, nodalization is integral to defining both the initial and transient states of the system, requiring detailed specification of boundary conditions like break openings, automated safety system actuations, and so on.

The choice of time step management in the input deck is another crucial user-defined parameter that can significantly influence the accuracy of computations. Taken together, the 0-D and 1-D versions of the two-fluid six-equation model commonly serve as the foundational framework for most SYS-TH codes [100].

0-D and 1-D approaches

In the framework of system codes for nuclear reactor analysis, the importance of 0-D and 1-D models cannot be overstated. These models serve as the foundational modules that enable the simulation of complex two-phase flows across various reactor components, such as pipes and core assemblies.

In scenarios where flow directionality is predominant, 1-D models are particularly apt at capturing the fluid dynamics. These models can be tailored to accommodate distinct closure laws that correspond to specific duct geometries. Generally, the codes differentiate among various geometrical constructs like pipes, annuli, and rod bundles, each used in specific components like the circulation loop, pressure vessel, and steam generators. These 1-D models have proven to be highly effective in capturing the majority of phenomena relevant to accidental transients in LWRs. Nonetheless, there are limitations to these 1-D models, particularly when dealing with low-velocity, natural circulation scenarios that give rise to complex 3-D velocity fields and possible recirculation cells, or when applied to components with intricate 3-D geometries [100].

In contrast, 0-D models are incorporated in system codes to address specific fluid behaviors that are not adequately captured by the conventional 1-D mesh or control volumes. For example, when large capacities are connected to various ducts or pipes at different elevations and orientations, 0-D models like a two-node volume module may be used. These models make certain assumptions, such as relatively small internal velocities compared to junction velocities, and predominantly hydrostatic pressure fields. Consequently, they can depict phenomena like phase stratification by dividing the total volume into two subvolumes, separated by a free surface.

Both 0-D and 1-D models are indispensable for capturing the nuances of thermal-hydraulic behaviors in reactor circuits, which can be further influenced by specific local geometries. While 1-D models are capable to handling a broad range of situations with directional flow, 0-D models offer the ability to capture specific flow behaviors that arise in more complex or specialized settings. Therefore, the judicious application of these models in system codes is crucial for achieving accurate and reliable simulations, vital for both operational and safety assessments [100].

4.1.1 SYS-TH - CFD coupling

It is worth mentioning that, in the last few years, some researchers have explored the possibility to realize a coupling methodology between system codes and CFD tools [94].

The employment of SYS-TH and CFD codes for the modeling and simulation of complex systems has been elaborated in the previous sections. It is evident that although each modality has its merits, a novel strategy might provide a more comprehensive, yet agile, evaluation of fusion blankets. The fusion blanket serves as an excellent candidate for the incorporation of a coupled-methodology approach. In this setting, systems codes can capture sections amenable to component-level analysis (fully devolped flow regions), while CMHD can provide details about intricate layouts (junctions).

This tactic has already proven effective in various engineering contexts, including the scrutiny of advanced fission reactor systems [102]. Endeavors in fusion applications have engaged in code coupling, where one-dimensional systems codes furnished boundary conditions for three-dimensional models and vice versa [103, 104]. However, these simulations were executed separately, with data manually transferred from one code to another [105].

Aumiller initially validated the feasibility of coupling RELAP with a CFD code in his study on the Edwards Pipe Blowdown issue [106]. This tackled a myriad of universal challenges linked to code coupling, such as the implementation of artificial boundary conditions, synchronization of time steps, and data consistency in variables like temperature and pressure. Comparative analyses involving CFD, RELAP5, and the coupled simulations yielded a disparity of less than 5%, laying the foundation for inquiries into more complex reactor problems. More recent investigations, such as Yans study, delve into coupling RELAP5-3D with the FLUENT CFD code for the analysis of both PWR and Gen IV Gas Turbine Modular Helium Reactors (GTMHR) [102]. Validating this coupled framework using a simplistic pipe flow system, initially simulated by standalone CFD and subsequently by RELAP5-3D, has shown strong congruence across the board, rendering it valuable for testing in the current study.

Research on code coupling in the domain of thermal-hydraulics remains emergent, with newer works building upon early foundational efforts. For instance, Li et al. demonstrated that a simplified explicit coupling approach can yield credible outcomes for nuclear thermal-hydraulic challenges, provided the time step dimensions are judiciously selected [107]. A successful coupling of RELAP5/MOD 3.1 and FLUENT was executed for rudimentary pipe test scenarios before progressing to more intricate systems like reactor loops. Validation of this coupled code involved constructing a composite pipe model from three discrete smaller pipes. Standalone simulations with each individual code were performed, and the pressure drop calculations were compared to those of the coupled case, affirming the validity of the coupled approach.

More recently, Wolfendale et al. developed a 1D thermal hydraulic systems code, MHD-SYS, which incorporates MHD effects and has been validated using LLCB TBM data [105, 108]. To enhance the model fidelity for complex components like junctions, MHD-SYS is interfaced with OpenFOAM `mhdFoam` solver through TCP socket connections. This coupled solver performs reliably, as validated against test cases, demonstrating its utility for comprehensive thermal-hydraulic analyses of fusion blanket systems.

4.1.2 RELAP5.Mod3.3

The foundation chosen in this study for implementing a MHD module is the SYS-TH RELAP5/Mod3.3, which is an advanced version of the RELAP code (Reactor Excursion and Leak Analysis Program) specifically designed for transient analysis in light water reactors. RELAP was originally developed at the Idaho National Engineering Laboratory (INEL) under the auspices of the U.S. Nuclear Regulatory Commission (NRC). Its applications are manifold, ranging from regulatory rule-making and licensing audit calculations to the assessment of accident mitigation techniques, operator guideline evaluations, and experimental planning. RELAP5 has also been employed as a foundational element for nuclear plant analyzers. It has been utilized in simulating a myriad of transient scenarios in LWRs, including but not limited to, loss of coolant, anticipated transients without scram, and various operational transients such as loss of feedwater and station blackout events [109].

Furthermore, the code is not restricted to nuclear systems, but is also adaptable for simulating a wide array of thermal and hydraulic transients in non-nuclear settings involving different fluid phases like steam, water, and non-condensable gases. The development of RELAP5/MOD3.3 involved collaborative efforts between the NRC and a consortium comprising multiple international and domestic organizations, which were part of the International Code Assessment and Applications Program and its succeeding entity, the Code Applications and Maintenance Program. Additional funding and support were provided by various Department of Energy sponsors, including discretionary funding programs directed by INEL [98].

The RELAP5/Mod3.3 version operates on a non-homogeneous, non-equilibrium two-phase system model, utilizing a swift, partially implicit numerical method to facilitate cost-effective transient system calculations. The aim from the inception of the RELAP5 initiative was to engineer a tool that encapsulated crucial first-order effects vital for accurate transient prediction while maintaining computational simplicity and cost-effectiveness for parametric or sensitivity analyses. To this end, the software incorporates an extensive array of generic component models, covering pumps, valves, pipes, reactors, and heat structures, among others. Specialized process models for phenomena like form loss, flow area change, branching, choked flow, and boron tracking have also been integrated into the code to enhance its predictive capabilities. For further details regarding the numerical schemes and reduced models, the reader is referred to Volumes 1 and 4 of the code manual [110].

4.2 Computational Magnetohydrodynamics

As elucidated in Chapter 3, the role of MHD is crucial when dealing with LM in fusion BB, especially in the presence of magnetic fields. To address these complex issues, there is a growing demand for sophisticated Computational Magnetohydrodynamics (CMHD) codes. Such codes should be adept at handling large-scale three-dimensional geometries, steady and unsteady states, multi-material domains, as well as intricate boundary conditions, all within the bounds of fusion-relevant parameters like high Hartmann, Reynolds, and Grashof numbers.

Beginning with early work in the 1970s that focused on straightforward geometries and lower magnetic fields, the field has grown to accommodate more complex structures and higher magnetic field intensities, thanks in part to advancements in computational resources and numerical methods. Over time, hybrid analytical-numerical methods were developed to mitigate the limitations of earlier techniques, allowing for more accurate and efficient simulations.

In the landscape of available computational tools, both specialized and general-purpose codes coexist. General-purpose codes like Fluent, COMSOL, and OpenFOAM offer user-friendly interfaces but may lack the flexibility required for highly specialized applications. On the other hand, tailored codes specifically designed for MHD applications offer enhanced performance and a more extensive selection of dedicated models. Nevetheless, only HiMAG exists as a CFD code designed specifically for LMMHD. Additionally, there are research codes developed at specific institutions, which are typically not available to the general public. While these codes can be highly effective for particular applications, they tend to have limitations [111].

Despite considerable progress, no existing CMHD code is yet fully capable of meeting all the stringent requirements necessary for simulations under fusion-relevant parameters. Consequently, there is an ongoing need for intensive code development, rigorous testing, and the creation of a comprehensive benchmark database.

In the sections that follow, some CFD tools will be briefly outlined. These tools have been employed by the authors during the course of the Ph.D. for research activities that are tangential to the primary focus of this thesis, and are therefore not elaborated upon in this work. For example, a novel OpenFOAM solver for MHD flows in conductive rectangular channels is discussed in [112]. Another instance is [113], where the thermal-hydraulic performance of the bottom-cap breeding cells of the WCLL OB segment is analyzed. It is worth noting that an OpenFOAM MHD solver has also been utilized in this thesis for the purpose of code-to-code benchmarking, as will be discussed in Chapter 9.

4.2.1 CMHD tools

ANSYS-CFX

ANSYS CFX is a comprehensive Computational Fluid Dynamics software suite that encompasses pre-processing, solving, and post-processing functionalities. The software is modular, consisting of CFX-pre for case setup, CFX-Solver for numerical solutions, and CFD-Post for result visualization. An additional module, the CFX-

Solver Manager, provides enhanced control over simulation runs. One key feature of ANSYS CFX is its coupled solver, which simultaneously solves hydrodynamic equations. This approach is computationally expensive but converges faster than the traditional segregated solvers. ANSYS CFX addresses common fluid dynamics equations, excluding MHD terms. However, an MHD module was introduced in 2009 and has undergone testing and validation. Being a proprietary software, its source code is not publicly accessible, restricting the evaluation to theoretical setups documented in user manuals [6].

In ANSYS CFX, the implementation of MHD effects is closely aligned with the approach outlined in Section 3.4. Two key source terms are introduced in the governing equations: the Lorentz force in the momentum equation (Equation (3.3)) and Joule dissipation in the energy equation (Equation (3.4)). To streamline the set of PDEs, the formulation employs the electric scalar potential ϕ and the magnetic vector potential $\mathbf{A}$. Starting from the general electromagnetic equations,

$$E = -\nabla\phi - \frac{\partial \mathbf{A}}{\partial t}, \tag{4.1}$$

$$B = \nabla \times \mathbf{A}, \tag{4.2}$$

and applying specific assumptions, such as the Coulomb gauge and uniform magnetic permeability, the MHD module in CFX is based on the equations,

$$\nabla \cdot (-\sigma\nabla\phi) = \nabla \cdot [-\sigma(\mathbf{u} \times \mathbf{B})], \tag{4.3}$$

$$\nabla \cdot (\mu_1 \nabla \mathbf{A}) = \sigma[E + \mathbf{u} \times (\nabla \times \mathbf{A})]. \tag{4.4}$$

Solving these yields the current density $\mathbf{j}$,

$$\mathbf{j} = -\nabla^2 \mathbf{A}. \tag{4.5}$$

Notably, CFX-Pre allows for separate activation of electric and magnetic models, offering flexibility in problem setup. While CFX theoretically can model finite and high-Rm MHD problems, no applications specific to fusion reactors have yet been reported, to the best of the Author knowledge.

OpenFOAM

OpenFOAM, an acronym for Open source Field Operation And Manipulation, serves as a comprehensive open-source CFD toolkit. Designed for customized physics solvers, it enables simulations across a broad range of domains such as basic CFD, combustion, turbulence modeling, electromagnetism, heat transfer, multi-phase flow, and stress analysis. The distribution includes a wealth of standard libraries featuring numerical algorithms, thermophysical properties, as well as turbulence and reaction models [114]. It is constructed as an object-oriented C++ framework grounded in continuum mechanics, primarily utilizing the Finite Volume Method (FVM). The framework employs C++ to establish a syntactic model for "equation mimicking" and scalar-vector-tensor manipulations. At the heart of these libraries lie object classes that offer high-level operations for geometries, meshes, and discretization techniques [115]. Given its high flexibility, customizability, absence of licensing fees, and excellent parallelization capabilities, OpenFOAM is particularly suitable for developing specialized models, like, for instance, one dedicated to simulate LM MHD phenomena [12, 24, 116].

The official OpenFOAM distribution includes a MHD solver, termed mhdFoam [117]. This solver is designed for the simulation of incompressible and laminar MHD flows, utilizing the magnetic induction formulation for the MHD governing equations and a PISO-like algorithm to ensure the divergence-free nature of the induced magnetic field. This approach is computationally intensive due to the vector nature of the magnetic induction equation, which accounts for both externally applied and self-induced magnetic fields, resulting in a robust bi-directional, non-linear coupling between fluid velocity and magnetic fields. Numerous models have emerged in recent years, with a significant portion employing the ϕ-formulation approach (that exchanges the vectorial transport equation for magnetic field with a scalar one for electric potential, that is selected as main electromagnetic variable), covering a wide range of phenomena pertinent to blanket design. These include steady and time-dependent flow around obstacles [118], integrated MHD/heat transfer/tritium transport [119], and magneto-convection coupled with electrical interactions across multiple domains [120].

4.3 Summary

This chapter aims to offer a comprehensive survey of the principal computational instruments utilized in the field of nuclear thermo-hydraulics research and development. A thorough evaluation of Nuclear Power Plants (NPPs) and Fusion Power Plants (FPPs) requires an integrated approach that encompasses a range of tools and methodologies, including scaling criteria, experimental analysis, computational modelling, software engineering, and Validation and Verification protocols in conjunction with Uncertainty Quantification. System codes, such as RELAP5/Mod3.3, are engineered to facilitate agile analyses of even the most intricate nuclear phenomena. However, these codes have intrinsic limitations. For example, numerous processes are sensitive to geometrical configurations, mandating that models be individually tailored and validated. Closure laws, integral to these models, often exhibit considerable uncertainties, originating from either simplified physics, omitted processes or a lack of focused research as their impact on prevalent transients is generally minimal. Additionally, the inherent shortcomings of 0-D and 1-D models become conspicuous when attempting to capture local three-dimensional phenomena like buoyancy-driven circulations. The empirical basis of many closure laws further complicates their application beyond validated scopes, making such extrapolations perilous. Conversely, Computational Fluid Dynamics (CFD) codes possess the ability to model intricate components and processes but are currently prohibitive in terms of computational and temporal resources for system-level evaluations. The subsequent Chapter 5 is dedicated to providing an overview of the recently developed system code, REDMaHD, which signifies an advancement in the establishment of a System Thermal-Hydraulic (SYS-TH) framework for assessments pertinent to fusion applications.

Chapter 5

Towards a MHD system code

5.1 MHD SYS-TH codes state-of-the art

The most critical MHD effects influencing liquid metal blanket performance are generally pressure losses and modified heat transfer coefficients. Therefore, it has been deemed of paramount importance to prioritize their implementation in thermal-hydraulic system codes. For MHD pressure losses, SYS-TH should predict both distributed (2D) and concentrated (3D) losses influenced by factors such as electromagnetic coupling, buoyancy, and Q2D turbulence. While well-defined scaling laws exist for fully developed flows in standard geometries, predicting 3D losses is challenging due to multiple governing parameters, complex geometries, and scenarios like fringing magnetic fields or variable wall conductivity. Accurate coefficients for these losses typically require expert selection based on detailed simulations or specialized experiments. Recent comprehensive reviews on 3D MHD losses are available in the literature [121].

While 2D and certain 3D MHD effects in duct flows are well-understood for incorporation into SYS-TH codes via adapted friction factors, challenges arise from unique MHD phenomena. For instance, electromagnetic coupling due to leakage currents in parallel channels with conductive walls requires specialized 2D or 3D simulations for friction coefficient determination [24, 121, 122]. This complexity intensifies in the presence of multiple coupled bends, resulting in uneven flow distribution as shown in works by Madarame et al. [93] and Stieglitz et al. [123].

The impact of buoyancy forces, especially in the presence of temperature gradients causing flow separation and vortex formation, is another challenge [124, 125]. Additionally, heat transfer modeling remains an active research area, particularly for low-Prandtl-number fluids like liquid metals. Established correlations for Nusselt and Peclet numbers, a brief review of which can be found in Ref. [126], must be extended to account for additional MHD parameters. Some experiments suggest that MHD flows can have superior heat transfer characteristics, attributed to phenomena like high-amplitude low-frequency temperature fluctuations and reorganization of flow structures, and thin boundary layers [84, 88, 127, 128]. Yet, a unified scaling law incorporating these insights into SYS-TH codes is still lacking.

To the best of the Author's knowledge, there are six SYS-TH codes that currently provide MHD modelling capabilities for liquid metal blanket systems. These include REDMaHD (developed during this PhD research), MARS-FR [129], MELCOR [130], MHD-SYS [108], GETTHEM [131], and RELAP5-3D [132, 133]. While RELAP5-3D offers built-in MHD modeling features, other codes have been adapted to incorporate these capabilities. Specifically, MHD-SYS is tailored to simulate MHD phenomena. A comprehensive comparison of these codes, based on their features like MHD pressure losses, electromagnetic coupling, MHD heat transfer, V&V status, and CFD-coupling, is presented in Table 5.1.

All aforementioned codes predict MHD pressure losses for fully-developed flows by adjusting the friction loss coefficients. Their approach to 3D losses, however, varies. Notably, no SYS-TH code can address all scenarios causing additional pressure drops. MARS-FR and MELCOR do not support 3D loss predictions. RELAP5-3D focuses on fringe magnetic fields, while MHD-SYS provides boundary conditions to a coupled CFD tool, specifically the mhdFoam solver in OpenFOAM. REDMaHD offers a generalized model for 3D losses with automatic coefficient calculations based on given geometrical parameters. GETTHEM uses a similar approach for bends but employs a fixed loss coefficient for cross-sectional changes and lacks support for FCI.

Concerning electromagnetic coupling and heat transfer, MHD-SYS is equipped to handle them using models strictly based on analytical solutions for specific wall conductivity and magnetic field orientations. This narrows their applicability to general blanket designs. As discussed in Chapters 8 and 9, REDMaHD is the only alternative code that can address the absence of a direct EM coupling model by allowing the selection of specific wall thickness values. Additionally, a forced convection model for the MHD regime is in the development.

Among the listed codes, only REDMaHD boasts a comprehensive and documented V&V procedure. A preliminary validation is available for MHD-SYS, while MARS exclusively the accurate reproduction of analytical results for 2D losses is discussed. Neither RELAP5-3D, GETTHEM nor MELCOR provide details on validation activities.

MHD-SYS is the only one equipped for coupling with other tools. However, its coupling limitations stem from depending on an OpenFOAM solver that lacks rigorous validation and is computationally demanding. There is potential for REDMaHD (or RELAP5) to couple with ANSYS-CFX, currently being explored within the context of fission reactors [134]. No information are available for CFD - coupling for the other SYS-TH codes.

None of these codes support modeling of MHD effects on molten salts and phenomena related to mass transport, tritium permeation, and corrosion. It should also be emphasized that there are no implemented correlations specific to mixed and natural convection, which limit their applicability. The exclusive support for single-phase flows further constrains their use for simulating incidental transients such as LOFA/LOCA and the like. Naturally, magnetic field transients, like disruptions and VDE, cannot be simulated either. While the applicability to operational transients seems theoretically feasible, it remains questionable, mainly due to the lack of validation cases.

5.2 RELAP5 Development for MagnetoHydrodynamics - REDMaHD

As previously elaborated in Chapter 4, the central objective of this Ph.D. research is to lay the foundational groundwork for the creation of a SYS-TH code able to represent MHD effects in liquid metal components and systems. The aim is to facilitate their planning and engineering, with a special focus on liquid metal breeding blankets. Among the various complexities, MHD phenomena stand out as both critically important and inadequately represented in existing system codes (see Chapter 3). Specifically, the impact of MHD effects on pressure losses within liquid metal flow systems warrants meticulous examination. The existing body of literature provides

Table 5.1: SYS-TH capabilities for MHD modelling. The updated validation status of REDMaHD is discussed in this thesis, while the initial implementation is detailed in Ref. [15].

Code	2D Loss	3D Loss	EM coupling	Forced Convection	Mixed Convection	V&V	CFD - coupling
RELAP5-3D [132, 133]	Yes	Only for fringing magnetic field	n.a.	n.a.	n.a.	n.a.	n.a.
REDMaHD [15]	Yes	Yes	Partial	Yes	n.a.	Acceptable	Under investigation
MARS-FR [129]	Yes	n.a.	n.a.	n.a.	n.a.	n.a.	n.a.
MELCOR 1.8.5/1.8.6 [130]	Yes	n.a.	n.a.	n.a.	n.a.	n.a.	n.a.
MHD-SYS [108]	Yes	Estimated through coupling	Based on analytical relations	Based on analytical relations	Based on analytical relations	Preliminary	Yes
GETTHEM [131]	Yes	n.a.	n.a.	n.a.	n.a.	n.a.	n.a.

sufficient characterization for the development of reduced models compatible with system-level codes, which will be further explored in Chapter 6. Moreover, Chapter 9 discusses the ongoing efforts to develop an initial model focusing on forced convection behaviors in MHD environments. It should be noted that the code leverages the capabilities of the existing RELAP5/Mod3.3 framework, extended to incorporate what is referred to as RELAP Development for MagnetoHydroDynamics, or REDMaHD.

As previously discussed in Section 4.1.2, RELAP5/Mod3.3 is a one-dimensional thermo-hydraulic code developed in Fortran language. It employs a non-homogeneous, non-equilibrium model for two-phase (liquid-vapor) systems, resolved through a partially implicit numerical method to expedite system transient computations. Specifically, the foundational hydrodynamic model is numerically resolved via a semi-implicit finite-difference technique, wherein the two-fluid momentum equations are formulated based on volume and time-averaged flow parameters. Non-axial gradient phenomena, such as frictional losses and heat transfer, are characterized through empirically-derived transfer coefficient correlations [110]. RELAP5 is principally designed for transient simulations of light water reactor coolant systems under hypothesized accident conditions, coupling the reactor coolant system with the core dynamics. It employs a generic modeling strategy, allowing for the simulation of diverse thermal-hydraulic systems [110].

The code has garnered extensive validation across an array of fission reactor applications and is held as the benchmark standard within this realm. Hence, it emerges as an optimal candidate for enhancement and adaptation for fusion reactor design. As is obvious, the original code lacks MHD functionalities pertinent to liquid metals, as these features are not relevant for fission reactor designs.

Modifications incorporating MHD effects commence from a newer version of the RELAP5 code [135–137], developed collaboratively by the Department of Astronautical, Electrical and Energy Engineering (DIAEE) at Sapienza University of Rome and ENEA. This version improves the modeling capabilities specifically for fusion reactors and their primary cooling systems [138].

Enhanced physical properties for PbLi and sodium-potassium (NaK) liquid metals are integrated in the framework of REDMaHD. PbLi is identified as the most promising coolant and/or breeder for fusion reactors [139, 140], whereas NaK serves as a model fluid for empirical MHD studies [29, 141, 142]. Future versions may incorporate other breeder fluids like liquid lithium or molten salt like FLiBe and FLiNaBe. Thermo-physical properties for the implemented liquid metals are based on methodologies outlined in [143] for lead (Pb) and lead-bismuth (LBE) properties. PbLi properties reference the work by Martelli et al. [144], while NaK properties follow Foust [145].

Electrical conductivity for various pertinent structural materials, including Eurofer97, is presently computed via a designated subroutine within REDMaHD. For Eurofer97, conductivity is auto-calculated based on correlations presented by Mergia and Boukos [146]. The source code must be altered if alternative wall materials are used. Future releases plan to automate this process, along with expanding the database for wall materials commonly used in fusion blanket designs, such as vanadium alloys and Inconel steels. In Table 5.2, electrical conductivities for relevant materials within this scope are tabulated.

Table 5.2: Electrical Conductivities of Various Materials. (*) Temperature T in Kelvin. (**) Temperature T in Celsius.

Material	Electrical Conductivity σ [S/m]
PbLi [144]	$\sigma = \frac{1}{(1.0333\times10^{-6} - 6.75\times10^{-11}\times T + 4.18\times10^{-13}\times T^2)}$ (*)
NaK [145]	$\sigma = \frac{10^8}{(37.66 + 2.307\times10^{-2}\times T + 7.187\times10^{-5}\times T^2)}$ (**)
Eurofer97 [146]	$\sigma = \frac{10^8}{(8.536 + 0.1484\times T - 2.84\times10^{-5}\times T^2)}$ (*)
Stainless-Steel	$\sigma = 1.26 \times 10^6$

5.2.1 Pressure drops Factors

The software accounts for MHD effects by calculating two distinct factors: one associated with frictional losses and planar currents (2D friction factor), and another perceived as a localized loss coefficient (3D coefficient) due to the induction of longitudinal currents [124] (see also Section 3.8). These factors are determined by separate subroutines, invoked when a liquid metal is specified as an input. The algorithm is engineered to combine MHD-induced pressure loss components with conventional hydrodynamic ones for both distributed (FWF_{MHD}) and localized (k_{MHD}) pressure drops, as illustrated in equation (5.1) [110].

$$\alpha_l\rho\frac{\partial v}{\partial t} + \frac{1}{2}\alpha_l\rho\frac{\partial v^2}{\partial x} = -\alpha_l\frac{\partial p}{\partial x} + \alpha_l\rho BF - (\rho FWF + FWF_{MHD})\alpha_l v - \frac{1}{2}\alpha_l\rho\frac{\partial v^2}{\partial x}(k + k_{MHD}) \quad (5.1)$$

This equation outlines the fundamental one-dimensional, single-phase (liquid) momentum conservation formulation, where α_l represents the liquid volume fraction and the term BF accommodates the effects of body forces. The x is the main flow direction, whereas p, v and ρ stand for fluid pressure, velocity and density. Understandably, standard behaviour is reinstated when the magnetic field is nullified. Here, on the left hand-side of the equation the momentum rate and advection terms are represented, respectively. On the right hand-side, the pressure gradient and the contribution of distributed and local losses are collected. The terms FWF have the dimension of Pa/m.

Only equations for the liquid phase are influenced by MHD effects; no effort has been made to establish a multi-phase MHD model. This limitation is acceptable, as solely sub-cooled liquid metal flows are deemed significant for near-term fusion endeavors. Moreover, the nucleation and transport of helium bubble in the breeder, a by-product of the tritium breeding reaction, although deemed possible in certain conditions of temperature and pressure existing within the blanket [147], is assumed to do not substantially alter the component overall performance, at least at the level of detail accessible to a SYS-TH code. Finally, it is essential to note that compatibility tests involving steam and liquid water were performed throughout the implementation process, confirming that the new routines do not compromise the existing capabilities of the software when they are not invoked.

2D MHD Pressure Drop Factor implementation

The code architecture is changed to add a coefficient FWF_{MHD} to the hydrodynamic friction factor, to assess the hydraulic head loss attributable to MHD phenomena. The 2D MHD pressure loss factor is formulated under the assumption of a uniform magnetic field that is orthogonal to the flow and aligned with at least one pair of duct walls (refer to Figure 5.1).

The FWF_{MHD} coefficient is a function of duct shape, geometric parameters, and material properties of both the fluid and walls. In Section 6.1 the FWF_{MHD}

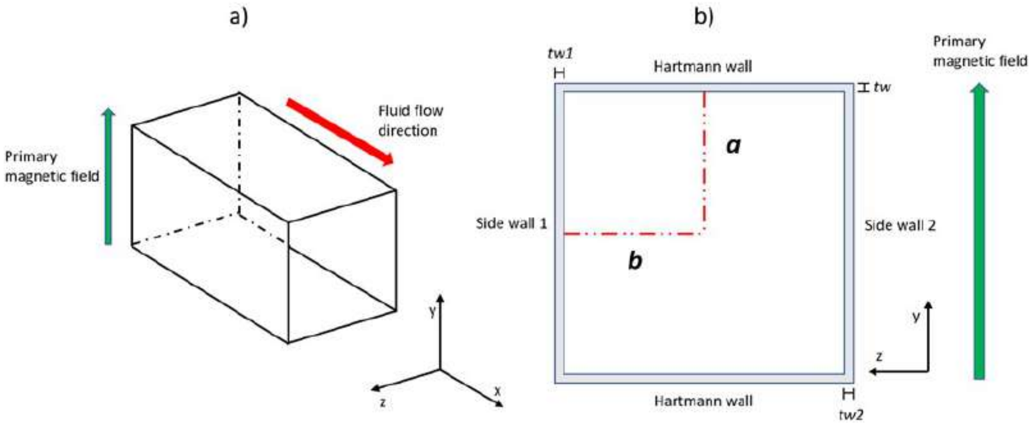

Figure 5.1: (**a**) A three-dimensional depiction of a typical hydraulic element, which is represented as a single volume. The applied magnetic field is illustrated by the green vector, which is assumed to be orthogonal to the direction of fluid flow (indicated by the red arrow). (**b**) A cross-sectional representation of the hydraulic element. Walls that are perpendicular to the magnetic field are termed Hartmann walls, whereas those parallel to the magnetic field are known as Side walls. The component characteristic lengths a and b are highlighted, along with the wall thickness (t_w) [15].

employed correlations are presented.

Table 5.3 summarizes all the parameters required for computing FWF_{MHD} factors. The user is essentially required to specify, during the problem modeling phase, the geometrical attributes and the magnetic field strength for each individual volume that constitutes the component affected by MHD phenomena.

3D MHD Pressure Drop Coefficient implementation

The simulation code computes a local MHD pressure drop coefficient, denoted as k_{MHD}, in three-dimensional scenarios when it identifies variances in cross-sectional areas, flow direction, or electrical conductivity between adjacent hydraulic elements. This nondimensional coefficient k_{MHD} captures the influence of axially induced currents, resulting in three-dimensional pressure drops, denoted as ΔP_{3D}. These are determined in accordance with equation (5.2) [32, 148]:

$$\Delta P_{3D} = \frac{1}{2} \cdot \rho \cdot v^2 \cdot k_{MHD} \, [\text{Pa}] \tag{5.2}$$

Here, ρ signifies the fluid density, which is temperature-dependent, and v represents

Table 5.3: Parameters used to compute Magnetohydrodynamic 2D additional pressure drop factor [15].

Parameter	**Description**	**Units**
Primary magnetic field B (defined in input by the user).	Magnetic field, always considered perpendicular to the stream direction.	$[T]$
Characteristic length a (defined in input by the user).	Component half-length along magnetic field direction.	$[m]$
Characteristic length b (defined in input by the user).	Component half-length perpendicular to magnetic field direction.	$[m]$
Wall thickness t_w (defined in input by the user).	Thickness of component walls perpendicular to magnetic field direction	$[m]$
Wall thickness t_{w1} and t_{w2} (defined in input by the user).	Thickness of component walls parallel to magnetic field direction.	$[m]$
Electrical conductance ratio for Hartmann walls, c.	$c = \frac{\sigma_w t_w}{\sigma_f a}$	-
Electrical conductance ratio for Side wall, c_1.	$c_1 = \frac{\sigma_w t_{w1}}{\sigma_f a}$	-
Electrical conductance ratio for Side wall, c_2.	$c_2 = \frac{\sigma_w t_{w2}}{\sigma_f a}$	-
Aspect ratio of the component divided by 3, δ	$\delta = \frac{a}{3b}$	-
Fluid and wall electrical conductivity, σ_f and σ_w	Electrical conductivity of fluid and wall, depending on input temperature.	$[S/m]$

the mean fluid velocity. The coefficient K_{MHD} is constituted by the summation of three distinct K factors, each indicative of a specific condition that induces 3D MHD pressure losses.

$$k_{MHD} = k_{Exp/Contr} + k_{Bend} + k_{FCI} \tag{5.3}$$

In equation (5.3), $k_{Exp/Contr}$ corresponds to the factor associated with changes in cross-sectional area, k_{Bend} is linked to alterations in the flow direction, and k_{FCI} accounts for the pressure loss stemming from significant disparities in electrical conductance between two adjacent components. In Section 6.2 a broader overview for the k models is presented. Additional variables have been introduced to specifically characterize local phenomena, complementing those previously discussed in

Section 5.2.1. These variables are summarized in Table 7.3.

Table 5.4: Parameters used to compute 3D MHD pressure drop factor, defined by the user.

Parameter	**Description**	**Units**
Secondary magnetic field B_p.	Poloidal field.	$[T]$
Angle ψ between B and bending plane.	Physical angle between the primary magnetic field and the plane on which the change of stream direction occurs.	$[deg]$
Angle θ between B and area change.	This variable stands for the physical angle between the primary magnetic field and the direction in which the change of cross-section is executed.	$[deg]$
Flag for flow channel inserts presence.	Activation of FCI model.	logical value

5.2.2 MHD heat transfer coefficient implementation

The fundamental thermal energy equation for the liquid phase, as described in RELAP5, is given by Equation 5.4 [110]:

$$\frac{\partial}{\partial t}\left(\alpha_l \rho U_l\right) - \frac{1}{A}\frac{\partial}{\partial x}\left(\alpha_l \rho_l U_l v A\right) = -P\frac{\partial \alpha_l}{\partial t} - \frac{P}{A}\frac{\partial}{\partial x}\left(\alpha_l v A\right) + Q_{wl} + \mathrm{DISS}_l \tag{5.4}$$

Here, Q_{wl} denotes the heat exchange between the fluid and the wall as elaborated in Equation 5.5. The heat transfer coefficient to the liquid is represented by h_l in $\frac{W}{m^2K}$, while T_w and T_{bulk} stand for the wall and bulk temperatures, respectively.

$$Q_{wl} = h_l(T_w - T_{\mathrm{ref}}) \tag{5.5}$$

Additional variables P, A, U, and DISS signify the liquid pressure, cross-sectional area of a single volume, internal energy, and a dissipation function[1], respectively. When a convective boundary condition is applied, whether it be for internal or exter-

[1] The conversion of mechanical energy into thermal energy through friction is included in this term, along with the Ohmic heating. However, the latter is often negligible for liquid metals and has thus been overlooked.

nal flows, the code calculates h_l and integrates it into the corresponding conduction equation. In cases involving both liquid and gas phases, the wall heat flux for each is taken into account. Heat transfer coefficients are determined using an extensive collection of experimental correlations to cover a wide range of flow regimes and thermal boundary conditions [109, 137]. In the context of REDMaHD, forced convection models for MHD flow in circular and rectangular channels have been implemented in terms of the Nusselt number, as presented in Equation 5.6.

$$h_{MHD,rect} = \frac{\mathrm{Nu}_{MHD,rect} \cdot k}{D_h}, \quad h_{MHD,circ} = \frac{\mathrm{Nu}_{MHD,circ} \cdot k}{D_h} \tag{5.6}$$

When a uniform heat flux is imposed through a heat structure, the code is designed to distinguish between different geometries and employs either $h_l = h_{\mathrm{MHD,rect}}$ or $h_l = h_{\mathrm{MHD,circ}}$ to solve Equation (5.5).

A more exhaustive discussion is available in Chapter 9. For the computation of $\mathrm{Nu}_{\mathrm{MHD}}$, no extra variables are required beyond those already presented in Tables 5.3 and 7.3.

5.3 Summary

The challenges in developing SYS-TH codes for MHD effects in liquid metal blankets primarily revolve around accurately predicting pressure losses and heat transfer coefficients. These codes must address both 2D and 3D MHD effects, influenced by various factors like electromagnetic coupling and buoyancy. While several SYS-TH codes exist, none can fully handle all the complexities involved, including 3D pressure losses and specialized heat transfer scenarios. Therefore, future work remains essential in extending the capabilities of SYS-TH codes to cover these phenomena comprehensively. his Ph.D. research establishes the groundwork for a SYS-TH code tailored for fusion power plants (FPPs), focusing particularly on MHD effects in liquid metal breeding blankets. The code, referred to as REDMaHD, builds upon the robust RELAP5/Mod3.3 framework and aims to model complex thermal-hydraulic phenomena in liquid metal systems. Developed at Sapienza University, this enhanced version brings specific improvements for fusion reactors. It incorporates refined thermo-physical properties for PbLi and NaK liquid metals, and provides electrical conductivity computations for key structural materials like Eurofer97. REDMaHD distinguishes itself in its domain through its capabilities for calculating both distributed and localized MHD pressure losses, complemented by an under-development feature for evaluating MHD heat exchange. In the next chapter, the main models of the code are presented along with its V&V.

Part III

SYS-TH Code Development

Chapter 6

Pressure losses models

6.1 Distributed pressure losses

The FWF_{MHD} factor is a function of channel shape, geometry parameters, and fluid/walls material. For square/rectangular cross-section conduits, it is derived from engineering correlations reported by Tillack et al. [89] and is expressed as:

$$FWF_{MHD} = \sigma_f B^2 \frac{\frac{\partial p_H}{\partial x}}{1 + \delta[\frac{\partial p_H}{\partial x}\left(\frac{1}{2c_1^*} + \frac{1}{2c_2^*}\right)]} [kg/m^3 s] \tag{6.1}$$

Where:

$$\frac{\partial p_H}{\partial x} = \frac{c_H + Ha^{-1}}{c_H + 1} \tag{6.2}$$

$$c_s^* = Ha^{-1/2} + c_s \tag{6.3}$$

In equation (6.1), c_H is the wall conductance ratio of the Hartmann walls c_1 and c_2 are the wall conductance ratio for the side walls. Note that the original Tillack equation has been modified for ducts that may have different walls thickness or, equivalently, non-uniform wall conductance ratio ($c \neq c_1 \neq c_2$), that is a common feature in liquid metal circuits. It is valid only for channels that have a uniform Hartmann wall conductivity. For duct geometries that cannot be treated with this approach, the wall with the highest conductive ratio should be conservatively assumed to be representative of the whole channel.

If the duct walls have a uniform thickness, equation (6.1) can be simplified [79, 88, 149]:

$$FWF_{MHD} = \frac{\sigma_f B^2}{1 + c^{-1}(1 + \delta)}[kg/m^3 s] \tag{6.4}$$

Similarly, a conduit with circular cross section and uniform wall conductivity is treated with another simplified expression of equation (6.1), such as $\delta = 0$ [79, 88, 149]:

$$FWF_{MHD} = \frac{\sigma_f B^2}{1 + c^{-1}}[kg/m^3 s] \tag{6.5}$$

Where for those channels,

$$c_{circ} = \frac{\sigma_w}{\sigma} \frac{r_{outer}^2 - r_{inner}^2}{r_{outer}^2 + r_{inner}^2} \tag{6.6}$$

It is important to keep in mind that predictions from equations (6.1), (6.4) and (6.5) show slight deviation from experimental data (i.e. $\pm 15\%$), according to the overview provided by Tassone et al. in [32].

6.2 Localized pressure losses

6.2.1 Bend Pressure Drops

MHD pressure drops in bends, as depicted in Figure 6.1a, utilize correlations symbolized by K_{BEND}. These correlations, for a bending plane parallel to **B**, stem primarily from Kirillov et al. [79] for circular pipes, denoted as $K_{BEND-circ||}$, and from the experimental research by Reimann [150] for square channels, represented as $K_{BEND-sq||}$.

$$K_{BEND-circ||} = 0.125 \cdot \frac{\Psi_{BEND}}{90} \cdot N \tag{6.7}$$

$$K_{BEND-sq||} = \frac{1.063 \cdot c}{4/3 + c} \cdot \frac{\Psi_{BEND}}{90} \cdot N \tag{6.8}$$

The formulation in equation (6.7) caters to a 90° bend pressure drop for insulated circular channels and is deemed appropriate for electrally conductive channels due to its conservative nature. In contrast, equation (6.8) caters to 90° bends in square or rectangular channels. Under the assumption of inertia-free flow, both equations can accommodate any bend angle, symbolized by Ψ_{BEND} (measured in degrees), through the correction coefficient $\Psi_{BEND}/90$. Thus, a bend of 180° can be conceptualized as two consecutive 90° bends. Please note that this assumption is tantamount to the statement that inertia can be neglected in these hydraulic elements, which is well justified for $N \gg 1$. Several analyses have explored the phenomenon of bends in flow paths either parallel or orthogonal to the magnetic field orientation. Notably, the pressure loss for a bend that's perpendicular to the magnetic field direction ($\perp B$) is consistently lower, occasionally even insignificant, in contrast to a parallel magnetic field orientation ($||B$) [79].

The fundamental physics governing such behavior is intricate. Nevertheless, a qualitative elucidation is presented below. Within an MHD flow, the magnetic field acts to suppress the components of angular momentum not aligned with the field itself. As a result, fluid substructures, such as vortexes, possessing angular momentum predominantly perpendicular to B, are swiftly diminished, consuming the fluid overall energy in the process. The angular momentum in line with the field remains intact[151]. When the fluid undergoes a bend in a direction $\perp B$, the angular momentum largely conforms with the field, leading to minimal energy expenditure to reconfigure the fluid substructures. In contrast, when the flow encounters alterations in the direction of $||B$, the fluid angular momentum tends to be predominantly orthogonal to the magnetic field, leading to a notable energy loss to reestablish stable conditions.

$$K_{BEND-circ\perp} = \frac{1}{3} \cdot K_{BEND-circ||} \tag{6.9}$$

$$K_{BEND-sq\perp} = \frac{1}{3} \cdot K_{BEND-sq||} \tag{6.10}$$

The correlations given by equations (6.7) and (6.8), which were initially devised for the latter scenario, have been adapted for bends perpendicular to the field by introducing a scaling factor of 1/3 [32]. This adjustment factor was selected to account for the reduced influence that $\perp B$ bends exhibit on the total energy loss in comparison to $||B$ bends. Such a model has demonstrated reasonable accuracy for simulating intricate piping systems with bending conduits, as further elaborated in the subsequent sections (Chapter 8). As more comparative analyses become available in literature for these configurations, a revisit to the scaling is intended to achieve a closer representation of the physical phenomena. Equations (6.9) and (6.10) delineate $K_{BEND-circ\perp}$ and $K_{BEND-sq\perp}$, respectively.
Hence, at present, REDMaHD possesses the capability to process both $\perp B$ and $||B$ bends across any angle.

6.2.2 Abrupt Changes in Cross-Section

The approach to determine the MHD local pressure loss coefficient ($K_{EXP/CONTR}$) resulting from the velocity gradient induced in the axial direction by the alteration of the cross section between two regions is founded upon the experimental studies conducted by Bühler and Horanyi as discussed in [141]. Their examination involved a rectangular conduit experiencing an abrupt cross-section expansion aligned with the magnetic field direction (refer to Figure 6.1b). An empirical relationship predicting the 3D pressure drop was established and is provided in a condensed form as:

$$\Delta p_{3D} = \Delta p_{3D\infty} + \Delta p_{3D,viscous}(Ha^{-1/2}) + \Delta p_{3D,inertial}(Re^{1/3}) \qquad (6.11)$$

At its core, the pressure differential imposed by the expanding geometry is an aggregation of three components: $\Delta p_{3D\infty}$ is a component deduced from an asymptotic evaluation for conditions $Ha \to \infty$ and $N \to \infty$. The elements $\Delta p_{3D,viscous}$ and $\Delta p_{3D,inertial}$ represent the impact of viscosity and inertial forces. Equation (6.11) holds for $c = 0.028$ and an expansion ratio of $Z_c = 4$ (expressed as the proportion between the characteristic lengths of the downstream and upstream ducts), the parameters maintained during the experiments. However, the base REDMaHD model from equation (6.11) has been broadened to accommodate a more extensive range of expansion and contraction ratios.

The $K_{EXP/CONTR}$ formulation rests on the presumption that expansions and contractions are interchangeable configurations (an expansion transforms into a contraction if the flow direction is inverted and vice-versa), suggesting identical pressure drops given the expansion and contraction ratios are reciprocals. This holds true primarily for flows where inertial influences are minimal, that is, $N \to \infty$. To elucidate, the coefficient $K_{EXP/CONTR}$ is postulated to be symmetric concerning the cross-section variation ratio. Additionally, we assume that there exists a maximum for the local MHD factor, that it is to say that for $Z_c \to \infty$, then $K_{EXP/CONTR} =$ const. In line with the computational analysis conducted by Feng et al. [152], it is discerned that the supplementary pressure loss for $Z_c \geq 8$ remains invariant with respect to Z_c. Therefore, an upper bound of $K_{EXP/CONTR} = 2 \cdot N$, as proposed by Smolentsev et al. in [148], is adopted. Conclusively, for characterizing cross-section modifications transverse to B ($\perp B$), a prudent scaling coefficient is utilized, consistent with the methodology elaborated for bends (refer to Section 6.2.1).

The current $K_{EXP/CONTR}$ formulation is equipped to address ranges $0 < Z_c < \infty$ with B being either parallel or orthogonal to the cross-section alteration. However, the model does not presently incorporate the effects of wall conductivity and further geometrical parameters, such as the expansion length.

This gap is anticipated to be bridged in subsequent research, using as a foundation the computational studies undertaken by Rhodes et al. in [153] and Fan et al. [154].

6.2.3 Flow Channel Inserts (FCI)

For variations in wall electrical conductivity, the formulations integrated for K_{FCI} are derived from both experimental and computational studies, as presented in a series of papers discussing the Flow Channel Inserts (FCIs) setup [142, 155, 156]. The primary purpose of an FCI is to diminish MHD pressure loss within a channel by establishing electrical isolation between the fluid and the duct wall. A characteristic FCI is constructed with a slender dielectric material layer (typically alumina) sandwiched between steel panels, and is strategically placed within the duct requiring insulation, as schematically depicted in Figure 6.2. However, present manufactur-

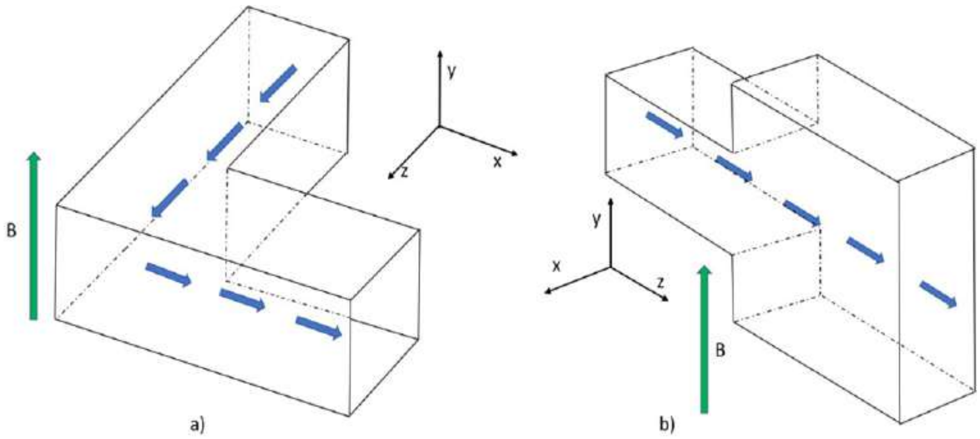

Figure 6.1: Exemplary geometric configurations that can be simulated using the newly incorporated features in the software. The green vector indicates the external magnetic field, B. (**a**) Bended square pipe design, where the bending plane is orthogonal to the magnetic field direction. (**b**) Transition from a square to a rectangular duct parallel to the B orientation.

ing capabilities constrain the production of FCIs to lengths of about $0.5m$ and to very simple geometries. This limitation signifies that crafting a flawlessly insulated piping framework becomes infeasible, especially when considering intricate geometric components intrinsic to a fusion reactor blanket structure [157]. As a result, insulation irregularities invariably arise when FCIs are utilized, culminating in augmented MHD pressure drops. This is attributed to the abrupt switch from regions with minimal conductivity to regions with pronounced conductivity along the wall. Within the REDMaHD environment, two distinct discontinuity models are incorporated. One such model corresponds to the inlet/outlet discontinuity category, observed during the transition between a section equipped with an FCI and another devoid of it, or the inverse. The second model deals with a gap discontinuity that may arise when two adjacent ducts, both equipped with FCIs, are divided by a minuscule section where the liquid metal is in contact with the bare pipe surface.

6.2.4 Verification and Validation (V&V)

The IAEA guidelines advocate that computational tools or methods intended for design and safety analyses undergo a rigorous Verification and Validation (V&V) process to ensure their dependability and precision [101]. According to IAEA Quality Assurance guidelines for nuclear codes, the V&V procedure must be supported by:

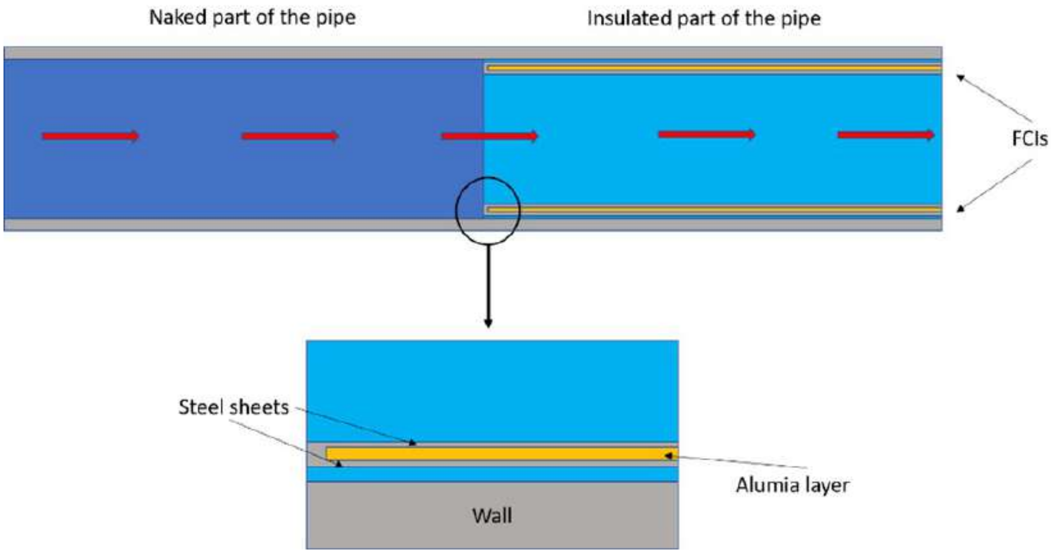

Figure 6.2: Diagram showcasing a representative Flow Channel Insert setup within a duct (entry into the insulated zone). Red vectors represent the path of the liquid metal. The layered nature of the FCI is emphasized at the bottom section of the figure.

- **Separate Effect Test (SET):** These tests are designed to investigate specific phenomena in isolation. The test conditions are deliberately simplified to focus on a single phenomenon or a small subset of phenomena. The results from SETs can be used to develop or validate specific models or correlations within a system code.
- **Integral Effect Test (IET):** These tests are designed to investigate multiple interacting phenomena in conditions that replicate as closely as possible the full-scale plant behavior during transients or accidents. IETs provide data to validate the overall predictive capability of system codes, especially in complex scenarios where multiple phenomena might interact.

Therefore, for the V&V process of REDMaHD, the outcomes from the software are compared with the results from direct numerical simulation tools and findings from experimental studies. Pertinent instances of V&V for MHD numerical solvers are documented in [125, 158–161].

In the subsequent chapters, the most representative verification and validation exercises are presented. Initially, SET cases are employed to ensure the code consistently utilizes the implemented models and correlations, devoid of bugs or mathematical errors. In other words, they are used for verification purposes. Later, more intricate configurations are explored to evaluate the effectiveness of the MHD module subroutines in producing physically accurate results (see Chapter 8). These tests should be understood as approximations of IETs, limited solely to the pressure loss.

For validation, the computational analysis by Swain et al. on the Lithium Lead Ceramic Breeder (LLCB) TBM under pertinent magnetic field intensities is replicated using REDMaHD [28] (see Section 8.1). Subsequently, experimental findings from the study conducted by KIT researchers on a Helium Cooled Lithium Lead (HCLL) TBM prototype are used as a reference to further validate the software capability against a more pragmatic benchmark [29] (see Section 8.2). Ultimately, the findings from the experimental campaign conducted by Courtessole et al. [16, 162], which examined the MHD characteristics of a WCLL TBM mock-up test section, are employed as a benchmark for the code predictions (see Section 8.3).

6.3 Summary

This chapter offers a general analysis of pressure loss models implemented in REDMaHD, segmenting the discussion into two main categories: distributed (2D) and localized (3D) pressure losses. The first section delves into 2D losses. Key equations are presented for calculating the pressure gradient factor, FWF_{MHD}, for both square/rectangular and circular cross-section conduits. These formulations stem from empirical engineering correlations and have been adjusted to account for ducts with non-uniform wall thicknesses. The second section focuses on 3D losses, examining three primary phenomena: MHD pressure drops in bends, abrupt changes in cross-section and FCI. For bends, two types of equations are outlined based on whether the flow encounters bends parallel or perpendicular to the magnetic field ($\|B\|$ and $\perp B$). The equations are built upon empirical correlations and take into account different bend angles. A scaling factor is introduced to account for the reduced energy losses for bends perpendicular to the magnetic field. For abrupt cross-sectional changes, the chapter discusses a model based on empirical studies that considers various factors such as viscosity and inertial dynamics. The model is expanded to include a broader range of expansion and contraction ratios, and introduces a maximum bound for the local MHD factor based on computational analysis. Formulations for K_{FCI} are based on experimental studies FCIs. In the REDMaHD context, two discontinuity models are used: inlet/outlet and gap discontinuities. These models address issues arising from insulation irregularities and transitions in wall conductivity. In line with IAEA guidelines for Verification and Validation (V&V), the following chapters detail REDMaHD V&V process. The process starts with single-effect tests for verification and advances to complex configurations. For validation, the code is benchmarked against computational and experimental studies in the realm of various TBMs.

Chapter 7

Verification cases

The results presented in this chapter are taken from Ref. [15]. In this context, two of the prototypical cases used for the development of the MHD losses model for expansion/contraction and the correlation for electrical conductivity discontinuity are simulated using REDMaHD. This exercise ensures that the code accurately computes the relevant factors for both 2D and 3D drops. The first case involves a square/rectangular pipe, while the second pertains to a circular channel.

7.1 Abrupt area changes

The experimental investigation conducted by Buhler and Horanyi as detailed in [141] serves as a reference point for the verification of the REDMaHD model predictions for 3D MHD pressure reductions caused by abrupt transitions in duct geometry. This benchmark also showcases the model proficiency in approximating 2D pressure losses within square or rectangular channels. The specific experiment examines the flow dynamics of a liquid metal (NaK) within a rectangular channel experiencing a sudden geometric expansion, subsequently adopting a square cross-sectional profile, as depicted in Figure 7.1. Notably, the expansion is solely along the magnetic field trajectory, resulting in a purely parallel alteration in geometry. The designated expansion ratio is denoted as $Z = 4$ and the conductivity ratio for the expanded segment is $c = 0.028$. As the fluid encounters this geometric deviation, a reorganization of its flow profile ensues, generating an axial potential gradient. This induces stream-wise electrical currents that, upon interacting with the dominant magnetic

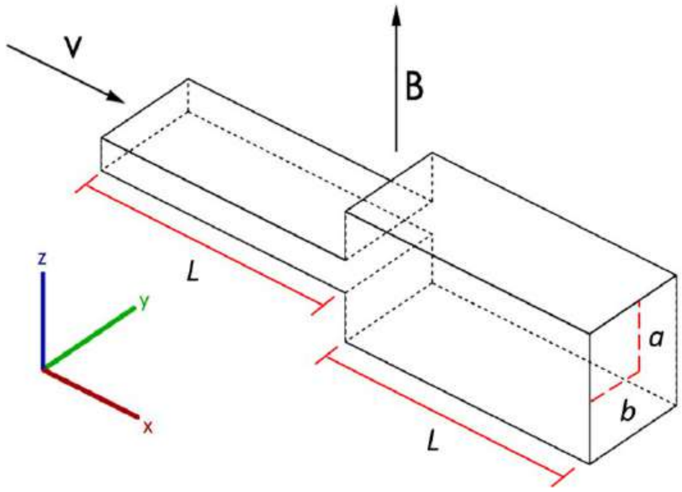

Figure 7.1: Schematic representation of the experimental apparatus geometry.

field, produce augmented Lorentz forces accountable for the additional pressure drop (Δp_{3D}). The test section is crafted from stainless-steel with a constant wall thickness, held constant both before and after the expansion. The flow is characterized as horizontal and isothermal, thereby facilitating material thermo-physical property evaluations at a fixed temperature of $293.15K$, as delineated in Table 7.3. The applied magnetic field is uniform and parallel to the expansion direction. The experimental parameters span a range of nondimensional values: $10^3 \leq Ha \leq 5 \cdot 10^3$ and $30 < N < 1.3 \cdot 10^5$ [141].

The nodalization layout of the model is depicted in Figure 7.2. Fluid entry conditions are defined by both a time-dependent volume component (TMDPVOL #10) and a time-dependent junction (TMDPJUN #15). The metal inlet temperature is supplied by the TMDPVOL, while the mass flow rate is determined by the TMDPJUN. The liquid exit pressure is controlled by an additional time-dependent volume (TMDPVOL #30). The conduit is emulated using a pipe component (PIPE #20), which is partitioned into 12 volumes interconnected by 11 junctions. The principal parameters associated with the model are gathered in Table 6.

In Figure 7.3, a characteristic curve illustrates the relationship between scaled pressure and nondimensional axial length. The pressure undergoes scaling with $p_0 = \sigma f v a B^2\ Pa$ while the geometrical attributes are scaled using the reference length $a = 0.047m$. In the domain where flow has reached equilibrium, as elucidated by Bühler, the nondimensional pressure gradient for the rectangular conduit

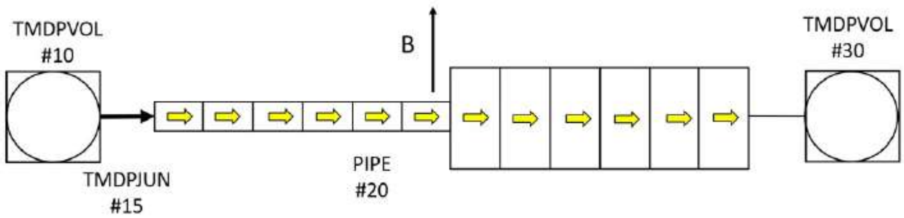

Figure 7.2: Diagrammatic representation of the RELAP5 nodalization. Yellow arrows indicate the fluid trajectory, while the magnetic field (B) is represented by a black vector.

Table 7.1: Geometrical Parameters of the Model.

Parameter	**Rectangular Duct**	**Square Duct**
a $[mm]$	11.75	47
b $[mm]$	47	47
L $[mm]$	300	300
t_w $[mm]$	3	3
c	0.112	0.028

stands at $k_p = 0.37479$. Conversely, for the square conduit, $k_p = 0.02057$, under the operational conditions defined by $Ha = 4000$ and $N = 29604$.

According to the findings presented in Table 7.2, the REDMaHD model provides a precise quantification of the pressure gradient arising from MHD 2D phenomena in square/rectangular channels, demonstrating a relative error invariably below +0.5%. The pressure gradient error is evaluated as $err = 100 \times \frac{(\sigma v B^2)_{calculated}}{(\sigma v B^2)_{exp}}$. The overall 3D loss is also adeptly captured by the code, providing results that align closely with those derived from equation (6.11).

Table 7.2: Errors in 2D and 3D Pressure Losses for Varied Ha and N.

Parameters	Computed k_p for Rectangular Duct	Error in Pressure Gradient for Rectangular Duct [%]	Computed k_p for Square Duct	Error in Pressure Gradient for Square Duct [%]	Measured $\Delta P_{3D}[kPa]$	Computed $\Delta P_{3D}[kPa]$	Relative Error [%]
$Ha = 2000, N = 7455$	0.375	0.056	0.02053	0.1	1.46	1.462	0.13
$Ha = 3000, N = 3160$	0.37512	0.09	0.02057	0.29	4.9	4.9	0.54
$Ha = 4000, N = 29608$	0.3754	0.17	0.0206	0.46	3.9	3.87	-0.12

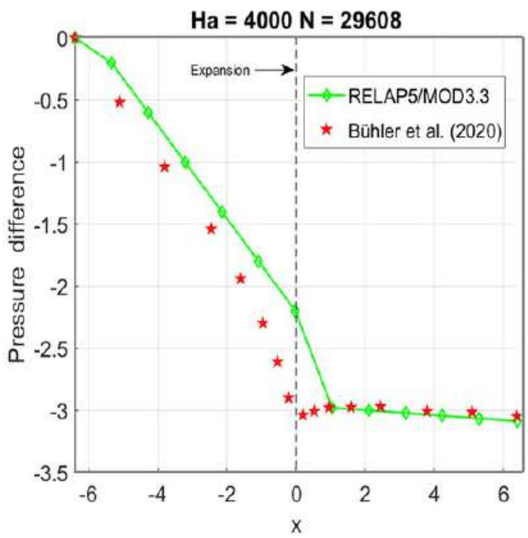

Figure 7.3: Nondimensionalized Total Pressure Drop versus Scaled Axial Length for $Ha = 4000$ and $N = 29608$. The vertical dashed line delineates the abrupt expansion.

7.2 Flow channel inserts

Bühler et al. experimental analysis in [155] was utilized as a benchmark to ascertain the software accuracy in addressing FCI configurations and comprehending pressure deviations in circular cross-section channels with fully developed flows.

The model geometry, shown in Figure 6.2 and Figure 7.4, comprises a linear conduit divided into an uncoated segment and an FCI section (denoted darker in Figure

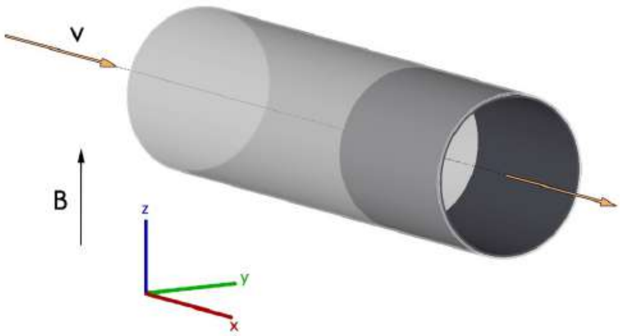

Figure 7.4: 3D representation of the experimental segment. The more shaded section of the conduit indicates the FCI-insulated portion. The magnetic field vector B and flow velocity v are illustrated.

Table 7.3: Thermophysical properties at a temperature of $293.15K$.

Constituent	**Electrical Conductivity** (S/m)	**Density** (kg/m^3)	**Viscosity** $(Pa \cdot s)$
Na22K78	2.62×10^6	874.15	8.5×10^{-4}
Stainless Steel	1.26×10^6	-	-

7.4). The liquid metal flows from the bare segment into the insulated section. This transition is by a sudden change in the duct electrical conductivity, thereby inducing an electric potential gradient aligned with the flow direction. Consequently, three-dimensional currents arise within the fluid, inducing additional Lorentz forces that augment the load losses when contrasted with the fully developed flow. Evaluating the three-dimensional pressure drop is imperative, as its presence at entrance/exit from insulation and for interstitial gaps might considerably curtail the efficacy of the FCIs.

The experimental setup utilized NaK as the molten metal. The horizontal conduit is constructed from stainless-steel, maintaining a consistent wall thickness. The flow regime is considered isothermal, and material characteristics are derived at a benchmark temperature of $293.15K$ (refer to Table 7.3).

Within the domain of the test section, a uniform and unidirectional magnetic field is employed. The field intensity, alongside the NaK mass flow rate, is adjustable. Therefore, the experimental procedure spans a spectrum of nondimensional numbers pertinent to fusion reactor implementations, specified as $10^3 \leq Ha \leq 5 \cdot 10^3$ and

Table 7.4: Parameters delineating model geometry. Notice that insulated wall is considered as thick as the first steel layer that separate the alumina from the liquid metal. Therefore, t_w is not to be intended as the whole thickness of the FCI.

Parameter	**Bare Conduit**	**Insulated Conduit**
Internal radius $[mm]$	48.6	47
Axial span $[mm]$	200	486
t_w $[mm]$	7.32	0.46
c	0.0727	0.00476

$10^4 \leq Re \leq 4.8{\cdot}10^4$. A conclusion that can be drawn from the experiment is that the pressure gradient (Δp_{3D}), originating from the LM transitioning into an insulated zone, is equal to the pressure gradient within an equivalently insulated conduit of approximately 4 characteristic lengths (a).

$$\Delta p_{3D} \approx 4 \cdot (k_{pFCI} \sigma v B^2 a) \tag{7.1}$$

In equation (7.1), the characteristic length is denoted by the internal radius of the uncoated conduit. The coefficient $k_p = c/(1+c)$ represents the nondimensional fully developed flow pressure gradient, as characterized by Miyazaki et al. in [149]. It's imperative to emphasize that the applicability of equation (7.1) spans the entirety of the experimental domain, encompassing all the Hartmann and Reynolds numbers explored [155]. Figure 7.5 depicts the computational mesh utilized for simulations. The boundary conditions for the liquid metal are established by a time-modulated volume (TMDPVOL #10) and a time-dependent junction (TMDPJUN #15). The TMDPVOL determines the NaK inlet temperature, while the TMDPJUN enforces the mass flow rate of the liquid metal. The liquid exit pressure is regulated by an auxiliary time-dependent volume (TMDPVOL #30). A conduit component (PIPE #20) mimics the pipe, subdivided into 15 distinct volumes and connected by 14 individual junctions. The insulating layer is incorporated in the final 10 volumes. This is achieved by simulating thinner stainless-steel walls, ensuring an equivalent conductance ratio as reported by Bühler, given by $c_{FCI} = 0.00476$ [155]. Table 7.4 enumerates the primary parameters.

The variation of the normalized pressure as a function of the nondimensional axial coordinate (x) is presented in Figure 7.6. The pressure is normalized using the reference value $p_0 = \sigma f v a B^2$ Pa, and all geometric parameters are scaled

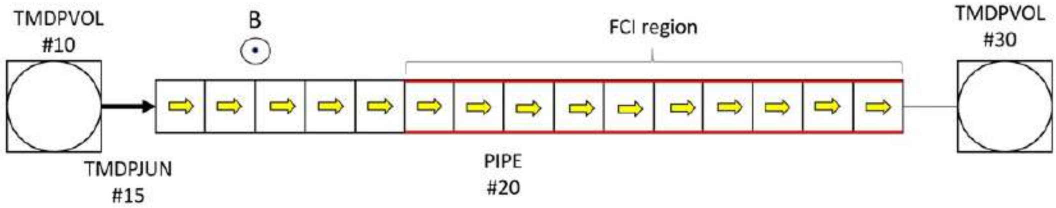

Figure 7.5: Illustration of the model detailing the RELAP5 discretization. The region implementing the flow channel insert is emphasized in red, and the fluid direction is marked by yellow arrows.

with the characteristic length a. It's important to remember that the overall trend of the nondimensional pressure drop, as documented by Bühler, remains consistent across varying Ha and Re values. Consequently, outcomes corresponding to other governing parameters are not presented. Throughout the conduit, REDMaHD demonstrates remarkable congruence with both the theoretical pressure drop predictions and the empirical findings. The nondimensional pressure gradient deduced by the software is in perfect alignment with the findings of Miyazaki for cylindrical conduits, as represented by the black line in Figure 7.6.

Table 7.5 consolidates the numerical outcomes from a multitude of computations. The software exhibits good precision (relative deviations $< +0.25\%$) in quantifying the fully developed flow loss of load. Moreover, the magnitude of the three-dimensional pressure drop is discerned with reasonable accuracy (deviation $< +10\%$). The slight overestimation associated with localized loss can be rationalized as follows: in addition to the interruption in wall electrical conductivity, the flow concurrently encounters a mild reduction in cross-sectional area owing to the insulation layer. Consequently, the total 3D head loss, given by equation (7.1), encompasses the effects of an abrupt cross-sectional contraction. However, this effect remains challenging to assess independently. Given that the FCI model in REDMaHD is constructed upon empirical results, which typically encompass these contraction/expansion effects, the variance in Δp_{3D} relative to the experimental findings in the current examination arises from RELAP5 accounting for the cross-sectional alteration in two distinct manners: both via the activation of the flow channel insert model itself and through the contraction model.

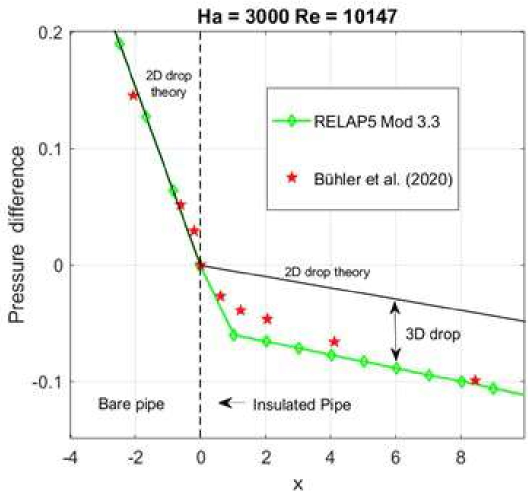

Figure 7.6: Depiction of the total nondimensional pressure drop against the scaled axial distance. The vertical dashed line indicates the onset of the insulated segment of the conduit. The disparity, between the fully developed flow theoretical prediction and the numerical/experimental results, manifesting post $x = 0$, is attributable to the three-dimensional pressure reduction.

Table 7.5: Percentile discrepancies between numerical computations and theoretical/empirical results.

Nondim. Parameters	**Error in Pressure Gradient (Bare Pipe) [%]**	**Error in Pressure Gradient (Insulated Pipe) [%]**	**3D Pressure drop Discrepancy [%]**
Ha = 2000, Re = 10186	0.0076	0.06	9.4
Ha = 2000, Re = 20155	0.008	0.021	9.43
Ha = 3000, Re = 10147	0.25	0.17	9.7

7.3 Summary

This chapter assessed the results produced by REDMaHD against the experiments by Buhler and Horanyi [141]. The focus was on 3D MHD pressure reductions arising from abrupt geometric transitions in ducts. The model effectively approximated both 2D and 3D pressure losses in square and rectangular channels. Various parameters, such as expansion ratio Z, conductivity ratio c, and magnetic field intensity, were considered. The REDMaHD model yielded pressure gradients and losses with relative errors consistently below $+0.5\%$, validating its reliability for complex MHD flow systems. Moreover, Bühler et al. provided an experimental framework, cited as [155], that serves as a benchmark for analyzing FCI configurations. The experiments cover a range of nondimensional numbers relevant to fusion reactor applications, and exhibit a pressure gradient consistent with the one derived by Miyazaki et al. [149]. It's crucial to note that the formula holds over the entire experimental domain and REDMaHD shows close agreement with both theoretical and empirical results. The only discrepancy occurs due to the effects of cross-sectional changes, which the software partially accounts for.

Chapter 8

Validation exercises

The subsequent chapter introduces the thorough validation of REDMaHD. For this purpose, high-quality experimental data, associated with intricate geometric configurations, are utilized. This ensures the concurrent manifestation of multiple 2D and 3D pressure drops, allowing for a comprehensive evaluation of the code capabilities. Outcomes here gathered refer to two different works Melchiorri et al. [15, 163] .

It is worth noting a general feature that has been implemented to partially account for the effects of electromagnetic coupling. In the analyzed circuits, this coupling frequently occurs due to the presence of multiple channels or flow paths separated by a shared partition. When LM flows in parallel directions on either side of this partition, there can often be a favorable impact on pressure drop. This is attributed to a mutually beneficial pumping effect [122, 164]. To represent this phenomenon in simulations, an approach is adopted where the thickness of the shared walls between channels is adjusted to half its actual value, allowing for a qualitative representation of the electromagnetic effects. If the metal flows in opposite directions between the coupled channels, the actual thickness of the shared walls is specified in the model.

8.1 Lead-Lithium Ceramic Breeder test blanket module

Computational fluid-dynamic analyses of MHD flow within a full-scale model of the proposed Lithium-Lead cooled Ceramic Breeder (LLCB) TBM for the ITER experimental campaign have been conducted by Swain et al. [28] under fusion-relevant conditions, specifically at a Hartmann number of $Ha \approx 1.8 \times 10^4$. Numerical investigations into MHD phenomena in high magnetic fields for such intricate configurations are scarce, making their results invaluable for the validation phase of system codes. In the work by Swain et al., an exhaustive thermal-hydraulic analysis is presented; however, the focus of this section is specifically on the outcomes pertaining to pressure drop.

Figure 8.1a depicts a two-dimensional schematic illustrating the geometry and flow path of the TBM. The LM, which in this case is PbLi, enters the module via an inlet header channel, denoted as segment A-B. Subsequently, the fluid ascends through five vertical (poloidal) channels, labeled as segment B-C. These poloidal channels are sequentially numbered from 1 to 5 as one moves away from the return channel, with Channel 1 being the nearest. The fluid is then accumulated in the upper header region before descending through the poloidal return channel (segment D-E). Ultimately, the PbLi is collected in the outlet header (segment E-F) prior to exiting the TBM. All PbLi ducts are of rectangular cross-section.

In the LLCB concept, the liquid metal serves as the coolant responsible for extracting thermal power from the breeding zone, which comprises boxes filled with solid breeder material (lithium-titanate) enclosed by thin walls of Reduced-Activation Ferritic-Martensitic steel (RAFMS). For the purposes of MHD calculations, it can be assumed that the breeder modules are perfectly insulating, and only the bounding walls should be considered for estimating the equivalent wall conductivity.

The geometrical parameters employed in this study are those delineated in [28]. The thermo-physical properties of both RAFMS and PbLi are evaluated at a reference temperature of $623\,K$, with the flow considered to be isothermal. The magnetic field B is set at $4\,T$ and is assumed to be unidirectional, aligned with the toroidal axis. A mass flow rate of 12 kg/s is imposed at the inlet.

The nodalization scheme, predicated on the geometry delineated in Figure 8.1a, is illustrated in Figure 8.1b. The scheme comprises 118 control volumes and 121 hydraulic junctions. A sliced modeling approach is employed, in which vertically oriented volumes at the same level are assumed to have equivalent lengths. Inlet conditions for the liquid metal are specified through a time-dependent volume (TMDPVOL # 10) and a time-dependent junction (TMDPJUN # 15). Specifically,

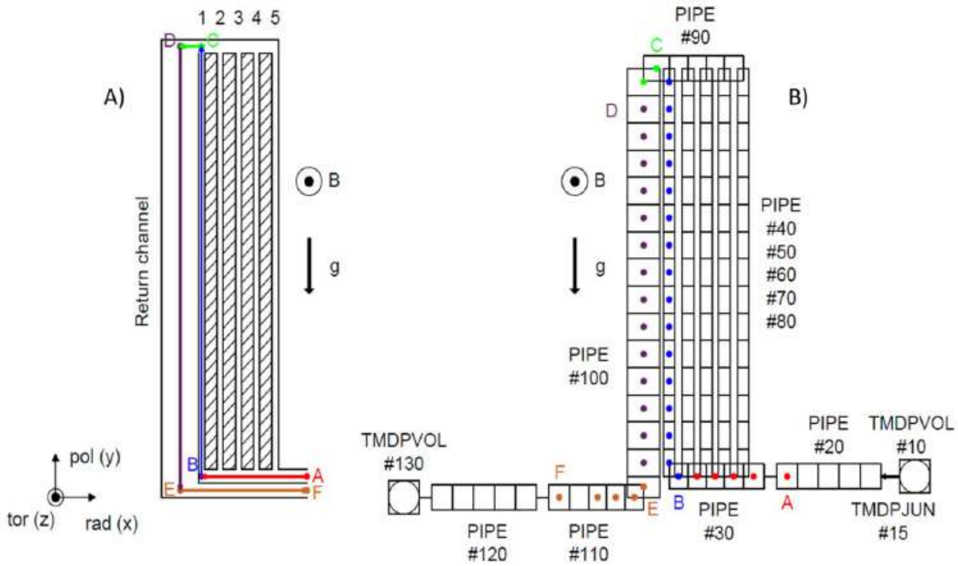

Figure 8.1: a) 2D schematic of the LLCB TBM with the shaded area representing the breeding modules. **b**) Nodalization scheme for the geometry.

TMDPVOL dictates the inlet temperature of the Lithium-Lead (PbLi), while TMDPJUN regulates its mass flow rate. Outlet pressure of the PbLi is constrained by an additional time-dependent volume (TMDPVOL # 130).

All constituent sections of the Test Blanket Module are simulated using equivalent pipe components. The modeling paradigm aims to preserve the actual inventory and flow area for each section. Hydraulic loss coefficients for abrupt area changes, bends, and tees are calculated employing the correlations found in Idelchik handbook [165], to yield a reliable representation of standard hydrodynamics.

In Figure 8.1b, colored markers identify the pressure measurement points within the model. Corresponding colors are attributed to the key hydraulic elements delineated in Figure 8.1a: red signifies the inlet header, blue represents the poloidal channel, green indicates the top header, purple designates the return channel, and orange marks the outlet header. The differential pressure dp_i for the i-th control volume is computed as $dp_i = p_i - p_F + \rho g h_{i-F}$, where p_i is the pressure recorded in the i-th control volume, p_F is the pressure at position F, ρ signifies the density of PbLi, g is the acceleration due to gravity, and h_{i-F} represents the elevation difference between the i-th control volume and the F level.

Prior to embarking on the principal numerical investigations, an initial hydrodynamic simulation is conducted with a $B = 0\,\mathrm{T}$ in [28] to evaluate the relative

Table 8.1: Principal Geometrical Parameters of the LLCB Flow Path as Reported in [28].

Component	$a[m]$	$b[m]$	**Axial Length** $[m]$	$t_{Ha}[m]$	$t_{Side1}[m]$	$t_{Side2}[m]$
Inlet Header	0.214	0.025	0.373	0.026	0.004	0.004
Poloidal Channels	0.214	0.012	1.47	0.026	0.004	0.004
Top Header	0.214	0.025	0.391	0.026	0.0025	0.002
Return Channel	0.214	0.038	1.545	0.026	0.004	0.004
Outlet Header	0.214	0.025	0.373	0.026	0.004	0.004

Table 8.2: Comparative assessment of mass flow rates at $B = 0\,T$ between CFD analysis and REDMaHD. (*) Indicates the total mass flow Rate at the inlet as a boundary condition.

Channel No.	**Flow Rate** $[kg/s]$ **Swain [28]**	**Flow Rate** $[kg/s]$ **RELAP5**	**Deviation** [%]
Channel-1	4.0068	4.0043	-0.0624
Channel-2	3.0568	3.0167	-1.3118
Channel-3	2.2790	2.3378	2.5801
Channel-4	1.6100	1.5632	-2.9068
Channel-5	1.0400	1.0780	3.6538
Return Channel	12.0(*)	12.0(*)	0

importance of MHD effects with respect to inertial and viscous phenomena. This preliminary simulation is replicated using REDMaHD to scrutinize the effectiveness of the selected geometrical and nodalization configurations. Exceptional congruence in terms of mass flow rate distribution across the vertical channels is observed when utilizing the code; the divergence from the numerical analysis is less than 3.7% for each channel. The data comparison is reported in Table 8.2. For benchmarking, the pressure drop in the hydrodynamic LLCB TBM is assessed to be 0.432 kPa, which constitutes approximately 1.2% of the pressure drop predicted by the MHD model.

Upon establishing the effectiveness of the input geometry, simulations are conducted under a magnetic field of $B = 4\,\mathrm{T}$. The governing parameters are $Ha = 17845$ and $N = 4697$, with the toroidal half-length of the entire module, $a = 0.214\,\mathrm{m}$, serving as the characteristic length. Figure 8.2 depicts the dimensional pressure drop against axial length, which manifests in the fluid path delineated by colored sections in Figure 8.1a. Remarkably, REDMaHD provides an accurate prediction of the total pressure drop, exhibiting a relative error, $\epsilon = -0.97\%$. It is pertinent to note that the magnetic field is consistently oriented perpendicular to the blanket module. Thus, this computation substantiates the reliability of the implemented 3D MHD

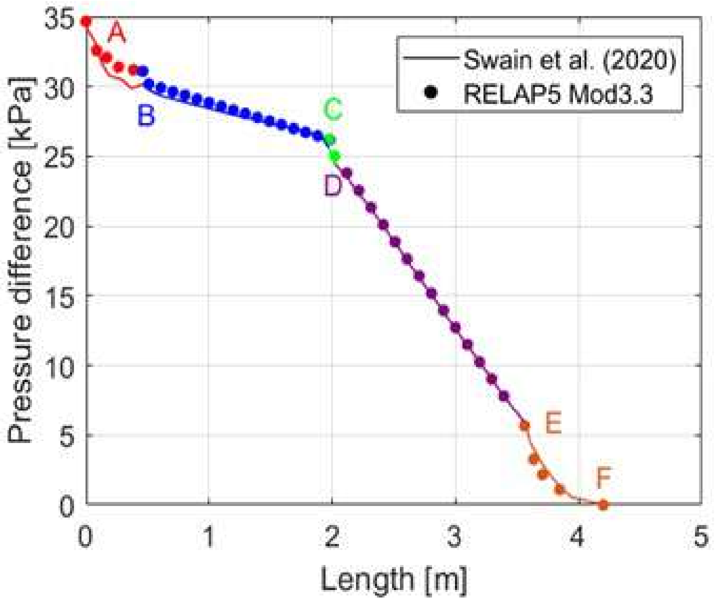

Figure 8.2: Trend of Pressure Drop Along the Designated Fluid Path for $Ha = 17845$ and $N = 4697$.

Table 8.3: Comparison of Mass Flow Rate Results for MHD Case ($B = 4\,T$) Between CFD Analysis and REDMaHD.

Channel No.	**Flow Rate** $[kg/s]$ **Swain [28]**	**Flow Rate** $[kg/s]$ **RELAP5**	**Deviation** [%]
Channel-1	7.2600	2.8323	-60.9876
Channel-2	1.4300	2.5061	75.25175
Channel-3	1.0100	2.3328	130.9703
Channel-4	1.1500	2.0886	81.61739
Channel-5	1.1500	2.2402	94.8
Return Channel	12.0	12.0	0

models for simulating bends and cross-sectional changes that occur perpendicular to B, even in a complex geometry as considered in this research.

Nonetheless, it is crucial to underline a notable limitation of REDMaHD. Specifically, it lacks the ability to model electromagnetic coupling effects, such as those present in the LLCB due to a common conductive wall between Channel-1 and the return channel. This absence is glaringly evident when comparing the mass flow rate distribution across the TBM vertical channels predicted by RELAP5 and CFD analyses, as detailed in Table 8.3.

From the CFD results, electromagnetic coupling phenomena intensify the flow

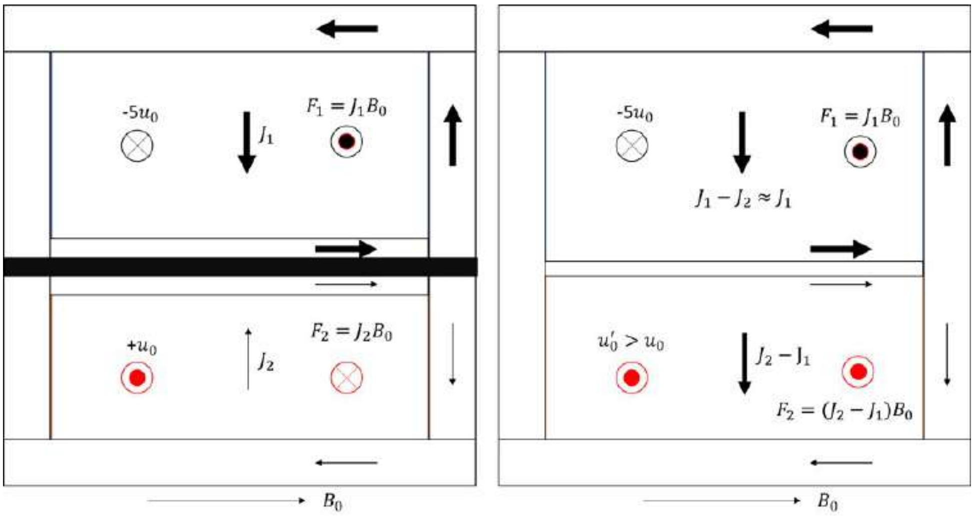

Figure 8.3: Left) In the absence of electrical contact between the return (top) and Channel-1 (bottom), represented by a thin layer of perfect electrical insulation (black band), no cross-channel currents occur. Consequently, $j_1 > j_2$ owing to the varied flow rates, and the self-induced Lorentz forces counteract fluid motion. **Right**) When electrical contact is present, currents from the return channel can complete their circuits in Channel-1, leading to a net Lorentz force that augments the flow rate in Channel-1. The resultant increase in average velocity eventually leads to $j_1 > j_2$, restoring equilibrium via the reemergence of a decelerating Lorentz force in Channel-1.

rate disparity in the poloidal channels, which in the OHD scenario is solely attributable to inertial forces. Specifically, the pressure gradient in Channel-1 experiences a noticeable reduction owing to localized electrical coupling effects arising from its proximity to the return channel. Assuming a uniform flow distribution, the return channel transports up to five times the flow rate of Channel-1. A qualitative understanding can be elucidated as follows, refer to Figure 8.3. Due to the electrical interconnection between the channels, currents initiated in one can flow into and complete their circuit in the other. Since $\mathbf{j} \propto u_0$, currents in the return channel exceed those in Channel-1, influenced by the greater flow rate. When these currents flow into Channel-1, they facilitate fluid motion rather than hindering it, as they would in their originating channel, given $\mathbf{j} = u \times B$. The velocity in Channel-1 escalates until the resistive Lorentz forces produced by the induced currents counterbalance the infiltrating currents. The overarching impact manifests as Channel-1 attracting a larger flow rate compared to other poloidal channels, corroborating the flow imbalance observed by Swain et al. in their study [28]. Moreover, the effects of counter-flow coupling are not limited to these channels but extend to the inlet and outlet headers, specifically in regions proximate to Channel-1 and Channel-2. This leads to a further reduction in the hydraulic resistance encountered along the pathways through Channel-1 and, to a lesser extent, Channel-2. It is worth emphasizing that electromagnetic coupling does not seem to have a marked impact on poloidal channels 3-5, as they are in a less intimate electric contact, being separated from each other by the depth of the solid breeder modules.

REDMaHD, in its current form, cannot account for these phenomena and thus calculates the flow distribution across the poloidal channels solely based on 2D and 3D pressure losses. At $N = O(10^3)$ and $Ha = O(10^4)$, inertial effects become inconsequential, leading to an almost homogenous flow distribution. In simpler terms, the primary cause of flow rate imbalance in hydrodynamic calculations, namely inertia, is entirely eclipsed by MHD influences. These, in turn, are significantly shaped by electromagnetic coupling in the given system. Thus, it can be deduced that REDMaHD, in its current state, falls short in accurately predicting the flow rate distribution in configurations that involve channels in electrical contact with adjacent counter-flowing ducts with substantially higher flow rates. However, it is noteworthy that this limitation does not affect the computation of pressure drops in this specific setup, as evident from the data displayed in Table 8.4, which aligns well with CFD predictions.

This can be explained since over half of the total pressure drop in the TBM occurs in the return channel, as substantiated by the data in Table 8.4, due to the elevated velocity within the return channel as compared to the poloidal ascending channels, making the contributions from expansions and contractions notably significant. On the contrary, the impact of electrical coupling within the descending channel is minimal, corroborated by the results presented in Table 4 of Ref. [28], where the calculated pressure gradient closely aligns with its theoretical counterpart, which naturally omits the effects of coupling. As a result, REDMaHD is proficient in determining the primary source of pressure drops within the entire TBM system.

Furthermore, it is essential to note that electromagnetic coupling mainly reduces distributed pressure losses (2D MHD), which linearly depend on the average fluid velocity. In contrast, concentrated losses (3D MHD), also linear with velocity, are negligibly impacted by electromagnetic coupling. The close agreement between REDMaHD and CFD calculations for the total pressure drop in poloidal Channel-1,

Table 8.4: Pressure drop differences in counterflow electromagnetically coupled conduits ($B = 4T$).

Channel Number	**Swain [28]** $\Delta p[kPa]$	**REDMaHD** $\Delta p[kPa]$	**Error** [%]
Channel-1	4.5700	4.8770	6.717724
Return channel	18.5000	19.3270	4.47027

despite significant differences in mass flow rate, could arise from a balanced offset between 2D and 3D MHD losses. In [28], 2D MHD losses are mitigated by coupling, while 3D MHD losses are heightened due to elevated mean velocities; the REDMaHD numerical model, in the absence of coupling, overestimates distributed MHD losses but underestimates localized MHD drops, owing to the moderate average fluid velocity. It is pivotal to bear in mind that the above observations are strictly applicable to the specific geometric layout of the LLCB TBM, as the effects of electromagnetic coupling are highly contingent upon the multi-channel configuration.

In summary, although RELAP5 MHD module can offer reliable estimates for MHD pressure losses, it exhibits shortcomings in accurately predicting mass flow distribution in configurations involving electrically interconnected channels with adjacent counter-flowing ducts featuring high flow rates. This limitation stems from the lack of a specialized electromagnetic coupling model.

8.2 Helium-Cooled Lead-Lithium test blanket module

The MHD flow within a scale model of the Helium-Cooled Lithium Lead (HCLL) TBM for ITER has been empirically assessed by Bühler et al. [29]. The objective of the study was to acquire experimental insights to validate the design concept and to serve as a benchmark for computational tools. The scaled model of the HCLL TBM is reduced by a factor of two to accommodate the constraints of the MEKKA experimental setup. A wide parametric range was explored in the experiments: $5 \cdot 10^2 \leq Ha \leq 5 \cdot 10^3$ and $2 \cdot 10^2 \leq Re \leq 10^4$.

The experimental setup employed NaK as the working fluid and stainless steel for the structural components. Material thermo-physical properties were evaluated at an operational temperature of 293 K, as presented in Table 7.3. The complex architecture of the HCLL involves multiple bends and abrupt changes in cross-sectional

Table 8.5: Principal Geometrical Parameters. (*) Denotes the average toroidal length of the narrow manifold along the poloidal direction. (**) Dimensions pertaining to the cooling plates are omitted [29].

Component	**Toroidal Length** $[mm]$	**Poloidal Length** $[mm]$	**Radial Length** $[mm]$	$t_w(Ha)$ $[mm]$	t_w(**Side1**) $[mm]$	t_w(**Side2**) $[mm]$
Feeding/Draining Pipe	14.75	14.75	181.5	3.88	3.88	3.88
Large Manifold (In/Out)	31	101.48	13	3	2.8	7.5
Narrow Manifold (In/Out)	14(*)	203	13	3	2.8	7.5
Breeding Unit (BU**)	90	9.48	171	1.38	2.75	2.75

areas, as illustrated in Figure 8.4. The design comprises two parallel Breeding Units (BU), each containing an inflow and an outflow unit, denoted as D-E and F-G, respectively. The liquid metal is introduced into the TBM at point A, marking the commencement of the circular feeding pipe. This fluid is then directed into an inlet manifold that bifurcates the flow into the BUs. This manifold is a slender, vertically oriented rectangular duct situated between the back plate of the BU and the external plate of the mock-up, as depicted in Figure 8.5. The manifold connects with the feeding pipe in an enlarged cavity that experiences an abrupt magnetic field-aligned contraction by approximately 50% at the location of the red dashed line in Figure 8.4. The manifold channel continues to diminish until it reaches 50% of its original size at the purple dashed line in Figure 8.4. The outflow manifold is analogous to the inlet, complete with a progressive expansion of the manifold channel and an abrupt enlargement before merging with the drainage pipe. Notably, helium manifolds, which would have reduced the available cross-sectional area for liquid metal in its manifold, were excluded from both the experimental mock-up and the REDMaHD simulations [29]. The connection between the manifold and the BUs is facilitated by a slender, elongated orifice located on the BU rear plate. Upon entering the inflow unit, the fluid undergoes additional bifurcation, guided by thin metallic plates that divide the volume into six parallel channels. These channels emulate the presence of helium cooling plates. At the first wall, the liquid encounters a narrow, elongated toroidal-radial aperture, establishing hydraulic communication with the outflow unit. The liquid metal is subsequently collected in the outlet manifold and exits the Test Blanket Module via the drainage pipe [29]. The dimensions of the mock-up are collated in Table 8.5.

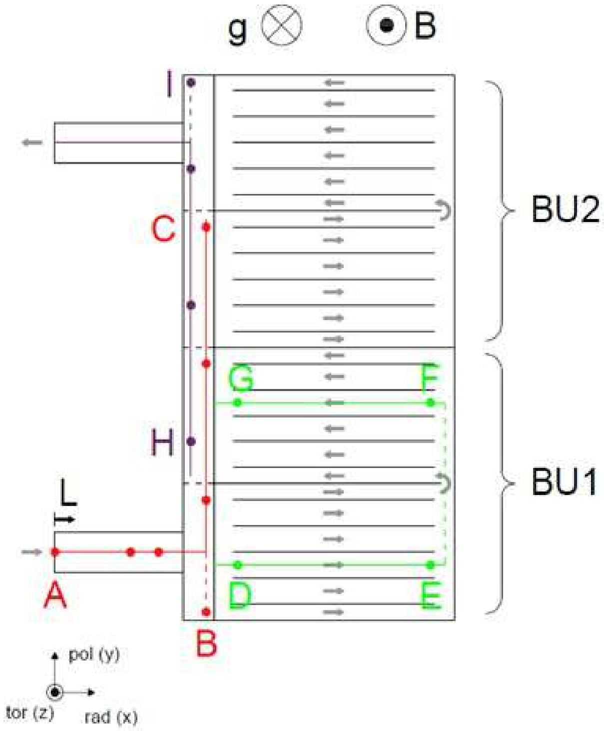

Figure 8.4: Radial-poloidal cross-sectional view of the TBM geometry. Colored segments from A to I delineate the flow path used for subsequent pressure drop calculations.

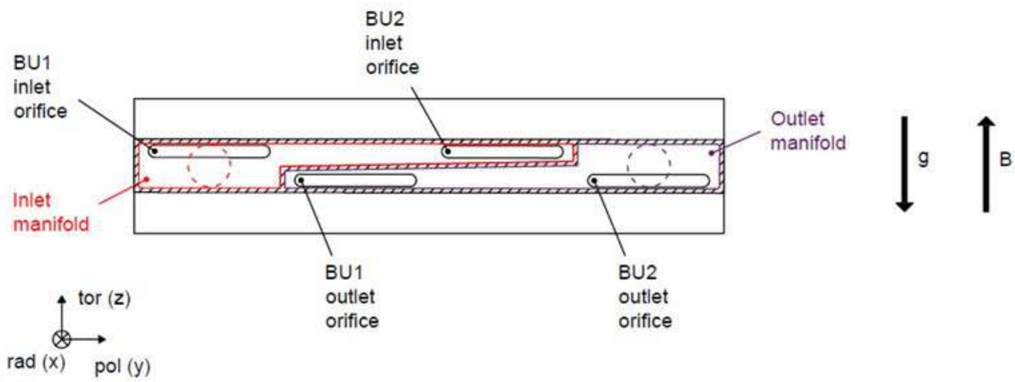

Figure 8.5: Toroidal-poloidal perspective of the mock-up. The feeding manifold is highlighted in red, while the collecting manifold is marked in purple. The cross-sectional profiles of both inlet and outlet pipes, as well as the interface between the manifold and BU, are illustrated.

The nodalization scheme utilized is illustrated in Figure 8.6. A pair of time-dependent volumes are employed to specify the inlet temperature and the outlet pressure of the NaK alloy. The liquid metal mass flow rate is regulated by the time-dependent junction that links the inlet time-dependent volume (TMDPVOL) to the inlet conduit (designated as PIPE #20 in Figure 8.6). Both inlet and outlet manifolds are modeled using two equivalent pipes.

Each unit is constructed from three control volumes (CVs) that capture the key features of the component. Specifically concerning the inlet manifold, the first and third CVs model the entry chambers that adjoin the initial interface with the breeding units, while the second CV emulates the interconnection between them. For the first and third control volumes, radial flow direction is chosen, facilitating an accurate assessment of the abrupt change in area at the interface with the Breeding Zone (BZ). Both breeding units are modeled using dual pipe components, wherein the six channels constituting each breeding unit are approximated by an equivalent singular pipe defined by the total flow area, equivalent hydraulic diameter, and geometric parameters significant for MHD analysis for one representative channel, specifically one of the four centrally located within the cell. Each pipe component comprises seven CVs, which mimic the inlet and outlet orifices, radial channels, and the reversal chamber. Figures 8.4 and 8.6 feature colored markers denoting the locations for pressure data acquisition in both the physical mock-up and the REDMaHD numerical model.

Figure 8.7 presents the comparative analysis between the experimental data and RELAP5 outputs for the nondimensional pressure drop along flow path A-I (as indicated by colored lines in Figure 8.4), relative to the pressure gauged at point A. The chosen characteristic length is the toroidal half-length of the BU, denoted as $a = 0.045\,m$, and the pressure is normalized with $p_0 = \sigma f v a B^2\,\mathrm{Pa}$. As observed in prior investigations, the employed scaling of pressure effectively consolidates results for various Reynolds numbers into a singular representation for a given Hartmann number, affirming that MHD flows under fusion conditions are minimally impacted by significant inertial effects. Consequently, only a limited set of results is displayed graphically.

As can be discerned, the predominant regions for pressure drops are the circular inlet conduit (A-B) and the inlet/outlet manifolds (B-C and H-I), attributable

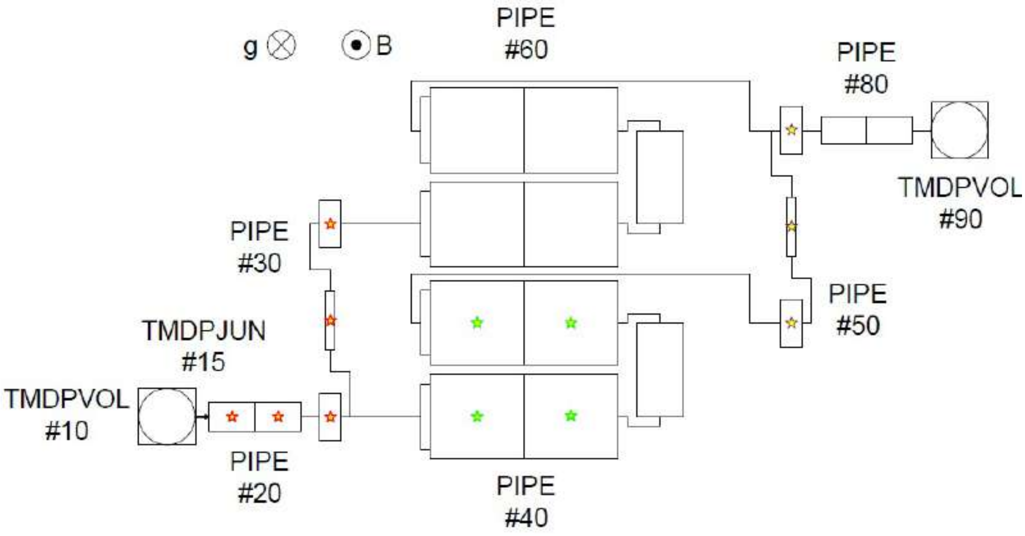

Figure 8.6: Schematic Representation of the Geometric Meshing.

to higher velocities caused by their smaller cross-sectional areas compared to the breeder units. Additionally, the augmented wall thickness of these pipes and manifolds leads to increased wall conductance ratios ($c_{\mathrm{MAN}} \approx 0.09$, $c_{\mathrm{BU}} \approx 0.01$), thereby amplifying the Lorentz forces and consequently exacerbating pressure head losses. Further pressure losses are incurred as the fluid navigates through constricted orifices at the ingress and egress of the BUs (B-D and G-H), giving rise to three-dimensional MHD effects. The flow constriction and subsequent expansion within the narrow interstice between the inflow and outflow units (delineated by dashed line E-F) as well as the 180° bend at the first wall, have a minimal impact on load loss as they transpire in a plane orthogonal to B. Remarkably, pressure loss within the breeding cells (D-E and F-G), where fluid velocities are moderate ($\approx 1\,\mathrm{mm/s}$), is trivial, particularly when compared with losses in pipes and manifolds.

REDMaHD demonstrates exceptional concordance with empirical observations. Table 8.6 exemplifies the computed results and their relative errors at $Ha = 3000$, and it is found that the model predicts total pressure loss with an error margin ranging between $-1\% < \epsilon < +14\%$. This outcome substantiates the utility of REDMaHD in accurately estimating pressure losses in intricate geometries such as the one envisioned for the HCLL TBM.

As previously noted for the LLCB, a significant limitation of the existing code version is the absence of an electromagnetic coupling model. As reported in [29],

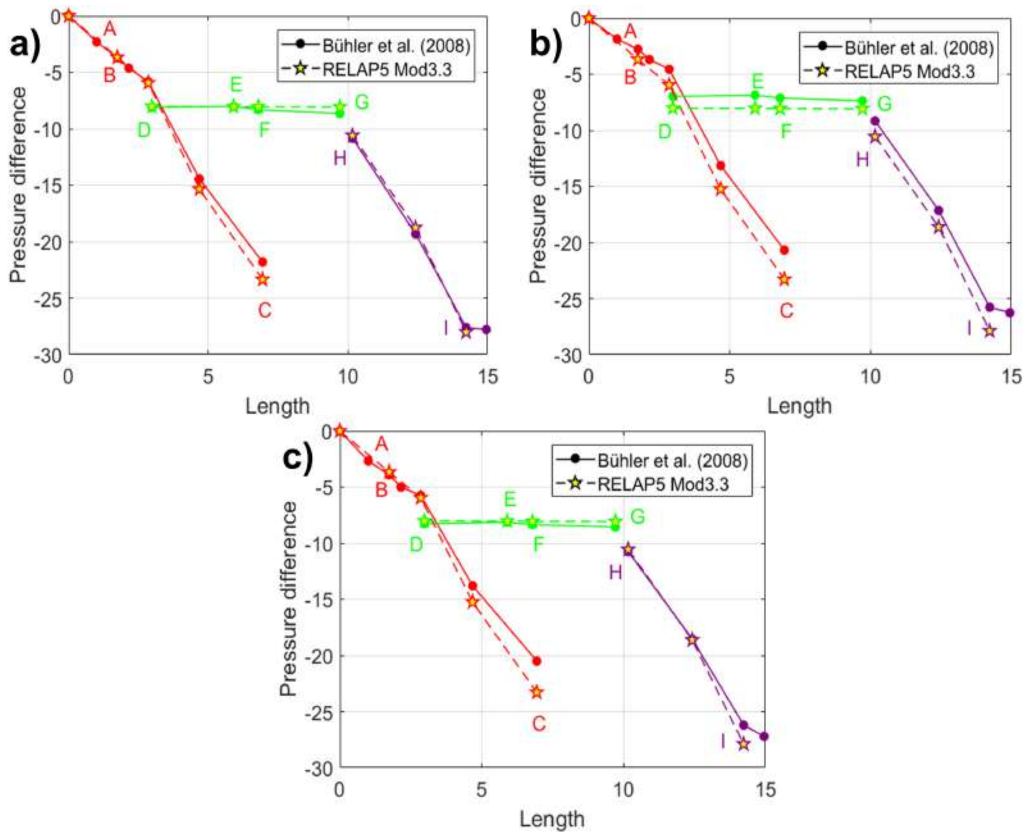

Figure 8.7: Comparison of Nondimensional Pressure Drop with Respect to Scaled Length between RELAP5 and the Reference Experiment. **a)** $Ha = 3000, Re = 3360$. **b)** $Ha = 4000, Re = 1140$. **c)** $Ha = 5000, Re = 2000$.

this omission is consequential for the flow distribution, especially within the internal channels of the BUs. Nonetheless, the lack of such a model does not substantially alter the pressure loss predictions. It should also be highlighted that the code tends to overestimate pressure loss arising from cross-sectional variations; this is particularly pronounced at the interface between the manifold and BU (B-D and G-H). This overestimation stems from conservative assumptions used in developing the 3D pressure loss model for this component, and refinements are expected as more data becomes available. Lastly, the lower fidelity of the code at $Ha = 4000$ may potentially be ascribed to anomalies in the experimental data collection, given that the RELAP5 performance remains relatively consistent for $Ha = 3000$ and $Ha = 5000$.

Table 8.6: Tabulation of Nondimensional Pressure Drops at Various Flow Path Positions and Overall Loss. Relative Errors are Indicated.

	$Ha = 3000, Re = 666$				$Ha = 3000, Re = 1172$		
Loc.	Δp **[29]**	Δp **Code**	**Rel. Err.**	**Loc.**	Δp **[29]**	Δp **Code**	**Rel. Err.**
B	-3.24	-3.661	12.99%	B	-3.73	-3.662	-1.82%
C	-21.84	-23.29	6.64%	C	-21.97	-23.29	6.01%
D	-8.09	-8.019	-0.88%	D	-8.16	-8.018	-1.74%
E	-7.82	-8.03	2.69%	E	-8.06	-8.03	-0.37%
F	-8.23	-8.061	-2.05%	F	-8.38	-8.06	-3.82%
G	-8.63	-8.072	-6.47%	G	-8.74	-8.072	-7.64%
H	-10.79	-10.55	-2.22%	H	-10.79	-10.56	-2.13%
I	-27.64	-27.89	0.90%	I	-28.26	-27.91	-1.24%

8.3 Water-Cooled Lead-Lithium test blanket module

This study aims to progress the validation process of the code another step forward. Courtessole et al. led an experimental campaign on a scaled-down version of the Water-Cooled Lithium Lead (WCLL) TBM, with the key findings discussed in [16]. The data sheds light on the MHD pressure drops within the module and how the LM mass flow rate is distributed among the eight breeding units (BUs). To capture the details, the mock-up hydraulic circuit has been simulated using REDMaHD, aiming for a high level of fidelity to each geometric feature. Several calculations were then performed, to simulate closely the experimental tests. When comparing the results from the code to the experimental data, it becomes clear that the numerical tool is quite adept at reproducing the underlying physics, especially when the magnetic field strength is closer to the one expected in a fusion reactor Ha $\approx 10^4$.

All the relevant information and a detailed description of how the experiments have been performed can be found in Refs. [16, 162]; an abridged version is provided thereafter. A scaled 1 : 2.5 mock-up of the WCLL TBM, capturing all essential geometric features, was developed for MHD experiments in MEKKA laboratory. Designed for horizontal orientation within the lab magnet gap, the mock-up has dimensions of $668.4 \times 222.6 \times 102\,\mathrm{mm}^3$, fitting well into the homogeneous magnetic field area. Particular attention was given to accurately replicating manifold geometries, as they contribute the most to pressure drop. Fabricated primarily from 1.4571 austenitic steel, the mock-up minimizes magnetic field distortions and is compatible with the NaK liquid alloy employed as dummy fluid instead of the PbLi foreseen in

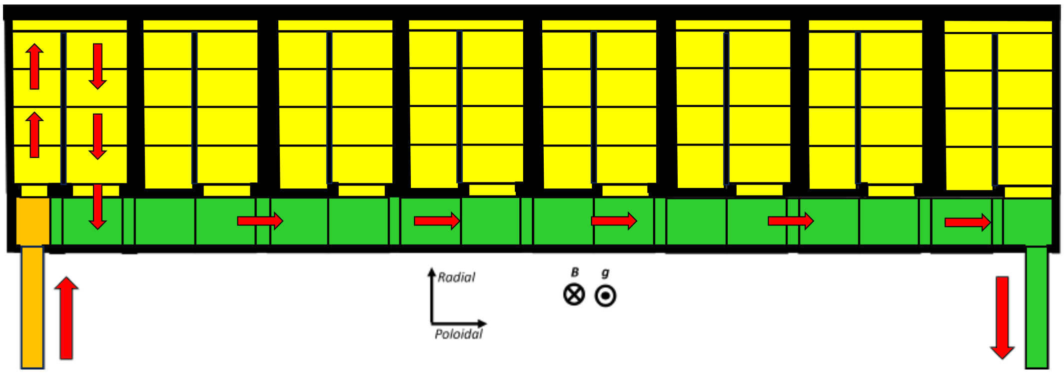

Figure 8.8: Radial-poloidal sketched view of the mock up. Red arrows serve to highlight one of the possible hydraulic path, specifically the one through the first breeding unit (BU1). B is the magnetic field vector and g the gravitational acceleration

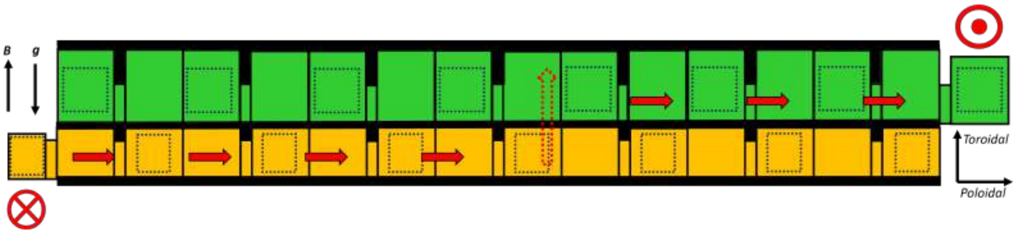

Figure 8.9: Toroidal-poloidal sketched view of the mock up. Red arrows serve to highlight one of the possible hydraulic path, specifically the one through the fifth breeding unit (BU5). B is the magnetic field vector and g the gravitational acceleration

the actual blanket.

Figures 8.8 and 8.9 showcase the schematic representations of the mock-up as simulated in the system code. The area highlighted in orange encompasses the inlet pipe and the feeder (or inlet manifold). The yellow region represents the BZ, which is divided into eight separate BUs. The green portion illustrates the collector (also known as draining manifold) and the outlet pipe. The mock-up lays horizontally (labelled as the radial-poloidal plane in Figure 8.8, in analogy with the ITER coordinate system for the actual WCLL TBM) in the magnet gap and, thus, the magnetic field is supposed to have only the vertical component as non-zero (the toroidal component, following the same analogy). Figure 8.9 illustrates how the feeder and collector lays side by side in the magnetic field direction.

Concerning the actual nodalization scheme employed, this is presented in Figure 8.10. The thermodynamic conditions of the LM at the inlet and outlet (i.e., temperature and pressure) are set using two time-dependent volumes (TMDPVOL

Table 8.7: Material Properties at at $T_{\text{Ref}} = 300\,\text{K}$ and $p_{\text{Ref}} = 0.1\,\text{MPa}$.

Material	σ [S/m]	ρ [kg/m^3]	μ [Pa·s]
NaK	2.61×10^6	872.3	8.1×10^{-4}
Stainless Steel	1.25×10^6	-	-

#181 and #220). A time-dependent junction (#182) enforces the assumed mass flow rate throughout the circuit. Pipe component #185 simulates the radial inlet channel. Each manifold is modeled using a pipe component consisting of 23 CVs, which mimics the chambers constituting the manifolds and their interconnections. Lateral junctions couple the BUs to the corresponding CVs in the distributing and draining manifold.

Every BU is replicated using a pipe component that comprises 11 CVs. The outlet manifold (#197) employs the same slice modeling approach used for the inlet manifold (#187), reflecting the actual geometric characteristics. The LM exiting the mock-up is collected in the outlet pipe (#199) and drains into TMDPVOL #220.

It is worth mentioning that the two junctions connecting #185 with #187 and #197 with #199 do not precisely replicate the geometry of the mock-up. Specifically, the poloidal-toroidal cross-sectional area of the first CV in the distributing manifold and the last CV in the draining manifold has been halved [16, 162]. This effectively means that each of these control volumes is half the size it should be. This adjustment was made because the missing halves would have constituted isolated volumes or "dead branches," according to the nodalization criteria of RELAP5, meaning they would have been regions of stagnant flow. Given that REDMaHD is not currently configured to accurately model such elements, a more simplified nodalization approach was adopted. Using the grid configuration described, the simulations have run times ranging from 20 seconds to 2 minutes on a single i7-11700K CPU.

The study is carried out under isothermal conditions with a reference temperature of $T_{\text{Ref}} = 300\,\text{K}$ and a reference pressure of $p_{\text{Ref}} = 0.1\,\text{MPa}$. The thermophysical properties of the materials involved are computed at these conditions and are listed in Table 8.7. The properties for steel are taken from [16].

All computations are led under conditions of steady-state. In total, thirteen

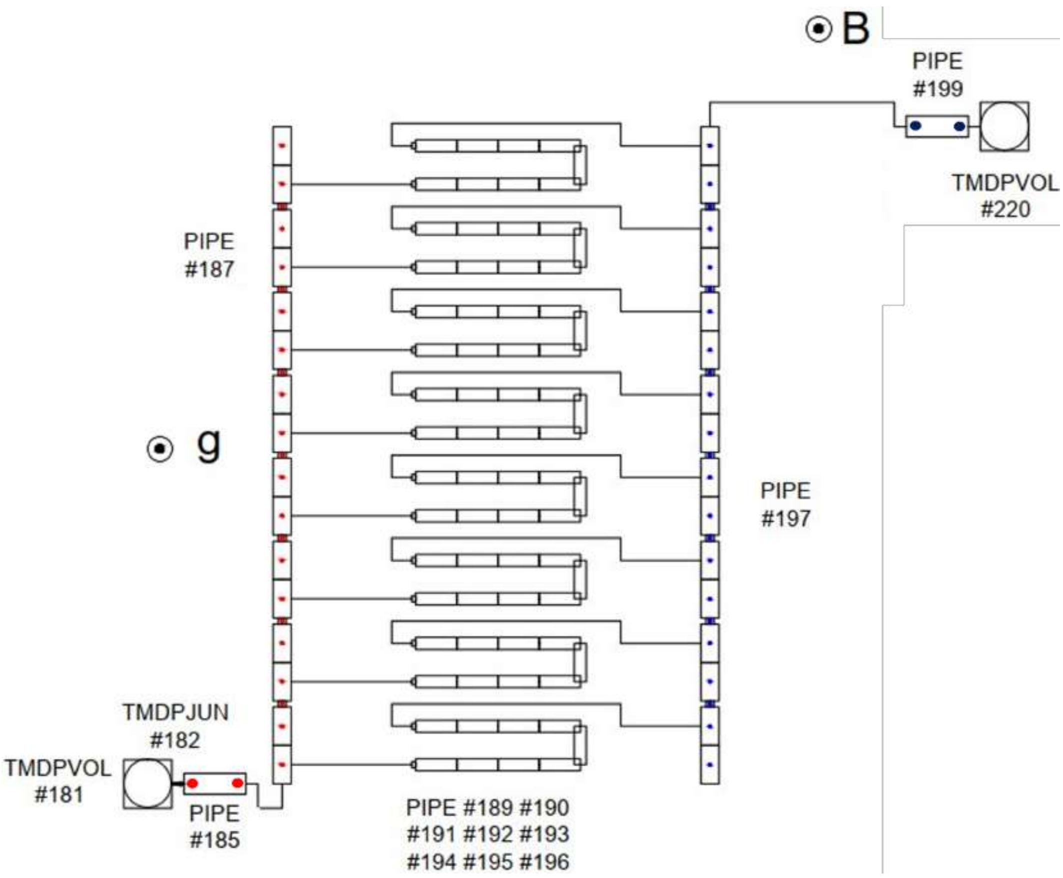

Figure 8.10: RELAP5 nodalization scheme of the circuit. Red and blue dots represent the points where the code samples the data.

different scenarios were simulated, each varying in magnetic field strength and mass flow rate. The parameters range for these simulations is $500 \leq \mathrm{Ha} \leq 3000$ and $200 \leq \mathrm{Re} \leq 2000$. These values are calculated based on representative scales for the BU, hence the characteristic velocity $v_0 = \frac{\Gamma}{8\rho(A_{\mathrm{BU}}/2)}$, which depends on the Γ of the test considered, and the characteristic length $a_{\mathrm{BU}} = 0.039[m]$, chosen as half of the internal toroidal dimension of a single BU. Here, $\Gamma[\frac{kg}{s}]$ denotes the total mass flow rate across the eight BUs, each with a cross-sectional area $A_{\mathrm{BU}} = 5.8 \cdot 10^{-3}[m^2]$.

Pressure scaling utilizes different characteristic quantities in order to be consistent with the approach described in Ref. [16] where these are defined considering the flow state in the manifold since the pressure losses in those components are the most significant factors for pressure distribution in the mock-up. Because the cross-sectional areas of these manifolds are smaller than those of the BUs, its characteristic velocity, defined as $v_{\mathrm{man}} = \Gamma/\rho A_{\mathrm{man}}$, is going to be different. In this equation, $A_{\mathrm{man}} = 1.87 \cdot 10^{-3}$ is the average cross-sectional area of the feeding and draining channels of the manifold. Additionally, the manifold channel half-width in the magnetic field direction, $a_{\mathrm{man}} = 0.0195[m]$, is reduced compared to a_{BU}. Therefore, the metric for assessing pressure distribution involves a scaled pressure variable p/p_{man}, defined as $p_{\mathrm{man}} = \sigma v_{\mathrm{man}} a_{\mathrm{man}} B^2$.

It should be noted that in a complex geometry like that of the MEKKA mock-up, electromagnetic coupling is expected to affect the LM flow. In the manifold region, the distributing and draining channels are separated by a common wall, referred to as the baffle plate. In this region, the LM flows in the same direction on both side of the partition resulting, in general, in a favorable impact on pressure drop due to a mutually beneficial "pumping" effect when the mass flow rate in the two channels is equal [122, 164]. To account for this phenomenon, at least qualitatively, the thickness of the Hartmann wallsthe upper one for the distributing channel and the lower one for the draining channelis considered to be half of the actual thickness of the shared plate.

It should be remarked that the condition of equal mass flow rate in the two manifold channels is not usually fulfilled but, rather, the imbalance tends to grow the further away the considered section is compared with the equatorial section of the mock-up (BU4/5). Focusing on the manifold terminal sections, CFD analyses have highlighted that this condition is responsible for a pressure build-up in the

Table 8.8: Discrepancy (%) between REDMaHD outcomes and various experimental tests, in terms of total pressure drop whithin the mockup.

Hartmann	Reynolds	Pressure Drop Error (%)
500	1000	22
500	2000	22
500	3000	23
1000	400	17
1000	600	16
1000	800	16
1000	1000	18
1000	2000	19
2000	200	9
2000	400	2
2000	600	3
2000	800	2
3000	300	1

channel with the smaller flow rate and the onset of a peculiar flow regime [24].

Conversely, for the walls shared by the BUs, the NaK flow is in counter-flow, leading to an increased pressure drop compared to a stand-alone duct [95]. Consequently, the entire poloidal thickness of the mock-up plates is considered in our model to represent the BU side walls. It should be noted that, in principle, the Madarame effect should also be present between the BUs and the manifolds, which share 3D currents generated at their interface (simultaneous cross-section variation and change of stream direction perpendicular to the magnetic field plane). It is not yet clear the importance of this effect on the system pressure drop but its simulation currently exceeds the capabilities of the REDMaHD model.

In Figures 8.11 and 8.12, the REDMaHD outcomes are compared with various experimental data. The results are reported in terms of scaled pressure drops. For the sake of clarity, the diagrams refer to the hydraulic path through the fifth BU, which nonetheless serves to emphasize key features of the LM flow. The associated relative errors for the total loss of load are summarized in Table 8.8.

The majority of the total pressure drop Δp_{tot} occurs in the inlet and outlet circular pipes as well as in the manifolds. In the BUs, the pressure drop is relatively small. However, there exists a discrepancy in the pressure drops between BU1 and BU8 in contrast to the other BUs, attributable to the notable differences in mass flow rate distribution among the units, as discussed subsequently.

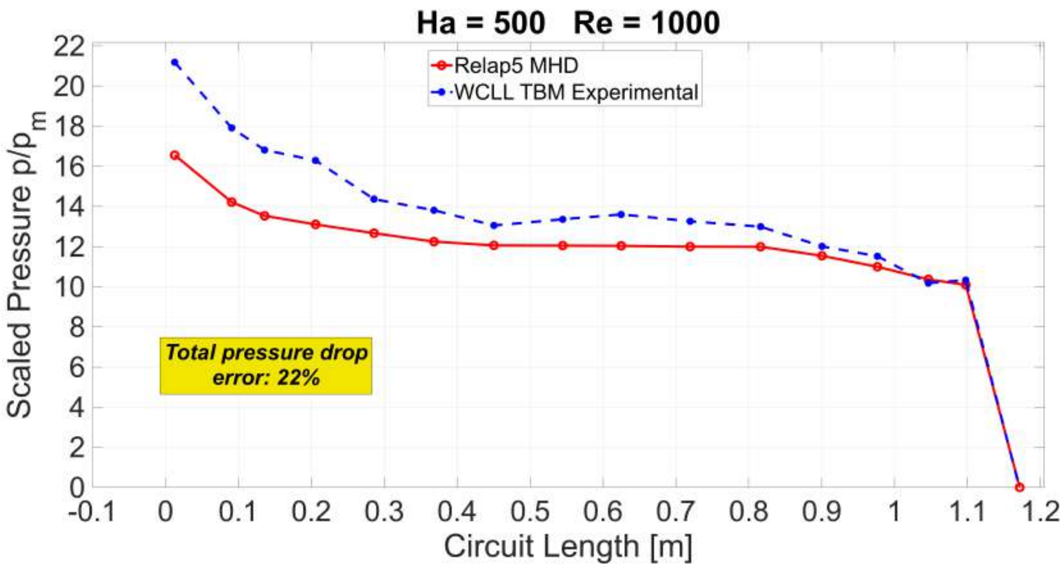

(a)

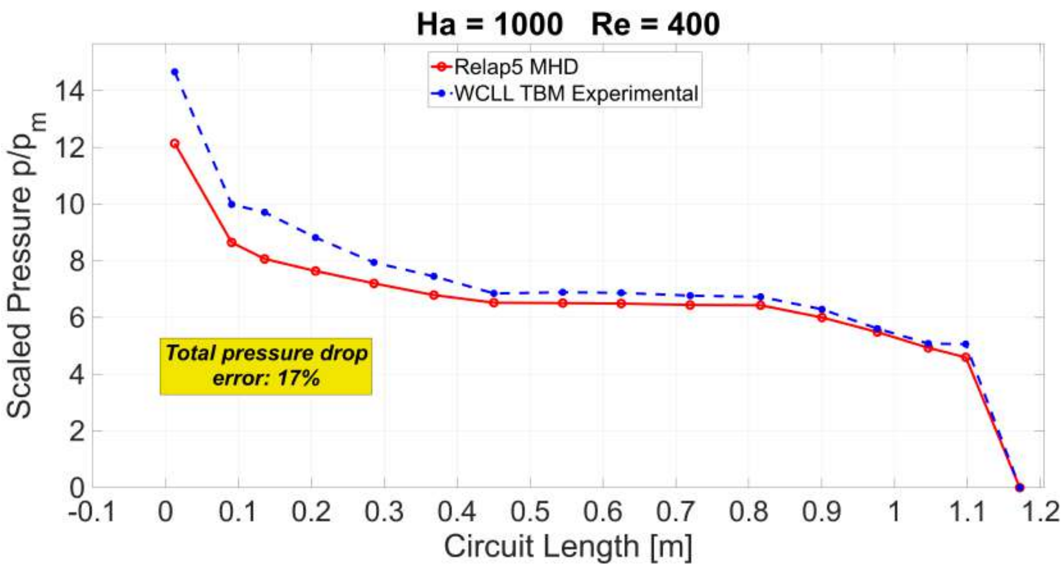

(b)

Figure 8.11: Comparison between REDMaHD and experimental tests, in terms of scaled pressure drops along the circuit length of the mockup as defined in [16].

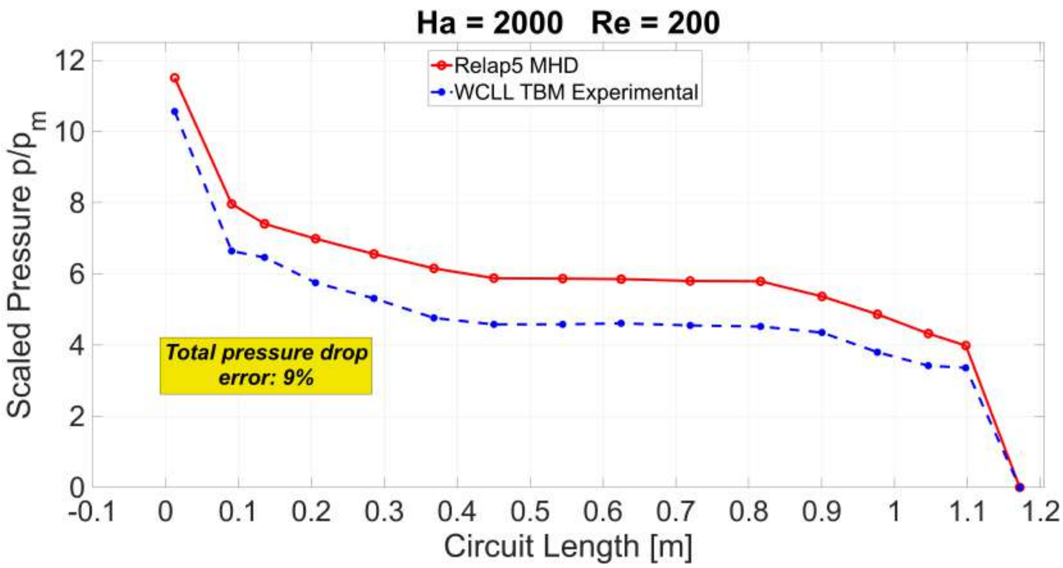

(a)

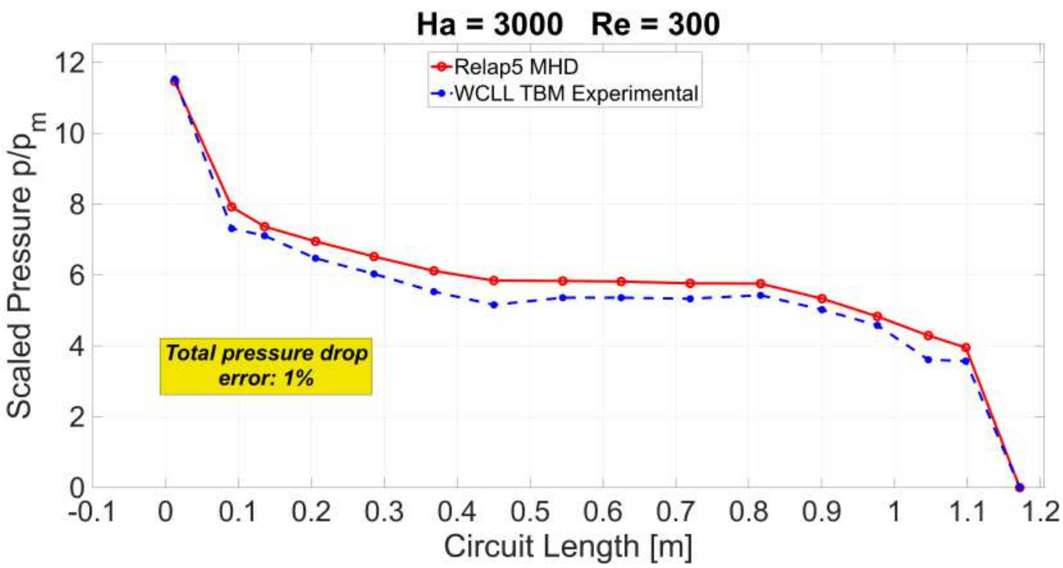

(b)

Figure 8.12: Depiction of scaled pressure drops in the circuit length of the mockup using REDMaHD versus the experimental findings cited in [16].

The purely hydraulic distributed pressure losses in the mockup module amount to approximately $0.5 - 1\%$ of the total. For hydrodynamic localized drops, the k factor has been specified during the geometry modeling phase, following guidelines provided in the Idel'chik handbook for complex geometries such as bends or abrupt area changes [109, 165].

From Figure 8.12a, Figure 8.12b, and the data gathered in Table 8.8, it becomes evident that the results produced by REDMaHD are in a reasonable agreement with the experimental data. This agreement improves notably when both the Hartmann number (Ha) and interaction parameter (N) are increased. Such behavior aligns well with expectations, as the correlations implemented within the code are particularly formulated to address fluid flows that are relevant to fusion conditions, where MHD effects are dominant over inertial and viscous forces. When the interaction parameter N is decreased, the model tends to deviate more from the experimental data, although this deviation remains within the acceptable ranges for system thermal-hydraulic codes as indicated by [100]. The primary source of this deviation can be attributed to the pressure losses that occur in the specific area that links the inlet pipe to the distributing manifold, and consequently, the manifold to the BU1. This area is characterized by the simultaneous presence of abrupt changes in cross-sectional area and bends.

A deeper understanding of the observed behavior can be gained by considering that the governing parameters, and thus the interactions between forces of various types, deviate from the reference values for the BZ. For instance, in a case marked by $\mathrm{Ha} = 2000$ and $\mathrm{Re} = 800$, the governing parameters in the entrance region can be approximated as $\mathrm{Ha} \approx 200$ and $\mathrm{Re} \approx 16000$, with an interaction parameter of $\mathrm{N} \approx 2.5$. These estimates are based on the characteristic length of the circular inlet pipe ($a_{circ} = 8 \cdot 10^{-3}\,\mathrm{m}$) and an average NaK velocity ($v \approx 2.24\,\mathrm{m/s}$).

In this specific region, REDMaHD functions under MHD and geometrical conditions that differ considerably from its intended application. The code $\Delta P_{exp-contr}$ MHD model, that is likely to contribute the most in that part of the grid, is calibrated for high interaction parameters ($N \gg 10$) and straight channels [15]. The complex geometry at the exit of the inlet duct introduces inertial phenomena imperfectly accounted for, at best, in the model. This area, which interfaces with the distributing manifold and the first BU, differs significantly from a long straight duct.

The inlet pipe and the BU1 inlet window are facing each other, causing most of the flow to be directed through the latter. The cross-sectional area of this window is approximately 33% smaller than that of the distributing manifold, contributing to considerable pressure loss in that part of the mock-up. However, this specific pressure loss becomes less significant as the magnetic field strengthens and the flow is increasingly governed by MHD forces.

The local pressure drop coefficient $k_{MHD-exp/contr}$ is formulated under the assumption that symmetrical expanding and contracting geometries result in equivalent pressure losses [15]. This assumption holds reasonably well only for flows characterized by high Ha and N [166]. This is corroborated by the experimental data presented in Figures 8.11 and 8.12. Pressure losses in the exit region, which connects BU8 to the draining manifold and subsequently to the outlet channel, vary considerably from those in the inlet region at lower Ha values. As the magnetic field increases, these losses begin to exhibit a more symmetrical behavior.

Interestingly, even at low magnetic field strengths, the code manages to model more accurately the pressure drop in the exit region, as evidenced by Figure 8.11a, compared with the inlet one. This is surprising since one would expect that, if our proposed explanation for the discrepancy in the inlet regions holds true, then a similar or even larger error should be observed at the outlet manifold where the hydraulic element appears to be rather similar to the inlet one in terms of governing parameters. A substantial phenomenological difference in the interaction between electromagnetic and inertial forces could be present at the outlet manifold, possibly lessening the influence of the latter ones, thus resulting in the onset of a 3D flow more akin to the one simulated by our model, at least in terms of local pressure drop, even if characterized by a moderate value of N that should not allow it. It is important to bear in mind that this is a qualitative speculation driven by the observation of experimental results and is not intended to serve as an actual explanation. This is likely to be confirmed (or falsified) when direct numerical simulations of the experimental layout become available from the KIT research team, as anticipated in [167].

In Figure 8.13, the predicted pressure losses within the manifold region are presented. Given that these losses constitute the dominant contribution to the overall pressure drop in the experiment, they can serve as a reliable test for the model accuracy. The pressure losses calculated using REDMaHD closely resemble those obtained from experimental data. However, the red and blue curves begin and end at different ordinate values, which is likely a result of the different pressure losses calculated by the code in the regions immediately following or preceding the inlet and outlet channels. On the other end, the gap between the pressure profiles in the two manifolds essentially represents the pressure head available for each BU and serves as a direct measure of the mass flow rate passing through it. For this metric, it is observed a significant deviation from the experimental data.

In Figure 8.14, the mass flow rate distribution among the BUs is displayed, normalized to $\Gamma/8$. The experiments indicate that the bulk of the mass flow rate is actually circulated through BU1 and BU8, a feature that is adequately captured by REDMaHD in a qualitative sense, but not in a quantitative one. This discrepancy may be due to the unique layout, as already discussed, in which the inlet channel directly faces BU1, causing the fluid to exit the inlet pipe at a high velocity. As a result, the fluid inertia conveys it preferentially into BU1. Even at high magnetic field strengths, this behavior is not adequately dampened. The model starts to yield a more accurate depiction of the mass flow rate distribution only when the magnetic field approaches its higher experimental value, as shown in Section 8.3. The deviation still observed in this more favourable case could be attributed to electromagnetic coupling phenomena occurring between the BUs, which are currently only coarsely accounted for in REDMaHD.

8.4 Summary

This chapter is dedicated to a rigorous validation study of the REDMaHD software, which aims to assess its proficiency in modeling MHD phenomena within complex geometrical layouts, specifically in the LLCB, HCLL, and WCLL TBM mock-ups. For the LLCB, the validation is versus CFD results, while for HCLL and WCLL, it leans on actual experimental flow data obtained from mock-up studies. The Verification & Validation (V&V) results are encouraging. REDMaHD demonstrates a commendable degree of accuracy in forecasting both two-dimensional and three-dimensional pressure drop behaviors. The code exhibits optimal performance when MHD forces dominate over inertial and viscous effects. However, when the electromagnetic cou-

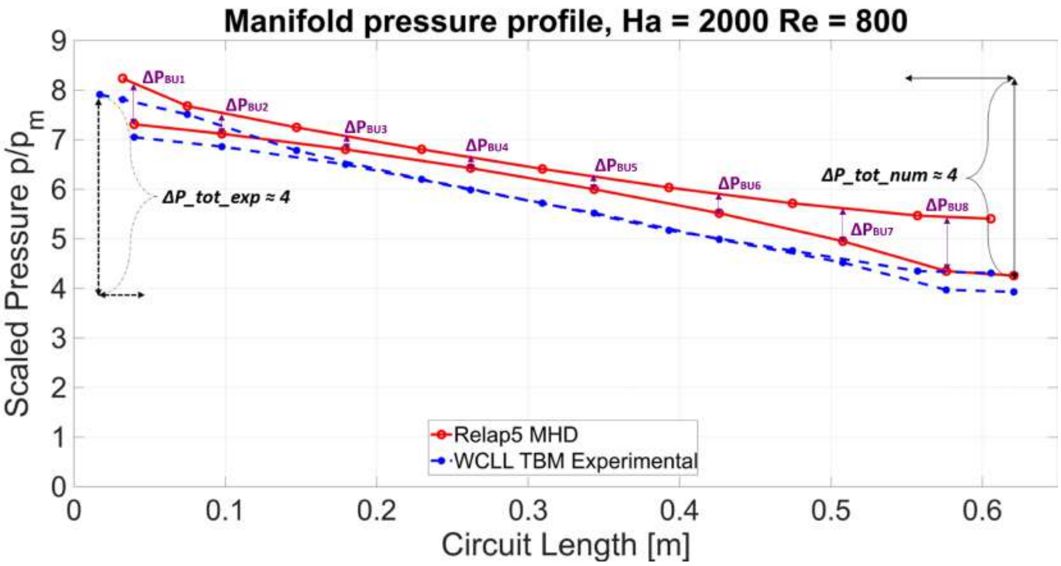

Figure 8.13: Details of the non-dimensional pressure drop in the manifold regions are presented. The upper curve for each color represents the pressure loss in the distributing manifold, while the lower curve corresponds to the draining manifold. The pressure head for each unit is indicated in purple.

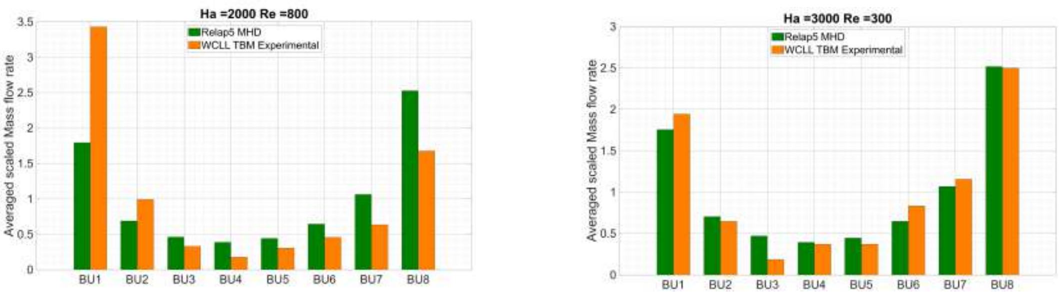

Figure 8.14: Comparison of the distribution of the NaK mass flow rate among the breeding units: REDMaHD vs experimental data.

pling becomes significant, there is a discernible reduction in the prediction accuracy of REDMaHD. This is primarily because a specialized model to account for the Madarame effect is not yet incorporated into the software. Generally, this leads to less accurate estimations of mass flow rate distribution, rather than a fundamental issue in predicting pressure drops; a prediction that remains rather good even in these cases.

Chapter 9

MHD heat transfer

This chapter is devoted to outlining the fundamental principles and phenomena that govern heat transfer within incompressible MHD-flows relevant for fusion reactors. The derivation of the most sophisticated, albeit partial, models for simple bounded flows is elaborated upon in this section.

9.1 State of the Art

Numerous analytical, numerical, and experimental investigations have been conducted to assess the impact of an external magnetic field on convective heat transfer in confined flows.

To identify the optimal approach for the development of a reliable MHD heat transfer model, a range of papers discussing analogous issues were examined. The most significant contributions, along with the reasons they are considered beneficial, will be detailed in the following. But first, it is deemed useful to provide a brief discussion about how the MHD regime influences heat exchange, so that some recurring themes will be established. Henceforth, unless otherwise stated, the magnetic field will be assumed to be exclusively transverse, that is, perpendicular to the principal flow direction.

It is recalled here that the forced and/or natural convective heat transfer mechanism experiences a substantial enhancement due to turbulence [168]. In other words, the heat transfer coefficient (h) significantly increases when turbulent structures are present. This effect is straightforward to comprehend: as the flow transitions into turbulence, inertial forces overcome viscous ones and, thus, macroscopic fluid mixing is enhanced, a process that can be readily visualized through the onset of eddies and vortexes. This additional motion augments the rate at which energy and momentum are exchanged between particles, consequently promoting heat transfer (and increasing the friction coefficient).

It is widely recognized that magnetohydrodynamic conditions exert a significant influence on turbulent flow characteristics, a manifestation of the broader phenomenon known as magnetic damping [151]. Regarding the behaviour of eddies and vortexes, it becomes evident that the magnetic field tends to dissipate angular momentum components perpendicular to the field lines while conserving those parallel to it. This distinct behavior leads to a reconfiguration of turbulent structures, aligning their vorticity axes with the magnetic field vector (B-vector), thereby imparting to MHD turbulence a distinct anisotropic character, which can even result, under certain conditions, in the appearance of a distinct phenomenology called quasi-two-dimensional (Q2D) turbulence [169]. This regularization of turbulence inherently chaotic nature tends to detrimentally impacts heat transfer mechanisms.

The dissipating action of the magnetic field can potentially yield a significantly more pronounced outcome, giving rise to the phenomenon referred to as "relaminarization" or simply "laminarization". This, essentially, signifies the reversal of an otherwise turbulent flow in hydrodynamic conditions into a laminar one under the action of a magnetic field or, equivalently, an increase in the critical Reynolds number for the onset of the laminar-turbulent transition (Re_c). Several authors have provided formalization for the prevalence of this phenomenon, by mean of the dimensionless ratio $R = \mathrm{Re}/\mathrm{Ha}$, whom critical value falls within the range $225 < R_c = Re_c/\mathrm{Ha} < 250$ [170, 171]. As is obvious, the heat transfer coefficient, whenever turbulence is completely suppressed, undergoes an even more steeply decreasing trend.

It is evident that MHD effects have a detrimental impact on the cooling efficiency of an electrically conductive fluid when it operates under turbulent conditions. However, it's noteworthy that this phenomenon is reversed when the enforced regime of the coolant is laminar.

This is due to the development of extremely thin viscous boundary layers close to the fluid-solid interface. As previously discussed in Chapter 3, the velocity gradients in the Hartmann and side layers experience a significant increase in MHD flows compared to their hydrodynamic (Ordinary hydrodynamics (OHD)) counterparts. Consequently, fluid velocity attains its maximum values closer to the wall in MHD flows, facilitating heat exchange between the fluid and solid domains (see e.g. [172]). This feature becomes more pronounced if liquid metal overshoots occur near the duct walls, as observed in the prototypical flows discussed in Chapter 3.

A further layer of complexity emerges when natural circulation (buoyancy-driven) phenomena integrate the forced ones within a MHD confined flow, giving rise to what is commonly known as a "mixed convection" regime. In the existing literature, it is generally acknowledged that MHD effects interact with buoyancy structures (cells) similarly to the interactions with turbulent structures. Specifically, the magnetic field tends to suppress convective cells that have momentum axes not parallel to it. As an example in the context of a vertically heated channel with upward laminar flow, it is observed that the heat transfer coefficient would reduce compared to the OHD scenario [173, 174]; this is attributed to the hindrance of favorable buoyancy phenomena that would normally facilitate the upward movement of the liquid metal [175].

Due to the anisotropic nature of the heating conditions in breeding blankets, mixed convection flow is anticipated to be the main heat transfer regime [176]. From a numerical standpoint, however, portraying this accurately presents a substantial challenge. Generally, numerical computations involving only forced convection are less demanding because the MHD equations and the energy equation are "loosely coupled" or, differently put, the velocity field influences the temperature distribution, but the latter does not reciprocally affect the fluid momentum, with the only exception of the dependence of thermophysical properties by temperature. On the other hand, in the mathematical delineation of mixed convection, this is unacceptable and both the terms representing the pressure gradient and buoyancy forces are incorporated in the motion equations. Frequently, the buoyancy force term is expressed through the Boussinesq approximation [177], which neglects the functional dependence of density by temperature except in the buoyancy volumetric force, which is represented by a source term function of g, the gravitational acceleration. In this latter case, it emerges a "tight coupling" between the fluid flow and energy equations, necessitating a simultaneous resolution of all equations.

A notable example is the work led by Chen et al., where is proposed an integral thermo-fluid analysis of a DCLL (Dual Coolant Lead Lithium) blanket [178]. The study is interesting since four scenarios were explored: case 1 involving a conducting blanket, case 4 pertaining to an insulating blanket, and cases 2 and 3 examining a partially insulated blanket through the deployment of flow channel inserts at specific locations. The heating conditions for the blanket are purely volumetric. An in-house CFD code is utilized, with the domain discretized into an extensive grid consisting of 4.5×10^7 elements. It is found that while buoyancy forces have a minor impact on MHD pressure drops, they significantly alter the flow structure and heat transfer in vertical (poloidal) flows. One notable effect is a more uniform temperature distribution across the flow cross-section. Unexpectedly, reverse flows were observed, not just in downward flows but also in upward flows.

Developing a reduced model that sufficiently encapsulates the primary MHD effects crucial in the design of breeding blankets is a remarkable challenge due to the complex underlying physics which we have just examined. Therefore, the initial approach adopted herein is centered on the most fundamental phenomena the laminar forced convection within an electrically insulated channel. While this topic has been considerably explored in existing literature, there remains a notable scarcity of models built on correlations. While many studies have ventured to provide detailed analytical solutions that delineate the dependencies of heat transfer on MHD variables, the mainstream approach heavily relies on 2D/3D codes grounded in finite differences or finite volumes to fully resolve the MHD equations. This prevalent methodology contrasts with the fundamental requisites of system codes, typically favoring 1D formulations and algebraic expressions as closure laws.

A substantial body of research focuses on examining forced-convection MHD regimes in square and rectangular cross-sectioned ducts, since their widespread use in the design of fusion power plant piping networks. Also circular pipes, although less representative from a design perspective, have not been overlooked. The intrinsic symmetry of circular pipes not only simplifies both analytical and numerical studies of flow but also, coupled with the ease of manufacturing compared to square/rectangular channels, has facilitated a wealth of experimental studies. This substantial base of experimental data justifies their consideration in the REDMaHD development process, along side the square/rectangular geometries.

In the following, numerical works perceived to be of substantial value regarding procedure and outcomes will be addressed. Although not directly utilized in the development of a fitting model, they highlight critical parameters and offer a perspective on structuring the heat transfer model. In Table 9.1 those works are summarized and their main features are reported.

As mentioned in Chapter 3, the parameter governing the convective mechanism is the Nusselt number, which represents a non-dimensional form of the heat transfer coefficient. It is important to note, however, that it is this latter quantity that is required in the code to finalize the calculations in the energy balance equation. Henceforth, these two parameters will be treated as interchangeable (see Section 5.2.2).

MHD heat transfer in square/rectangular pipes

The first notable example is represented by the works carried out by Ying & Tillack, about self-cooled liquid metal blankets, where a parametric study about laminar heat transfer in square/rectangular pipes is performed [179, 180]. The thermal boundary conditions is a uniform heat flux applied to the walls. The Authors find that changing the aspect ratio of a square duct (at fixed mass flow rate) is of great impact to the heat transfer. If the duct is elongated along the direction of the magnetic field, it results in a reduction in the average temperature at the side walls compared to that of a square channel. However, the peak wall temperature substantially increases. The average temperature enhancement reaches a saturation point at an aspect ratio of 2, while the peak temperature persists in increasing. This behavior results in a substantial reduction of the local Nusselt number at the hot spot, diminishing by more than half compared to the condition characterized by a square channel. In parallel, the attenuated average wall temperature yields an increment in the Nusselt number less than 25%, moderating the overall beneficial effects derived from the side layers. For an aspect ratio less than 1, wherein the duct is elongated perpendicular to the magnetic field, it is observed that both the average and peak wall temperatures are consistently higher. This occurrence is due to the reduced influence of the side overshoots since the length of the side wall decreases. These conclusions are drawn while maintaining a fixed and finite value for the wall conductance ratio as well as a fixed Hartmann number. It is noted that with a rise in these two parameters, holding the aspect ratio constant, there is an enhancement in the overall average Nusselt number due to the emergence of side wall velocity jets.

Similar outcomes are obtained by Cuevas et al. [181]. The study deals with heat transfer in liquid-metal flows within a horizontal square duct influenced by a transverse magnetic field, focusing on understanding the impact of side-layer flows on cooling ducts of fusion blankets. Heat flux is applied exclusively to one side wall, while the remaining walls are maintained as adiabatic. The study is of particular interest because turbulent phenomena are taken into account by the finite difference solving method.

Various scenarios are actively explored, considering distinct wall electrical conductivity, magnetic field strength, and turbulence intensity. It is observed that distinct trends in wall temperature profiles materialize through adjustments in c, Ha, and Pe parameters in both laminar and turbulent MHD flows. Enhancing Pe fosters improved heat removal, thereby reducing wall temperatures, a process unaffected by variations in Ha and c. Conversely, lowering Ha gives rise to increased wall temperatures, independent of the other parameter settings. Notably, the c parameter substantially influences the laminar velocity profiles, directly impacting the peak axial velocity and consequently affecting the convective outcomes and wall temperatures. The study emphasizes the superior efficacy of laminar MHD heat transfer mechanisms powered by high-velocity side-wall jets over turbulent mixing for a specified Pe, at least for the thermal boundary conditions considered. The research however relies on the Boussinesq eddy diffusivity approach to solve the Reynolds-averaged NavierStokes equations (modelling and eddy viscosity and an eddy thermal diffusivity), potentially neglecting the effects of large-scale motions in MHD turbulent flows. This, in fact, assumes that the transport mechanism is governed by gradient-type diffusion due to small-scale eddies. Consequently, the convective influence of large-scale motion (i.e., large eddies) is not accurately captured in this model, although it has been shown to be present in other studies [169]. A proper validation of the in-house code is unfortunately not provided by the authors.

In another significant study undertaken by Umeda & Takahashi [170], the authors consider laminar lithium flow in a conducting horizontal rectangular channel. This setup features heating exclusively from a side wall, with the remaining walls held adiabatic, similarly to Cuevas et al. The researchers maintain a constant conductance ratio of $c = 0.25$, while allowing for variations in both Ha and Re numbers. Their observations reveal that the central region of the heating surface exhibits a reduced temperature in comparison to its neighboring areas on the inner facet of the heating wall, a phenomenon indicative of significant cooling effects spurred by the convective heat transfer of the side layer jet. The research underscores a notable enhancement in the Nusselt number with increasing Hartmann numbers, a phenomenon attributed to the effective cooling induced by the side layer jet. This trend manifests with a growth between 42% and 50% of Nu at elevated Hartmann numbers ($\approx 2 \times 10^3$), compared to a zero-field condition. Additionally, the Reynolds number seems to exert a marginal effect on the Nusselt number, a phenomenon possibly caused by the relaminarization of the flow induced by the strong magnetic field. The significance of this study is heightened by the partial code validation undertaken, where numerical results are compared with the experimental results detailed by the same authors in [182].

Al-Khawaja et al. [183] present a numerical solution to explore the behavior of a fully developed MHD laminar forced-convection flow within a square duct with electrically insulated surfaces. Differing from many studies in the field, this work sets thermal boundary conditions based on constant wall temperature instead of heat flux parameters. Despite this distinctive approach, the research verifies the consistent trend of an increasing Nusselt number with rising magnetic field strength. Furthermore, the study offers a detailed comparison between square duct and circular tube flows, unveiling that the influence of the magnetic field is slightly less significant in square duct scenarios.

The most recent work that can be considered meaningful in setting a procedure for the derivation of forced-convection MHD flow model is the one carried out by Wang et al. [184]. The study is focused on a rectangular duct, characterized by one wall being subject to a constant temperature, and the others being adiabatic. A Hunt flow is enforced within the model and a parametric study is performed to assess the effect of the Reynolds and Hartmann numbers on the Nusselt parameter. A critical achievement of the study is identifying a correlation through a fitting analysis of the numerical data, deriving a formalized dependency of the convection heat transfer mechanism on the interaction parameter N.

MHD heat transfer in circular channels

Considering now circular channels, a meaningful work is the one performed by Al-Khawaja et al. [185]. The study numerically explores the fully developed, laminar, steady, and forced convection heat transfer phenomenon occurring in an electrically conducting fluid flowing through an electrically insulated, horizontal, circular pipe, with the pipe wall being subject to uniform heat flux. The study stands out notably for arriving at an analytical solution for the Nusselt number $\mathrm{Nu} = f(\mathrm{Ha})$, which is then compared with the foundational solution initially brought forward by Gardner in his work [186]. The work by Gardner serves as the cornerstone for the reduced model currently utilized in REDMaHD, necessitating a more detailed discussion in section 9.2.

Another noteworthy contribution to the development of a model for circular channels comes from the Ph.D. thesis by Sorensen [187]. The author synthesized new and existing data to develop a heat transfer correlation for turbulent MHD flows, which are expected to occur in molten salt breeding blankets; concepts often considered for compact fusion reactors like ARC [188]. Using an experimental flow loop with a specific setup to study phenomena in areas with sharp magnetic field gradients and transitional flows, the research formulated a novel correlation. This correlation integrates the heat transfer coefficient with Reynolds and Hartmann numbers, accommodating a broad range of turbulent MHD flow conditions and enabling the prediction of heat transfer behaviors for molten salts. It is, however, unclear the general validity of the correlation in the context of liquid metals and high Hartmann numbers. Moreover, the influence of the walls electrical conductivity on the heat transfer coefficient is unaddressed in this study.

Finally, it is worth noting that a comprehensive examination of the interconnection between MHD and heat exchange is detailed in the book by Blums et al. [172]. This reference also compiles analytical solutions for heat transfer problems pertinent to basic prototype scenarios, including the one-dimensional flow occurring between two surfaces, known as the Hartmann flow, and the two-dimensional flow over a semi-infinite plate.

Table 9.1: Prototypical numerical works dealing with MHD heat transfer effects.

Authors and Ref.	**Channel geometry**	**Heat conditions**	**Governing parameters**	**Solving tool**
Ying & Tillack [179, 180]	horizontal square/rect.	Imposed heat flux on a side wall	Ha = $[0, 1\times10^4]$, Re $< 2\times10^3$	Finite difference in-house code
Cuevas et al. [181]	horizontal square	Imposed heat flux on a side wall	Ha = $[0, 1\times10^5]$, Re = $[1, 5\times10^5]$	Finite difference in-house code
Umeda & Takahashi [170, 182]	horizontal rectangular	Imposed heat flux on a side wall	Ha = 2×10^3, Re = $[1, 3\times10^3]$	Finite difference in-house code
Al-Khawaja et al. [183]	horizontal square	$T_{walls} = const$	Ha = $[0, 1\times10^3]$, Re $=< 2\times10^3$	Spectral method
Wang et al. [184]	horizontal rectangular	$T_{sidewall} = const$	Ha = $[0, 3\times10^2]$, Re $=< 2\times10^2$	In-house code
Al-Khawaja et al. [185]	horizontal circular	Imposed heat flux on the walls	Ha = $[0, 1\times10^3]$, Re $=< 2\times10^2$	Analytical solution
Ph.D. thesis by Sorensen [187]	horizontal circular	-	-	Literature/ Experimental derived correlations
Blums et al. [172]	Reference book for MHD heat transfer			

9.2 Heat transfer model for circular pipes

As previously indicated, the foundational work for the REDMaHD model concerning the MHD heat transfer coefficient is the study conducted by Gardner et al. [186]. This study addresses laminar MHD pipe flow within a magnetic field, with a uniform radial heat flux at the wall of an electrically insulated circular pipe. The objective was to pinpoint the exact solutions for velocity and temperature fields in the fluid region. Given the complexity of the exact solution, calculating the temperature distribution and Nusselt number numerically poses a substantial challenge. Consequently, a simplified approach to the velocity profile equation is employed to derive a manageable solution, where the Nusselt number is expressed as a function of the magnetic field, denoted as Nu = f(Ha) and shown in Fig. 9.3. This allows for the derivation of an algebraic correlation through a fitting procedure applied to the Nusselt number solution provided by Gardner, resulting in equation 9.1. The best-

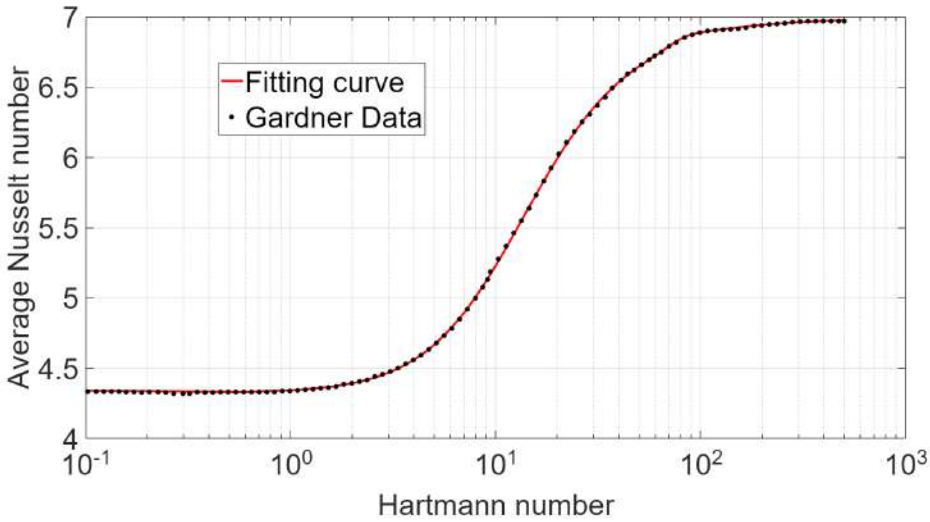

Figure 9.1: Average Nusselt number along the pipe circumference as a function of the Hartmann number.

fit procedure adopted is resolved through a rational function of eleven coefficients reported in Table 9.2.

$$Nu_{\text{Lam}} = \frac{c_1 \cdot \text{Ha}^5 + c_2 \cdot \text{Ha}^4 + c_3 \cdot \text{Ha}^3 + c_4 \cdot \text{Ha}^2 + c_5 \cdot \text{Ha} + c_6}{\text{Ha}^5 + c_7 \cdot \text{Ha}^4 + c_8 \cdot \text{Ha}^3 + c_9 \cdot \text{Ha}^2 + c_{10} \cdot \text{Ha} + c_{11}} \tag{9.1}$$

Table 9.2: Coefficients for Equation 9.1

Coefficient	Value
c_1	6.58
c_2	38544.94
c_3	85437.48
c_4	3430314.81
c_5	-3897826.29
c_6	-26008.26
c_7	5478.46
c_8	22978.82
c_9	794722.05
c_{10}	-902693.91
c_{11}	-5605.35

Furthermore, Ji & Gardner [189] carried out detailed numerical studies to explore turbulent flows in the same geometric setting. They mapped the Nusselt number against the Péclet number for Hartmann numbers ranging from 0 to 375. This analysis allowed them to establish a Nu correlation that is functionally dependent on both Pe and Ha parameters, using a curve-fitting equation on the generated data. This equation reads as

$$Nu_{\text{Turb}} = 7 + \frac{0.00782Pe^{0.811}}{[1 + 0.0004Ha^{1.5}f(\text{Pe})]} \tag{9.2}$$

where $f(\text{Pe})$ is expressed as

$$f(\text{Pe}) = 0.3 + 4.75 \cdot \text{Pe} \cdot 10^{-5} - 2.1 \cdot \text{Pe}^2 \cdot 10^{-9} \tag{9.3}$$

The REDMaHD correlation, as presented in Equation 9.4, is formulated through the amalgamation of the laminar and turbulent contributions from Equations (9.1) and (9.2). In fact, within the turbulent formulation, there exists a constant value of 7, representing the peak value for the laminar Nusselt number. It can be recognized that, for a finite Pe, both Equations (9.1) and (9.2) returns $\text{Nu} = 7$ when $\text{Ha} \to \infty$. The combined relation can then be expressed as

$$\text{Nu}_{\text{Circ, Tot}} = \text{Nu}_{\text{Lam}} + (\text{Nu}_{\text{Turb}} - 7) \tag{9.4}$$

In the work by Ji & Gardner [189], the numerical model used to generate the data later collated in Equation (9.2) is validated against the experimental data compiled by Gardner and Lykoudis [190]. The very same exercise has been reproduced with REDMaHD as a verification process for the correct implementation of the correlation into the system code.

The essential geometry and boundary conditions are encapsulated in Figure 9.2. The experimental setup from Ref. [190] maintains a constant heat flux while varying the magnetic field intensities ($\text{Ha} = 50 - 600$) and mass flow rates ($\text{Re} = 2 \cdot 10^4 - 1 \cdot 10^6$). The fluid used is mercury, characterized by $\text{Pr} \approx 0.02$ at room temperature. The results, depicted in Figure 9.3 in terms of Nusselt number averaged on the pipe circumference towards the Peclet parameter, align well with the findings from in [189]. It should be noted that the comparison made here is between the code results and the experimental data, as originally carried out by Ji, rather than a comparison between RELAP5 outcomes and the numerical model described in Ref. [189]. The latter approach would have resulted in an overlap across all curves that would have been less representative. It should be noted that the properties of mercury, the

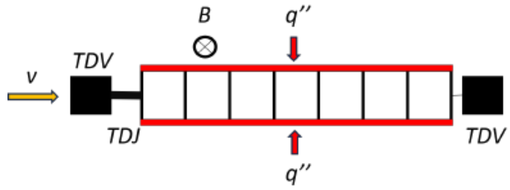

Figure 9.2: A schematic of the RELAP5 input along with the boundary conditions is presented. The time-dependent volumes (TDVs), where initial conditions for mass flow rates, pressure, and temperature are specified, are marked in black. Heat structures are highlighted in red. The one-dimensional channel is discretized into a total of seven single volumes for the simulation.

fluid used by the experiment in Ref. [190], are not yet implemented in REDMaHD. Consequently, all subsequent calculations are based on sodium-potassium properties, with the physical input parameters appropriately fine-tuned to operate within the same range of governing parameters as the considered experiments.

Nonetheless, the data presented in Figure 9.3 opens up avenues for further discussion that will be beneficial for the actual validation pursued in the following. The initial observation is that Nu diminishes as the magnetic field intensity increases, which is in line with expectations. Conversely, the heat transfer improves as the mass flow rate, namely Pe, increases enhanced by the effects of turbulence. While the range of mass flow rate used in the experiments should ensure a turbulent regime in OHD conditions, this may not hold true under MHD conditions for all tests conducted. In accordance with the criteria outlined in Section 9.1, flow laminarization is expected when $R = \frac{\mathrm{Re}}{\mathrm{Ha}} < 225$. Therefore, as the magnetic field strength increases, the required mass flow rate for achieving purely turbulent flow must also increases. Consequently, the rate of growth for the Nusselt number with flow rate becomes more gradual as Ha increases. In other words, as the magnetic field intensifies, the Nusselt number trends toward a constant value. Specifically, one could argue that $\mathrm{Nu} \to 7$ as $\mathrm{Ha} \to \infty$, where $\mathrm{Nu} = 7$ should represents the upper limit in a laminar MHD flow scenario. However, it is crucial to note that the magnetic field does not completely suppress all turbulent structures; a quasi-two-dimensional (Q2D) flow regime may still be found at a relatively high but technically achievable Ha. In these conditions, the Q2D MHD flow may still be able enhance heat transfer compared to a purely laminar MHD flow, resulting in a $\mathrm{Nu} > 7$.

The authors of [189] conclude that their model is in good agreement with the

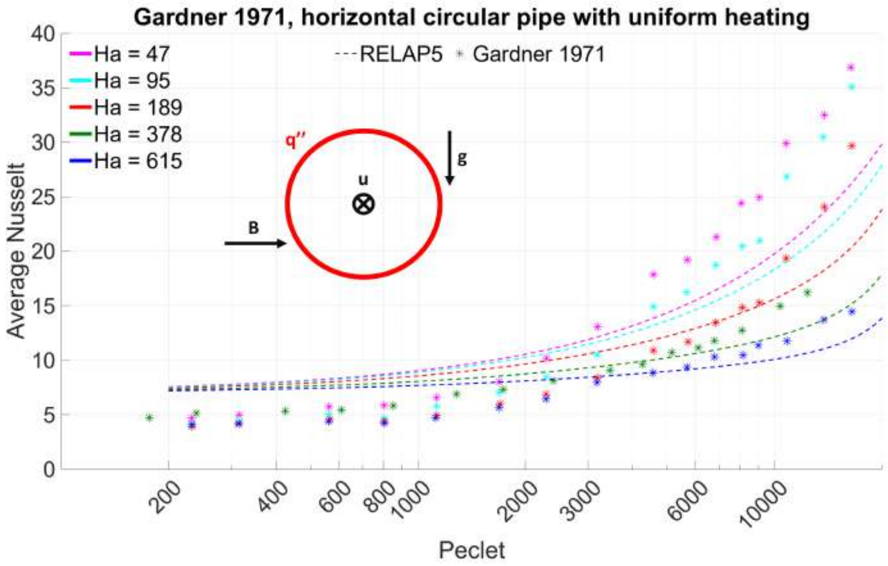

Figure 9.3: The average Nusselt number (Nu) along the pipe circumference is plotted as a function of the Peclet number. The averaging is performed over the circumference in a region where the flow is fully developed. Data sets corresponding to different Hartmann numbers (Ha) are evaluated against the numerical model predictions.

experimental results. Considering that their numerical model does not account for buoyancy effects, this concordance suggests that buoyancy-driven phenomena are negligible in the experiment as well. However, these assertions are subject to debate. In table 9.3, the average errors of the REDMaHD correlation as a function of the Hartmann number are presented. The errors are computed as follows: for each specific value of Ha and Pe, the local error between $\mathrm{Nu}_{\mathrm{Circ,\,Tot}} = f(\mathrm{Ha}, \mathrm{Pe})$ and the corresponding experimental point is determined. Subsequently, the average error over the range of Pe values is calculated for each Ha value.

While an error range of $20\% - 40\%$ may still be acceptable for the experimental validation of a system code, it remains challenging to understand why the model tends to overestimate the Nusselt number at lower Pe (Re) and underestimate Nu at higher flow rates. Surprisingly enough, the Nu for $\mathrm{Pe} \to 0$ seems to approach its laminar OHD value of 4.36 [168].

Nonetheless, according to the Author best understanding, the methodologies, concepts, and correlations presented in [189] and [190] continue to be the most advanced and immediately applicable strategies for quick integration into system code frameworks.

Table 9.3: Average error for the circumferential Nusselt number at varying Hartmann.

Hartmann number	Nusselt average error (%)
47	31.2
95	38
189	40
378	21
615	32.4

9.2.1 Preliminary validation

Consequently, it is deemed crucial to examine the performance of the correlation in scenarios not covered in its formulation. A substantial collection of experimental data is available from the MPEI Moscow Power Engineering Institute and IIHT Integrated Institute of High Temperatures, affiliated with the Russian Academy of Sciences. There is hosted a facility dedicated to investigating the behavior of mercury flows in heated circular channels under MHD conditions. A total of seven experimental campaigns were considered, each distinguished by varying initial conditions pertinent to channel heating and channel inclination, summarized in Table 9.4. With q''_{top} and q''_{bottom} are represented the boundary conditions of applied heat flux in horizontal channels, whereas with q''_{left} and q''_{right} the same conditions in vertically oriented pipes.

These experiments are primarily conducted to examine the influence of buoyancy-induced effects on flow and heat transfer. Therefore, it is particularly noteworthy to assess how REDMaHD non-buoyant model performs in replicating their results.

The RELAP5 input model employed for the initial validation corresponds to the one depicted in Figure 9.2. It should be noted that a condition of uniform heat flux has been consistently applied, as this is the scenario for which the implemented model is specifically designed.

It is essential to introduce the distinct effects of buoyancy-driven forces in forced upward and downward flows, at least qualitatively in OHD scenarios [168].

In an upward flow configuration, as the fluid progresses vertically and undergoes heating, a decrease in its density is observed. Buoyant forces, which originate from the temperature-induced density variations, act in an upward direction, aligning with the primary flow. Consequently, the forced convective transport mechanism is not only maintained but can also experience an enhancement due to the synergy of

Table 9.4: Validation references for circular channel model.

Author	**Geometry**	**Flow Direction (B transverse)**	**Thermal BC**	**Material**
Sviridov [17]	Circular	Horizontal	$q''_{top} = q''_{bottom}$, $q''_{top} \neq q''_{bottom}$, $q''_{top} = 0$	Mercury
Melnikov [18]	Circular	Downward	$q''_{left} \neq q''_{right} = 0$	Mercury
Zikanov (Genin) [19]	Circular	Horizontal	$q''_{bottom} \neq q''_{top} = 0$	Mercury
Belyaev [20]	Circular	Horizontal	$q''_{bottom} \neq q''_{top} = 0$	Mercury
Razuvanov [21]	Circular	Downward/ Upward	$q''_{left} \neq q''_{right}$	Mercury
Luchinkin [22]	Circular	Upward	$q''_{left} = q''_{right}$	Mercury
Beznosov [23]	Circular	Upward	$q''_{left} = q''_{right}$	Lead-Bismuth

these forces.

In contrast during forced downward flow, the buoyant forces generated in this scenario act in opposition to the primary flow direction because the warmer, less dense fluid tends to rise. This sets up a complex interplay between the natural tendency of the fluid to move downward and the opposing buoyant forces. Such interactions can give rise to flow instabilities, potentially evolving into oscillatory behaviors or transitioning to turbulent flow regimes, which have profound implications for heat transfer efficiency and the overall fluid flow characteristics [168].

In the case of a horizontal duct subjected to non-uniform heating, buoyant cells are also invariably formed. However, the magnitude and significance of buoyancy effects in this orientation are generally attenuated compared to vertical ducts. This can be attributed to the fact that in vertical configurations, buoyancy effects have a direct influence on the primary flow direction, while in horizontal configurations, buoyancy-induced perturbations are perpendicular to the main flow [168].

It is important to emphasize that the REDMaHD model does not depend on the conductance ratio of the channel walls. Consequently, all simulations presented herein are conducted assuming insulated pipes, i.e., $c = 0$.

Sviridov

The first work considered is the one led by Sviridov et al. [17], where different flow configurations are examined under both longitudinal and transverse magnetic field, where the latter is the one considered here. The study considers three distinct heating regimes: 1) Uniform heat flux (q'') distribution across the tube perimeter. 2) Asymmetric heat flux with the top half of the tube experiencing a higher heat flux compared to the bottom half. 3) A case where the heat flux is applied only in the lower halves of the tube. The experiments are performed in the characteristic range of $\mathrm{Re} = [5 \times 10^3, 120 \times 10^3]$, $\mathrm{Pe}[= 10^2, 3 \times 10^3]$, $\mathrm{Ha} = [0, 5 \times 10^2]$ and $Gr = [0, 7 \times 10^3]$.

In figure 9.4, are collected the REDMaHD outcomes versus the results provided by Sviridov et al. in [17]. Sviridov is being presented initially because its experimental conditions for the first scenario closely align with those of Ji & Gardner [189]. Conversely, the other experimental layouts are helpful in quantifying any discrepancies arising from boundary conditions that may not exactly match those specified in [189].

The channel orientation is consistent with the one of the correlation, although it is only in the scenario depicted in Figure 9.4a that a uniform heat flux is considered. Despite the varying heating conditions, which cause a difference in the fluid density and therefore induce buoyancy-driven flow , their impact on the flow characteristics appears moderate. The anticipated trends of $\mathrm{Nu} \propto \mathrm{Re}$ and $\mathrm{Nu} \propto \frac{1}{\mathrm{Ha}}$ are observed. Notably, the functional relationship between Nu and Pe appears to be fairly predicted only for higher Ha. Table 9.5 provides the average errors associated with increasing magnetic field levels. Interestingly, the model exhibits a high degree of accuracy in reproducing experimental data at lower Pe and higher Ha values. This observation may be attributed to the substantial dampening of vortical structures by the magnetic field, whether these movements are buoyancy-induced or due to turbulent phenomena. Consequently, the conditions under which the REDMaHD model operates closely align with the assumptions made during its formulation. Regrettably, the wall conductance ratio c_w that defines the experiments cannot be determined from the data presented in [17].

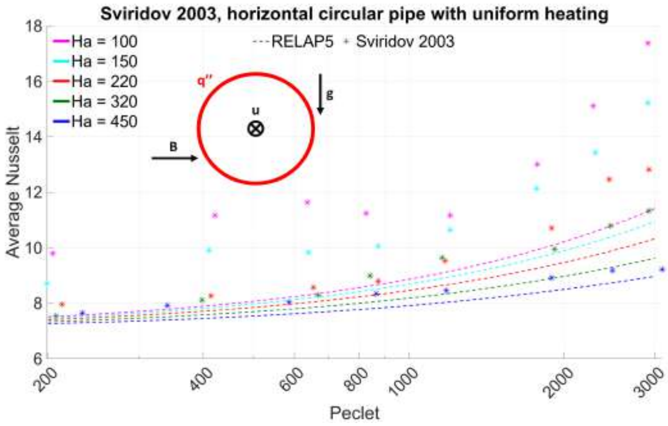

(a)

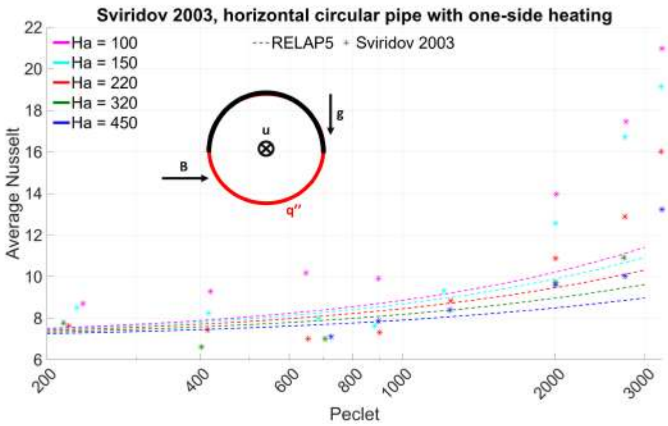

(b)

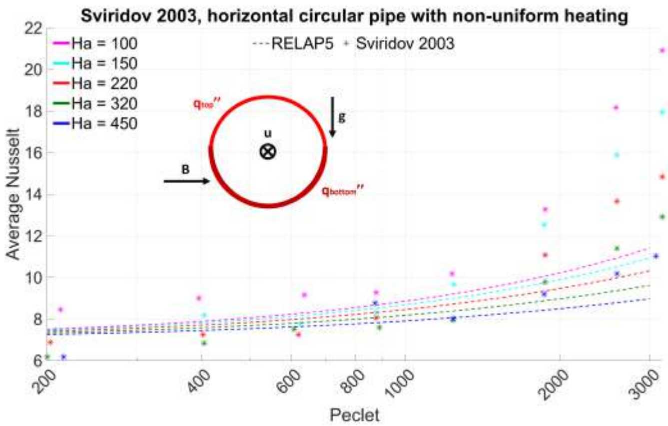

(c)

Figure 9.4: The average Nusselt number versus the Peclet number, with data from Sviridov et al. [17] serving as a benchmark for RELAP5. Different Hartmann numbers are represented by varying colors. Sub-figures include: *a*) uniformly heated, *b*) heated from below, and *c*) non-uniformly heated.

Table 9.5: Numerical average errors (%) for the Sviridov experimental cases [17], for various Hartmann values.

Hartmann	Uniform Heating	One-side heating	Non-uniform heating
100	26.4	23.6	19.7
150	19.6	17	14
220	11	13.2	14.2
320	9.8	10.8	12.1
450	5	11.2	11.54

Melnikov

Melnikov et al., in [18], present findings from experimental studies on the heat transfer phenomena occurring during the downward flow of mercury in a vertical round tube. A uniform heating is applied to only half of the channel circumference. The governing parameters are Re $= [10^4, 10^5]$, Ha $= [0, 6 \times 10^2]$ and $Gr = [0, 8 \times 10^9]$.

In Figure 9.5, the code results are analyzed alongside the experimental data provided by Melnikov et al. in [18], which is representative of a typical Grashof number $Gr = 6 \cdot 10^9$. The discrepancy with our laminar forced convection model are significantly higher compared with the previous case, as it can be seen in Table 9.6., where the errors computed over the entire data series with constant Ha are collected. Evidently, the downward flow exerts a substantial influence: the buoyant forces counteract the flow direction, and the magnetic field has limited capability to mitigate them. It is of particular note that at lower mass flow rates, the Nusselt number dips below the $Nu_{Lam-MHD} = 7$ and approaches the hydrodynamic laminar value $Nu_{Lam-OHD} = 4.36$ [168].

Table 9.6: Numerical average errors (%) for the Melnikov experimental cases [18], for various Hartmann values.

Hartmann Number	Nusselt Average Error
47	32.7
95	46
189	30
378	25.7
615	35.6

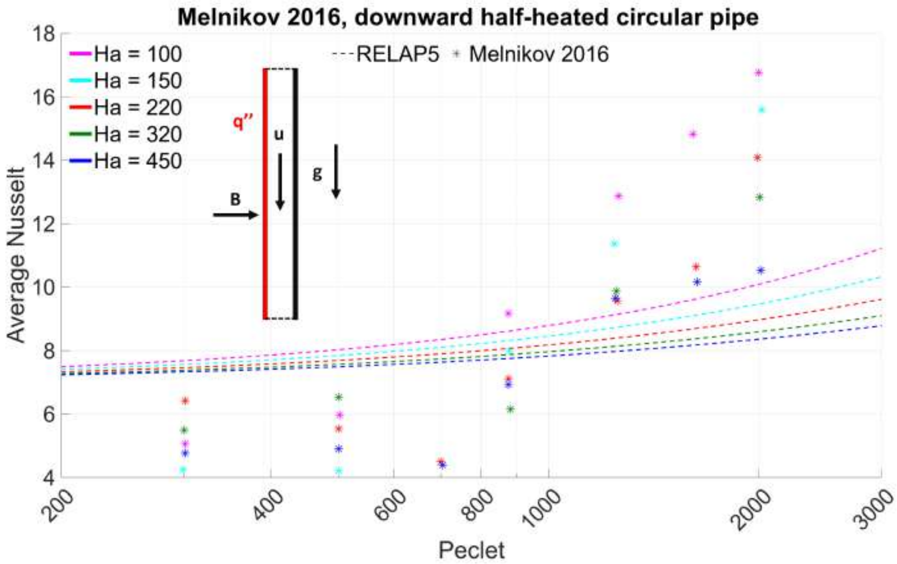

Figure 9.5: Comparison of the REDMaHD model with the downward flow data by Melnikov et al. [18]

Zikanov & Belyaev

Zikanov et al. in [19] and Belyaev et al., in [20], discuss their investigations from experimental studies centered on the heat transfer for the horizontal flow of mercury in a round tube, with heating applied uniformly but exclusively to the bottom half of the channel circumference. The critical parameters governing the experiments are: $\mathrm{Re} = [5 \times 10^3, 1.2 \times 10^5]$, $\mathrm{Pe}[= 10^2, 3 \times 10^3]$,$Gr = [0, 7 \times 10^8]$ and $\mathrm{Ha} = [0, 8 \times 10^2]$.

The code predictions are evaluated against the experimental data from Zikanov and Belyaev [19, 20] in figures 9.6a and 9.6b, correspondingly. The reference results are presented as Nusselt number evaluated on the flow cross-section but, contrariwise to the previous cases, are displayed as a function of the axial length of the pipe. In these cases a constant Reynolds number of $\mathrm{Re} = 1 \times 10^5$ is considered. As already pointed out, the non-uniform heat conditions in the channel seem to exert only a minimal influence on the flow characteristics. It is worth noting that measurements recorded at a non-dimensional length $l > 25$ may be affected by a fringing magnetic field. According to the authors, the magnet in the test section has a shorter axial extension compared to the channel, resulting in a reduction of the magnetic field near the pipe exit. A similar effect could occur at the inlet region $l < 10$ where, additionally, the flow might not yet be fully developed. Despite the

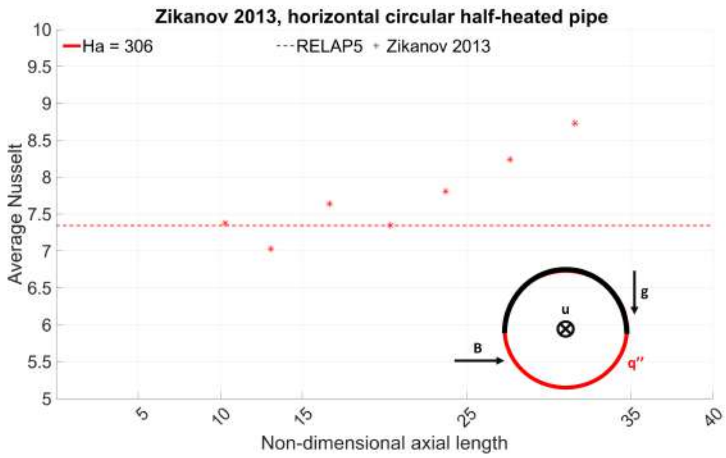

(a)

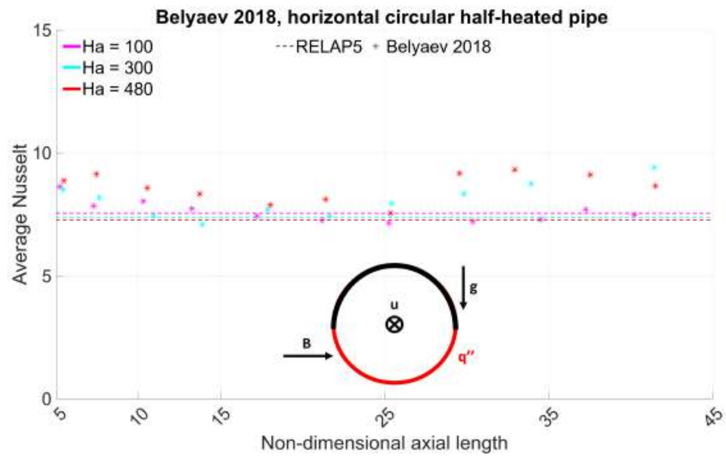

(b)

Figure 9.6: Numerical Nusselt number versus the non-dimensional duct axial length, with data from Zikanov and Belyaev [19, 20] serving as a benchmark. Different Hartmann numbers are represented by varying colors. Sub-figures include: *a*) Zikanov and *b*) Belyaev.

disparities in thermal boundary conditions the REDMaHD model alignment with the experimental data is satisfactory (see table 9.7).

Razuvanov, Luchinkin and Beznosov

In a follow-up research conducted by Razuvanov et al., documented in [21], they delve into the results obtained from an experimental campaign focusing on the upward flow heat transfer wherein the heating applied was non-uniform across the entire circumference of the channel. A similar analysis applying uniform heating for the pipe was carried out by Luchinkin et al., as seen in [22]. The experiments

Table 9.7: Numerical average errors (%) for the experimental cases described in [19, 20], for various Hartmann values.

Ha	Zikanov 2013	Belyaev 2018
100	-	4.26
300	-	10
306	5.93	-
480	-	15.21

have been led for Re $= [5 \times 10^3, 1.2 \times 10^5]$, Pe$[= 10^2, 3 \times 10^3]$, $Gr = [0, 6 \times 10^8]$ and Ha $= [0, 5 \times 10^2]$.

Pertinent outcomes have also been obtained by an alternative facility, FT-1 TOMHD, a high-temperature lead-bismuth setup. The experimental campaign is described by Beznosov et al. in [23], where the upward flow in a uniform heated duct is studied. The work is interesting because it proposes a discussion about electrical insulation coatings (EIC). To mitigate the effects of the magnetic field on liquid metal flow and reduce MHD resistance, EIC with high electrical resistance are applied to the surfaces containing the liquid metal flow. Comprehensive studies have been conducted on the formation techniques and properties of these coatings. In systems with heavy liquid metal coolants (HLMC), oxide coatings on the channel walls serve this purpose, created through the treatment of the coolant with oxygen and related compounds. Elevating the oxygen levels in the coolant refines both the EIC characteristics and the MHD resistance, enhancing the corrosion resistance of materials in a magnetic field. However, the introduction of EIC compromises heat transfer, increasing thermal resistance between the core flow and the heat-exchange wall element. Data referring to the lowest oxygen concentration have been used for the code-experiment comparison. The declared governing parameters are Reynolds number Re $= [(0.2 \times 10^5, 3.5 \times 10^5]$, Pe $= [3.2 \times 10^2, 4.6 \times 10^3]$ and Ha $= [0, 5 \times 10^2]$.

Figure 9.7 presents a comparison between the RELAP5 predictions and the experimental results for upward flow cases [21–23]. While buoyant forces still significantly influence the flow, it could be postulated that their impact should be less destabilizing as they act in the same direction as the flow. Moreover, the thermal boundary conditions do not seem to have a significant macroscopic impact on the flow characteristics. Unfortunately, no information is available regarding the electrical conductance ratio of the channels. The discrepancies between the numerical and experimental results remain within a reasonably acceptable range, as shown in Table 9.8. It can be observed that the error relative to the data reported in [23] is considerably higher. It is possible that the oxygen concentration in the fluid, although the lowest considered, may still affect the heat transfer.

Table 9.8: Numerical average errors (%) for the experimental cases described in [21–23], for various Hartmann values.

Ha	Razuvanov 2019	Luchinkin 2022	Beznosov 2016
150	13.2	15	-
285	-	-	17.5
300	14.3	14.5	-
335	-	-	26.2
385	-	-	24.1
400	11.24	14.8	-
435	-	-	22.7
490	-	-	22.9
550	8	15	-

9.3 Heat transfer model for square/rectangular channels

Due to the greater mathematical complexity of square or rectangular cross-sections compared to circular ones, straightforward analytical Nusselt correlations are, to the best of the authors knowledge, yet to be established in the literature. Although some papers cited in Section 9.1, such as those by Ying [180] or Al-Kawajha [183], offer derivations for heat transfer formulations, these are either not reproducible due to missing data or pertain to boundary conditions of limited practical applicability. From an experimental perspective, the sole known effort to establish a Nusselt correlation has been undertaken by Smolentsev et al. and it is presented in [191]. However, the relevance of this work is limited as it was derived specifically for slotted channels, characterized by an aspect ratio of 10.

The most comprehensive study on forced convection MHD in square and rectangular ducts under laminar flow conditions has been conducted by researchers at Imperial College London, discussed in a series of three papers.

In the work by M. J. Bluck, M. J. Wolfendale, and A. J. Marquis [192], the authors model forced convection in the context of Shercliff flow through a coupled

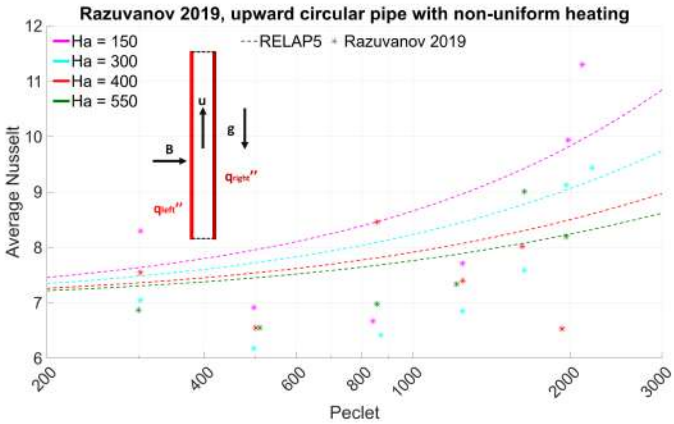

(a)

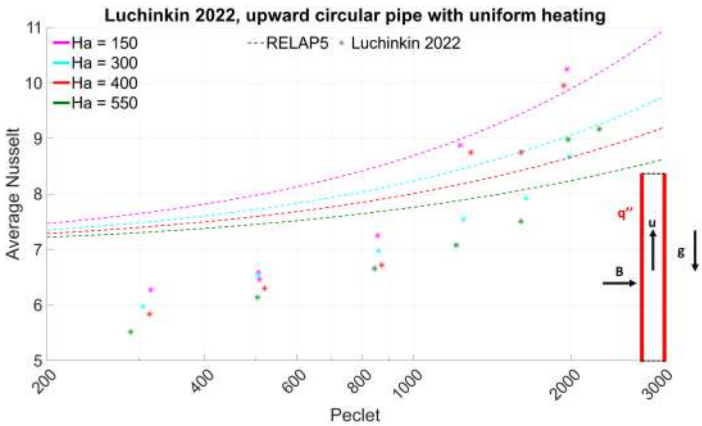

(b)

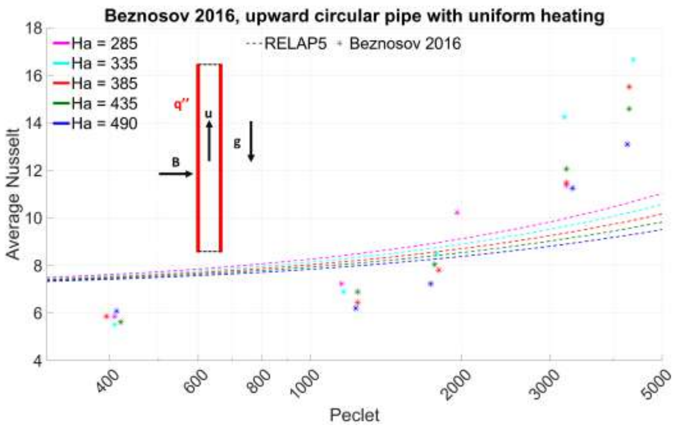

(c)

Figure 9.7: The average Nusselt number versus the Peclet number, with data from [21–23] serving as a benchmark for RELAP5. Different Hartmann numbers are represented by varying colors. Sub-figures include: *a*) Razuvanov experiment [21], *b*) Luchinkin experiment [22], and *c*) Beznosov data [23].

system of partial differential equations. They offer analytical results for $H1$ and $H2$ heat transfer regimes corresponding to certain heat flux and temperature conditions. Both temperature distributions and their corresponding Nusselt numbers are deduced as functions of the aspect ratio and the Hartmann number. For square channels, a diminishing temperature differential is noted as the Hartmann number elevates, attributed to the flow velocity suppression. Disparities in Nusselt numbers, especially at the Hartmann wall, emerge due to the electromagnetic forces outweighing the viscous forces when $\mathrm{Ha} \gg 1$. For rectangular ducts $b > a$, where b is the length of the wall perpendicular to the field while a is the length parallel to it, the Hartmann wall exerts a predominant influence on heat transfer, intensifying as the aspect ratio enlarges. Conversely, in ducts where $a > b$, the side walls chiefly control the heat transfer, becoming more evident as the aspect ratio shrinks. In either case, the Nusselt numbers approach those of non-MHD scenarios at minimal Hartmann numbers. The analysis further pinpoints that shear stresses at the Hartmann wall considerably augment heat transfer, unlike those at the side walls.

Bluck and Wolfendale extend their analytical solutions in [193], focusing on MHD flow in rectangular ducts with electrically insulated side walls and variable-thickness conducting Hartmann walls, termed as Hunt-II flow. For $H1$, an unambiguous escalation in Nusselt numbers is observed with increasing Hartmann numbers, even with core flow suppression. The side-wall jets outweigh the adverse influence of this suppression. Additionally, the Hartmann wall length significantly alters the Nusselt number at elevated magnetic fields. Contrastingly, in the $H2$ scenario, an eventual decline in the Nusselt number is observed at high magnetic fields. The diminished core flow overtakes the jet contributions in this case. The Nusselt number also exhibits strong dependency on the aspect ratio. With elongated Hartmann walls, an initial heat transfer enhancement is noticed as the magnetic field intensifies, peaking and then receding.

Bluck further broadens the scope in [194], incorporating a volumetric heat source term in the analytical solution to simulate the effects of neutron interaction with the liquid metal. The effect of the volumetric heat generation is express through the so called "volumetric Nusselt number". According to the author the temperature difference between the wall and the fluid bulk consists of two contributing terms: one proportional to the surface heat flux q'', and another proportional to the volumetric heat source q'''. For the surface Nusselt number, a corresponding heat transfer coefficient can be defined, serving as an indicator of the efficiency of heat transfer between the wall and the fluid. A low surface heat transfer coefficient signifies a higher thermal resistance, usually attributable to reduced wall shear stresses or thicker hydrodynamic boundary layers. Essentially, the fluid near the wall is ineffective in advecting heat away, resulting in a temperature gradient between the wall and the bulk fluid. The volumetric Nusselt number, however, encapsulates the additional layer of complexity introduced by volumetric heating. Slow-moving fluid near the walls accumulates heat at a rate higher than that of the bulk fluid, resulting in an elevated wall temperature. This metric quantifies the surplus heat in the boundary layer relative to that in the bulk. A low volumetric Nusselt number suggests an excessive heat accumulation within the boundary layer, which is typically observed in non-MHD laminar flows with thick boundary layers. Conversely, slug flow scenarios would exhibit an infinite volumetric Nusselt number, as there is no additional heat in a non-existent boundary layer when compared to the bulk.

It is useful to remember here what are the boundary conditions $H1$ and $H2$, as outlined in the book by Shah and London [195]. The constant axial heat rate per unit length (q') is a commonly employed thermal boundary condition in various applications such as electric resistance heating, nuclear heating, and counter-flow heat exchangers. This condition is denoted as H when no peripheral variation of wall temperature or heat flux exists. This is often the case in symmetrically heated straight ducts with consistent peripheral curvature and no corners, like circular ducts, parallel plates, and concentric annular ducts. In contrast, non-circular ducts with corners or varying peripheral curvature have variable peripheral wall temperature and/or heat flux. Four simplified cases can be considered:

1. **(H1) Boundary Condition:** The axial and peripheral wall heat transfer rates are constant. Mathematically, $q' = \gamma c_p \frac{dT}{dx}$ = constant and $T(x)|_{perimeter}$ = constant. Here, x is the axial direction whereas γ the mass flow rate.

2. **(H2) Boundary Condition:** The wall heat flux q'' is uniform in both axial and peripheral directions. It is formalized as $q' = \gamma c_p \frac{dT}{dx}$ = constant and $q'' = q'/P$ = constant. Here P is the perimeter of the duct.

The remaining conditions involve other variations of temperature and heat flux and are denoted as $H3$ and $H4$.

The condition $H1$ often applies to heat exchangers made from highly conductive materials like copper and aluminum. Condition $H2$ may be more difficult to achieve in practice for non-circular ducts but is mathematically convenient, thus frequently analyzed in the literature. The Nu_{H1} Nusselt number is generally higher than Nu_{H2} for a given duct geometry.

The $H1$ thermal boundary condition is of particular relevance in practical applications serving as an analog to the circular geometry in terms of its thermal characteristics when applied to square or rectangular ducts. To clarify, applying a uniform heat flux (q'') across the surface of a circular duct yields a symmetrical temperature distribution with respect to the duct central axis.

In order to approximate this symmetrical thermal behavior in a square or rectangular channel, high peripheral thermal conductivity must be enforced. Such an arrangement will maintain a nearly uniform temperature along the duct perimeter while allowing for a gradient of increasing temperature in the axial direction. Figure 19.8 serves as an illustrative example. It depicts Computational Fluid Dynamics (CFD) results of temperature contours at a heated pipe outlet. The left panel of this figure shows a channel with a constant q'' and low thermal conductivity, while the right panel exhibits a channel operating under the $H1$ boundary condition. For this particular $H1$ setting, the Nusselt number is commonly represented as $Nu_{q''}$, which is consistent with seminal literature on heat transfer, such as the text by Bergman et al. [168].

The mentioned works focus on the characterization of forced convection under laminar flow conditions. While incorporating turbulence modeling capabilities holds promise for future enhancements, its absence does not compromise the current utility of the REDMaHD model. Particularly under MHD flow conditions, laminarization becomes notably relevant in breeding blankets, where Hartmann numbers often reach values on the order of $O(10^4)$. Additionally, in specific cases such as the WCLL BB concept, the extremely low velocities of the liquid metal would inherently lead to laminar flow conditions, even without the influence of the magnetic field.

For the Nusselt number model in the system code, the primary reference is the first cited work by Bluck et al. [192], which considers an electrically insulated channel. The motivation for this choice lies in the understanding that analytical solutions

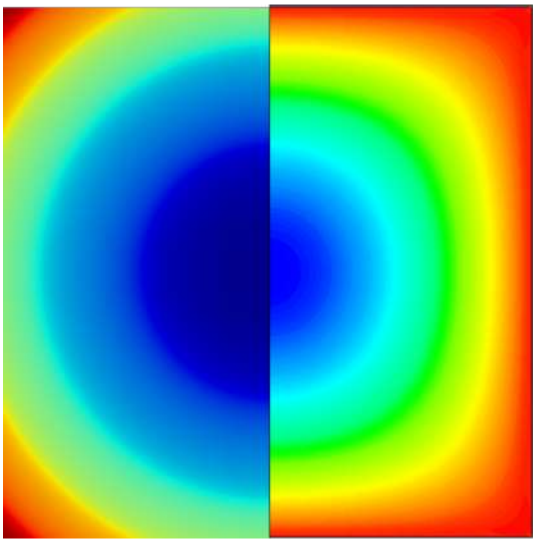

Figure 9.8: Different temperature field in a condition: $\neq H1$ (left) and $H1$ right.

incorporating the electrical conductivity effects of the Hartmann walls, as in Hunt-II flows, may not fully represent the flow regimes observed in breeding blankets. As a matter of fact, in practical cases a channel within the BB often possesses non uniform wall thickness (hence finite wall conductance ratio) rather than an hybrid perfectly insulated - conductive configuration [24, 58]. Moreover, Hunt-II represents a limiting case where the jets attain their maximum velocity for an arbitrary value of c_w. Therefore, it is not a conservative assumption in terms of heat transfer. On the other hand, although the Shercliff case represents an idealized scenario, it closely approximates the flow characteristics that some prominent breeding blanket designs, such as the DCLL [7, 8, 92], aim to achieve. Furthermore, the decision was made to omit the part of the analytical solution by Bluck [194] that addresses volumetric heating, since further evaluation of its applicability is deemed necessary. The REDMaHD model employs the Nusselt solution exclusively for the $H1$ case, which corresponds to the uniform q'' boundary condition permitted by the thermal structure of RELAP5.

To tailor the Nusselt number analytical solution to the requirements of the system code architecture, modifications were made to its original functional form $Nu_{\text{analytical}} = f(\text{Ha}, \alpha)$. In this expression, $\alpha = \frac{a}{b}$ represents the aspect ratio of the channel. Rather than considering both Ha and α as independent variables, focus was placed solely on the Hartmann number (Ha) for the purpose of system code integration. A best-fit procedure was employed to approximate the function $\mathrm{Nu} = f(\mathrm{Ha})$ for a total of 19 distinct aspect ratios. The curves derived by the Bluck et al. [192] solution are depicted in Figure 9.9. The aspect ratios (α) were selected with varying step sizes: from 0.1 to 0.9 with a step of 0.1, 1, and then from 2 to 10 with a step of 1. An aspect ratio of $\alpha = 1$ corresponds to a square channel. For $\alpha > 1$, the channel assumes a rectangular geometry elongated in the direction parallel to the magnetic field. Conversely, an aspect ratio $\alpha < 1$ signifies that the channel is stretched perpendicularly to the magnetic field.

The fitting of the 19 curves has been performed through rational functions characterized by eleven coefficients, similar to the methodology employed for circular pipes (see Eq. 9.1 and Table 9.2). When the input channel dimensions do not match any of the selected aspect ratios, a weighted average is computed using the closest α values to estimate the Nusselt number. The computational procedure for the Nusselt number calculation owns a dedicated Fortran 77 subroutine, which can be found in Appendix A. The MATLAB script for calculating and representing the Nusselt number is also provided in Appendix A.

From Figure 9.9, it is evident that the aspect ratio profoundly influences the thermal behavior of the flow. This influence is a direct outcome of the asymmetry inherent in MHD flows, setting them apart from conventional flows. Notably, for $\mathrm{Ha} < 10$, the Nusselt numbers approach the OHD value, specifically 3.608 for a square duct [168]. In ordinary hydrodynamics, the orientation of the cross-section does not impact heat transfer, leading to the observation that $\mathrm{Nu}(\alpha) = \mathrm{Nu}(\alpha^{-1})$. Conversely, as elaborated in Section 3.7, the velocity profiles differ significantly along the $B_{//}$ and $B_{\perp}$ directions. Consequently, the Hartmann and side layers contribute differently to heat transfer. The Nusselt number for the Hartmann wall rises more swiftly than that for the side layer, attributed to its thinner boundary layer, which scales as $O(\mathrm{Ha}^{-1})$ for the Hartmann wall and $O(\mathrm{Ha}^{-0.5})$ for the side wall. For large Ha, the Shercliff flow develops a flat core region with a velocity that tends to $O(\mathrm{Ha}^{-1})$, as demonstrated in [81]. The wall shear stress, essentially the ratio of the core velocity to the boundary layer thickness, becomes asymptotically $O(1)$ for the Hartmann wall. Consequently, the heat transfer reaches a plateau at high Ha, corroborating the findings by [186] for a circular duct.

The influence of the Hartmann layer is especially pronounced when $\alpha < 1$ (see

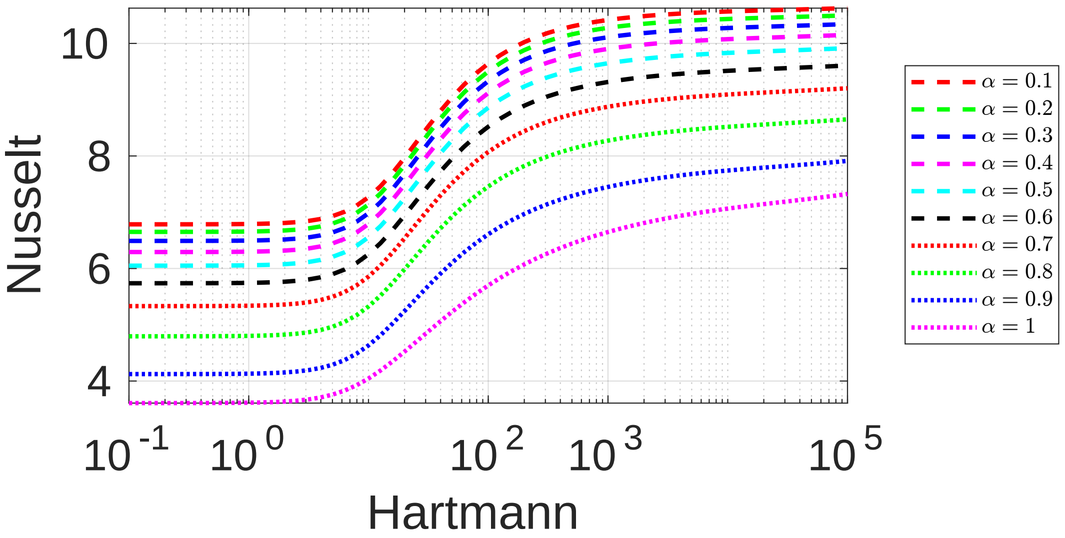

(a)

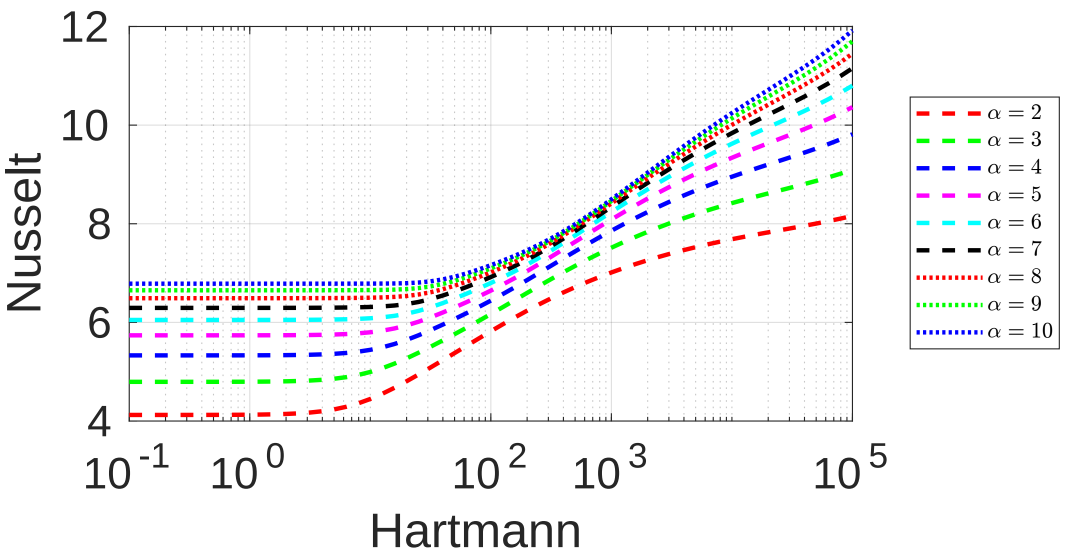

(b)

Figure 9.9: Bluck analytical solution (Shercliff flow) for Nusselt number as a function of Hartmann and duct aspect ratio for the $H1$ regime. Sub-figures include: a) aspect ratio ≤ 1, b) aspect ratio > 1.

Figure 9.9a). As α decreases (with a fixed pipe perimeter), heat transfer becomes progressively governed by the elongated Hartmann wall. The lower the aspect ratio, the more dominant the heat transfer from the Hartmann wall becomes relative to the side wall, leading to a steeper increase in Nu. At low α, a saturation point is attained in the heat transfer rate from the Hartmann wall. Conversely, for $\alpha > 1$, the length of the Hartmann wall diminishes in comparison to the side wall, causing its contribution to heat transfer to wane with increasing aspect ratio and ceding dominance to the side walls. As a result, the onset of the plateau is increasingly deferred as the aspect ratio rises, and an asymptotic Nusselt value is not achieved if not for $\mathrm{Ha} > 10^5$.

In summary, the Hartmann wall, characterized by higher wall shear stresses, outperforms the side wall in terms of heat transfer per unit length. In a square duct ($\alpha = 1$), the Hartmann wall contribution to the overall heat transfer is predominant, causing a rapid escalation in Nu as Ha increases. As the aspect ratio enlarges, the Hartmann wall contribution diminishes, resulting in a more gradual increase in Nu dictated by the heat transfer through the side wall.

9.3.1 Preliminary Validation

To the best of the author understanding, no existing experimental data can effectively validate the analytical solutions proposed in [192–194]. Although several experimental studies address MHD heat transfer in square or rectangular channels, they are considered inapplicable for validation purposes. This decision is justified either because the experimental conditions substantially deviate from those assumed in the analytical solution or essential information required for system code modeling is absent. However, it is worth noting that there are a few experimental studies that could be particularly valuable for future validation efforts, once the REDMaHD model has matured and gained capabilities.

One of those work has been carried out by Burr et. al and it is described in [84]. The study concentrates on the wall-adjacent jets behavior of a MHD turbulent flow. The channel is characterized by a $\alpha = 2$, electrically conductive walls and it has been heated on one of the side walls with a constant heat flux. The governing parameters are $2 \cdot 10^3 < \mathrm{Re} < 5 \cdot 10^3$ and $0 < \mathrm{Re} < 4.8 \cdot 10^3$.

The turbulence observed is strongly anisotropic and quasi-two-dimensional, featuring large-scale vortex formations that travel parallel to the sidewalls. These vortices overshadow smaller, more isotropic turbulent eddies in terms of turbulent kinetic energy contribution. Direct measurements indicate that magnetic field intensification significantly amplifies turbulent heat transport at walls parallel to the field. This is significant because could potentially lower the required coolant flow rates in MHD heat transfer units, challenging traditional laminar-flow-based design assumptions.

Another study considered to be of significant relevance is the research conducted by Sahu et al. [196]. The investigation examines the magnetic field impact on heat transfer, using the temperature distribution at the exit of the heated section as the primary metric for flow characterization. The channel has an aspect ratio $\alpha = 1$ and it is heated with $q'' = const$ from a side wall, that is located on the lower part of the pipe.

Three prominent flow regimes were discerned: (i) a regime dominated by buoyancy forces, identified for $\mathrm{Ri} > 10$ and $\mathrm{Ha} = 220$, (ii) a regime governed by electromagnetic forces, applicable for $0.1 < Ri < 10$ and $\mathrm{Ha} \geq 220$ or $Ri > 10$ and $\mathrm{Ha} \geq 440$, and (iii) an inertia-dominated regime, relevant for $Ri < 0.1$ and $\mathrm{Ha} \geq 220$. In the buoyancy-led regime, buoyancy forces notably outweigh both electromagnetic and inertial forces, causing a transition from an M-shaped velocity profile to a 3D flow pattern. This alteration leads to the manifestation of low-frequency temperature fluctuations at the heated section exit. In the electromagnetic force-driven regime, electromagnetic forces prevail over buoyancy and inertial forces, culminating in a stratified temperature distribution at the outlet. In contrast, the inertia-dominated regime shows little variation in the temperature profile between flow cases with and without the magnetic field. The Nusselt number (Nu) remains approximately constant in this regime, whereas it varies significantly in the other regimes. Nu is observed to follow an inverse power law relationship with $\frac{Gr}{\mathrm{Re}^2\, Ha^2}$ in the mixed convection region under study. The experimental section possesses a finite electrical conductivity, although its precise value is not detailed within the main text. As a result, the MHD regime is anticipated to diverge notably from the Shercliff one and, additionally, Nu data for all three regimes are presented in relation to the buoyant forces, making it challenging to isolate the data specifically for regime (ii).

Code-to-code Comparison

To assess the typicality of the analytically-derived reduced model, its results have been compared with numerical simulations performed with a CFD code. In this analysis, the average Nusselt number from the REDMaHD model was compared with results generated by a customized MHD OPENFoam solver, currently under development at Sapienza University of Rome, that is already well validated to deal with simple MHD flows such as the Shercliff case [116].

The geometric configuration and primary boundary conditions are illustrated in figure 9.10. The duct axial length is computed so that at the exit the flow is in fully developed conditions, the aspect ratio is maintained at $\alpha = 1$ with dimensions $a = b = 1\,\mathrm{m}$ and a constant heat flux is imposed on the walls. With the specified mass flow rate, the flow remains laminar with a Reynolds number $\mathrm{Re} = 10^{-4}$. At the outlet, the zero reference pressure is enforced using the `fixedValue` boundary condition (BC), while the `zeroGradient` BC is applied for velocity ($\partial u/\partial x = 0$) and temperature ($\partial T/\partial x = 0$). For the walls, the conventional `noSlip` BC ($u_w = 0$) is utilized. Concerning the electromagnetic BCs, the `zeroGradient` BC is set for the electric potential on all boundaries, as the walls are assumed to be perfectly insulated. The initial reference temperature is established at 600 K, and the thermo-physical properties of the modeled materials are considered to be temperature-invariant at this value. The liquid metal used in the simulations is PbLi [41], while the walls are assumed to be constructed from Eurofer97 [197] (see table 9.9).

Four steady-state simulations have been executed with varied Hartmann numbers $\mathrm{Ha} = 100, 500, 5000, 15000$, in forced convection regime. The structured computational grid is depicted in figure 9.10. The grid is designed such that within the Hartmann layer thickness, $\tau_{HL} = \frac{a}{\mathrm{Ha}}$, it contains a total of 6 elements, which has been identified as optimal for reliable results by multiple researchers [198]. The same grid grading is also applied in the direction orthogonal to the magnetic field, ensuring that the number of elements in the side layers scales in accordance with the thickness $\tau_{HL} = \frac{a}{\sqrt{\mathrm{Ha}}}$.

The qualitative outcomes are displayed in Figure 9.11. The velocity profile characteristic of Shercliff flow is reaffirmed: a steeper velocity gradient manifests within the Hartmann layers compared to that observed in the side layers, and a flat-velocity

Property	PbLi [41]	Eurofer[197]
Density (kg m^{-3})	9806	7750
Kinematic Viscosity (m^2 s^{-1})	1.994×10^{-7}	-
Thermal Conductivity (W m^{-1} K^{-1})	20.93	29.8405
Thermal Expansion Coefficient (K^{-1})	1.214	-
Electrical Conductivity (S m^{-1})	8.747×10^5	-
Surface Tension (N m^{-1})	0.4561	-

Table 9.9: Thermo-physical properties at reference temperature 600 K for the modelled materials

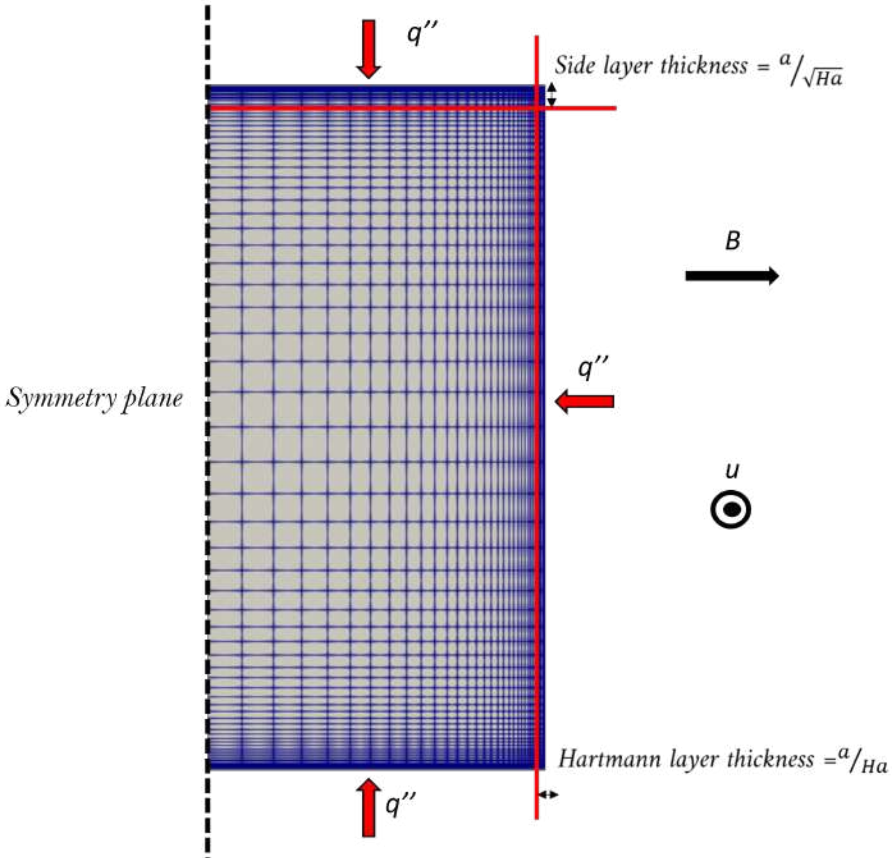

Figure 9.10: Typical mesh grid (for Ha = 500) employed for the calculations. The main boundary conditions are specified with vectors. A symmetry BC is applied on the radial-poloidal plane.

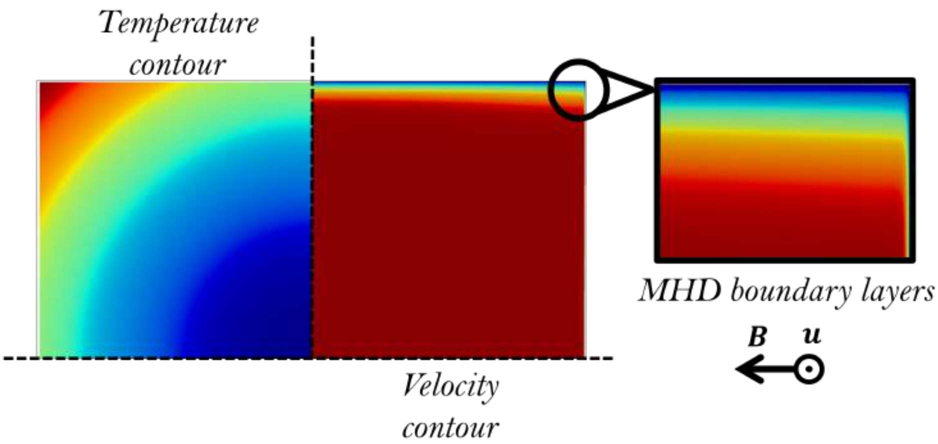

Figure 9.11: Temperature (left) and velocity (right) contours are shown for one-fourth of the outlet in the case where Ha = 5000. The region corresponding to the layers is magnified to better illustrate the evolution of velocity gradients.

core region emerges [6, 81].

Nevertheless, deviations in the temperature field within the liquid domain from the expected $H1$ regime are evident (see Figure 9.8). Although the temperature is lower at the channel center as anticipated, it does not maintain a constant value along the wall; it is elevated at the corners and diminished at the center of the walls. A plausible explanation for this behavior lies in the intrinsic challenges of enforcing an exact $H1$ condition within a CFD code. The primary issue stems from the thermal conductivity of the solid walls. Utilizing a realistic parameter, such as the conductivity of Eurofer97, satisfies only one of the two $H1$ regime conditions, specifically, $\partial T_{\text{wall}}/\partial x = \partial T_{\text{bulk}}/\partial x = \text{constant}$. In essence, both the fluid and solid components experience a uniform temperature increase as the fluid flows along the heated channel. However, a constant temperature cannot be established along the wall perimeter due to the material inadequate thermal conductivity, i.e., $T(x)|_{\text{perimeter}} \neq \text{constant}$.

Despite this limitation, the agreement in terms of Nusselt number, as presented in Table 9.10, between the reduced model and the OpenFOAM calculations remains satisfactory. Even in a preliminary manner, this suggests that REDMaHD should be capable of modeling, with reasonable accuracy, realistic scenarios that are pertinent for the design and development of liquid metal components where MHD effects play a significant role.

Ha	Nu_{Bluck} [192]	Nu_{CFD}	Error (%)
100	5.80	5.75	-1.7
500	6.42	5.83	-9.7
5000	6.88	6.07	-11.8
10000	6.97	6.01	-13.9

Table 9.10: Comparison between the analytical model and the OpenFOAM results in terms of Nusselt. Relative error is reported.

Finally, to explore the influence of the solid thermal conductivity k_{wall} and varying heating conditions on the walls, a series of CFD simulations was conducted by altering these two parameters. This approach provides a more comprehensive understanding of how well the reduced model can adapt to scenarios that deviate to some extent from the conditions under which it was originally derived. The results of these simulations are summarized in Table 9.11. All outcomes pertain to Ha $= 100$ and Re $= 10^{-4}$, and the employed geometry and meshing grid adhere to the criteria previously discussed. The problem setup is consistent with that shown in Figure 9.10.

Calculations were performed with the assumption of constant heat flux on the walls, whether those are only the side walls (SW), only the Hartmann walls (HW), or all walls. If a pair of wall is not heated, is set as adiabatic. The thermal conductivity of the solid was set at a realistic, practical value of $k_{\text{wall}} = 29.8\,\frac{\text{W}}{\text{m}\cdot\text{K}}$ and at an arbitrarily high value of $650\,\frac{\text{W}}{\text{m}\cdot\text{K}}$ to simulate a perfectly conducting medium. Note that this value is approximately 50% higher than that of silver and copper under standard conditions. Additionally, five simulations were executed without the inclusion of the solid domain, including an OHD simulation, thereby directly applying the heat flux to the fluid side layers (SL) or Hartmann layers (HL).

It can be observed that the maximum discrepancy between the analytically-derived model and the CFD calculations is approximately $\approx 10\%$. This suggests that the REDMaHD model can be used confidently for various heating conditions. The penultimate simulation, featuring all four heated walls and a perfectly conductive solid, most closely approximates the $H1$ condition.

Type of Simulation	Average Nusselt	Error
$q'' = \text{const}$ OHD	3.1	14.3%
$q'' = \text{const}$ on HL and SL	5.7	8.0%
$q'' = \text{const}$ on SL	5.5	9.7%
$q'' = \text{const}$ on HL	5.7	5.9%
$q'' = \text{const}$ on SW with $k_{\text{wall}} = 650$	5.5	9.4%
$q'' = \text{const}$ on SW with $k_{\text{wall}} = 29.8$	5.5	9.7%
$q'' = \text{const}$ on HW with $k_{\text{wall}} = 650$	5.8	5.1%
$q'' = \text{const}$ on HW with $k_{\text{wall}} = 29.8$	5.7	5.8%
$q'' = \text{const}$ on all walls with $k_{\text{wall}} = 650$	6.0	0.7%
$q'' = \text{const}$ on all walls with $k_{\text{wall}} = 29.8$	5.8	4.4%

Table 9.11: Calculation matrix for different boundary conditions. Errors from the reference values $\text{Nu}_{Bluck} = 6.0615$ for $\text{Ha} = 100$ and $\text{Nu}_{OHD} = 3.61$ are reported. The k_{wall} is in $\frac{W}{m \cdot K}$

9.4 Summary

In this chapter, the influence of MHD effects on convective heat transfer in turbulent and laminar flows has been discussed. MHD conditions generally dampen turbulence, affecting heat transfer mechanisms adversely. This is in part due to magnetic damping and the phenomenon known as "relaminarization," where turbulent flows revert to laminar flows under the influence of an external magnetic field. On the other hand, in laminar flows, MHD effects can facilitate heat exchange by thinning viscous boundary layers. Natural circulation adds another layer of complexity, with the magnetic field also affecting buoyancy-driven structures.

A thorough review of the state-of-the-art in the domain is presented, with an emphasis on seminal numerical studies that can inform and guide the development of REDMaHD. Reduced models for calculating the heat transfer coefficient (or the Nusselt number) in forced convective MHD flows are derived from selected studies, applicable to both circular and square channels. Preliminary validation for the circular pipe model is conducted against a set of experimental results under varying heating conditions and flow directions. As for the square/rectangular model, a comprehensive set of experimental data is currently unavailable. Hence, the model validity is assessed through a code-to-code benchmark against a newly implemented OpenFOAM solver.

Part IV

Support activities

Chapter 10

Application of REDMaHD to the WCLL BB and TBM design

Given the demonstrated reliability of REDMaHD in simulating intricate MHD phenomena, the software has been utilized to conduct some studies aimed to provide direct contributions to the WCLL BB concept development and design. Activities have been performed on both the WCLL BB and Tritium Extraction and Removal (TER) system conceptual design, intended for deployment in DEMO, and on the TBM foreseen to be tested during ITER experimental campaigns.

10.1 Support to the WCLL TBM design

10.1.1 TBM box optimization

This investigation is centered on simulating and optimizing the LM flow path within the WCLL TBM, the test section slated for data acquisition on blanket concepts during ITER experimental runs [30] (see also Section 2.9). Insights from comprehensive numerical studies on the TBM manifold and breeding zone, as delineated in Refs. [24, 31], serve as benchmark criteria for evaluating the accuracy of our MHD subroutines. The REDMaHD-generated predictions for pressure loss and flow distribution in the TBM reference configuration act as the foundational guidelines for the optimization procedures. Two iterations to the reference design of the manifold area, initially suggested in Ref. [24] to mitigate the flow rate discrepancies among the breeding units, are incorporated into the REDMaHD model. The impacts of these modifications on pressure loss and flow distribution are analyzed both individually and in combination, along with additional configurations proposed.

Reference geometry

The TBM is slated for deployment during ITER experimental stage to collect data on a BB concept that employs a low-pressure liquid breeder cooled by a high-pressure coolant, specifically water, in this instance [25, 30]. Figure 10.1 provides a 3D visualization of the TBM pre-conceptual design. The TBM consists of two parallel sections that are identical in construction, with each section containing 8 vertically stacked breeding units, which are supplied by a vertical duct serving as the feeding manifold. These 16 BUs collectively form the breeding zone. Post transit through the BUs, whose flow schematic is outlined in Figure 10.2, the fluid is gathered in a separate vertical channel, identified as the draining manifold. The breeder is sequentially channeled from the feeding manifold to the BZ, consequently experiencing a decrement in mass flow rate as it ascends in poloidal height. Conversely, the opposite occurs in the draining manifold. Structural intricacies in the manifold channels, stemming from toroidally aligned stiffening plates that define each BU and bolster the TBM mechanical integrity, induce a series of fluid contractions and expansions. Figure 10.1 omits the inlet and outlet pipes of the TBM, which are situated at the heights of the bottom and top BUs, respectively, in a central alignment [199].

In Figure 10.3, the inlet manifold flow path is delineated by the red line, while the blue line designates the outlet manifold. The working fluid is a PbLi alloy, and the structural material is Eurofer97. For the scope of this study, the liquid metal flow is assumed to be isothermal, with thermo-physical properties assessed at a temperature of 623 K [41, 197]. A constant, unidirectional magnetic field of $B = 4\,\mathrm{T}$ is imposed along the z (toroidal) axis as illustrated in Figure 10.3. The poloidal component of the magnetic field, which generally accounts for roughly one-third of the toroidal component, is neglected for this analysis. This assumption is customarily accepted due to its relatively minor impact on pressure losses [58].

The characteristic length for the case is chosen as the BU toroidal half-width, $a = 0.097\,\mathrm{m}$, and the reference velocity is $v_0 = 0.1\,\mathrm{mm/s}$. Key parameters governing the flow are $Re = 50$ and $Ha = 8600$. The selected reference values for the REDMaHD analysis are in line with the expected conditions of the WCLL DEMO blanket [54].

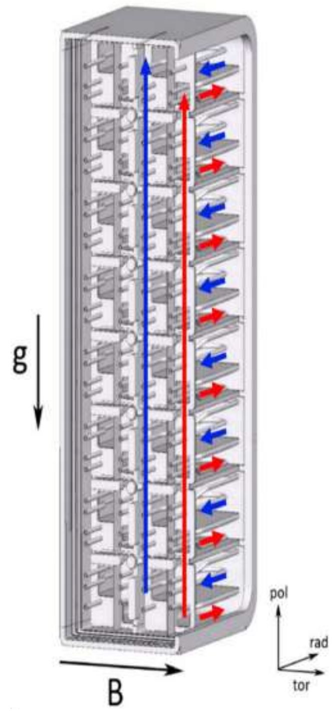

Figure 10.1: Three-dimensional representation of the benchmark geometry, adapted from Ref. [24]. The directional flow of PbLi is indicated by arrows: red arrows signify the distribution leg, while blue arrows denote the collection leg.

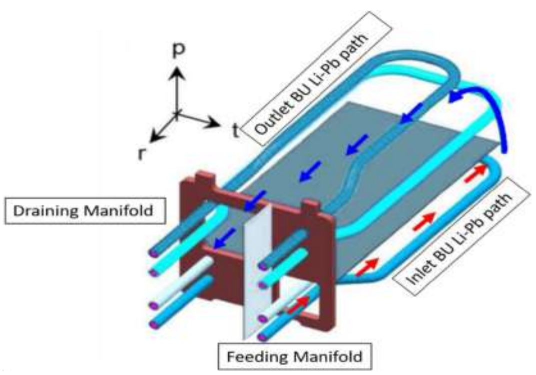

Figure 10.2: Three-dimensional CAD representation of an individual Breeding Unit. The flow trajectory is highlighted by colored arrows [25].

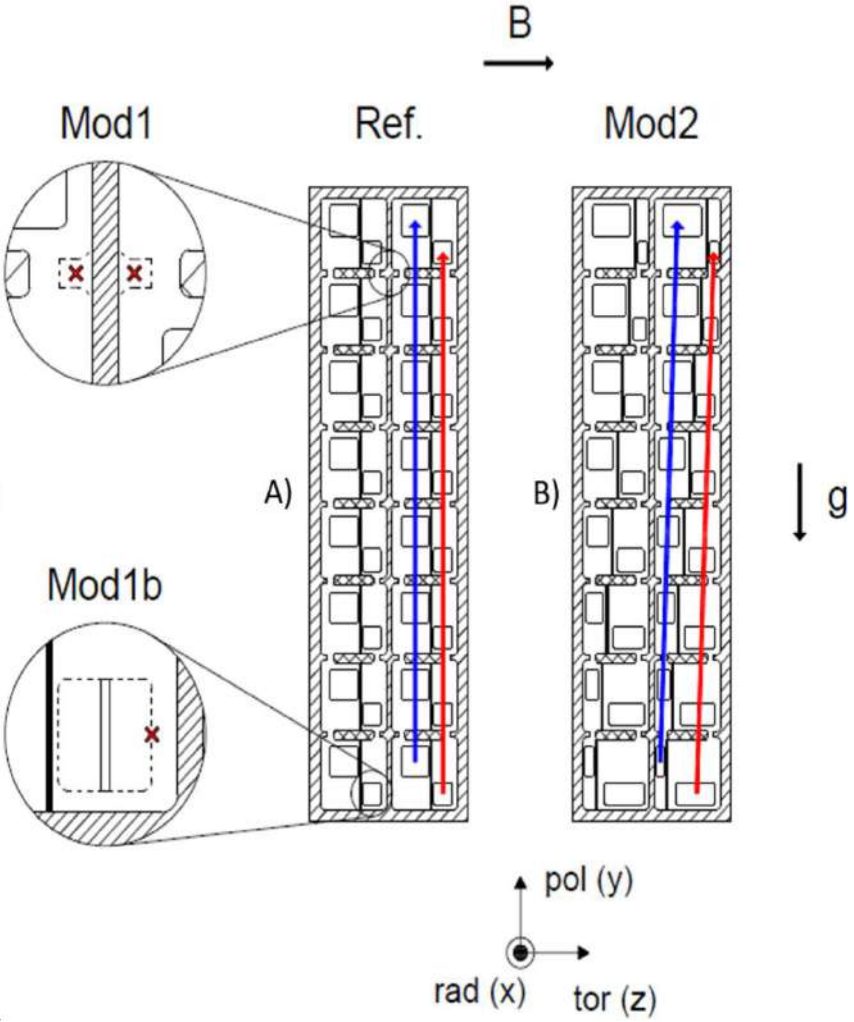

Figure 10.3: A poloidal-toroidal view of the TBM is shown, where the liquid metal flow paths in the feeding and collection manifolds are indicated by red and blue arrows, respectively. Panel A portrays the baseline geometry, highlighting two design optimizations labeled as Mod1 and Mod1b. Panel B presents another optimized configuration, known as Mod2, as proposed in [24].

Table 10.1: Main geometrical parameters. (*) Stiffening plate not considered [24, 30, 31].

Component	Toroidal width [mm]	Poloidal height [mm]	Radial length [mm]	$t_w(Ha)$ [mm]	t_w(Side1) [mm]	t_w(Side2) [mm]
Feeding Manifold	76	1610	60	30	15	15
Draining Manifold	115	1610	60	30	15	15
Breeding Unit (*)	193.5	190	430	30	30	30

The average velocity yields a total mass flow rate of 0.12 kg/s per TBM section.

Figure 10.3 also illustrates alternative geometry configurations denoted as Mod1 and Mod2, which were proposed in [24]. Mod1 enlarges the manifold sections gap and removes non-functional protrusions in the toroidal-radial stiffening plate. Mod2 proposes a stepwise shift of the stiffening plate separating the feeding and draining manifolds, conforming to mass flow rate changes along the poloidal axis. Additionally, a new layout, Mod1b, tailors the hydraulic connections between the manifold and BUs to achieve uniform flow distribution. Combined effects of these configurations are studied, resulting in Mod3 and Mod3b layouts. In Table 10.1, the principal dimensions of the module are detailed.

Baseline configuration

Concerning the nodalization scheme employed, as depicted in Figure 10.4, the WCLL TBM model has been adapted from the model formulated at Sapienza within the scope of the ITER WCLL Test Blanket System (TBS) Water Cooling System (WCS) analysis [200, 201]. This initial model already incorporated PbLi volumes within the WCLL TBM, accompanied by segments of both the inlet and outlet ducts. The representation illustrated in [201] underwent enhancements adhering to insights acquired from the HCLL study [15] (also presented in Section 8.2). Inlet and outlet thermodynamic states of the liquid metal, notably temperature and pressure, are determined by two time-dependent volumes (TMDPVOL #181 and #220, as seen in Figure 10.4). A time-dependent junction (#182) enforces the stipulated mass flow rate across the circuit. The pipe component #185 establishes a link between the TMDPVOL and the dual inlet manifolds. Each manifold is mimicked using a pipe component consisting of 23 CVs, which simulate the chambers forming the manifold and their respective connections. Lateral junctions facilitate the coupling of the BUs with the relevant volumes in both the inlet and outlet plenum. Every BU is emulated

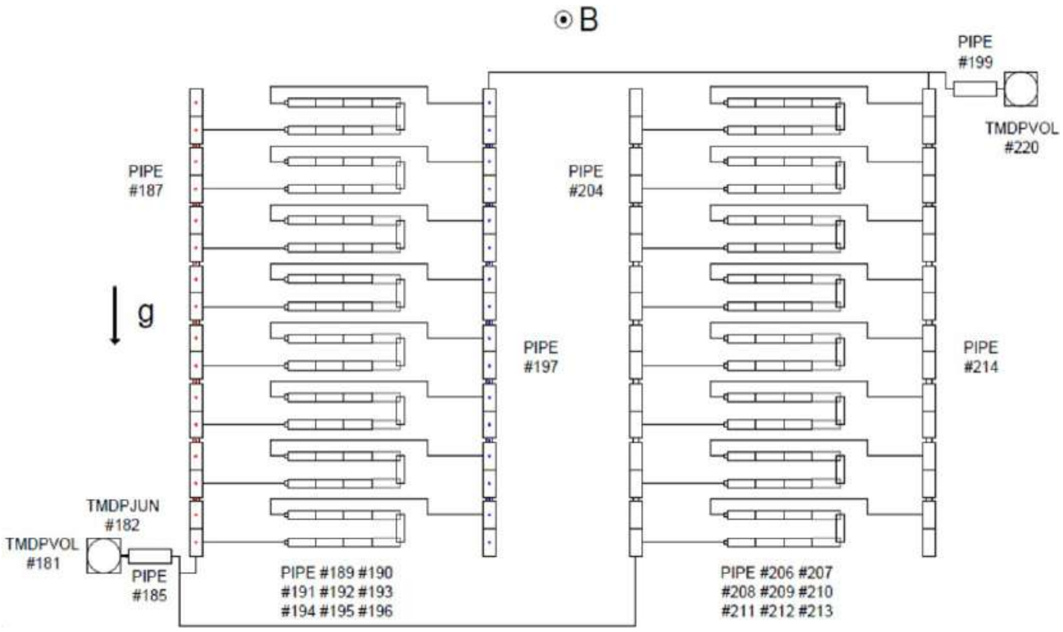

Figure 10.4: Nodalization scheme employed for RELAP5 computations. Red and blue markers emphasize the pressure data points pertinent to all diagrams presented subsequently.

using a pipe component comprised of 11 CVs. Outlet manifolds adopt an identical modeling technique (namely, slice modeling) as their inlet counterparts, mirroring authentic geometric attributes. The PbLi discharging from the TBM accumulates within the outlet pipe (#199) and is subsequently directed to the TMDPVOL #220. The twin parallel sections of the WCLL TBM showcase analogous geometric properties, with the sole exception being the Hartmann wall thickness of the manifold channels. On the left flow trajectory (blue arrow, as shown in Figure 10.1), the TBM lateral plate, possessing greater thickness than the reinforcement plates, serves as the Hartmann wall for the draining manifold. Conversely, the inverse is true for the feeding conduit on the right flow trajectory (red arrow).

Results

Computational MHD studies on the manifold have underscored the influence of fluid velocity and pressure distribution in such a complex geometry due to the presence of 3D MHD effects. These effects are most pronounced at locations where the flow encounters variations along the magnetic field lines (toroidal changes). Specifically, the space between two sections of the manifold and the transitions at the manifold/BU interface play a crucial role in the pressure head loss within the TBM. Moreover, the structural plate separating the feeding and draining manifolds is electrically conductive, causing the fluid regions to be electrically interconnected. The two manifold conduits possess distinct geometric characteristics, including Hartmann wall thickness and cross-sectional area. This leads to asymmetries in the velocity distributions, resulting in notable differences in the peak velocity values on opposing layers. Additionally, with varying pressure gradients in the two manifolds and a marked discrepancy in the mass flow rates between the feeding and draining sections, regions of reverse flow are observed. This means that the velocities in the manifold central sections are consistent in direction across both ducts, but in the outer sections, where the driving forces differ, streams with negative velocities emerge in the fluid layers parallel to **B** [24].

Dealing with the pressure drop within the TBM, it was determined that $\Delta p_{\mathrm{CFD}} =$ 14kPa under reference conditions based on CFD simulations [24]. A similar assessment using REDMaHD, with the nodalization pattern previously outlined, yielded $\Delta p_{R5} = 13.91$kPa. While this result seems encouraging, given the relative difference $\epsilon < 0.65\%$, it is pivotal to delve into the uncertainties intrinsic to our modeling technique. As stipulated in [24], Δp_{CFD} strictly pertains to the pressure drop in the manifold, explicitly excluding the contribution from the flow in the BU, as well as the contractions and expansions at the manifold/BU juncturefactors which are factored into Δp_{R5}. Moreover, as elaborated upon in V&V Chapter 8 [15], the REDMaHD model tends to overestimate 3D MHD losses for cross-section variations. In contrast, the loss computed in [24] encompasses also the effect of electromagnetic coupling. Owing to the co-current flow setup, this is anticipated to amplify the pressure drop given the pronounced flow discrepancy between the input and output conduits over the manifold extensive poloidal dimension. As previously discussed in Chapter 8, the present version of REDMaHD does not satisfactorily simulate the impact of such phenomena on pressure reduction. Consequently, the total pressure drop is comparably consistent between both calculations. This arises as the absence of a coupling model in REDMaHD is offset by the conservative nature of the 3D MHD model and the incorporation of BUs path in the evaluation. However, it warrants mentioning that this latter component influence is presumed to be marginal ($0.3 - 0.5$kPa), as documented by meticulous CFD studies in Ref. [31].

It can be reasonably asserted that the code proficiently predicts, with a commendable degree of precision, the trend of MHD pressure drop within this intricate liquid metal circuit. Furthermore, it offers a plausible estimate of the pressure loss across the module. In Figure 10.5, the pressure adjusted for the hydrostatic head is graphically represented against the vertical poloidal directionencompassing the entire span of the manifolds. The gap discerned between the red and blue curves (highlighted by black arrows in Figure 10.5a) signifies the pressure variation between the feeding and draining manifolds. Put differently, it denotes the available pressure head from the inlet to the outlet of the relevant BU. The augmented three-dimensional pressure decline, evident at the juncture of manifold segments, is illustrated by the evident steps in the pressure pattern. Here, the plotted MHD pressure gradient is composed by the superposition of the fully developed flow contribution and that from the abrupt contractions and expansions in the manifold architecture. A noteworthy observation is that the pressure loss across the BUs exhibits variation for each individual unit, as presented in Figure 10.6.

The pronounced flow rates observed in the top (BU8) and bottom (BU1) channels, particularly in the latter, when compared with the central channel, are responsible for this phenomenon. It is important to highlight that this flow disparity is intrinsically rooted in the manifold design. This design culminates in a diminished pressure head for the central BUs, which subsequently draw a reduced flow rate. Electromagnetic coupling phenomena tend to exacerbate this imbalance, a notion evident when contrasting Figure 10.5a with Figure 10.5b. In the latter figure, data derived from Ref. [24] is shown. In both BU1 and BU8, regions with elevated mass flow rates, the load loss approximately doubles in comparison to our REDMaHD model, which omits the coupling factor. Yet, REDMaHD aptly mirrors the qualitative progression of the pressure head across the poloidal axis. As a result, one could anticipate that the flow rate distribution delineated in Figure 10.6 aligns closely with the CFD one, except for a discrepancy caused by the lack of modelling of coupling effects. This realization spurred our endeavors to employ REDMaHD in refining the TBM design to diminish the flow rate discrepancies.

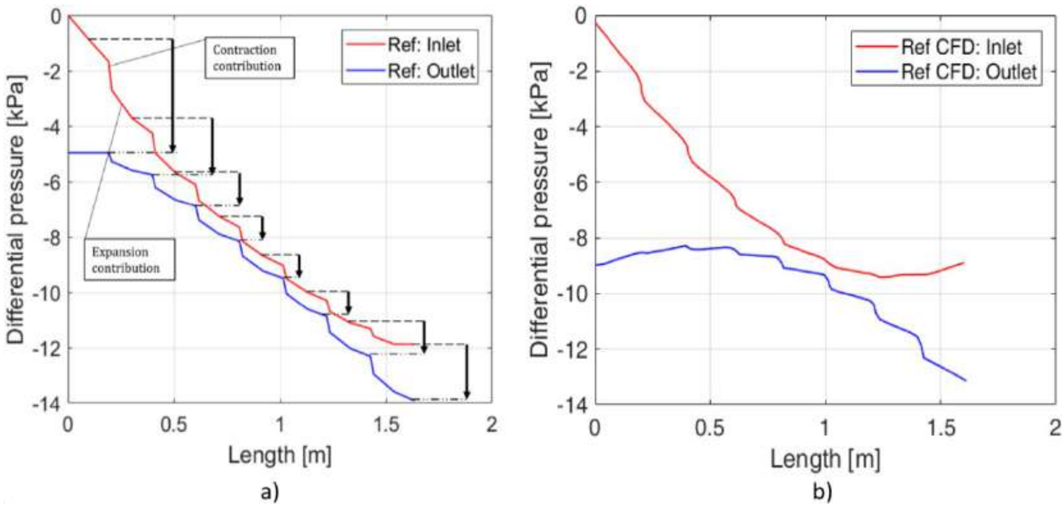

Figure 10.5: a) Pressure distribution in the manifold of the baseline geometry plotted against vertical elevation. The feeding manifold is represented in red, while the collecting one is depicted in blue. Additionally, the influence of contraction and expansion is emphasized. Black arrows pinpoint the pressure head allocated to each BU. b) Estimation of pressure distributions for the same architecture based on CFD analyses, data sourced from Ref. [24].

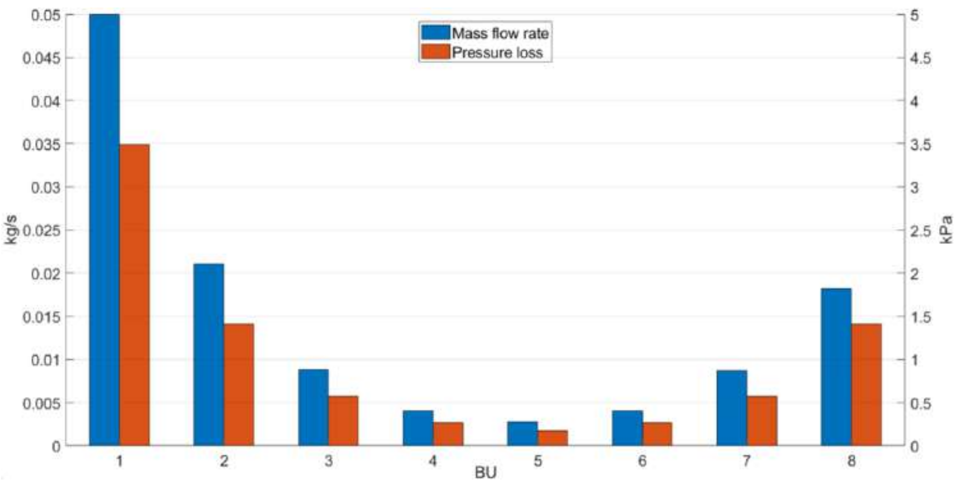

Figure 10.6: Bar chart illustrating the pressure drop and mass flow rate across each breeding unit in the baseline configuration.

Effect of WCLL TBM geometry on pressure loss and flow rate

To attain a consistent fluid distribution among the BUs and avert detrimental tritium inventory accumulation due to stagnant breeder, it is desirable to maintain an equalized pressure head across each BU. Neglecting the BU inter-coupling effects, such equilibrium would materialize only if both manifolds exhibit linear pressure variations with analogous gradients [24]. Given the prevailing manifold design, there are distinct cross-sections for the two ducts which persist unvaried throughout the module poloidal extent. As an outcome, the feeding manifold, with its diminished cross-section and elevated velocity, predominantly undergoes a steeper pressure reduction than its draining counterpart with a more expansive cross-section [24].

To achieve a more uniform mass flow distribution among the BUs, the TBM geometric design, both manifold and BU, can be tweaked following the proposals described in Figure 10.3. REDMaHD is employed to independently assess these geometric adjustments separately and when all combined.

Table 10.2 summarizes the principal outcomes regarding overall pressure reductions and mass flow rate distribution. These results for alternative designs are compared against the standard TBM geometry. Mod1 leads to a commendable decrease in total pressure losses, registering a cutback of 25%. On the contrary, Mod2 showcases a marginal surge in pressure drop, approximately by 3%. This upswing is attributed to its pronounced cross-section variation ratio (peaking at 50%). This intrinsic trait of Mod2 amplifies the 3D loss arising from cross-sectional enlargements and reductions along the poloidal manifold. Mod3, on the other hand, mirrors the tendencies of Mod1, as the alterations in its stiffening plate design counteract the augmented losses from cross-sectional changes that marked the behavior of Mod2. The diagrams in Figure 10.7 and Figure 10.8 delineate how manifold pressure drop patterns adjust with the geometric variations.

Delving into the flow distribution analysis, we observe only a marginal improvement in terms of mass flow rate distribution relative to the baseline design. The most promising flow distribution metrics are found for Mod3, yet, a pronounced flow disparity persists. While the updated manifold geometry reduces the global pressure drop, it falls short in delivering a homogenized flow distribution.

Given the challenges, an additional geometric alteration, Mod1b, is introduced

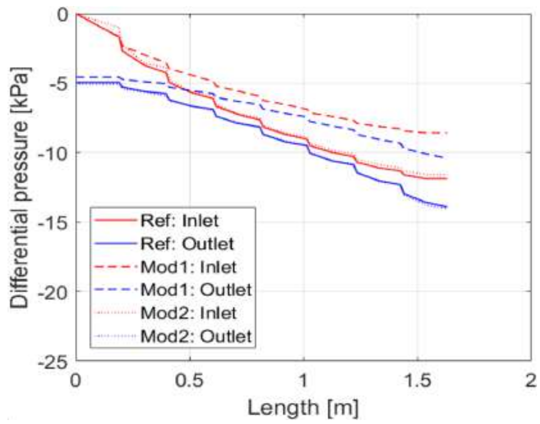

Figure 10.7: Pressure drop in feeding/draining manifold (red/blue) versus poloidal length of the module. The comparison is realized for three geometries: Reference geometry (full line), Mod1 (dashed line) and Mod2 (dotted line).

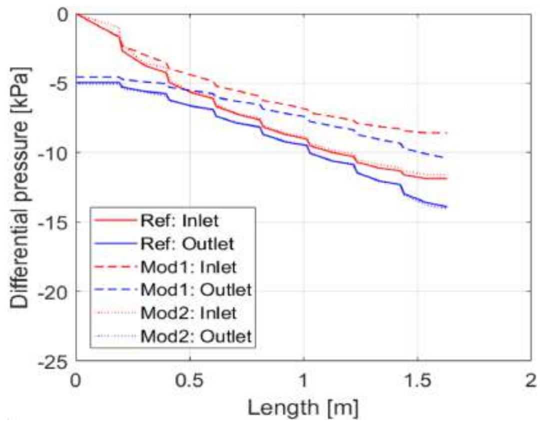

Figure 10.8: Pressure difference in the feeding/draining manifold (depicted in red/blue) against the poloidal extent of the module. This contrasts the Reference geometry (using a solid line) with Mod3 (represented by a dashed line).

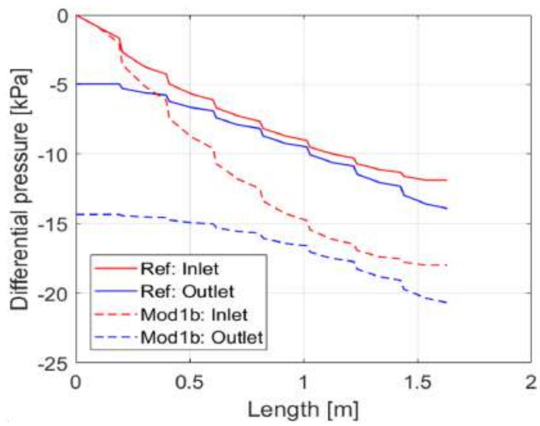

Figure 10.9: Pressure drop in feeding/draining manifold (red/blue) versus poloidal length of the module. The comparison is realized for two geometries: Reference geometry (full line), Mod1b (dashed line).

Table 10.2: Percentage of the total mass flow rate crossing each breeding unit (BU 18) for different configurations and total associated pressure drop.

Parameter	Unit	Reference design	Mod1	Mod2	Mod3	Mod1b	Mod3b
Total Δp	kPa	13.91	10.42	14.35	10.41	20.7	13.23
Flow rate BU1	%	42.517	38.455	35.708	26.270	11.90476	11.905
Flow rate BU2	%	17.942	18.712	20.271	19.294	12.15986	11.990
Flow rate BU3	%	7.483	9.099	10.008	13.092	12.07483	12.160
Flow rate BU4	%	3.401	4.893	4.919	8.785	11.81973	11.990
Flow rate BU5	%	2.381	3.519	3.477	6.891	12.32993	12.245
Flow rate BU6	%	3.401	4.292	4.835	7.063	12.32993	12.245
Flow rate BU7	%	7.398	7.554	8.227	8.527	12.67007	12.160
Flow rate BU8	%	15.476	13.476	12.55	10.077	12.5	11.905

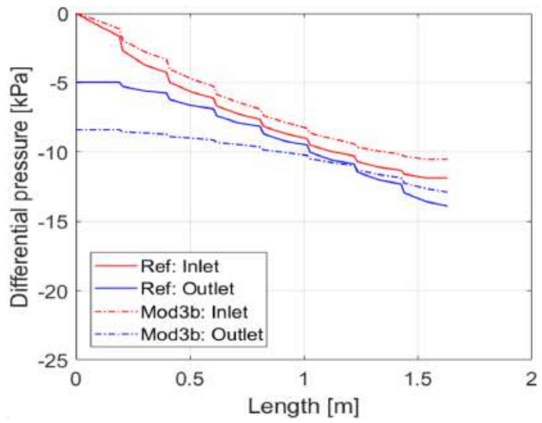

Figure 10.10: Pressure drop in feeding/draining manifold (red/blue) versus poloidal length of the module. The comparison is realized for two geometries: Reference geometry (full line), Mod3b (dashed line).

with a focus on the manifold/BZ junction. The foundational idea behind the Mod1b design is to set a target flow distribution, $\Gamma_t = \frac{\Gamma}{n} \approx 12\%$, where Γ represents half of the TBM flow, accounting for the symmetry in the flow paths, and $n = 8$ denotes the number of BUs per flow path. If the flow in a BU surpasses the target, i.e., $\Gamma_i > \Gamma_t$, the orifice is decreased, whereas it is enlarged if $\Gamma_i < \Gamma_t$. This iterative procedure continues until a uniform flow is achieved. Similarly, this strategy is imposed on Mod3, culminating in the design labeled Mod3b.

As anticipated, both Mod1b and Mod3b are characterized by improved outcomes concerning flow rate uniformity. Referring to Table 10.2, one can discern that these TBM designs elevate the overall pressure loss relative to Mod3. The pressure profile for these modifications is depicted in Figure 10.9 and Figure 10.10. Notably, Mod1b manifests almost twice the pressure loss when compared with Mod1, marking a pronounced increment even against the baseline design. In contrast, while Mod3b bears a higher loss than Mod3, its performance aligns closer with the benchmark setup, promoting near-uniform flow. Consequently, a TBM geometry revision predicated on Mod3b is recommended to improve the BU flow distribution.

A crucial point to emphasize is the inevitable impact of electromagnetic coupling on TBM flow distribution. Thus, even a Mod3b-based structure might not achieve absolute flow uniformity. As evidenced in the HCLL mock-up studies, an augmented flow rate in the terminal channels, namely BU1 and BU8 [29], [202], is observed. However, any inherent flow disparity, attributed to variable pressure heads among BUs, will accentuate the coupling effect, a phenomenon aggravated by flow rate differences. The geometry recommended in this study aims to circumvent any imbalances originating from foundational MHD losses and, at the very least, should be able to minimize the coupling effect in terms of added pressure loss and flow non-uniformity.

10.1.2 TBM liquid metal loop design

The objective of this study is to assess the influence of MHD pressure losses in the piping system of the WCLL TBM filled with lithium-lead, under varying conditions for mass flow rate (Γ) and magnetic field intensity (B). A comprehensive set of 50 simulations has been carried out, each featuring a unique pairing of Γ and $\mathbf{B}$.

The PbLi circuit that is anticipated to be significantly influenced by MHD phenomena is depicted in Figure 10.11. The REDMaHD model incorporates various components: the cold and hot legs of the pipe forest (PF), the shield pipes, and the box. The TBM box is the same as the one shown in Figure 10.1.

The RELAP5 model faithfully represents all the features of the circuit, including bends, contractions, and expansions. However, a simplification has been made concerning the PF: both channels have been modeled as straight paths, simplifying the nodalization. This is deemed acceptable given the relatively low magnetic field intensity in this region. Additionally, due to the extensive axial length of these channels, the 3D MHD pressure drops induced by the bends are negligible compared to the 2D MHD load losses.

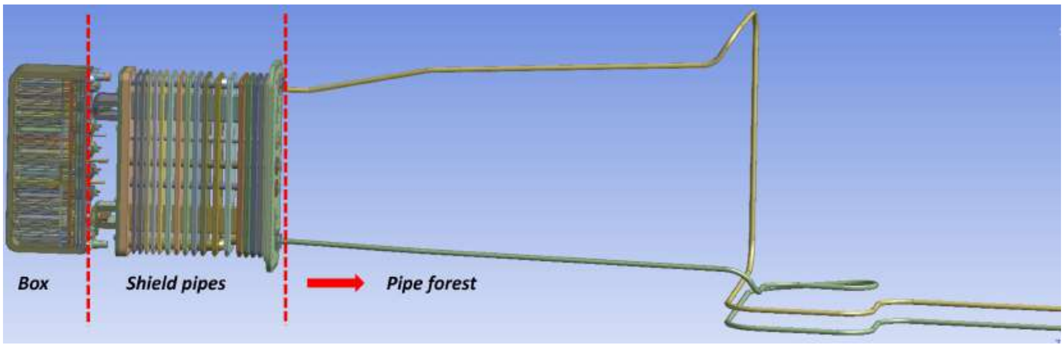

Figure 10.11: CAD view of the modelled WCLL-TBM PbLi circuit.

Geometric parameters and nodalization

The geometric parameters for the modeled system are extracted from the latest TBM design [30, 32] and additional information provided by Fusion for Energy. The same dimensions of the TBM box are already been gathered in Table 10.1, while Table 10.3 lists the dimensions of the circular pipes

Table 10.3: Geometrical parameters of the circular pipes.

Component	Internal diameter [mm]	Wall thickness [mm]	Axial length [m]
PF cold leg	26.64	3.38	17.024
PF hot leg	26.64	3.38	15.454
Shield pipes	62.7	5.16	1.71
TBM inlet/outlet pipe	46	4	0.154

The components of the shield pipes connect the interface of the shield and pipe forest to the TBM box, as illustrated in Figure 10.12a. The inlet and outlet channels within the box (Figure 10.12b) facilitate the connection between the shield ducts and the TBM manifolds. Regarding the nodalization strategy, a similar configuration as the one described in Section 10.1.1 has been adopted. The thermodynamic boundary conditions for the liquid metal, specifically temperature and pressure, are set by two time-dependent volumes (TMDPVOL #181 and #220 in Figure 10.13). A time-dependent junction (#182) prescribes the assumed mass flow rate within the circuit. The pipe forest channels (PIPE#649 and #603) comprise 31 individual volumes, while shield pipes #183 and #218 consist of 12 volumes. Pipe component #185 establishes the link between the shield duct and the inlet manifold. Each manifold is represented by a pipe component with 23 control volumes, mimicking the chambers and their interconnections within the manifold. Lateral junctions

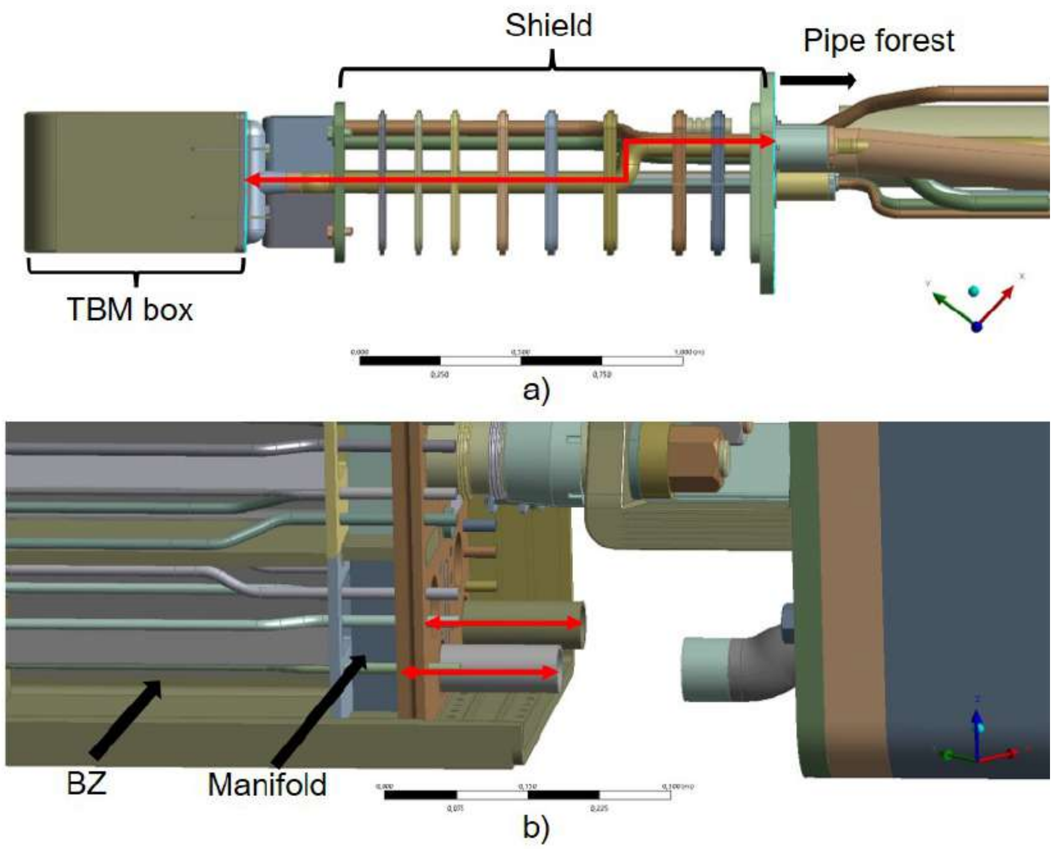

Figure 10.12: a) Shield pipe component considered in red. b) Bottom inlet pipes of the TBM box in red.

couple the breeding units to the associated volumes in the inlet and outlet plenums. Each BU is modeled using a pipe component of 11 CVs. The modeling approach for outlet manifolds mirrors that of the inlet, maintaining fidelity to actual geometrical properties. Finally, the PbLi exiting the TBM is collected in the outlet pipe (#199) and directed into TMDPVOL #220.

Boundary conditions and test matrix definition

The analysis operates under isothermal conditions, utilizing a reference temperature $T_{\text{ref}} = 580\,\text{K}$, which represents the average operational temperature of PbLi [203]. Consequently, the thermophysical characteristics of all materials are determined at T_{ref} [41] for PbLi and [197] for Eurofer-based solid structures, as outlined in Table 10.4. The circuit nominal mass flow rate of the liquid metal is set at $\Gamma = 0.65\,\text{kg/s}$ [203]. This value is approximately four times greater than that determined

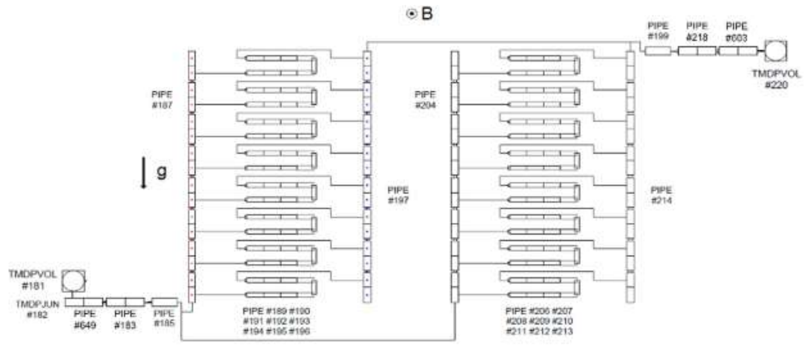

Figure 10.13: Scheme of the adopted nodalization. Pipes outside the TBM box are here sketched with few volumes for readability sake of the figure. **B** is the magnetic field vector and g stands for the gravitational acceleration.

Table 10.4: Thermophysical Properties of Materials

Material	Electrical Conductivity [S/m]	Density [kg/m^3]	Dynamic Viscosity [Pa^s]
PbLi	8.81×10^5	9830	1.22×10^{-3}
Eurofer	1.18×10^6	-	-

in [24]. The decision was motivated by the observed minimal pressure drops within the TBM box. Moreover, increasing the flow velocity is an effective strategy to reduce tritium permeation in the coolant.

The vertical (B_Z) and radial (B_X) magnetic field components are based on data from [26] and complemented by additional information for the pipe forest region from [27]. These magnetic field components are shown as a function of the radial coordinate in Figure 10.14. Average values of these magnetic field components are taken for various regions such as the TBM box, shield pipes external and internal to the toroidal field coil (TFC), and the initial part of the PF. Nonetheless, these values do not cover the entire extension of the pipe forest, planned to be situated in room 11-L1-C17 of the reactor building, as shown in Figure 10.15. For the outermost part of the PF, average magnetic field intensities are inferred from field maps in [27].

Two distinct methodologies are employed for determining the toroidal magnetic field component B_Y. The initial approach employs a refined discretization of data gleaned from [26], given that this component markedly exceeds the vertical and radial components. Conversely, the second methodology adopts a more conservative strategy, where B_Y solely depends on the radial coordinate, as elucidated by Equation (10.1). The defining parameters for this equation, $R_0 = 6.3\,\mathrm{m}$ and $B_0 = 5.3\,\mathrm{T}$,

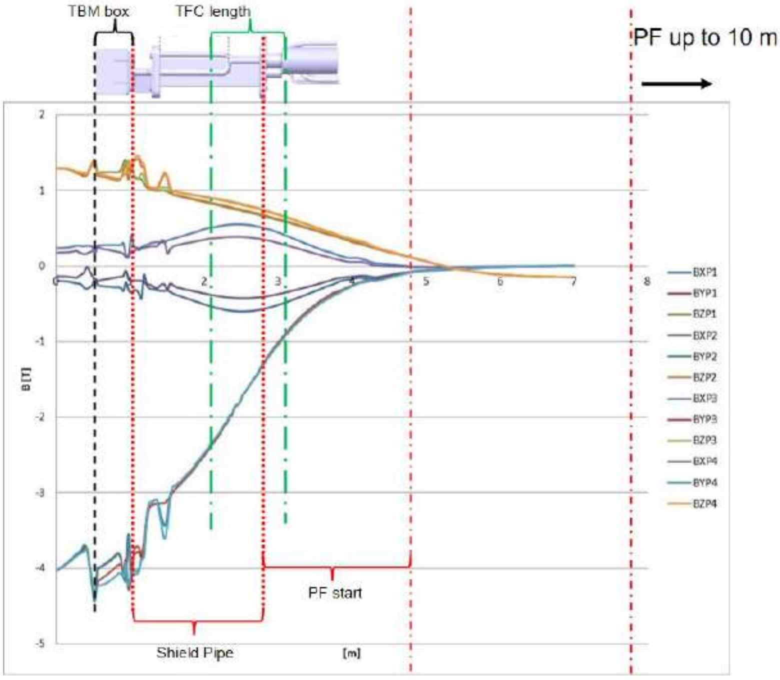

Figure 10.14: Magnetic field components data for different planes (P1, P2, P3, P4) vs radial coordinate [26]. The whole length of the PF in not covered.

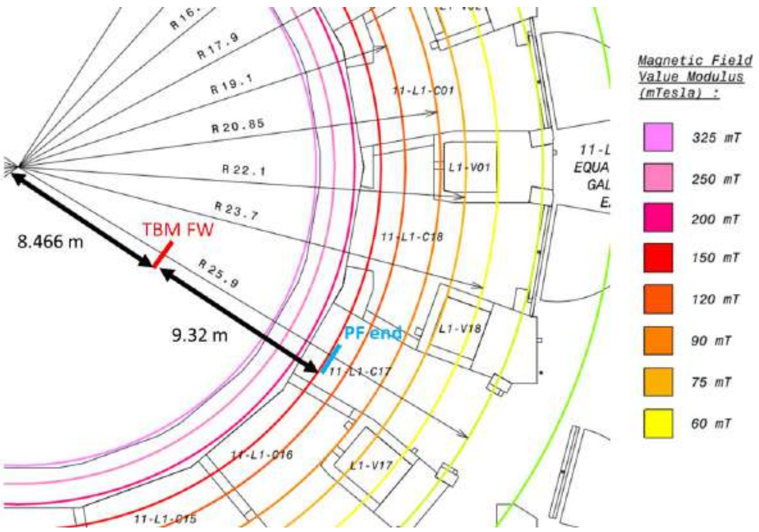

Figure 10.15: Magnetic field contour on the Level 1 of ITER [27]. The relative distance (from the reactor center) between TBM first wall and the final part of the PF are highlighted.

represent the coordinate of the torus chamber center-point and the magnetic field intensity at this position, respectively. Within the thickness of the TFC, the toroidal field is represented by a hyperbolic tangent function, as specified in Equation (10.2) [58]. The coefficients for this equation are $a = 0.4244$, $b = 352.8013$, $c = 33.049\,\mathrm{m}^{-1}$, and $B_{\mathrm{TFC}} = 3.273\,\mathrm{T}$, indicating the magnetic field intensity at the internal surface of the coil.

$$B_{\mathrm{tor}}(R) = \frac{B_0 R_0}{R} \tag{10.1}$$

$$B(R_{\mathrm{TFC}}) = \frac{B_{\mathrm{TFC}}}{2} \left\{1 - \tanh\left[a \cdot (c \cdot R - b)\right]\right\} \tag{10.2}$$

Both sets of calculations encompass 25 tests, each with variations in the operational mass flow rate (0.65 kg/s) and the nominal total magnetic field. The variations are described by the following ratios:

$$\Gamma_{\mathrm{ratio}} = \frac{\Gamma}{\Gamma_{\mathrm{ref}}} \rightarrow 0.5;\ 0.75;\ 1;\ 1.25;\ 1.5$$

$$B_{\mathrm{ratio}} = \frac{B}{B_{\mathrm{ref}}} \rightarrow 0.5;\ 0.75;\ 1;\ 1.25;\ 1.5$$

The governing reference parameters for each test, namely the Hartmann number (Ha) and the Reynolds number (Re), are calculated at the inlet channel of an individual BU, where the magnetic field reaches its peak intensity ($\approx 4\,\mathrm{T}$). The reference velocity of PbLi, $v_0 \approx 0.0046\,\mathrm{m/s}$, is determined under the assumption that the flow rate is uniformly distributed across the 16 BUs. Consequently, in operational conditions, $\mathrm{Ha} \approx 8.6 \times 10^3$ and $\mathrm{Re} \approx 2.5 \times 10^3$.

Outcomes

Figure 10.16 depicts the profile of the MHD pressure drop along the complete circuit under operational conditions ($\Gamma_{\mathrm{ratio}} = B_{\mathrm{ratio}} = 1$), where the liquid metal traverses the TBM box via the central breeding unit. Comparable profiles are observed for other breeding units as reference. An expanded view within Figure 10.16 illustrates the pressure loss solely in the TBM box. Under nominal conditions, the total MHD pressure loss amounts to approximately 208 kPa, whereas the pressure drop in the

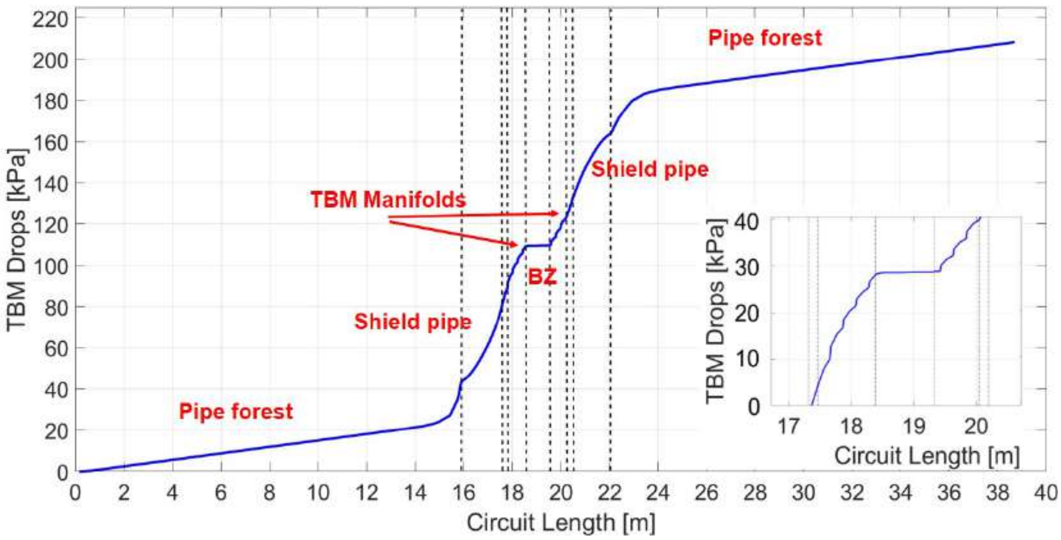

Figure 10.16: Cumulative MHD pressure drops in the TBM circuit in operational conditions versus the total axial length.

TBM box is 51 kPa. For the same mass flow rate, the total conventional hydrodynamic pressure drop (i.e., $B = 0$) is around 2.7 kPa.

The pressure loss in the pipe forest (PF) constitutes roughly 42% of the total, while about 33% can be attributed to the flow within the shield pipe. The remaining pressure losses ($\approx$ 24%) occur inside the TBM box. It is essential to emphasize that these proportions are consistent across all tests, independent of the varying parameters. Table 10.5 provides a breakdown of the pressure drop values for each hydraulic region, as illustrated in Figure 10.16.

Table 10.5: Tabulated pressure drop for TBM circuit from Figure 10.16 broken down by hydraulic regions.

Region	Δp (kPa)	%
PF - inlet	43.6	20.9%
Shield pipe - inlet	38.7	18.6%
TBM	39.9	19.2%
Shield pipe - outlet	41.8	20.1%
PF - outlet	44.2	21.2%
Total	208.25	100%

In Table 10.6, the total pressure drops calculated for all scenarios are collated. It is worth noting that the first MHD drop matrix utilizes magnetic field data from [26, 27], whereas the second MHD drop matrix employs the field Equations (10.1)

Table 10.6: Hydrodynamic and MHD losses (in kPa) as a function of Re and Ha.

Ha (B_{ratio})	Re (Γ_{ratio}) $1.23 \times 10^3(0.5)$	$1.85 \times 10^3(0.75)$	$2.47 \times 10^3(1)$	$3.08 \times 10^3(1.25)$	$3.70 \times 10^3(1.5)$
	Hydrodynamic drops (kPa)				
	0.9	1.7	2.7	3.9	5.3
	MHD Drops Matrix 1 (kPa)				
$4.31 \times 10^3(0.5)$	26.3	39.4	52.6	65.7	78.9
$6.46 \times 10^3(0.75)$	59.1	88.6	118.2	147.7	177.4
$8.57 \times 10^3(1)$	105.1	157.5	210.2	262.6	315.3
$1.08 \times 10^4(1.25)$	164.2	246.1	328.4	410.3	492.6
$1.29 \times 10^4(1.5)$	236.5	354.3	472.9	590.7	709.3
	MHD Drops Matrix 2 (kPa)				
$4.31 \times 10^3(0.5)$	27.1	40.7	54.2	67.8	81.3
$6.46 \times 10^3(0.75)$	61.1	91.7	122.1	152.8	183.2
$8.57 \times 10^3(1)$	108.6	163.0	217.2	271.6	325.7
$1.08 \times 10^4(1.25)$	169.7	254.8	339.3	424.4	508.9
$1.29 \times 10^4(1.5)$	244.3	366.8	488.6	611.1	732.8

and (10.2).

By normalizing the total calculated pressure losses with respect to a standard MHD pressure scale, a unique characteristic pressure coefficient for the circuit, denoted as ΔP_{TBM}, can be obtained (refer to Table 10.7). The coefficient can be understood as a K factor for the entire circuit, facilitating additional parametric studies under varying initial conditions. Importantly, ΔP_{TBM} remains invariant with respect to both the Hartmann number (Ha) and Reynolds number (Re). The discrepancy between ΔP_{TBM1} and ΔP_{TBM2} is solely attributable to variations in the magnetic field boundary conditions.

Table 10.7: Non-dimensional MHD loss coefficients as a function of Re and Ha.

Ha (B_{ratio})	Re (Γ_{ratio}) $1.23 \times 10^3(0.5)$	$1.85 \times 10^3(0.75)$	$2.47 \times 10^3(1)$	$3.08 \times 10^3(1.25)$	$3.70 \times 10^3(1.5)$
	Characteristic coeff. Matrix 1				
$4.31 \times 10^3(0.5)$	33.5	33.5	33.5	33.5	33.5
$6.46 \times 10^3(0.75)$	33.5	33.5	33.5	33.5	33.5
$8.57 \times 10^3(1)$	33.5	33.5	33.5	33.5	33.5
$1.08 \times 10^4(1.25)$	33.5	33.5	33.5	33.5	33.5
$1.29 \times 10^4(1.5)$	33.5	33.5	33.5	33.5	33.5
	Characteristic coeff. Matrix 2				
$4.31 \times 10^3(0.5)$	34.2	34.2	34.2	34.2	34.2
$6.46 \times 10^3(0.75)$	34.2	34.2	34.2	34.2	34.2
$8.57 \times 10^3(1)$	34.2	34.2	34.2	34.2	34.2
$1.08 \times 10^4(1.25)$	34.2	34.2	34.2	34.2	34.2
$1.29 \times 10^4(1.5)$	34.2	34.2	34.2	34.2	34.2

10.2 Support to the development of PbLi loop for WCLL DEMO

10.2.1 MHD pressure drops in the WCLL reference design

The overall MHD pressure losses in both the left IB and central OB circuits has been re-evaluated using REDMaHD, serving as an update to the prior assessment conducted in 2020 [58].

Overview of the WCLL Blanket

For an in-depth examination of the blanket geometry, see Section 2.6. Some information is reiterated here for clarity.

The WCLL blanket fully encircles the vacuum vessel and is partitioned into 16 individual sectors. Each sector spans a toroidal arc of approximately 22.5ř. These sectors are further segmented into inboard and outboard regions, comprising 2 and 3 modules respectively. A single unit within a segment is a monolithic module, often referred to as a "banana". A radial depth of ≈ 1 m is allocated for the blanket, and its weight is supported by the VV via the Back Supporting Structure.

Plasma containment is facilitated by low-temperature superconducting Nb_3Sn magnets, consisting of one Central Solenoid, 16 Toroidal Field Coils (TFC), and 6 Poloidal Field Coils (PFC) [54]. The PbLi system, illustrated in Figure 10.17, has two branches dedicated to either the IB or OB segment and is propelled by mechanical pumps. These pumps are preferred over electromagnetic or permanent magnet pumps due to their superior efficiency [54].

Each segment is autonomously connected by two elements: a feeding pipe and a draining pipe, which serve to circulate PbLi. As a result, only a limited segment of the loop is exposed to a significant magnetic field (> 0.1 T). It is in this region, referred to as the "in-magnet" PbLi loop, where MHD losses begin to significantly affect performance. Specifically, the loop section enclosed by the TFC, termed the "in-vessel" loop, is most susceptible to MHD effects.

Defining the exact boundaries of the in-magnet loop is intricate, owing to the far-reaching magnetic field generated by the PFC. In this study, it is assumed that the magnetic field becomes negligible in the domain defined by the radial and poloidal coordinates $\Delta R \geq 24$ m and $|\Delta Z| \leq 14$ m. This domain is further categorized into connection pipes (FP and DP) and the blanket, which itself is subdivided into three distinct hydraulic regions: terminal collector, spinal manifold, and breeding zone.

Inboard and outboard FPs are directed through the lower port of the VV, while DPs are positioned in the upper port. Despite similarities in FP layouts, the DP attachments differ: the IB DP connects at the segment top, and the OB DP is positioned at two-thirds of the blanket height, necessitating an additional spinal collector housed within the BSS. Intermediate manifolds manage the flow from the OB sector DPs to minimize clutter in the upper port.

The breeding zone adopts a modular geometry, segmented into elementary cells by toroidal-radial and radial-poloidal stiffening plates, as already discussed in Section 2.6. Within these cells, PbLi follows a quasi-radial flow path and is cooled by radial-toroidal-radial cooling pipes. The breeder velocity in this region approximates 0.2 mm/s for the OB and is even lower for the IB, thus its contribution to MHD losses is negligible [32]. The distribution and retrieval of PbLi are achieved via a spine-like manifold with alternating channels for both feeding and draining. This geometry differs from the assessment done in 2020 in Ref. [58], where the PbLi distribution and retrieval utilized a spine-like manifold made of two coaxial rectangular channels. Collectors at the segment ends link the manifold to the FP/DP (see Figure 10.18).

The most up-to-date baseline data is employed to accurately calculate the magnetic field intensity within the defined region of interest [204]. The magnetic field in the DEMO reactor consists of two primary components: toroidal and poloidal.

The the magnetic field is described by Equation (10.1) here rearranged for clarity sake:

$$\frac{B(R)}{B_0} = \frac{R_0}{R} \tag{10.3}$$

where this time $R_0 = 8.9316$ m and $B_0 = 4.8935$ T. This equation is strictly applicable within the region bounded by the internal surface of the TFC. Outside this boundary, the toroidal field effectively becomes zero. The TFC thickness also encompasses a fringing field region characterized by substantial field gradients. Within this region, field intensities typically vary from 3.35 to 5.20 T for the OB and 5.20 to 8.64 T for the IB. The poloidal magnetic field is a result of the cumulative effect of the six PFC. Though weaker in comparison to the toroidal field, the poloidal field has a notable impact on flows aligned toroidally in the terminal collectors and connection pipes ($0.5 \leq B_{pol} \leq 1.2$ T).

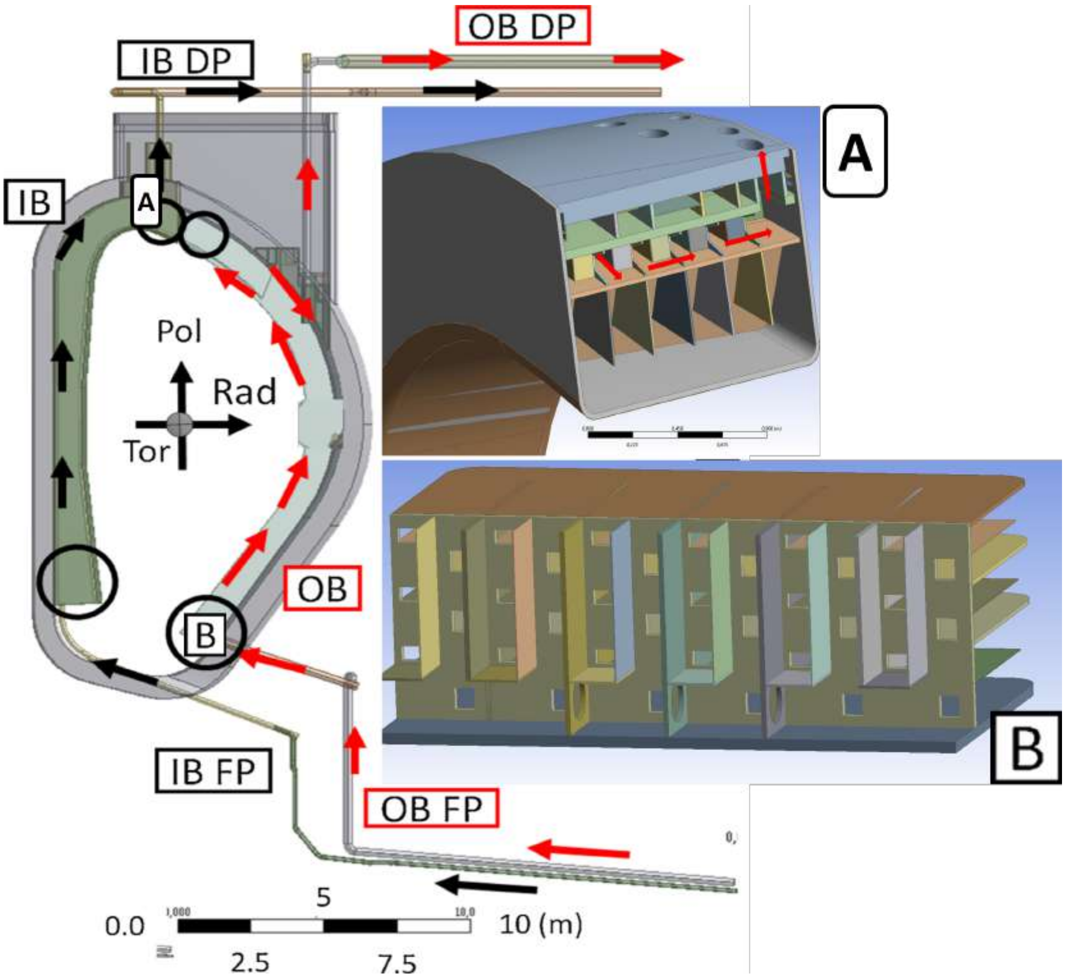

Figure 10.17: WCLL left IB/ central OB PbLi Fluid path: Arrows indicate the flow direction of PbLi in the IB and OB regions. Terminal collector locations are emphasized with circles. Detail A showcases the top collector area of the IB. Detail B illustrates the bottom collector/manifolds of OB. One can also notice the windowing of the back plate that serves as connection between the manifolds and BZ.

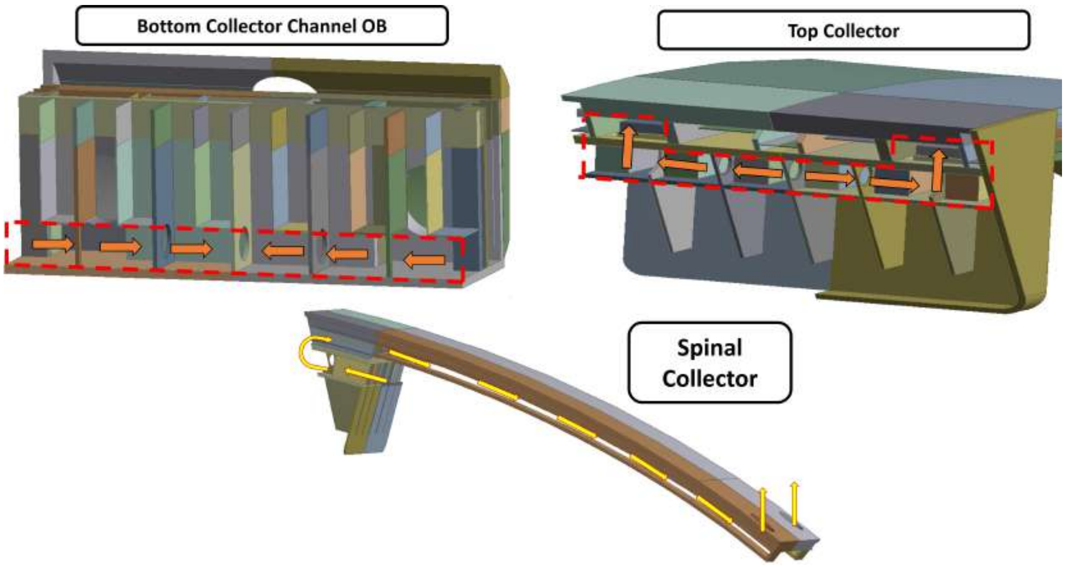

Figure 10.18: WCLL OB PbLi Fluid Dynamics: Arrows indicate the flow path of PbLi in the OB regions.

Outcomes

Both the IB and OB loop systems are nodalized using the slice technique to maintain uniformity in the mesh height and hydrostatic pressure definitions. An ad-hoc nodalization is employed to resolve the complex elements, such as the collectors (see e.g. Figure 10.20). A sketch of the nodalization scheme is depicted in Figure 10.19. The PbLi is modeled to flow isothermally at $T = 600\,\mathrm{K}$. For the IB and OB segments, the flow rates are specifically set as $\Gamma_{\mathrm{OB}} = 16.38\,\mathrm{kg/s}$ and $\Gamma_{\mathrm{IB}} = 5.34\,\mathrm{kg/s}$ [58].

The pressure profiles, from which the hydrostatic head component has been subtracted, are depicted for the central channel in the equatorial cell of the OB model in Figure 10.21. Detailed contributions by each hydraulic section for both IB and OB are elaborated in Table 10.8. The IB profile has qualitative similarities and it is not included here for the sake of brevity. The manifold-to-BZ connection is approximated as $1\,\mathrm{cm} \times 1\,\mathrm{cm}$ square windows (see e.g. Figure 10.17). The total pressure loss for both OB and IB aligns with previous estimates, ranging from 23.5 to 25.8 bar, thus corroborating the substantial contributions of the inlet and outlet pipes that link the BB and the Tritium Extraction Removal (TER) loop.

The flow distribution across the radial-poloidal cells is projected to be relatively

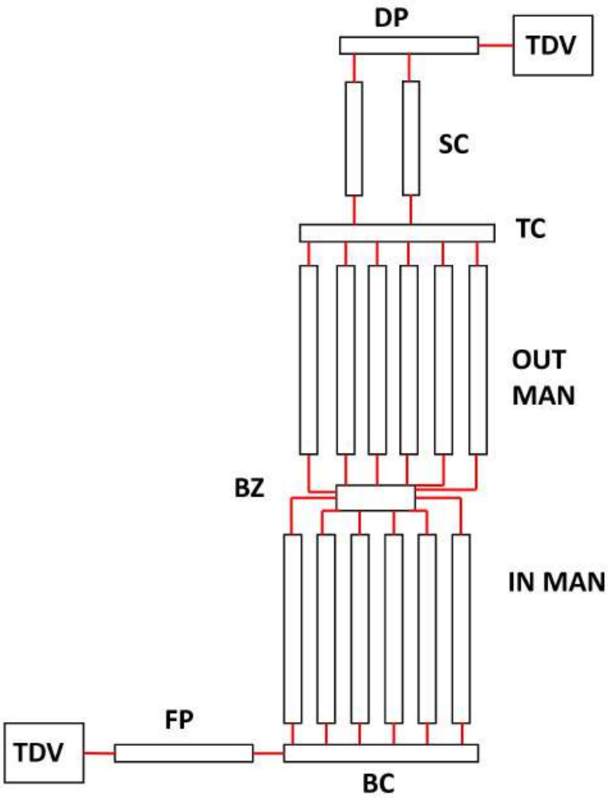

Figure 10.19: Nodalization Scheme of the WCLL COB Segment: For the purpose of conceptual elucidation, the total number of volumes constituting each component is intentionally omitted. The depicted dimensions of the components are symbolic and do not accurately represent the scales employed in the numerical simulation. It is noteworthy that the IB scheme is substantially analogous, albeit devoid of the Spinal Collector.

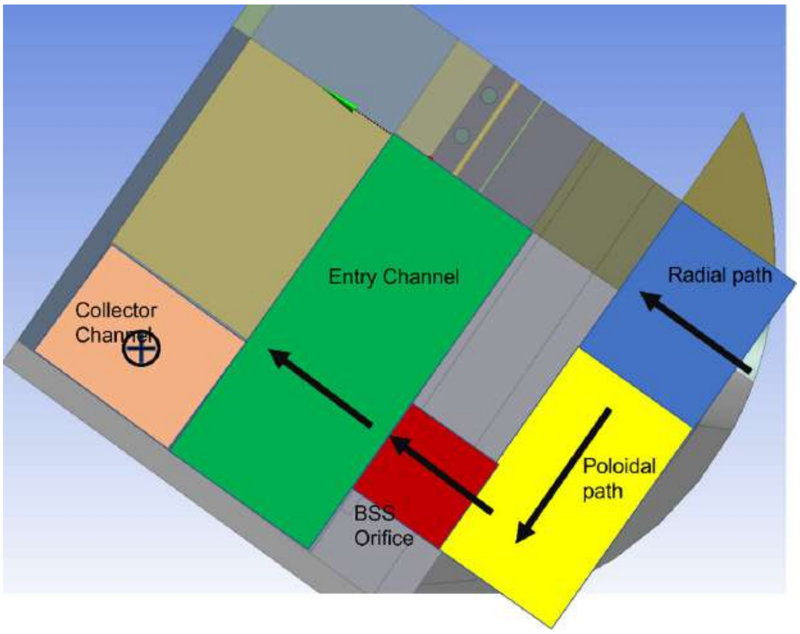

Figure 10.20: Poloidal-radial perspective of the bottom collector assembly of the central outboard segment. The colored sections highlight the divisions used for nodalization, while vectors indicate the primary flow direction.

uniform due to electromagnetic coupling effects, although some deviations may be present owing to the layout of the manifold. Figure 10.22 presents the differential pressure across OB BZ cells, showing qualitative consistency with Ref. [95]. Two distinct geometrical options for the BU/manifold square connection (see Figure 10.17 detail B), namely $1 \times 1\,\mathrm{cm}^2$ and $4 \times 4\,\mathrm{cm}^2$, are considered. While these dimensions have minimal influence on the total pressure drop, they significantly impact the flow rate distribution, as depicted in Figure 10.23 for the OB segment. The implications of these findings will be assessed in light of coupling effects in future analyses.

10.2.2 Estimate of MHD pressure loss in the WCLL-double bundle BB

The WCLL - double bundle (db) variant represents a novel configuration currently undergoing conceptual development. A detailed exposition of its geometric characteristics is essential given the limited coverage in the existing literature. Here, the left outboard segment (LOBS) is taken as a reference for the analysis. In this context, the results from the code have been benchmarked with those derived from an independent analytical assessment of the pressure losses in the module, as detailed

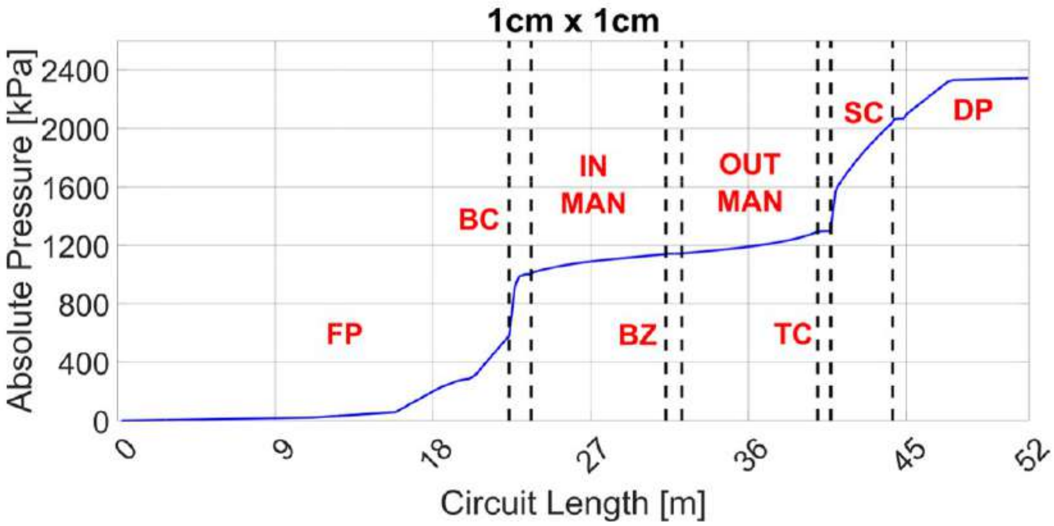

Figure 10.21: Pressure as a function of circuit linear length in OB loop. Hydraulic sections: feeding pipe (FP), bottom feeder assembly (BC), inlet manifold (IN MAN), breeding zone (BZ), outlet manifold (OUT MAN), top collector (TC), spinal collector (SC), outlet pipe (DP).

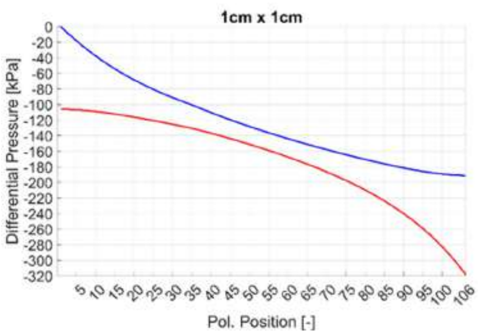

(a)

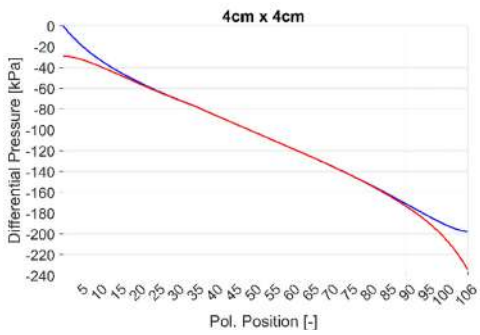

(b)

Figure 10.22: Differential pressure between OB inlet and outlet manifolds as function of the discretized poloidal position (i.e. BZ cell) for two different BU/manifold geometrical assumptions.

in [58].

In the WCLL-db BB, four main geometrical modifications are introduced that cause a significant deviation in the MHD flow pattern compared with baseline WCLL, thus requiring a detailed study to estimate the overall MHD pressure loss. These changes are schematically presented in Figure 10.24. These are:

1. Radial-toroidal SP are removed.

2. PbLi manifold (and collector) region is integrated with BZ.

Table 10.8: Pressure drop (measured in kPa) in OB and IB loop broken down by hydraulic section.

	OB		IB	
	This Study	Ref. [32]	This Study	Ref. [32]
FP	581	613	1499	1557
BC	422	122	84	92
IN MAN	136	68	275	328
BZ	5	n.a.	17	n.a.
OUT MAN	148	190	275	122
TC	30	55	5	76
SC	718	444	null	null
DP	303	429	428	260
TOT	2343	1921	2583	2435

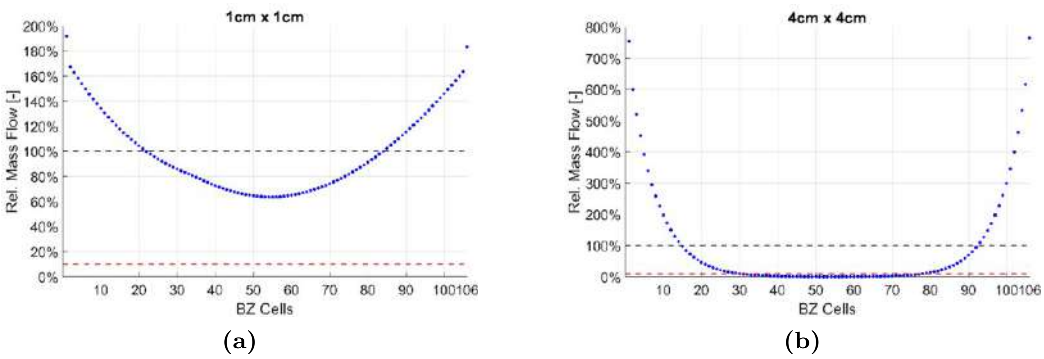

Figure 10.23: Mass flow distribution between BZ OB cells for two different BU/manifold geometrical assumptions. Dashed black line identifies the flow rate for uniform distribution ($\dot{m}_{BU}$ = 150 g/s) whereas the red dashed line the minimum flow rate considered to be acceptable by this analysis ($\dot{m}_{\min} = 0.1\dot{m}_{BU} = 15$ g/s).

3. BZ cooling system layout is changed from radial-toroidal, horizontal, C-shaped pipes to an assembly composed by two larger radial water feeders that supply the coolant to an array of poloidal, vertical, tubes.

4. An intermediate "third chamber" is introduced to reduce the probability of contact between PbLi and water.

The first two changes shift the PbLi flow from the radial-poloidal version adopted by the WCLL, in which poloidal manifolds at the back are tasked to supply and retrieve PbLi from a large number of elementary cells (where the flow is almost exclusively radially oriented), into a purely poloidal flow split into four channels. These changes result in a smaller available cross-section for the flow circulation

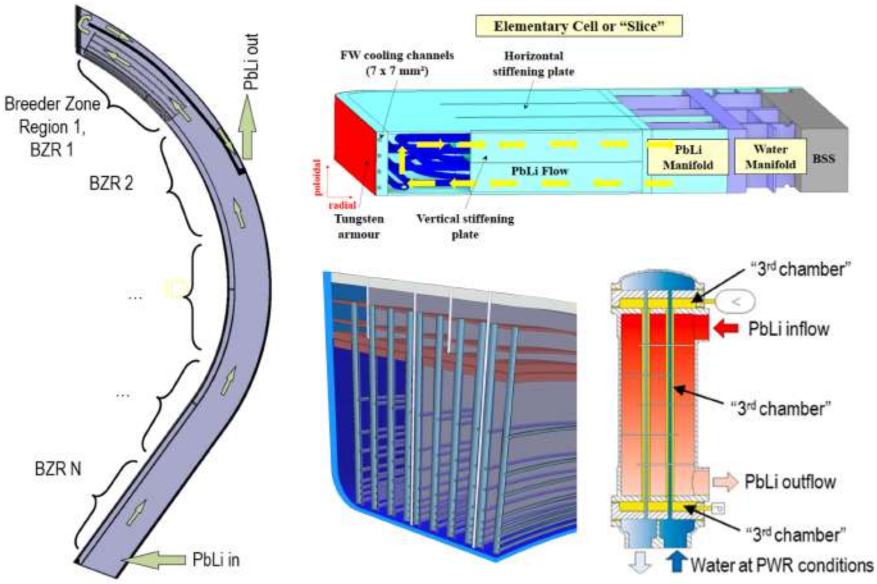

Figure 10.24: Left: PbLi hydraulic path in the WCLL-db, radial-poloidal cross-section. Right, top: WCLL elementary cell layout with PbLi flow highlighted by yellow arrows, radial-poloidal cross-section. Right, bottom: WCLL-db cooling system feeder and tube array, intermediate chamber concept.

in the BZ, which raises the mean velocity from ≈ 0.1 mm s^{-1} to ≈ 1 mm s^{-1}. Simultaneously, it simplifies the layout compared with the WCLL one by removing the distribution tank and entry channel in the BC assembly (two hydraulic elements rather onerous in terms of pressure loss) and dispensing altogether from additional (and quite narrow) poloidal manifolds.

To carry the PbLi back to the outlet pipe, placed roughly at 2/3 of the segment poloidal height, a return channel is used in both configurations. In the baseline WCLL, this region is composed of two narrow channels integrated in the BSS, whereas a larger cross-section is available for the same purpose in the WCLL-db thanks to the space gained by integrating the PbLi manifolds with the BZ.

The cooling system acts like a group of obstacles impeding the flow circulation and providing additional surfaces for current closure. From the point of view of the cooling system, WCLL-db BZ is split in five independent regions compared with >100 elementary cells of the WCLL BZ. Each BZ channel region is identified by feeder tubes (four at the top and four at the bottom), each one supplying water to eight tubes. Two interaction mechanisms are identified: feeders are transverse obstacles that introduce a concentrated pressure loss due to cross-section reduction, whereas cooling tubes interact just with the fully developed flow by altering the current pattern. These effects are also present in the WCLL and numerical simulations have demonstrated that they are negligible in terms of pressure drop. Nevertheless, it cannot be said that the same will hold true for the WCLL-db since, first, blockage ratio for transverse obstacles is very high (from $\beta \approx$50% to even 90% depending on poloidal position versus 22.5% in the WCLL) and likely causing a larger concentrated loss and, second, stream-wise obstacles are characterized by a similar blockage ratio ($\approx$ 2-3%) but provide more surface for current closure since they are more numerous (32 in the WCLL-db vs 4 to 6 in the WCLL).

From the MHD point of view, the introduction of the third chamber decreases c_w for some of the walls in electrical contact with PbLi: thin chamber wall that replaces the thicker and more electrically conductive FW, thinner cooling pipe wall.

It has been anticipated that these modifications will result in a lower overall pressure loss compared with the baseline WCLL since they simplify the flow path. Indeed, the WCLL-db configuration share similarities with WCLL layouts considered in a previous design iteration: WCLL2017.T02 (poloidal "once-through" flow) and WCLL2017.T03 (vertical pipes). MHD pressure loss has been found to be lower for both of these configurations compared with the current reference WCLL design (WCLL2017.T01.A, see [58] for more details).

Hydraulic path nodalization guidelines

PbLi flow path has been broken down in five regions to ease the calculation procedure, as shown in Figure 10.25. Bottom and top collector are located at the BB extremities. Cooling system is assumed to introduce no additional pressure loss in these regions. BZ is divided into three sub-regions of different radial depth: lower and equatorial BZ , upper BZ , and return channel.

The BC receives the flow rate incoming from the inlet pipe ($\dot{m}$ = 12 kg s^{-1}) and is tasked with distributing the breeder across the BZ channels, which are labeled depending on distance from the inlet attachment point: first lateral channel (CL1), first central channel (CC1), CC2, and CL2. Lateral channels (CL) in the BC are bounded by the back plate (BP), a SP and, on two sides, by the chamber wall, as shown in Figure 10.26. One of the chamber walls and the SP are perpendicular to the magnetic field and act as Hartmann walls. Central channels (CC) are electrically

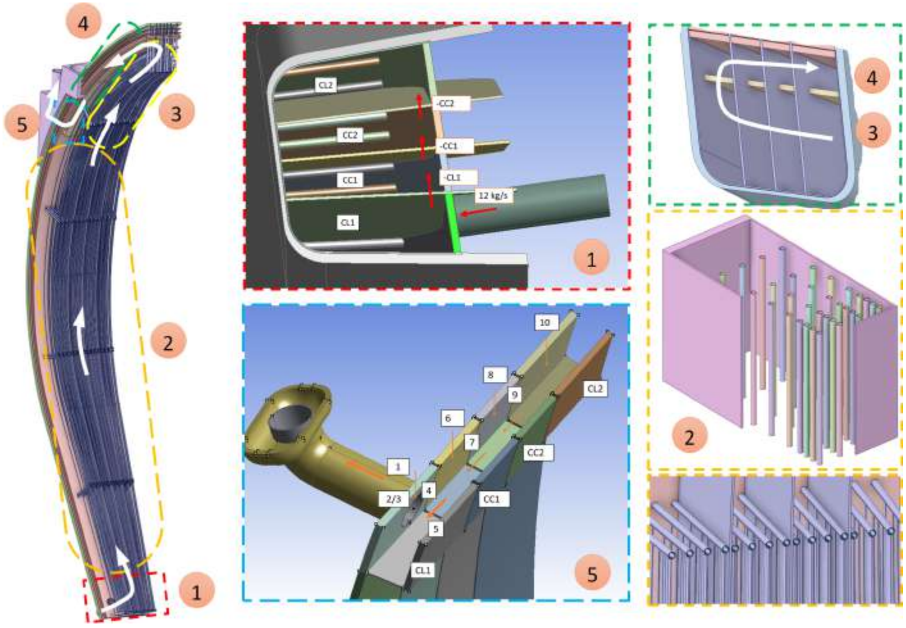

Figure 10.25: Left, PbLi flow hydraulic regions: bottom collector (BC - 1), lower and equatorial BZ (LE-BZ - 2), upper BZ (U-BZ - 3), return channel (RCH - 4), top collector (TC - 5). Center, detail of BC and TP. Right, detail of connection between U-BZ and RCH and of cooling pipes in the LE-BZ.

similar to CL but SP act as Hartmann wall on both sides. Note that SP are in electrical contact with two adjacent channels, hence they are going to host currents coming from both. This effect is taken into account by considering only half the wall thickness to calculate c_w. The same methodology is applied to the return plate (RP) that separates U-BZ and RCH.

The fluid enters the BC radially within CL1, where it undergoes a sudden expansion from the inlet pipe. Part of the flow is redirected poloidally and crosses into the next flow region, the LE-BZ, whereas the rest flows through an orifice drilled in the SP. Thus, PbLi is distributed among the other BZ channels. To reach CL2, PbLi has to undergo flow through a succession of three orifices.

Channel arrangement in Figure 10.26 is representative of that in the LE-BZ since the BC constitutes the initial section of this region. Progressing along the poloidal direction, toroidal width of the segment increases and, as a result, both $2a_{CC}$ and $2a_{CL}$ grow. Maximum width is reached on the equatorial plane, then the segment begins to shrink as we gradually move toward its top point. At $\approx 2/3$ of the poloidal height of the segment, a sudden radial contraction marks the transition between the

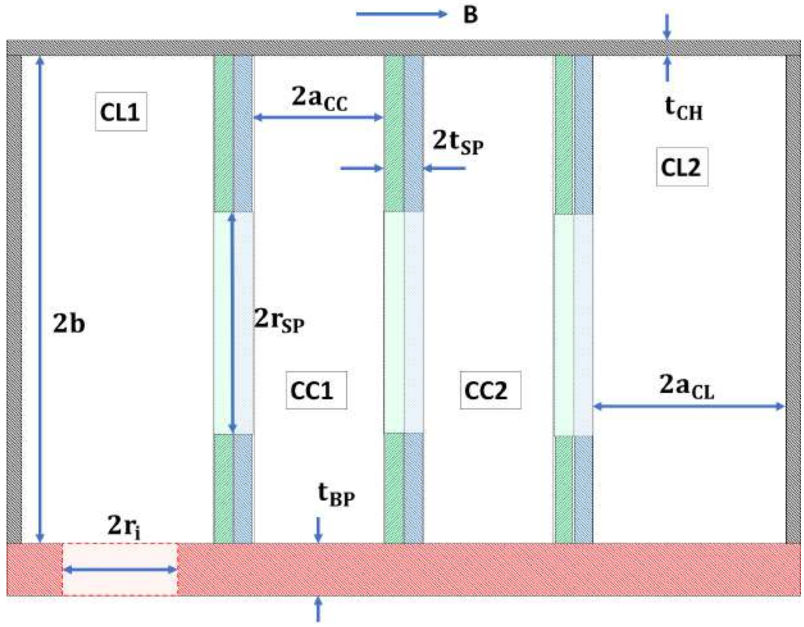

Figure 10.26: Toroidal-radial sketch of the LE-BZ channels close to the BC. Wall thickness not to scale. Please note that cooling system is not represented.

LE-BZ and U-BZ.

In Figure 10.27 is sketched the channel distribution in the U-BZ. Reduced radial depth is required to accommodate the RCH, which is separated from the U-BZ by the RP. Maximum toroidal width in this region is observed at the contraction point as it continues to decrease moving towards the top of the segment. Transition to the RCH occurs with a 180° turn. RCH PbLi flow moves downward rather than upward, therefore toroidal width will tend to increase with an equal but positive rate approaching the outlet pipe.

The RCH final section is reserved for the TC, which collects all the flow rate into CL1 before routing it toward the outlet pipe. Flow path can be described as the reverse of the BC one with fluid passing through orifices drilled in the SP to reach the outlet pipe. Due to the limited radial depth, TC orifices are assumed to be smaller than the BC ones.

In addition to the LOBS segment, inlet and outlet pipe are modeled as 2D flow elements to calculate the MHD pressure drop from the connection with the Tritium Extraction and Removal (TER) PbLi loop to the BB proper. These components cross the water manifolds and the BSS and are analogues of elements included in

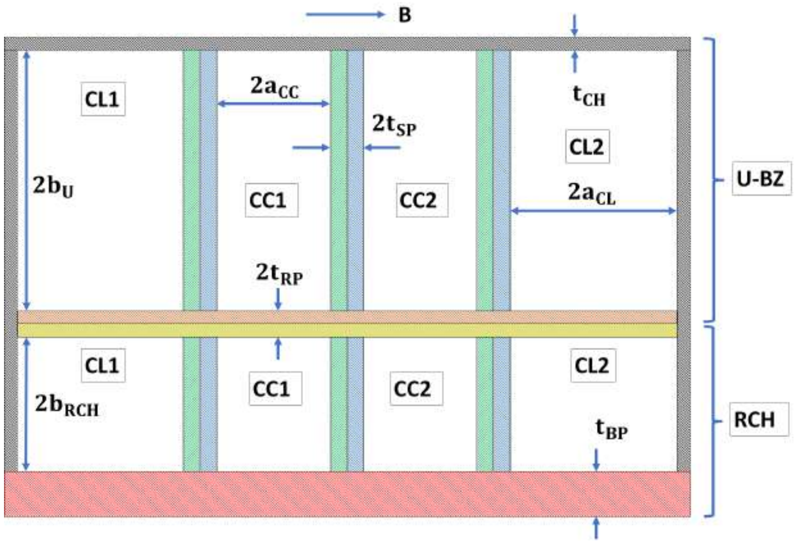

Figure 10.27: Toroidal-radial sketch of the U-BZ and RCH channels. Wall thickness not to scale. Please note that cooling system is not represented.

the BC and TC assembly in the WCLL baseline. These pressure loss are included in the BB estimate to properly compare the performance of the WCLL-db variant.

It should be noted that TER PbLi loop always constitute a significant fraction of the overall MHD pressure loss [32]. These are estimated assuming that TER PbLi loop layout is the same for WCLL-db and baseline, so that they can be obtained from the most recent baseline estimate, Ref. [33] at the time of writing, by scaling for the appropriate flow rate.

Numerical model

The input model for REDMaHD is constructed based on the discussions in Section 10.2.2. A concise diagram illustrating the nodalization approach can be found in Figure 10.28. Given that the WCLL-db geometry is designed to address the complexities of the WCLL-base layout, its nodalization is less intricate compared to the process detailed in Section 10.2.1. However, it still encompasses a total of 1026 control volumes and 1048 hydraulic junctions.

TDV, at the inlet and outlet of the circuit, serve to enforce the desired boundary conditions in terms of reference pressure and temperature. The TDJ between the entrance TDV and the feeding pipe (Pipe705) is needed to set the mass flow rate conditions. The Pipe707 and Pipe736 components are used to model the bottom

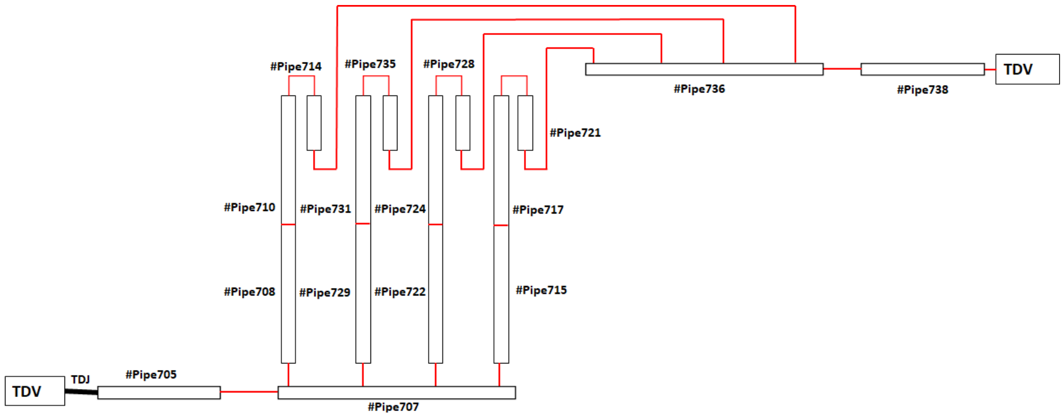

Figure 10.28: REDMaHD nodalization scheme of the WCLL-db LOBS. In red are highlighted the hydrodynamic junctions not included in the equivalent pipe components.

collector and the top collector, respectively. The lower equatorial breeding zone of the four different paths is simulated with Pipe708-729-722-715, whereas the top equatorial region with Pipe710-731-724-717. The return channels are modeled with components Pipe714-735-728-721. The draining duct of the system is Pipe738. In the REDMaHD model, the local vertical inclination of the segment has been kept as accurately as possible. The sliced modelling approach has been applied by assuming the same axial length for vertically oriented volumes at the same height. The actual inventory of the PbLi has been conserved, as well as the flow area for each section.

Results

The MHD pressure drop estimated for the WCLL-db BB variant is presented in Table 10.9. Pressure loss in inlet and outlet pipe are presented separately from the BB contribution, which is composed by the contributions from the five hydraulic regions detailed in Section 10.2.2.

Due to the imposed pressure head, $\dot{m}$ distributes unevenly across the four hydraulic paths, as it can be seen in Figure 10.29, thus BB results are presented into two columns in Table 10.9, one for CC and one for CL, which aggregates the data from the corresponding channel groups.

In order to validate the accuracy of the REDMaHD computed outcomes related to pressure losses in the segment, an analytical methodology was also employed to estimate the MHD losses, similar to the methods elaborated upon in Refs. [32, 58] for the WCLL-base layout. Additionally, efforts were made to semi-empirically assess

Table 10.9: MHD pressure drop in the WCLL-db LOBS. All data are reported in kPa (100 kPa = 1 bar). Bold lines mark the table sub-section related to pressure loss in the hydraulic regions located within the proper BB segment. †Flow rate in channel is averaged over the two paths. §Under others are classified all 3D pressure drop contributions in the BZ regions.

Region		Central channel† 2.25 $kg\,s^{-1}$	Lateral channel† 3.75 $kg\,s^{-1}$
Inlet pipe		35.666	
Bottom collector		25.565	22.985
Breeding zone	Lower-Eq.	5.982	6.106
	Upper	5.719	5.877
	Return ch.	12.314	9.214
	Others §	18.493	24.014
	Total BZ	42.440	45.090
Top collector		24.840	24.854
Total BB		92.845	92.930
Outlet pipe		23.484	
Total BB + pipes		152.037	

the impact of electrical coupling, aiming to gauge the discrepancies in the code results.

From Figure 10.29 it can be noticed that there is a slight difference in the mass flow rate distribution between the analytical calculations and the REDMaHD model, around 7%. This deviation is likely to be caused by the unavoidable differences in the discretization of complex geometry elements (collectors, obstacles, etc), that do not allow a perfectly matching outcomes for 3D pressure losses. Nevertheless, such a shortcoming does not impact significantly the circuit overall pressure loss, which is around 151.5 kPa for the RELAP5 model, in excellent accordance with the one found by the analytical analysis, i.e. 152 kPa. In Figure 10.30, the REDMaHD result is shown in terms of cumulative pressure drop versus the total length of a specified path within the segment.

It should be remembered that the estimate of the present study has two important limitations since it neglects both electromagnetic coupling and buoyancy forces. Concerning the effect of electromagnetic coupling, LE-BZ channels are expected to exchange currents through the Hartmann walls, i.e. the SP, which are shared from

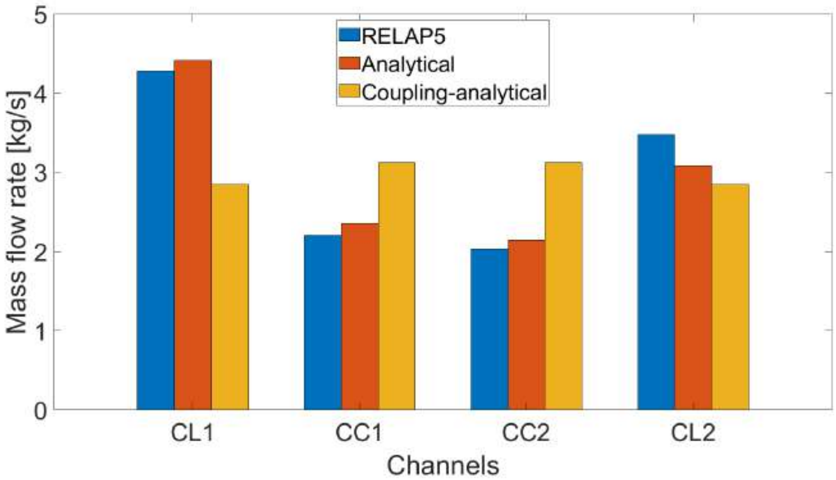

Figure 10.29: Mass flow rate in the different BZ flow paths.

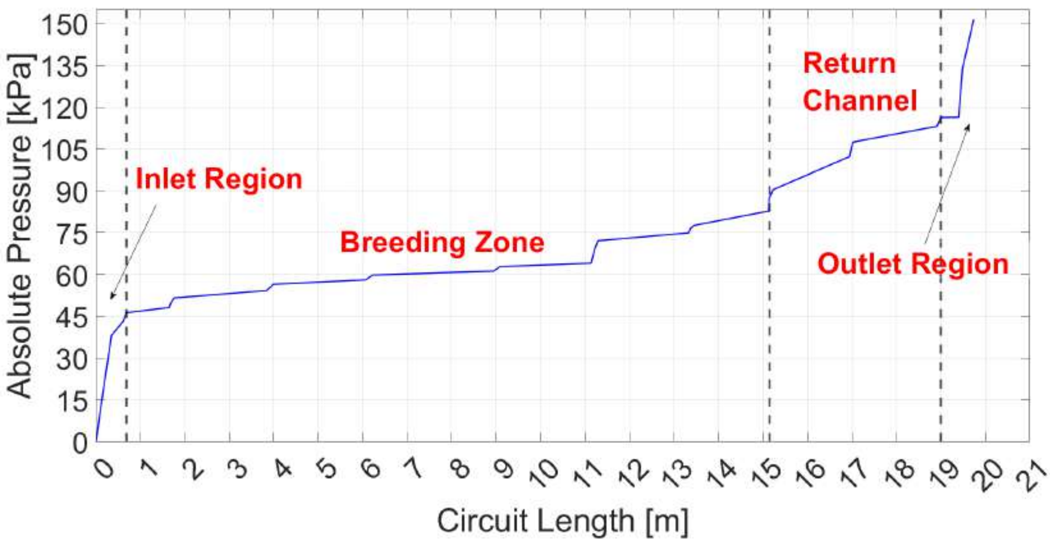

Figure 10.30: Total pressure drops along the whole circuit, considering the PbLi flowing in the BZ-CL1.

currents coming from the two adjacent channels [205]. By considering only half wall thickness in the computation of the k_p, one should expect to partially account for the effect on pressure loss due to coupling, at least for the simple case of an array of square channels under a constant pressure head. In this case, the coupling flow distribution should resemble the result presented in Figure 10.29 [94]. Given the more complicated arrangement foreseen in the WCLL-db though (variable toroidal width and larger cross-section for CL) and unforeseen effects at the collectors, this result may not be representative of the flow distribution in presence of coupling. What can be said for sure is that coupling will compensate part of the flow imbalance predicted by the current model. Moreover, U-BZ and RCH are also coupled through the shared side wall (return plate). This case generally leads to reduced pressure loss and, in particular, the higher mean velocity in RCH could contribute in effectively pumping the flow in the U-BZ [205].

A comparison with the pressure loss for the WCLL Central Outboard BB segment, discussed in the previous Section 10.2.1 (see also [33]), is presented in Table 10.10. Pressure losses in the WCLL-db segment are about 10% of those foreseen in the WCLL BB. Lower flow rate (≈ 73% of baseline) contributes to this reduction in the WCLL-db variant, but this can be regarded as a secondary contribution. To explain this result it is more significant the adoption of a straightforward poloidal flow in channels with large cross-section and bounded by the thin chamber wall and, perhaps even more so, a much simpler collector layout which minimizes large cross-section variation in the direction of the toroidal magnetic field. Pressure loss in the feeding and draining pipe (components of the PbLi loop subjected to a high magnetic field) are included in the comparison to provide a more system-level estimate. In this case, the same layout is assumed for the two BB concepts (neglecting the connection with BB pipes) and, therefore, the lower value in the WCLL-db is only due to the reduced mass flow rate. Looking at the whole PbLi loop, pressure loss in the WCLL-db is predicted to be approximately one-third of that in the baseline.

10.3 Summary

In this chapter, the main activities involving the use of REDMaHD to support the design and development of the WCLL BB and TBM are presented.

Table 10.10: Comparison of the MHD pressure drop in the WCLL-db and WCLL BB PbLi loop. All data are reported in kPa (100 kPa = 1 bar). The section of the PbLi loop considered is that subjected to a significant magnetic field [32]. Bold lines mark the table sub-section related to the proper BB segment, refer to [33] for WCLL BB hydraulic path. †Inlet and outlet pipe for the Wcll-db are included in the respective collector assemblies. ‡Includes poloidal inlet and outlet manifolds.

Region	WCLL-db	WCLL BB
Feeding pipe	425.6	581.0
Bottom collector†	61.24	421.0
Breeding Zone	42.44	288.0‡
Top collector†	48.32	748.0
Total BB	152.0	1457.0
Draining pipe	222.0	303.0
Total PbLi loop	799.6	2341.0

In the first activity, the baseline layout of the WCLL TBM box is investigated in terms of pressure losses and flow distribution. After, various geometric configurations are scrutinized to evaluate their impact. The configuration identified as most favorable, denoted as Mod3b, excels in achieving a balanced mass flow rate and minimizing pressure drops. In this specific arrangement, calibrated orifices are introduced at the interfaces between the manifolds and the BUs. Moreover, the structural plate separating the feeding and collecting manifolds is modified with a toroidal stepwise shift. This shift is designed to accommodate the variations in flow rates within these hydraulic components. Additionally, the apertures between manifold sections have been optimized to further enhance flow distribution and reduce pressure losses.

After that, under varying boundary conditions of total mass flow rate and magnetic field intensity, a total pressure drop of 2.13 bar was observed in the WCLL TBM PbLi piping system. A scaling parameter ΔP_{TBM}, independent of magnetic field (B) and mass flow rate (Γ), was also derived, offering a useful tool for future studies on MHD pressure drops.

An updated assessment of the overall MHD pressure drop in both the IB and OB loops was conducted using REDMaHD, updating the 2020 estimates. The pressure drops span from 23.5 bar in the OB loop to over 28 bar in the IB loop. The impact of the BU/manifold connection geometry on flow distribution was also examined.

Despite the manifold layout inducing significant flow imbalance, it can be partially mitigated by a sufficiently small BU/manifold connection. A size of $1\times1\,\mathrm{cm}^2$ appears adequate for achieving a reasonably uniform breeder distribution.

At last, the analysis of MHD pressure drop for the WCLL-db BB variant was conducted using both REDMaHD and analytical methods. The mass flow rate was found to be unevenly distributed across different hydraulic paths. Despite minor discrepancies, about 7%, between the analytical and REDMaHD models, the overall pressure loss was consistent at around 152 kPa. The study also revealed that the pressure loss in the WCLL-db variant is approximately 10% of that in the baseline WCLL BB, primarily attributed to design simplifications.

Chapter 11

Enhancement of water two-phases models

This chapter discusses some additional enhancements to water two-phase models that are included in REDMaHD. Although these modifications are not exclusively related to blanket technology, they hold significance within the broader context of nuclear reactors power removal systems, encompassing both fission and fusion. Specifically, the heat transfer models of RELAP5 have been refined to more accurately represent two distinct heat exchange regimes:for water nucleate boiling and film condensation. An abridged overview is provided of the current knowledge regarding these phenomena to substantiate the choice of the closure laws to be integrated into REDMaHD. For a more comprehensive discussion of the state of the art and of the validation procedure, the interested reader is referred to Refs. [136, 137].

Historically, the limitations of system thermal- hydraulic codes in accurately modeling heat transfer in in-pool passive power removal systems have been highlighted through various studies. Investigations involving the PERSEO facility have examined the predictive capacities of commonly utilized BE codes like RELAP5, TRACE, and CATHARE. An extension of these works has been conducted under the OECD/NEA/CSNI/WGAMA initiative on "Thermal-hydraulics of passive safety systems in water-cooled reactors". The recurrent issue across these studies was a notable underestimation of heat transfer in systems inclusive of an in-pool heat exchanger. The deficiency was attributed to inadequacies in Heat Transfer Coefficient (HTC) calculations, spurred by the use of unsuitable correlations for the operational conditions of passive systems [136, 137].

In contemporary practice, the prevailing methodology involves optimizing heat transfer assessments by calibrating HTC using multiplicative factors. Despite the adequacy of this approach in generating satisfactory results, it introduces uncertainties that hinder its applicability in BE calculations. Various research groups have proposed different solutions to this problem, further underscoring its complexity [206, 207].

The original version of RELAP5 lacked a specialized boundary condition for pool boiling and relied on the Forster and Zuber correlation [208], as utilized in Chen HTC formulation [209]. The modified version incorporates a new boundary condition, replacing the Chen equation with a more appropriate pool boiling correlation by Cooper [210]. This newly implemented correlation considers various operational parameters such as surface roughness, pressure, and fluid properties.

For film condensation in vertical tubes, the original code utilized the maximum of the Nusselt and Shah values for HTC computation. In the modified version, this set of correlations has been enhanced to include more appropriate equations for laminar wavy condensation [211] and an updated Shah correlation [212]. The goal of these changes is to broaden the code applicability to scenarios involving low flow rates and high operational pressures.

The V&V process for the modified code included single-effect validation through basic test cases and integral effect analysis supported by PERSEO facility data [136, 137]. The modified version demonstrated a significant reduction in the Root Mean Square Relative Error (RMSRE) of wall superheat and wall temperature, as verified through experimental campaigns by Sateesh et al. and Kuhn et al. [213, 214].

11.1 State of the Art and Modifications

This section reviews key configurations in in-pool passive heat exchangers, specifically focusing on nucleate pool boiling in vertical tubes. It also discusses the original correlations in RELAP5 and the improvements.

11.1.1 Nucleate Pool Boiling on Vertical Tubes

Nucleate boiling is a crucial mechanism in passive heat removal systems for advanced nuclear power plants. While horizontal geometries are well-studied, vertical tubes present unique heat transfer characteristics [215, 216].

Kang found that increased tube length results in diminished heat transfer rates due to larger vapor slugs, especially when the non-dimensional length (length-to-diameter ratio) exceeds 50 [217]. Surface roughness is also a significant factor; higher roughness increases nucleation site density and thus enhances heat transfer [218].

Chun and Kang demonstrated heat transfer deterioration at higher heat flux levels (> 50 kW/m^2), more so for vertical tubes due to uniform bubble coalescence [219]. Sateesh et al. reported minimal inclination effects but highlighted temperature variations along the tube length [213].

Contrary findings by Gupta et al. indicate that HTC increases with vertical length at lower heat flux levels, partially contradicting earlier work by Kang when heat flux exceeds 50 kW/m^2 [220].

11.1.2 Film Condensation in Vertical Tubes

Film condensation within vertical tubes is another vital phenomenon for the safety mechanisms in advanced NPPs.

The literature on high-pressure steam condensation in large diameter tubes is sparse. Kim and No studied this, collecting 984 data points over a pressure range of $0.35 - 7.2$ MPa [221]. Their findings indicate that heat flux increases with pressure while HTC remains constant within $4000 - 7000$ W/m^{2}K [221].

Kuhn et al. conducted experiments at low pressures $(0.1 - 0.5MPa)$ [214], providing valuable insights into steam condensation relevant for both low and high-pressure systems. Their test setup included 42 runs and examined steam flow rates between $30 - 60kg/h$. Though focusing on low pressures, their findings are applicable across a broad pressure range.

11.1.3 Default pool boiling HTC

In the default RELAP5 workflow, a specific boundary condition for nucleate pool boiling cannot be enforced, instead the Chen correlation for the forced two-phase flow boiling HTC is employed. The formula is given by:

$$h_{tp} = S \cdot h_{\text{nb}} + F \cdot h_{\text{sp,f}} \tag{11.1}$$

S is the suppression factor of nucleate boiling, and F is the two-phase correction factor for single-phase forced convection. In this equation, h_{nb} is calculated using the Forster and Zuber correlation for pool boiling [208]:

$$h_{nb} = 0.00122 \left(\frac{\lambda_f^{0.79} c_{p,f}^{0.45} \rho_f^{0.49}}{\sigma^{0.5} \mu_f^{0.29} h_{fg}^{0.24} \rho_g^{0.24}} \right) \Delta T_{sat}^{0.24} \Delta p_{sat}^{0.75} \tag{11.2}$$

Here, the subscript f represents the saturated liquid or liquid phase, while the subscript g denotes the saturated vapor or vapor/gas phase, whereas where h_{fg} is the enthalpy of vaporization. ΔT_{sat} is the difference between wall and saturation temperature, and Δp_{sat} is the difference between saturated pressure at the wall temperature and the operative pressure. The Greek symbol λ is the thermal conductivity The single-phase forced convection $h_{\text{sp,f}}$ is determined by the Dittus and Boelter equation for single-phase liquid (sp,f) [222]:

$$h_{\text{sp,f}} = 0.023 \, \text{Re}_{\text{f}}^{0.8} \, \text{Pr}_{\text{f}}^{0.4} \, \frac{\lambda_{\text{l}}}{D_{\text{H}}} \tag{11.3}$$

Re_{f} and Pr_{f} are the Reynolds and Prandtl numbers for the fluid phase, respectively.

Limitations and Proposed Solutions

The existing correlations implemented in RELAP5 have limitations. For instance, the Forster and Zuber correlation, derived analytically, has limited applicability as it neglects surface effects [216]. Alternative correlations have been proposed that either require specific experimental data [223] or are more universally applicable [210, 224, 225].

Therefore an improved correlation specifically designed for pool boiling heat transfer have been developed and implemented for RELAP5. This is achieved by replacing the conventional Chen formulation with a new correlation stemming from Cooper work [210]. The reasoning behind this choice is substantiated through a single-effect validation process and is further discussed in [137]. The enhanced heat transfer coefficient is expressed as:

$$h = 55 \left(p_r^{0.12-0.2\log_{10} R_{p,\text{old}}}\right) - (\log_{10} p_r)^{-0.55} M^{-0.5} q''^{0.67} \tag{11.4}$$

In Equation (11.4), p_r denotes the reduced pressure, M signifies the molecular weight, and q'' stands for the heat flux. The term $R_{p,\text{old}}$ specifies the surface roughness in micrometers, conforming to the DIN 4762/1:1960 standard. Cooper adaptation simplifies prior models by incorporating reduced properties while maintaining a reasonable level of accuracy. The roughness effect is predominantly influential at lower pressures, as also observed by Nishikawa et al. in [226].

11.1.4 Default film condensation HTC

For film condensation heat transfer, the default model in RELAP5 calculates the heat transfer coefficient as the greater of the values obtained from Nusselt [227] and Shah [228] correlations. Nusselt theoretical framework is:

$$h_{\text{Nu,z}} = \frac{\lambda_f}{\delta z} \tag{11.5}$$

The corresponding film thickness δz is formulated as:

$$\delta z = 0.9086 \left(\frac{\mu_f^2 \, \text{Re}'_f}{g\rho_f \left(\rho_f - \rho_g\right)} \right)^{\frac{1}{3}} \tag{11.6}$$

In this context, g represents the acceleration due to gravity and Re'_f denotes the condensate Reynolds number for unit width of the surface.

When referring to the Shah formulation the correlation is expressed as:

$$h_{\text{Shah,1979}} = h_{sp} \left(1 + \frac{3.8}{Z^{0.95}}\right) \tag{11.7}$$

Here, h_{sp} is the HTC when only the liquid phase flows within the tube and is given by:

$$h_{sp} = h_{sp,l}(1-x)^{0.8} \tag{11.8}$$

Where x is the flow quality. Additionally, Z is the Shah correlating parameter, which is defined as:

$$Z = \left(\frac{1}{x} - 1\right)^{0.8} p_r^{0.4} \tag{11.9}$$

Another model, proposed by Vierow and Schrock in 1991 [229], has been previously analyzed by Kuhn et al. and subsequently integrated into RELAP5-3D as an alternative option [214]. This latter model introduces two correction factors toEquation (11.5). An enhancement factor accounts for the shearing effects of the steam/gas phase on the liquid film, while a suppression factor addresses the influence of non-condensable gases. Narcisi et al. in [136] evaluated the efficacy of this model in simulating passive safety systems by comparing RELAP5-3D simulations with PERSEO experimental results. Although this optional model mitigates the discrepancies between experimental and simulated outcomes, it does not sufficiently improve the estimate of heat transfer [136, 137].

Limitations and Proposed Solutions

The limitations of the RELAP5 code in simulating film condensation under specific conditions have been extensively addressed. Bersano et al., in [207], highlighted concerns about the suitability of Equation (11.7) for modeling passive safety systems with large tube diameters. In such systems, where the steam velocity is approximately 2 m/s, the Nusselt HTC in Equation (11.5) supersedes the Shah formulation in Equation (11.7), leading to inaccuracies in heat transfer predictions. Shah, in [230], had previously suggested using Equation (11.7) only for steam velocities above 3 m/s. Additionally, Papini and Cammi reported the equation poor performance in high-pressure systems [231].

Shah later revisited Equation (11.7) in 2009 [212], optimizing the correlation to extend its applicability to lower flow rates and broader reduced pressure ranges. The updated equation is as follows:

$$h_{\text{Shah,2009}} = h_{sp}\left(1 + 3.8/Z^{0.95}\right)\left(\frac{\mu_f}{14\mu_g}\right)^{0.0058+0.557p_r} \tag{11.10}$$

This version incorporates a viscosity ratio factor to address discrepancies at higher reduced pressures. Shah also identified three heat transfer regimes for vertical tubes: laminar, turbulent, and transition . Shah suggested using a modified version of Equation (11.5) for the laminar regime, while the turbulent regime could be described using Equation (11.10).

For the transitional regime, Shah proposed a hybrid approach that combines the McAdams equation [232] with Equation (11.10). The boundaries between these regimes are established through dimensionless parameters such as the Shah correlating parameter Z and the dimensionless vapor volumetric flux J_g, which is defined as

$$J_g = \frac{\psi G}{\sqrt{gD\rho_g(\rho_f - \rho_g)}} \tag{11.11}$$

Where G the total mass flux. The conditions for the laminar and turbulent regimes are then given by Equation (11.12) and Equation (11.13), respectively.

$$J_g \leq 0.89 \times 0.93 \exp(-0.087Z^{1.17}) \tag{11.12}$$

$$J_g \geq \frac{1}{2.4Z + 0.73} \tag{11.13}$$

This approach shows good agreement with experimental data across a wide range of reduced pressures and steam flow rates. Recently, Shah further revised Equation (11.10), in [233], to redefine the boundary conditions for horizontal tubes, while a subsequent modification was made in [234] to evaluate the heat transfer coefficient in mini and microchannels. However, these updates do not influence the performance of the equation for standard vertical tubes [137].

In light of Shah revisions, the default correlation set used in RELAP5 has been reevaluated. Equation (11.7) proposed by Shah in [228] has been supplanted by Equation (11.10) for the turbulent regime. For the laminar regime, Equation (11.5) remains unchanged. An explanation is required: the 20% enhancement in the Nusselt HTC for laminar flow, posited by McAdams [235], could be attributed to wave formations in the liquid film as pointed out by Guichet & Jouhara [236]. Such disturbances induce a turbulent-like flow and also reduce the mean film thickness, leading to enhanced heat transfer [237]. This phenomenon is significant for $Re'_f > 30$ [236, 238].

To properly simulate the phenomena occurring in this so-called wavy laminar condensation, Kutateladze introduced an alternative correlation in place to Equation (11.5), formulated as [211]:

$$h_{\text{Kutateladze},z} = 0.69 Re'^{0.11}_f \times h_{\text{Nu},z} \tag{11.14}$$

Equation (11.14) is incorporated into the REDMaHD updated set for pure steam film condensation. The HTC is computed by taking the maximum value among Equation (11.5), Equation (11.10), and Equation (11.14). This methodology aligns with RELAP5 standard practice of ensuring a seamless transition between different correlations (see [229]). Moreover, this approach aptly captures the transition from laminar to wavy laminar regimes, particularly since the results from Equation (11.14) surpass those from Equation (11.5) for $Re'_f > 30$.

11.2 Summary

This chapter addresses the limitations of established thermal-hydraulic codes such as RELAP5, TRACE, and CATHARE in accurately simulating heat transfer mechanisms in passive power removal systems. A recurrent issue identified across multiple studies is the significant underestimation of heat transfer, largely attributed to inappropriate heat transfer coefficient correlations. The prevalent remedy is to adjust the HTC using calibrated multiplicative factors, a practice that falls short of being ideal for best-estimate simulations.

To address these shortcomings, an enhancement of the two-phase flow REDMaHD model has been proposed. These modifications target two crucial heat transfer mechanisms: nucleate boiling (in pool) and film condensation (in vertical pipes). In the original version of the code, there is an absence of a specialized boundary condition for pool boiling, and the calculation for nucleate boiling is grounded on the Forster and Zuber correlation (Equation (11.2)), as incorporated into Chen HTC Equation (11.1). However, in the enhanced version, a novel boundary condition has been introduced, supplanting the Chen equation with a more appropriate correlation conceived by Cooper (Equation (11.4)). This updated correlation takes into account pivotal factors such as surface texture, operational pressure, and the properties of the fluid. Regarding film condensation in vertical tubes, the base version of the code estimates the HTC based on the greater value between Nusselt and Shah equations (Equations (11.5) and (11.10)). The improved REDMaHD version incorporates a more fitting correlation for evaluating HTC in situations involving laminar wavy condensation, specifically Kutateldze correlation (Equation (11.14)), and also updates Shah formula with its most current version. These modifications are intended to broaden the code utility, making it applicable to scenarios with low flow velocities and elevated operating pressures.

A rigorous validation and verification (V&V) process confirms marked improvements in the modified code predictive capabilities [136, 137].

Part V

Conclusions and future work

A novel advancement for the state-of-the-art SYS-TH code RELAP5/Mod3.3 has been pursued at Sapienza, University of Rome, enhancing the software capability to simulate MHD pressure drops within liquid metal circuits. This enhanced version is designated as REDMaHD. Both two-dimensional and three-dimensional MHD pressure losses, analogous to distributed and localized friction losses in conventional hydrodynamic flows, can now be computed for a wide range of geometries. Such capabilities are notably salient for fusion-relevant analyses, especially in the context of LM BB designs where the MHD pressure loss predominates. Presently, the code is assessed as reliable in simulating LM BB and associated circulating loops during standard operations and postulated transients, devoid of rapid temporal fluctuations in the reactor magnetic field.

A solid Verification and Validation (V&V) campaign has been undertaken, benchmarking numerous computational and experimental investigations, to corroborate the code aptitude for mirroring physical outcomes. Initially, individual sub-routines undergo verification for simple single effect cases to confirm their optimal functionality. In subsequent stages, REDMaHD is employed to replicate findings from direct numerical simulation and experimental works for three different BB concepts, namely the LLCB (simulation of TBM module) [28], the HCLL [29], and the WCLL [16] (both experimental mock-ups of TBM modules). These test cases are as close as possible to an integral effect test for the purposes of the validation of the MHD model and have been intentionally chosen to cover a wide range of BB concepts: from separately-cooled BB, where the LM is only a tritium breeder and carrier (WCLL/HCLL) and is characterized by slow velocity (from 0.1 to 1 mm/s), to dual coolant BB where the LM is circulated at higher speed.

REDMaHD has proven its dependability in evaluating pressure drops in fusion-relevant LM circuits. The software predicts two-dimensional loss accurately, exhibiting a minor variation approximately 1% from the numerical or experimental findings. This performance places REDMaHD on par with other notable numerical tools proficient in similar analyses, like MARS-FR [239] and MHD-SYS [108]. Moreover, the three-dimensional MHD pressure drop module in RELAP5 displays commendable concordance with TBM validation test case outcomes, with a deviation $1\% \leq \epsilon \leq 25\%$ that seems to diminish significantly with the increase in field intensity. This deviation primarily stems from the conservative approach adopted for the 3D pressure drop models, a strategy chosen to navigate existing uncertainties in predicting these effects. While REDMaHD currently does not encompass a specific subroutine for the prediction of electromagnetic coupling, its omission does not notably hinder the pressure drop evaluation. Instead, it impacts the software proficiency in predicting mass flow rate distributions in multichannel setups. Notably, the impeccable alignment with the HCLL/WCLL TBM experimental data showcases the code adaptability to reactor conditions.

To summarize, the advancements described in this dissertation have notably enhanced the functionalities of the adapted RELAP5, positioning it as a dependable instrument for MHD pressure drop assessments in LM circuits.

The encouraging outcomes of the V&V process have paved the way for REDMaHD application in practical design and support undertakings for the WCLL breeding blanket. An array of distinct geometrical arrangements has been examined to determine their influence on flow distribution and pressure loss within the WCLL TBM box. An optimized design of the WCLL TBM test section has been proposed with calibrated constraints at the manifold/BU junctures, accompanied by a toroidal, incremental adjustment of the structural plate segregating the feeding and collecting manifold. This adjustment aligns with the decreasing and increasing flow rate in these hydraulic components. Additionally, optimization of openings between manifold sections has been executed [240].

Additionally, the evaluation of 2D and 3D MHD pressure drops within the whole WCLL TBM PbLi, namely the WCLL TES, piping system was conducted under varying boundary conditions, specifically in terms of total mass flow rate and magnetic field intensity. Under nominal conditions, the cumulative pressure drop amounts to 2.13 bar. For the selected geometry, a scaling parameter ΔP_{TBM} has been introduced, which is independent of Γ and B. This parameter can prove valuable for subsequent investigations of this circuit, aiming to determine MHD drops across an expanded spectrum of Re and Ha.

The pressure drop estimation has also been extended to the entire circuit of the EU-DEMO WCLL TER. The cumulative MHD pressure drop for both the IB and OB loops was re-evaluated using REDMaHD, providing an update to the 2020 estimates [58]. The MHD pressure drop varies from 23.5 bar in the OB loop to over 28 bar in the IB loop. The influence of the BU/manifold connection geometry on flow rate distribution was studied. A significant flow imbalance is anticipated due to the manifold configuration, yet this can be partly mitigated by selecting an appropriately sized BU/manifold connection. A connection size of $1 \times 1\,\mathrm{cm}^2$ seems suitable to ensure a reasonably consistent breeder distribution.

Eventually, an overall estimate of the MHD pressure drop in the new concept of WCLL-double bundle LOBS has been performed with analytical methods and REDMaHD. The thin chamber wall, simplified collector layout, lower mass flow rate, and predominantly poloidal flow all contribute to a reduction of the MHD pressure drop in the WCLL-db BB segment to about one-tenth of the baseline value. When taking into consideration the entire PbLi in-magnet loop, the overall pressure drop in the WCLL-db is about one-third of the baseline value. This estimate may also be further reduced by considering the effect of buoyancy, which is expected to aid the BZ poloidal flow. By all means though, it should be stressed that this improvement in MHD performance, although welcome, is not critical for the feasibility of the water-cooled BB concept. The PBLi loop main pump is able to meet the head requirements derived by the MHD pressure drop estimate for the baseline WCLL BB.

While REDMaHD represents a commendable stride forward, it cannot yet be regarded as a fully functional system magneto-thermal-hydraulic code. Desirable physical models, for instance one dedicated to represent the effects of electromagnetic coupling, remain absent, and the correlations for 3D MHD losses demand further refinement to broaden their adaptability and applicability spectrum. Of these cited examples, the first stems from the lack of a comprehensive theoretical framework and the second due to a limited amount of experimental data. Upcoming endeavors will focus on the enhancement of bend and cross-section models to take into account arbitrary wall conductivity values. Preliminary explorations have been initiated regarding the establishment of an electromagnetic coupling model, grounded in the analytical approach proposed by Bluck et al. [192]. The inclusion of pertinent models for other 3D losses, such as the ones induced by fringing magnetic field or MHD flow around obstacles, is presently under scrutiny.

To provide a comprehensive understanding of MHD phenomena within the BB of a fusion reactor where the LM fulfills also the role of a coolant, this doctoral research commenced the development of a model able to predict heat transfer coefficients for

MHD forced convection, primarily grounded on pivotal studies from the literature [186, 190, 194]. An initial validation of the model results with experimental data obtained for MHD flows in circular heated ducts has been undertaken [17–20, 23]. For rectangular ducts, an assessment against CFD results has been performed due to the unavailability of suitable experimental data. The preliminary validation outcomes are promising, yet further refinement is imperative to evaluate the impact on the HTC due to factors such as wall conductance ratio and buoyant effects. Indeed, it is this latter characteristic that is considered paramount for the forthcoming enhancement of the heat transfer model. Comprehensive validation is challenged by the absence of experimental mock-up data, at least until measurements are undertaken in next generation facilities, like CHIMERA [241], that are going to approximate to a higher degree the requirements for an integral effect test. Moreover, once the steady-state thermal model is authenticated, there will be a necessity to validate it for operational transients, where both experimental and numerical data are currently lacking.

In the intermediate to distant future, it is anticipated that a model for assessing the MHD impact on mass transport phenomena (like tritium permeation and corrosion) will be conceived, contingent upon intensified research in this domain as suggested by Seo et al. in [97].

Ultimately, as the understanding of MHD phenomena during violent transients matures in the literature, it is projected that all the models will undergo revisions to better account for them, enabling the code to simulate a broader spectrum of scenarios, be they operational or incidental. There is a pressing need to address some notable scenarios, through models and validation cases, like the PbLi/water interaction during an in-box LOCA (see Refs. [242, 243]) or MHD effects triggered by intense and time-varying magnetic fields during a plasma disruption [244].

Bibliography

[1] Lehigh University. Plasma control laboratory: Fusion, 2023. URL https://www6.lehigh.edu/~eus204/lab/PCL_fusion.php#x1-10043. Available from: https://www6.lehigh.edu/~eus204/lab/PCL_fusion.php#x1-10043.

[2] Fusion Physics. Non-serial Publications. INTERNATIONAL ATOMIC ENERGY AGENCY, Vienna, 2012. ISBN 978-92-0-130410-0. URL http://inis.iaea.org/search/search.aspx?orig_q=RN:43116796.

[3] Raymond Murray and Keith E Holbert. Nuclear energy: An introduction to the concepts, systems, and applications of nuclear processes. Elsevier, 2014.

[4] Fundamentals of Magnetic Fusion Technology. Non-serial Publications. INTERNATIONAL ATOMIC ENERGY AGENCY, Vienna, 2023. ISBN 978-92-0-110721-3. URL https://www.iaea.org/publications/14898/fundamentals-of-magnetic-fusion-technology.

[5] Farrokh Najmabadi, A Abdou, L Bromberg, T Brown, VC Chan, MC Chu, F Dahlgren, L El-Guebaly, P Heitzenroeder, D Henderson, et al. The aries-at advanced tokamak, advanced technology fusion power plant. Fusion Engineering and Design, 80(1-4):3–23, 2006.

[6] Simone Siriano. Numerical simulation of MHD flows in breeding blanket and plasma-facing components. Phd thesis, University of Rome La Sapienza, Rome, Italy, February 2022. Available at https://hdl.handle.net/11573/1612721.

[7] FR Urgorri, S Smolentsev, I Fernández-Berceruelo, D Rapisarda, I Palermo, and A Ibarra. Magnetohydrodynamic and thermal analysis of pbli flows in

poloidal channels with flow channel insert for the eu-dcll blanket. Nuclear fusion, 58(10):106001, 2018.

[8] Sergey Smolentsev, Tyler Rhodes, Gautam Pulugundla, Cyril Courtessole, Mohamed Abdou, Siegfried Malang, Mark Tillack, and Chuck Kessel. Mhd thermohydraulics analysis and supporting r&d for dcll blanket in the fnsf. Fusion engineering and design, 135:314–323, 2018.

[9] Luciano M Giancarli, Xavier Bravo, Seungyon Cho, Marco Ferrari, Takumi Hayashi, Byoung-Yoon Kim, Artur Leal-Pereira, Jean-Pierre Martins, Mario Merola, Romain Pascal, et al. Overview of recent iter tbm program activities. Fusion Engineering and Design, 158:111674, 2020.

[10] JS Rao, Hari Sankar, and MA Dos Santos. Magneto hydro-dynamics and heat transfer in liquid metal flows. Developments in heat transfer, pages 55–80, 2011.

[11] H Wayne Beaty and Donald G Fink. Standard handbook for electrical engineers. McGraw-Hill Education, 2013.

[12] Viktor Klüber. Three-dimensional magnetohydrodynamic phenomena in circular pipe flow. Ph.d. thesis, Karlsruher Institut für Technologie (KIT), KIT-Fakultät für Maschinenbau, 2023.

[13] Chieh C Chang and Thomas S Lundgren. Duct flow in magnetohydrodynamics. Zeitschrift für angewandte Mathematik und Physik ZAMP, 12:100–114, 1961.

[14] Xiujie Zhang, Chuanjie Pan, and Zengyu Xu. Investigation of coupling mhd rectangular ducts flows based on a fully developed modeling. IEEE Transactions on Plasma Science, 42(6):1764–1769, 2014.

[15] Lorenzo Melchiorri, Vincenzo Narcisi, Fabio Giannetti, Gianfranco Caruso, and Alessandro Tassone. Development of a relap5/mod3. 3 module for mhd pressure drop analysis in liquid metals loops: Verification and validation. Energies, 14(17):5538, 2021.

[16] C Courtessole and L Bühler. Experimental investigation of mhd flows in a wcll tbm mock-up. Fusion Engineering and Design - To be submitted, -:–, -.

[17] V.G. Sviridov, Yu.P. Ivochkin, N.G. Razuvanov, V.G. Zhilin, L.G. Genin, O.N. Ivanova, and K.V. Averianov. Liquid metal mhd heat transfer investigations applied to fusion tokamak reactor cooling ducts. Magnetohydrodynamics, 39 (4):557–564, 2003.

[18] IA Melnikov, EV Sviridov, VG Sviridov, and NG Razuvanov. Experimental investigation of mhd heat transfer in a vertical round tube affected by transverse magnetic field. Fusion Engineering and Design, 112:505–512, 2016.

[19] Oleg Zikanov, Yaroslav I Listratov, and Valentin G Sviridov. Natural convection in horizontal pipe flow with a strong transverse magnetic field. Journal of Fluid Mechanics, 720:486–516, 2013.

[20] I Belyaev, L Genin, Ya I Listratov, I Melnikov, N Razuvanov, V Sviridov, and E Sviridov. Features of mhd heat transfer in simple channels. Magnetohydrodynamics, 54(3):245–260, 2018.

[21] NG Razuvanov, NA Luchinkin, VG Sviridov, and PA Sardov. Mhd and heat transfer in downflow and upflow of a liquid metal in the vertical pipe applied to tokamak reactor blanket module. In Journal of Physics: Conference Series, volume 1382, page 012034. IOP Publishing, 2019.

[22] NA Luchinkin, NG Razuvanov, ON Polyanskaya, MA Sokolov, and EA Burdyukova. Heat transfer in a liquid metal upflow in a pipe with mixed turbulent convection complicated by the influence of magnetic field. Journal of Engineering Physics and Thermophysics, 95(6):1548–1559, 2022.

[23] A Beznosov, O Novozhilova, S Yu Savinov, M Yarmonov, and R Alekseev. The magnetic field effect on heat-exchange characteristics and mhd resistance of lead-bismuth eutectic flow in the tokamak blanket heat-sink systems. Magnetohydrodynamics, 49(1–2):237–248, 2013.

[24] C Mistrangelo, L Bühler, C Koehly, and I Ricapito. Magnetohydrodynamic velocity and pressure drop in manifolds of a wcll tbm. Nuclear Fusion, 61(9): 096037, 2021.

[25] Amelia Tincani, Pietro Arena, Maurizio Bruzzone, Ilenia Catanzaro, Cristiano Ciurluini, Alessandro Del Nevo, Pietro Alessandro Di Maio, Ruggero Forte, Fabio Giannetti, Stefano Lorenzi, et al. Conceptual design of the main ancillary systems of the iter water cooled lithium lead test blanket system. Fusion Engineering and Design, 167:112345, 2021.

[26] P. Testoni. Kom of the grt-0897 grant. TSS/A&C group for Fusion for Energy, 2018. Private document, accessible only to authorized members within the EUROFusion framework.

[27] R. Roccella. Static and transient magnetic field maps at level l1 tokamak complex. IDM UID QQEB3J, 2019.

[28] P. K. Swain, Pratik Koli, S. Ghorui, P. Mukherjee, and A. V. Deshpande. Thermofluid MHD studies in a model of Indian LLCB TBM at high magnetic field relevant to ITER. Fusion Eng. Des., 150(July 2019), 2020. ISSN 09203796. doi: 10.1016/j.fusengdes.2019.111374.

[29] L Bühler, H.-J. Brinkmann, S Horanyi, and K Starke. Magnetohydrodynamic flow in a mock-up of a HCLL blanket. Part II. Experiments. Technical Report FZKA 7424, 2008.

[30] Julien Aubert, G Aiello, D Alonso, T Batal, R Boullon, S Burles, B Cantone, F Cismondi, A Del Nevo, L Maqueda, et al. Design and preliminary analyses of the new water cooled lithium lead tbm for iter. Fusion Engineering and Design, 160:111921, 2020.

[31] Alessandro Tassone and Gianfranco Caruso. Computational MHD analyses in support of the design of the WCLL TBM breeding zone. Fusion Eng. Des., 170(112535), 2021. doi: https://doi.org/10.1016/j.fusengdes.2021.112535.

[32] Alessandro Tassone, Gianfranco Caruso, and Alessandro Del Nevo. Influence of PbLi hydraulic path and integration layout on MHD pressure losses. Fusion Eng. Des., 155(July 2019):111517, 2020. ISSN 09203796. doi: 10.1016/j.fusengdes.2020.111517. URL `https://doi.org/10.1016/j.fusengdes.2020.111517`.

[33] Pietro Arena, Gaetano Bongiovì, Ilenia Catanzaro, Cristiano Ciurluini, Aldo Collaku, Alessandro Del Nevo, Pietro Alessandro Di Maio, Matteo DOnorio, Fabio Giannetti, Vito Imbriani, et al. Design and integration of the eu-demo water-cooled lead lithium breeding blanket. Energies, 16(4):2069, 2023.

[34] IEA. Energy technology perspectives 2023, 2023. URL `https://www.iea.org/reports/energy-technology-perspectives-2023`. License: CC BY 4.0.

[35] Nuclear energy and sustainable development, 2023. URL `https://world-nuclear.org/information-library/energy-and-the-environment/nuclear-energy-and-sustainable-development.aspx`. Accessed: [26/05/2023].

[36] JPHE Ongena and G Van Oost. Energy for future centuries: Prospects for fusion power as a future energy source. Fusion Science and Technology, 61 (2T):3–16, 2012.

[37] AJH Donné. The european roadmap towards fusion electricity. Philosophical Transactions of the Royal Society A, 377(2141):20170432, 2019.

[38] Gia Tuong Hoang and Jean Jacquinot. Controlled fusion: the next step. Physics world, 17(1):21, 2004.

[39] Mohamed Abdou, Neil B Morley, Sergey Smolentsev, Alice Ying, Siegfried Malang, Arthur Rowcliffe, and Mike Ulrickson. Blanket/first wall challenges and required r&d on the pathway to demo. Fusion Engineering and Design, 100:2–43, 2015.

[40] Guido van Oost and Sehila M. Gonzalez de Vicente. Fundamentals of Magnetic Fusion Technology. International Atomic Energy Agency (IAEA), 2021. URL `https://fusenet.eu/book/fundamentals-of-magnetic-fusion-technology`.

[41] D Martelli, A Venturini, and M Utili. Literature review of lead-lithium thermophysical properties. Fusion Engineering and Design, 138:183–195, 2019.

[42] R Wenninger, Raffaele Albanese, R Ambrosino, F Arbeiter, J Aubert, C Bachmann, L Barbato, T Barrett, M Beckers, Wolfgang Biel, et al. The demo wall load challenge. Nuclear Fusion, 57(4):046002, 2017.

[43] Gianfranco Federici, C Bachmann, L Barucca, Wolfgang Biel, L Boccaccini, R Brown, C Bustreo, S Ciattaglia, F Cismondi, M Coleman, et al. Demo design activity in europe: Progress and updates. Fusion Engineering and Design, 136: 729–741, 2018.

[44] L Giancarli, M Dalle Donne, and W Dietz. Status of the european breeding blanket technology. In Fusion Technology 1996, pages 57–74. Elsevier, 1997.

[45] Mario Dalle Donne. European demo bot solid breeder blanket. Technical report, Association Euratom-Kernforschungszentrum Karlsruhe GmbH (KFK)(Germany), 1994.

[46] MA Fütterer, G Benamati, I Ricapito, L Giancarli, G Le Marois, A Li Puma, Y Poitevin, J Reimann, J-F Salavy, J Szczepanski, et al. Further improvements of the water-cooled pb–17li blanket. Fusion engineering and design, 58:523–527, 2001.

[47] Siegfried Malang and K Schleisiek. Dual coolant blanket concept. Technical report, Association Euratom-Kernforschungszentrum Karlsruhe GmbH (KFK)(Germany), 1994.

[48] D Maisonnier, I Cook, Sardain Pierre, Boccaccini Lorenzo, Bogusch Edgar, Broden Karin, Forrest Robin, Giancarli Luciano, Hermsmeyer Stephan, Nardi Claudio, et al. The european power plant conceptual study. Fusion Engineering and Design, 75:1173–1179, 2005.

[49] S Hermsmeyer, B Dolensky, J Fiek, U Fischer, C Kohly, S Malang, P PeresIavtsev, J Rey, and Z Xu. Revision of the eu helium cooled pebble bed blanket for demo. In 20th IEEE/NPSS Symposium onFusion Engineering, 2003., pages 440–445. IEEE, 2003.

[50] A Li Puma, JL Berton, B Branas, L Bühler, J Doncel, U Fischer, W Farabolini, L Giancarli, D Maisonnier, P Pereslavtsev, et al. Breeding blanket design

and systems integration for a helium-cooled lithium–lead fusion power plant. Fusion Engineering and Design, 81(1-7):469–476, 2006.

[51] Gianfranco Federici, L Boccaccini, F Cismondi, M Gasparotto, Y Poitevin, and Italo Ricapito. An overview of the eu breeding blanket design strategy as an integral part of the demo design effort. Fusion Engineering and Design, 141:30–42, 2019.

[52] Francisco A Hernández, Pavel Pereslavtsev, Guangming Zhou, Qinlan Kang, Salvatore DAmico, Heiko Neuberger, Lorenzo V Boccaccini, Béla Kiss, Gábor Nádasi, Luis Maqueda, et al. Consolidated design of the hcpb breeding blanket for the pre-conceptual design phase of the eu demo and harmonization with the iter hcpb tbm program. Fusion Engineering and Design, 157:111614, 2020.

[53] Julien Aubert, Giacomo Aiello, Pietro Arena, Tom Barrett, Lorenzo Virgilio Boccaccini, Gaetano Bongiovì, Rémi Boullon, Fabio Cismondi, Ion Critescu, Phani Kumar Domalapally, et al. Status of the eu demo hcll breeding blanket design development. Fusion Engineering and Design, 136:1428–1432, 2018.

[54] A Del Nevo, P Arena, G Caruso, P Chiovaro, PA Di Maio, M Eboli, F Edemetti, N Forgione, R Forte, A Froio, et al. Recent progress in developing a feasible and integrated conceptual design of the wcll bb in eurofusion project. Fusion Engineering and Design, 146:1805–1809, 2019.

[55] Iván Fernández-Berceruelo, Iole Palermo, Fernando R Urgorri, David Rapisarda, Belit Garcinuño, and Ángel Ibarra. Remarks on the performance of the eu dcll breeding blanket adapted to demo 2017. Fusion Engineering and Design, 155:111559, 2020.

[56] I Ricapito, F Cismondi, G Federici, Y Poitevin, and M Zmitko. European tbm programme: First elements of rox and technical performance assessment for demo breeding blankets. Fusion Engineering and Design, 156:111584, 2020.

[57] Jonathan Keep, Steve Wood, Neelam Gupta, Matti Coleman, and Antony Loving. Remote handling of demo breeder blanket segments: Blanket transporter conceptual studies. Fusion engineering and design, 124:420–425, 2017.

[58] Alessandro Tassone, Simone Siriano, Gianfranco Caruso, Marco Utili, and Alessandro Del Nevo. MHD pressure drop estimate for the WCLL in-magnet PbLi loop. Fusion Eng. Des., 160(September 2019):111830, 2020. ISSN 09203796. doi: 10.1016/j.fusengdes.2020.111830. URL `https://doi.org/10.1016/j.fusengdes.2020.111830`.

[59] MS Tillack, XR Wang, J Pulsifer, S Malang, DK Sze, M Billone, I Sviatoslavsky, ARIES Team, et al. Fusion power core engineering for the aries-st power plant. Fusion Engineering and Design, 65(2):215–261, 2003.

[60] Hongyan Wang, Weihua Wang, Yunqing Bai, and Hongli Chen. Preliminary thermal-hydraulics design of the dual-cooled lithium lead blanket for fds-ii. Fusion engineering and design, 75:841–845, 2005.

[61] Clement PC Wong, M Abdou, M Dagher, Yutai Katoh, RJ Kurtz, Siegfried Malang, EP Marriott, BJ Merrill, K Messadek, NB Morley, et al. An overview of the us dcll iter-tbm program. Fusion engineering and design, 85(7-9):1129–1132, 2010.

[62] M Zmitko, P Vladimirov, R Knitter, M Kolb, O Leys, J Heuser, H-C Schneider, R Rolli, V Chakin, S Pupeschi, et al. Development and qualification of functional materials for the european hcpb tbm. Fusion Engineering and Design, 136:1376–1385, 2018.

[63] Hisashi Tanigawa, Hyoseong Gwon, Takanori Hirose, Yoshinori Kawamura, Mitsuru Ejiri, Kazuhito Watanabe, Shiro Asano, Takayuki Kokami, and Yasushi Oda. Cylindrical breeding blankets for fusion reactors. Fusion Engineering and Design, 136:1221–1225, 2018.

[64] Yoshinori Kawamura, Hyoseong Gwon, Wenhai Guan, Hisashi Tanigawa, Takanori Hirose, Atsushi Wakasa, Seiji Yoshino, Tamon Ouchi, Kentaro Hattori, Noriaki Chiba, et al. Progress of water cooled ceramic breeder test blanket module system. Fusion Engineering and Design, 161:112050, 2020.

[65] E Rajendra Kumar, KN Vyas, and T Jayakumar. Overview of llcb tbm design and r&d activities in india. Fusion Engineering and Design, 109:1522–1527, 2016.

[66] Paritosh Chaudhuri, Chandan Danani, Vilas Chaudhari, and E Rajendra Kumar. Overview of design and thermal–hydraulic analysis of indian solid breeder blanket concept. Fusion Engineering and Design, 88(4):209–215, 2013.

[67] XY Wang, KM Feng, YJ Chen, L Zhang, YJ Feng, XH Wu, HB Liao, XF Ye, FC Zhao, QX Cao, et al. Current design and r&d progress of the chinese helium cooled ceramic breeder test blanket system. Nuclear Fusion, 59(7): 076019, 2019.

[68] Luciano M Giancarli, Mu-Young Ahn, Ian Bonnett, Christophe Boyer, Paritosh Chaudhuri, William Davis, Giovanni DellOrco, Markus Iseli, Robert Michling, Jean-Christophe Neviere, et al. Iter tbm program and associated system engineering. Fusion Engineering and Design, 136:815–821, 2018.

[69] Deepak Sharma and Paritosh Chaudhuri. Design and analysis of manifolds for indian hccb blanket module. Fusion Engineering and Design, 129:40–57, 2018.

[70] Julius Hartmann and Freimut Lazarus. Hg-dynamics. Levin & Munksgaard Copenhagen, 1937.

[71] J Hartmann and F Lazarus. Hg-dynamics ii. Theory of laminar flow of electrically conductive Liquids in a Homogeneous Magnetic Field, 15(7), 1937.

[72] Hannes Alfvén. Existence of electromagnetic-hydrodynamic waves. Nature, 150(3805):405–406, 1942.

[73] Sergei S Molokov, René Moreau, and H Keith Moffatt. Magnetohydrodynamics: Historical evolution and trends, volume 80. Springer Science & Business Media, 2007.

[74] Ulrich Müller and Leo Bühler. Magnetofluiddynamics in channels and containers. Springer Science & Business Media, 2001.

[75] George Keith Batchelor. An introduction to fluid dynamics. Cambridge university press, 1967.

[76] John David Jackson. Classical electrodynamics. John Wiley & Sons, 2021.

[77] René J Moreau. Magnetohydrodynamics, volume 3. Springer Science & Business Media, 1990.

[78] Henk Kaarle Versteeg and Weeratunge Malalasekera. An introduction to computational fluid dynamics: the finite volume method. Pearson education, 2007.

[79] Igor R. Kirillov, Claude B. Reed, Leopold Barleon, and Keiji Miyazaki. Present understanding of MHD and heat transfer phenomena for liquid metal blankets. Fusion Eng. Des., 27(C):553–569, 1995. ISSN 09203796. doi: 10.1016/0920-3796(95)90171-X.

[80] HK Moffatt. On the suppression of turbulence by a uniform magnetic field. Journal of fluid Mechanics, 28(3):571–592, 1967.

[81] JA Shercliff. Steady motion of conducting fluids in pipes under transverse magnetic fields. In Mathematical Proceedings of the Cambridge Philosophical Society, volume 49, pages 136–144. Cambridge University Press, 1953.

[82] Ya S Uflyand. Flow stability of a conducting fluid in a rectangular channel in a transverse magnetic field. Soviet Physics: Technical Physics, 5(10):1191–1193, 1961.

[83] JCR Hunt. Magnetohydrodynamic flow in rectangular ducts. Journal of fluid mechanics, 21(4):577–590, 1965.

[84] Ulrich Burr, L Barleon, U Müller, and A Tsinober. Turbulent transport of momentum and heat in magnetohydrodynamic rectangular duct flow with strong sidewall jets. Journal of Fluid Mechanics, 406:247–279, 2000.

[85] JCR Hunt and K Stewartson. Magnetohydrodynamic flow in rectangular ducts. ii. Journal of fluid mechanics, 23(3):563–581, 1965.

[86] JA Shercliff. Magnetohydrodynamic pipe flow part2. high hartmann number. Journal of Fluid Mechanics, 13(4):513–518, 1962.

[87] PH Roberts. Singularities of hartmann layers. Proceedings of the Royal Society of London. Series A. Mathematical and Physical Sciences, 300(1460):94–107, 1967.

[88] Keiji Miyazaki, Shoji Inoue, Nobuo Yamaoka, Tomomitsu Horiba, and Kazushige Yokomizo. Magneto-Hydro-Dynamic Pressure Drop of Lithium Flow in Rectangular Ducts. Fusion Technol., 10(3 pt 2A):830–836, 1986. ISSN 07481896. doi: 10.13182/fst10-830.

[89] MS Tillack. Magnetohydrodynamic flow in rectangular ducts. design equations for pressure drop and flow quantity. UCLA-Report UCLA-FNT, 41, 1990.

[90] TQ Hua, JS Walker, BF Picologlou, and CB Reed. Three-dimensional mhd (magnetohydrodynamic) flows in rectangular ducts of liquid-metal-cooled blankets. Technical report, Argonne National Lab., IL (USA). Fusion Power Program, 1988.

[91] Zhen Tao and MingJiu Ni. Analytical solutions for mhd flow at a rectangular duct with unsymmetrical walls of arbitrary conductivity. Science China Physics, Mechanics & Astronomy, 58:1–18, 2015.

[92] S. Smolentsev, S. Badia, R. Bhattacharyay, L. Bühler, L. Chen, Q. Huang, H. G. Jin, D. Krasnov, D. W. Lee, E. Mas De Les Valls, C. Mistrangelo, R. Munipalli, M. J. Ni, D. Pashkevich, A. Patel, G. Pulugundla, P. Satyamurthy, A. Snegirev, V. Sviridov, P. Swain, T. Zhou, and O. Zikanov. An approach to verification and validation of MHD codes for fusion applications. Fusion Eng. Des., 100:65–72, 2015. ISSN 09203796. doi: 10.1016/j.fusengdes.2014.04.049.

[93] H. Madarame, K. Taghavi, and M. S. Tillack. Influence of Leakage Currents on Mhd Pressure Drop. Fusion Technol., 8(1 pt 2(A)):264–269, 1985. ISSN 07481896. doi: 10.13182/fst85-a40055.

[94] Michael J Bluck and Michael J Wolfendale. An analytical solution to electromagnetically coupled duct flow in mhd. Journal of Fluid Mechanics, 771: 595–623, 2015.

[95] L Bühler and C Mistrangelo. A simple mhd model for coupling poloidal manifolds to breeder units in liquid metal blankets. Fusion Engineering and Design, 191:113552, 2023.

[96] J Reimann, G Benamati, and R Moreau. Report of working group MHD for the blanket concept selection exercise (BSE). (FZKA 5652), 1995.

[97] Seok Bin Seo, Richard Hernandez, Miles O Neal, Nicholas Meehan, Felipe S Novais, Marina Rizk, G Ivan Maldonado, and Nicholas R Brown. A review of thermal hydraulics systems analysis for breeding blanket design and future needs for fusion engineering demonstration facility design and licensing Figure of Merit. Fusion Eng. Des., 172(February):112769, 2021. ISSN 0920-3796. doi: 10.1016/j.fusengdes.2021.112769. URL `https://doi.org/10.1016/j.fusengdes.2021.112769`.

[98] D. Bestion. The structure of system thermal-hydraulic (SYS-TH) code for nuclear energy applications. Elsevier Ltd., 2017. ISBN 9780081006627. doi: 10.1016/B978-0-08-100662-7.00011-7. URL `http://dx.doi.org/10.1016/B978-0-08-100662-7.00011-7`.

[99] Code Development Team. RELAP5-3D code manual: code structure, system models and solution methods., volume I. Idaho National Laboratory (INL), Idaho Falls, 2015.

[100] D. Bestion. System thermalhydraulics for design basis accident analysis and simulation: Status of tools and methods and direction for future R&D. Nucl. Eng. Des., 312:12–29, 2017. ISSN 00295493. doi: 10.1016/j.nucengdes.2016.11.010. URL `http://dx.doi.org/10.1016/j.nucengdes.2016.11.010`.

[101] International Atomic Energy Agency (IAEA). Safety assessment for facilities and activities. Technical report, Vienna, 2016.

[102] Yizhou Yan. Development of a coupled CFDsystem-code capability (with a modified porous media model) and its applications to simulate current and next generation reactors. University of Illinois at Urbana-Champaign, 2011.

[103] Jin Xuezhou and R Meyder. Thermal-hydraulic system study of the helium cooled pebble bed (hcpb) test blanket module (tbm) for iter using system code relap5. Plasma Science and Technology, 7(2):2753, 2005.

[104] Emilian L Popov, Graydon L Yoder Jr, and Seokho H Kim. Relap5 model of the divertor primary heat transfer system. Technical report, Oak Ridge National Lab.(ORNL), Oak Ridge, TN (United States); ITER , 2010.

[105] Michael James Wolfendale. A Coupled Systems Code - CMHD Solver for Fusion Blanket Design. PhD thesis, Imperial College London, Department of Mechanical Engineering, January 27 2016. Supervised by: Dr Michael J Bluck, Mr Ben Chuilon.

[106] DL Aumiller, ET Tomlinson, and RC Bauer. A coupled relap5-3d/cfd methodology with a proof-of-principle calculation. Nuclear Engineering and Design, 205(1-2):83–90, 2001.

[107] Wei Li, Xiaoli Wu, Dalin Zhang, Guanghui Su, Wenxi Tian, and Suizheng Qiu. Preliminary study of coupling cfd code fluent and system code relap5. Annals of Nuclear Energy, 73:96–107, 2014.

[108] Michael J. Wolfendale and Michael J. Bluck. A coupled systems code-CFD MHD solver for fusion blanket design. Fusion Eng. Des., 98-99:1902–1906, 2015. ISSN 09203796. doi: 10.1016/j.fusengdes.2015.04.025. URL http://dx.doi.org/10.1016/j.fusengdes.2015.04.025.

[109] CD Fletcher and RR Schultz. Relap5/mod3 code manual. Technical report, Nuclear Regulatory Commission, Washington, DC (United States). Div. of , 1992.

[110] Nuclear Safety Analysis Division. RELAP5/MOD3.3 Code manual volume I: code structure, syster volume I. Information Systems Laboratories, Inc., 2003.

[111] S Smolentsev, T Rhodes, Y Yan, A Tassone, C Mistrangelo, L Bühler, and FR Urgorri. Code-to-code comparison for a pbli mixed-convection mhd flow. Fusion Science and Technology, 76(5):653–669, 2020.

[112] L. Melchiorri. Baseline for developing a general openfoam solver for magnetohydrodynamic (mhd) flows. In H. Nilsson, editor, Proceedings of CFD with OpenSource Software, 2021. URL http://dx.doi.org/10.17196/OSCFD#YEAR2021.

[113] Lorenzo Melchiorri, Pietro Arena, Fabio Giannetti, Simone Siriano, and Alessandro Tassone. Cfd analysis and optimization of the demo wcll central outboard segment bottom-cap elementary cell. Journal of Nuclear Engineering, 3(4):409–420, 2022.

[114] Goong Chen, Qingang Xiong, Philip J Morris, Eric G Paterson, Alexey Sergeev, and Y Wang. Openfoam for computational fluid dynamics. Notices of the AMS, 61(4):354–363, 2014.

[115] John Crank and Phyllis Nicolson. A practical method for numerical evaluation of solutions of partial differential equations of the heat-conduction type. In Mathematical proceedings of the Cambridge philosophical society, volume 43, pages 50–67. Cambridge University Press, 1947.

[116] Simone Siriano, Fernando Roca Urgorri, Alessandro Tassone, and Gianfranco Caruso. 3d mhd analysis of prototypical manifold for liquid metal blankets. Nuclear Fusion, 2023.

[117] Henry G Weller, Gavin Tabor, Hrvoje Jasak, and Christer Fureby. A tensorial approach to computational continuum mechanics using object-oriented techniques. Computers in physics, 12(6):620–631, 1998.

[118] Vincent Dousset and Alban Pothérat. Numerical simulations of a cylinder wake under a strong axial magnetic field. Physics of Fluids, 20(1), 2008.

[119] L Batet, J Fradera, E Mas De Les Valls, V Medina, and L Sedano. Modelling of integrated effect of volumetric heating and magnetic field on tritium transport in a u-bend flow as applied to hcll blanket concept. 2011.

[120] Chiara Mistrangelo and Leo Bühler. Development of a numerical tool to simulate magnetohydrodynamic interactions of liquid metals with strong applied magnetic fields. Fusion Science and Technology, 60(2):798–803, 2011.

[121] C Mistrangelo, L Bühler, S Smolentsev, V Klüber, I Maione, and J Aubert. Mhd flow in liquid metal blankets: Major design issues, mhd guidelines and numerical analysis. Fusion Engineering and Design, 173:112795, 2021.

[122] Simone Siriano, Alessandro Tassone, Gianfranco Caruso, and Alessandro Del Nevo. Electromagnetic coupling phenomena in co-axial rectangular channels. Fusion Engineering and Design, 160:111854, 2020.

[123] R Stieglitz and S Molokov. Experimental study of magnetohydrodynamic flows in electrically coupled bends. Journal of Fluid Mechanics, 343:1–28, 1997.

[124] Sergey Smolentsev. Physical background, computations and practical issues of the magnetohydrodynamic pressure drop in a fusion liquid metal blanket. Fluids, 6(3):110, 2021. ISSN 23115521. doi: 10.3390/fluids6030110.

[125] S. Smolentsev, T. Rhodes, Y. Yan, A. Tassone, C. Mistrangelo, L. Bühler, and F. R. Urgorri. Code-to-Code Comparison for a PbLi Mixed-Convection MHD Flow. Fusion Sci. Technol., 00(00):653–669, 2020. ISSN 19437641. doi: 10.1080/15361055.2020.1751378. URL https://doi.org/10.1080/15361055.2020.1751378.

[126] Julio Pacio, LUCA Marocco, and Th Wetzel. Review of data and correlations for turbulent forced convective heat transfer of liquid metals in pipes. Heat and Mass Transfer, 51:153–164, 2015.

[127] Oleg Zikanov, Ivan Belyaev, Yaroslav Listratov, Peter Frick, Nikita Razuvanov, and Valentin Sviridov. Mixed convection in pipe and duct flows with strong magnetic fields. Applied Mechanics Reviews, 73(1):010801, 2021.

[128] Guillaume Authié, Toshio Tagawa, and René Moreau. Buoyant flow in long vertical enclosures in the presence of a strong horizontal magnetic field. part 2. finite enclosures. European Journal of Mechanics-B/Fluids, 22(3):203–220, 2003.

[129] Bub Dong Chung, Kyung Doo Kim, Sung Won Bae, Jae Jun Jeong, Seung Wook Lee, Moon Kyu Hwang, and Churl Yoon. Mars code manual volume i: code structure, system models, and solution methods. Technical report, Korea Atomic Energy Research Institute, 2010.

[130] Andrew Grief, Simon Owen, Julian Murgatroyd, Dobromir Panayotov, Brad Merrill, Paul Humrickhouse, and Catherine Saunders. Qualification of MELCOR and RELAP5 models for EU HCLL TBS accident analyses. Fusion Eng. Des., 124:1165–1170, 2017. ISSN 09203796. doi: 10.1016/j.fusengdes.2017.03.048. URL https://doi.org/10.1016/j.fusengdes.2017.03.048.

[131] Andrea Batti. System-level hydraulic modeling of the PbLi loop for the Breeding Blanket of a tokamak, 2020.

[132] RELAP5-3D Code Development Team. Relap5-3d code manual volume i: Code structure, system models and solution methods. Technical report, Idaho National Laboratory, Idaho Falls, ID, US, 2015.

[133] Nicholas Meehan, G Ivan Maldonado, and Nicholas R Brown. Demonstration of relap5-3d for transient analysis of a dual coolant lead lithium fusion blanket concept. Fusion Engineering and Design, 180:113192, 2022.

[134] P. Cioli Puviani et al. Cfd sth code coupling for the thermal hydraulic analysis of nacie-up experimental facility. In NURETH-20, 2023.

[135] Fabio Giannetti, Tommaso D'Alessandro, and Cristiano Ciurluini. Development of a RELAP5 mod3.3 version for FUSION applications. Technical report, Thecnical Report D1902_ENBR_T01, 2019.

[136] Vincenzo Narcisi, Lorenzo Melchiorri, Fabio Giannetti, and Gianfranco Caruso. Assessment of relap5-3d for application on in-pool passive power removal systems. Proc. 30th Eur. Saf. Reliab. Conf. 15th Probabilistic Saf. Assess. Manag. Conf., pages 1135–1142, 2020. doi: 10.3850/978-981-14-8593-0_4902-cd.

[137] Vincenzo Narcisi, Lorenzo Melchiorri, and Fabio Giannetti. Improvements of RELAP5/Mod3.3 heat transfer capabilities for simulation of in-pool passive power removal systems. Ann. Nucl. Energy, 160:108436, 2021. ISSN 18732100. doi: 10.1016/j.anucene.2021.108436. URL https://doi.org/10.1016/j.anucene.2021.108436.

[138] Gianluca Barone, Daniele Martelli, and Nicola Forgione. Implementation of Lead-Lithium as working fluid in RELAP5/Mod3.3. Fusion Eng. Des., 146 (February):1308–1312, 2019. ISSN 09203796. doi: 10.1016/j.fusengdes.2019.02.064. URL https://doi.org/10.1016/j.fusengdes.2019.02.064.

[139] H. Tas, S. Malang, F. Reiter, and J. Sannier. Liquid breeder materials. J. Nucl. Mater., 155-157(PART 1):178–187, 1988. ISSN 00223115. doi: 10.1016/0022-3115(88)90239-5.

[140] S. Malang and R. Mattas. Comparison of lithium and the eutectic lead-lithium alloy, two candidate liquid metal breeder materials for self-cooled

blankets. Fusion Eng. Des., 27(C):399–406, 1995. ISSN 09203796. doi: 10.1016/0920-3796(95)90151-5.

[141] L Bühler and S Horanyi. Experimental investigations of MHD flows in a sudden expansion. Wissenschaftliche Berichte FZKA, 7245(August): 1–65, 2006. ISSN 0947-8620. URL `http://cat.inist.fr/?aModele=afficheN{&}cpsidt=18097940`.

[142] L. Bühler, H. J. Brinkmann, and C. Koehly. Experimental study of liquid metal magnetohydrodynamic flows near gaps between flow channel inserts. Fusion Eng. Des., 146(September):1399–1402, 2019. ISSN 09203796. doi: 10.1016/j.fusengdes.2018.11.034. URL `https://doi.org/10.1016/j.fusengdes.2018.11.034`.

[143] P. Balestra, F. Giannetti, G. Caruso, and A. Alfonsi. New RELAP5-3D lead and LBE thermophysical properties implementation for safety analysis of Gen IV reactors. Sci. Technol. Nucl. Install., 2016, 2016. ISSN 16876083. doi: 10.1155/2016/1687946.

[144] D. Martelli, A. Venturini, and M. Utili. Literature review of lead-lithium thermophysical properties. Fusion Eng. Des., 138(November 2018):183–195, 2019. ISSN 09203796. doi: 10.1016/j.fusengdes.2018.11.028. URL `https://doi.org/10.1016/j.fusengdes.2018.11.028`.

[145] O.J. Foust. Sodium-NaK engineering handbook, volume I. Gordon and Breach, New York, 1972.

[146] K. Mergia and N. Boukos. Structural, thermal, electrical and magnetic properties of Eurofer 97 steel. J. Nucl. Mater., 373(1-3):1–8, 2008. ISSN 00223115. doi: 10.1016/j.jnucmat.2007.03.267.

[147] Michal Kordač and Lukáš Košek. Helium bubble formation in pb-16li within the breeding blanket. Fusion Engineering and Design, 124:700–704, 2017.

[148] Sergey Smolentsev, René Moreau, Leo Bühler, and Chiara Mistrangelo. MHD thermofluid issues of liquid-metal blankets: Phenomena and advances. Fusion Eng. Des., 85(7-9):1196–1205, 2010. ISSN 09203796. doi: 10.1016/

j.fusengdes.2010.02.038. URL `http://dx.doi.org/10.1016/j.fusengdes.2010.02.038`.

[149] Keiji Miyazaki, Shoji Kotake, Nobuo Yamaoka, Shoji Inoue, and Yoichi Fujii-e. MHD pressure drop of NaK flow in stainless steel pipe. Nucl. Technol., 4(2 pt 2):447–452, 1983. ISSN 02723921. doi: 10.13182/fst4-2p2-447.

[150] J. Reimann, S. Molokov, I. Platnieks, and E. Platacis. Mhd-Flow in Multichannel U-Bends: Screening Experiments and Theoretical Analysis. Fusion Technol. 1992, pages 1454–1458, 1993. doi: 10.1016/b978-0-444-89995-8.50285-x.

[151] PA Davidson. Magnetic damping of jets and vortices. Journal of Fluid Mechanics, 299:153–186, 1995.

[152] Jingchao Feng, Qingyun He, Hongli Chen, and Minyou Ye. Numerical Investigation of magnetohydrodynamic flow through Sudden expansion pipes in Liquid Metal Blankets. Fusion Eng. Des., 109-111:1360–1364, 2016. ISSN 09203796. doi: 10.1016/j.fusengdes.2015.12.023. URL `http://dx.doi.org/10.1016/j.fusengdes.2015.12.023`.

[153] Tyler J. Rhodes, Sergey Smolentsev, and Mohamed Abdou. Magnetohydrodynamic pressure drop and flow balancing of liquid metal flow in a prototypic fusion blanket manifold. Phys. Fluids, 30(5), 2018. ISSN 10897666. doi: 10.1063/1.5026404.

[154] Yuqiao Fan and Sergey Smolentsev. Optimal design of the liquid metal feeding system for fusion reactor blankets through high-fidelity mhd simulations. Bulletin of the American Physical Society, 2023.

[155] L. Bühler and C. Mistrangelo. Pressure drop and velocity changes in MHD pipe flows due to a local interruption of the insulation. Fusion Eng. Des., 127 (January):185–191, 2018. ISSN 09203796. doi: 10.1016/j.fusengdes.2018.01.010. URL `https://doi.org/10.1016/j.fusengdes.2018.01.010`.

[156] L. Bühler, C. Mistrangelo, and H. J. Brinkmann. Experimental investigation of liquid metal MHD flow entering a flow channel insert. Fusion Eng. Des.,

154(September 2019):111484, 2020. ISSN 09203796. doi: 10.1016/j.fusengdes.2020.111484. URL https://doi.org/10.1016/j.fusengdes.2020.111484.

[157] C. Koehly, H. Neuberger, and L. Bühler. Fabrication of thin-walled fusion blanket components like flow channel inserts by selective laser melting. Fusion Eng. Des., 143(April):171–179, 2019. ISSN 09203796. doi: 10.1016/j.fusengdes.2019.03.184. URL https://doi.org/10.1016/j.fusengdes.2019.03.184.

[158] Anita Patel, Gautam Pulugundla, Sergey Smolentsev, Mohamed Abdou, and Rajendraprasad Bhattacharyay. Validation of numerical solvers for liquid metal flow in a complex geometry in the presence of a strong magnetic field. Theor. Comput. Fluid Dyn., 32(2):165–178, 2018. ISSN 14322250. doi: 10.1007/s00162-017-0446-9.

[159] S. Sahu and R. Bhattacharyay. Validation of COMSOL code for analyzing liquid metal magnetohydrodynamic flow. Fusion Eng. Des., 127(November 2017):151–159, 2018. ISSN 09203796. doi: 10.1016/j.fusengdes.2018.01.009. URL https://doi.org/10.1016/j.fusengdes.2018.01.009.

[160] Jingchao Feng, Hongli Chen, Qingyun He, and Minyou Ye. Further validation of liquid metal MHD code for unstructured grid based on OpenFOAM. Fusion Eng. Des., 100:260–264, 2015. ISSN 09203796. doi: 10.1016/j.fusengdes.2015.06.059. URL http://dx.doi.org/10.1016/j.fusengdes.2015.06.059.

[161] Narendra Laxman Gajbhiye, Praveen Throvagunta, and Vinayak Eswaran. Validation and verification of a robust 3-D MHD code. Fusion Eng. Des., 128 (November 2017):7–22, 2018. ISSN 09203796. doi: 10.1016/j.fusengdes.2018.01.017.

[162] C Koehly, L Bühler, and C Courtessole. Design of a scaled mockup of the wcll tbm for mhd experiments in liquid metal manifolds and breeder units. Fusion Engineering and Design, 192:113753, 2023.

[163] L. Melchiorri, S. Siriano, and A. Tassone. Relap5/mod3.3 mhd module development and validation: Wcll-tbm mock-up model. Fusion Eng. Des., 2023. submitted.

[164] Xiujie Zhang, Lei Wang, and Chuanjie Pan. Effects of inclined transversal magnetic fields on magnetohydrodynamic coupling duct flow states in liquid metal blankets: Under uniform magnetic fields. Nuclear Fusion, 61(1):016005, 2020.

[165] I. E. Idel'chik. Handbook of hydraulic resistance - Coefficients of local resistance and of friction. Israel program for scientific translations, Jerusalem, 1966.

[166] Tyler Rhodes and Sergey Smolentsev. Pressure drop in a prototypical 3d magnetohydrodynamic flow across contraction of a fusion blanket manifold. Journal of Nuclear Science and Technology, 58(8):908–917, 2021. doi: 10.1080/00223131.2021.1892550.

[167] C Mistrangelo, L Bühler, V Klüber, and C Koehly. Towards the simulation of mhd flow in an entire wcll tbm mock-up. Fusion Engineering and Design, 193:113752, 2023.

[168] Theodore L Bergman, Adrienne S Lavine, Frank P Incropera, and David P DeWitt. Introduction to heat transfer. John Wiley & Sons, 2011.

[169] JoëL Sommeria and René Moreau. Why, how, and when, mhd turbulence becomes two-dimensional. Journal of Fluid Mechanics, 118:507–518, 1982.

[170] Naotaka Umeda and Minoru Takahashi. Numerical analysis for heat transfer enhancement of a lithium flow under a transverse magnetic field. Fusion Engineering and Design, 51:899–907, 2000.

[171] Oleg Zikanov, Dmitry Krasnov, Thomas Boeck, Andre Thess, and Maurice Rossi. Laminar-turbulent transition in magnetohydrodynamic duct, pipe, and channel flows. Applied Mechanics Reviews, 66(3):030802, 2014.

[172] Elmars Blums, Yu Mikhailov, and Roberts Ozols. Heat and mass transfer in MHD flows, volume 3. World Scientific, 1987.

[173] DD Papailiou and PS Lykoudis. Magneto-fluid-mechanic laminar natural convectionan experiment. International Journal of Heat and Mass Transfer, 11(9):1385–1391, 1968.

[174] O Lielausis. Liquid-metal magnetohydrodynamics. Atomic Energy Review, 13 (3):527–581, 1975.

[175] Kazuto Okada and Hiroyuki Ozoe. Transient responses of natural convection heat transfer with liquid gallium under an external magnetic field in either the x, y, or z direction. Industrial & engineering chemistry research, 31(3): 700–706, 1992.

[176] Sergey Smolentsev, René Moreau, Leo Bühler, and Chiara Mistrangelo. Mhd thermofluid issues of liquid-metal blankets: Phenomena and advances. Fusion Engineering and Design, 85(7-9):1196–1205, 2010.

[177] Donald D Gray and Aldo Giorgini. The validity of the boussinesq approximation for liquids and gases. International Journal of Heat and Mass Transfer, 19(5):545–551, 1976.

[178] L Chen, S Smolentsev, and M-J Ni. Toward full simulations for a liquid metal blanket: part 2. computations of mhd flows with volumetric heating for a pbli blanket prototype at ha 104 and gr 1012. Nuclear Fusion, 62(2):026042, 2022.

[179] A Ying, AS Lavine, and M Tillack. The effect of hartmann and side layers on heat transfer in magnetohydrodynamic flow. Fusion Technology, 15(2P2B): 1169–1173, 1989.

[180] Alice Y Ying and Mark S Tillack. Mhd heat transfer in elongated rectangular ducts for liquid metal blankets. Fusion Technology, 19(3P2A):990–995, 1991.

[181] S Cuevas, BF Picologlou, JS Walker, G Talmage, and TQ Hua. Heat transfer in laminar and turbulent liquid-metal mhd flows in square ducts with thin conducting or insulating walls. International journal of engineering science, 35 (5):505–514, 1997.

[182] Minoru Takahashi, Masanori Aritomi, Akira Inoue, and Mitsuo Matsuzaki. Mhd pressure drop and heat transfer of lithium single-phase flow in a rectangular channel under transverse magnetic field. Fusion engineering and design, 42(1-4):365–372, 1998.

[183] Mohammed J Al-Khawaja and Mohammed Selmi. Highly accurate solutions of a laminar square duct flow in a transverse magnetic field with heat transfer using spectral method. 2006.

[184] ZH Wang and TY Lei. Liquid metal mhd effect and heat transfer research in a rectangular duct with micro-channels under a magnetic field. International Journal of Thermal Sciences, 155:106411, 2020.

[185] MJ Al Khawaja, RA Gardner, and R Agarwal. Numerical study of magneto-fluid-mechanics forced convection pipe flow. 1994.

[186] Richard A Gardner. Laminar pipe flow in a transverse magnetic field with heat transfer. International Journal of Heat and Mass Transfer, 11(6):1076–1081, 1968.

[187] Caroline Sorensen. Magnetohydrodynamic Heat Transfer for Fusion Energy. PhD thesis, Massachusetts Institute of Technology, 2021.

[188] BN Sorbom, J Ball, TR Palmer, FJ Mangiarotti, JM Sierchio, P Bonoli, C Kasten, DA Sutherland, HS Barnard, CB Haakonsen, et al. Arc: A compact, high-field, fusion nuclear science facility and demonstration power plant with demountable magnets. Fusion Engineering and Design, 100:378–405, 2015.

[189] H-C Ji and RA Gardner. Numerical analysis of turbulent pipe flow in a transverse magnetic field. International journal of heat and mass transfer, 40(8):1839–1851, 1997.

[190] RA Gardner and PS Lykoudis. Magneto-fluid-mechanic pipe flow in a transverse magnetic field. part 1. isothermal flow. Journal of Fluid Mechanics, 47 (4):737–764, 1971.

[191] S Yu Smolentsev, AV Tananaev, VS Shmarov, and DA Dajeh. Laminar heat transfer in the mhd flow in a rectangular duct 2. experimental investigations. Magnetohydrodynamics, 33(2):155–160, 1997.

[192] Michael J. Bluck and Michael J. Wolfendale. An analytical solution to electromagnetically coupled duct flow in MHD. J. Fluid Mech., 771:595–623, 2015. ISSN 14697645. doi: 10.1017/jfm.2015.202.

[193] Michael J Bluck and Michael J Wolfendale. An analytical solution to the heat transfer problem in thick-walled hunt flow. International Journal of Heat and Fluid Flow, 64:103–111, 2017.

[194] Michael J. Bluck. Analytical solutions to nonuniform surface heat transfer with volumetric sources in magnetohydrodynamic duct flow. J. Heat Transfer, 141(4), 2019. ISSN 15288943. doi: 10.1115/1.4042776.

[195] Ramesh K Shah and Alexander Louis London. Laminar flow forced convection in ducts: a source book for compact heat exchanger analytical data. Academic press, 2014.

[196] S Sahu, C Courtessole, A Ranjan, R Bhattacharyay, T Sketchley, and S Smolentsev. Thermal convection studies in liquid metal flow inside a horizontal duct under the influence of transverse magnetic field. Physics of Fluids, 32(6), 2020.

[197] K Mergia and N Boukos. Structural, thermal, electrical and magnetic properties of eurofer 97 steel. Journal of Nuclear Materials, 373(1-3):1–8, 2008.

[198] Chiara Mistrangelo, Leo Bühler, Ciro Alberghi, Serena Bassini, Luigi Candido, Cyril Courtessole, Alessandro Tassone, Fernando R Urgorri, and Oleg Zikanov. Mhd r&d activities for liquid metal blankets. Energies, 14(20):6640, 2021.

[199] R Boullon, J Aubert, and A Morin. Definition of a wcll reference tbm set design based on the wcll bb design–first cad model and scoping calculations. IDM Ref. EFDA_D_ 2N7CDT_v1, 2, 2019.

[200] Cristiano Ciurluini, Fabio Giannetti, Amelia Tincani, Alessandro Del Nevo, Gianfranco Caruso, Italo Ricapito, and Fabio Cismondi. Thermal-hydraulic modeling and analysis of the water cooling system for the iter test blanket module. Fusion Engineering and Design, 158:111709, 2020.

[201] C Ciurluini, V Narcisi, A Tincani, C Ortiz Ferrer, and F Giannetti. Conceptual design overview of the iter wcll water cooling system and supporting thermal-hydraulic analysis. Fusion Engineering and Design, 171:112598, 2021.

[202] C Mistrangelo and L Bühler. Determination of multichannel mhd velocity profiles from wall-potential measurements and numerical simulations. Fusion Engineering and Design, 130:137–141, 2018.

[203] L. Bühler. Deliverable bb-tbm - s.02.01-t001-d003 report on full numerical analysis for pbli flow across the shield and manifolds coupled to bus report. Technical Report EFDA_D_2QDMUJ, IDM Reference EFDA, 2022.

[204] R. Wenninger. Sof and eof equilibria for demo1 reference design, 2021. EFDA_D_2MUW9R.

[205] C Mistrangelo and L Bühler. Electro-magnetic flow coupling for liquid metal blanket applications. Fusion Engineering and Design, 109:1452–1457, 2016. doi: 10.1016/j.fusengdes.2015.11.052.

[206] F Bianchi, P Meloni, R Ferri, and A Achilli. Assessment of relap5 mod3. 3 and cathare2 v1. 5a against a full scale test of perseo device. In International Conference on Nuclear Engineering, volume 4689, pages 655–661, 2004.

[207] A Bersano, C Bertani, N Falcone, M De Salve, F Mascari, and P Meloni. Qualification of relap5-3d code against the in-pool passive energy removal system perseo data. In Proceedings of the 30th European Safety and Reliability Conference and the 15th Probabilistic Safety Assessment and Management Conference. Italy Venice, 2020.

[208] HK Forster and Novak Zuber. Dynamics of vapor bubbles and boiling heat transfer. AIChE Journal, 1(4):531–535, 1955.

[209] John C Chen. Correlation for boiling heat transfer to saturated fluids in convective flow. Industrial & engineering chemistry process design and development, 5(3):322–329, 1966.

[210] MG Cooper. Heat flow rates in saturated nucleate pool boiling-a wide-ranging examination using reduced properties. In Advances in heat transfer, volume 16, pages 157–239. Elsevier, 1984.

[211] SS Kutateladze. Heat transfer theory fundamentals, 1963.

[212] M Mohammed Shah. An improved and extended general correlation for heat transfer during condensation in plain tubes. Hvac&R Research, 15(5):889–913, 2009.

[213] G Sateesh, Sarit Kumar Das, and Arcot R Balakrishnan. Experimental studies on the effect of tube inclination on nucleate pool boiling. Heat and mass transfer, 45:1493–1502, 2009.

[214] SZ Kuhn, VE Schrock, and PF Peterson. An investigation of condensation from steam–gas mixtures flowing downward inside a vertical tube. Nuclear Engineering and Design, 177(1-3):53–69, 1997.

[215] IL Pioro, W Rohsenow, and SS Doerffer. Nucleate pool-boiling heat transfer. i: review of parametric effects of boiling surface. International Journal of Heat and Mass Transfer, 47(23):5033–5044, 2004.

[216] Benjamin J Jones, John P McHale, and Suresh V Garimella. The influence of surface roughness on nucleate pool boiling heat transfer. 2009.

[217] Myeong-Gie Kang. Experimental investigation of tube length effect on nucleate pool boiling heat transfer. Annals of Nuclear Energy, 25(4-5):295–304, 1998.

[218] Myeong-Gie Kang. Effect of surface roughness on pool boiling heat transfer. International journal of heat and mass transfer, 43(22):4073–4085, 2000.

[219] Moon-Hyun Chun and Myeong-Gie Kang. Effects of heat exchanger tube parameters on nucleate pool boiling heat transfer. 1998.

[220] Akhilesh Gupta, Ravi Kumar, and Vineet Kumar. Nucleate pool boiling heat transfer over a bundle of vertical tubes. International communications in heat and mass transfer, 37(2):178–181, 2010.

[221] Sang Jae Kim and Hee Cheon No. Turbulent film condensation of high pressure steam in a vertical tube. International Journal of Heat and Mass Transfer, 43 (21):4031–4042, 2000.

[222] FW Dittus and LMK Boelter. Heat transfer in automobile radiators of the tubular type. International communications in heat and mass transfer, 12(1): 3–22, 1985.

[223] Warren M Rohsenow. A method of correlating heat-transfer data for surface boiling of liquids. Transactions of the American Society of Mechanical Engineers, 74(6):969–975, 1952.

[224] Dieter Gorenflo and Stephan Kotthoff. Review on pool boiling heat transfer of carbon dioxide. International Journal of Refrigeration, 28(8):1169–1185, 2005.

[225] W Leiner. Heat transfer by nucleate pool boilinggeneral correlation based on thermodynamic similarity. International journal of heat and mass transfer, 37 (5):763–769, 1994.

[226] Kaneyasu Nishikawa, Yasunobu Fujita, Haruhiko Ohta, and Sumitomo Hidaka. Effect of the surface roughness on the nucleate boiling heat transfer over the wide range of pressure. In International Heat Transfer Conference Digital Library. Begel House Inc., 1982.

[227] Wilhelm Nusselt. Die oberflachenkodensation des wasserdampfes. Z. Vereines Deutsch. Ing., 60:569–575, 1916.

[228] Mirza M Shah. A general correlation for heat transfer during film condensation inside pipes. International Journal of heat and mass transfer, 22(4):547–556, 1979.

[229] RELAP ISL. Mod3. 3 code manual volume iv: models and correlations. NUREG/CR5535/Rev P3, 4, 2006.

[230] MM Shah. Heat transfer during film condensation in tubes and annuli: a review of the literature. 1981.

[231] Davide Papini, Antonio Cammi, et al. Modelling of heat transfer phenomena for vertical and horizontal configurations of in-pool condensers and comparison with experimental findings. Science and Technology of Nuclear Installations, 2010, 2010.

[232] W.H. McAdams. Heat Transmission. McGraw-Hill, New York, 1954.

[233] Mirza Mohammed Shah. General correlation for heat transfer during condensation in plain tubes: Further development and verification. ASHRAE Transactions, 119(2), 2013.

[234] Mirza M. Shah. Comprehensive correlations for heat transfer during condensation in conventional and mini/micro channels in all orientations. International Journal of Refrigeration, 67:22–41, 2016. ISSN 0140-7007. doi: https://doi.org/10.1016/j.ijrefrig.2016.03.014. URL https://www.sciencedirect.com/science/article/pii/S0140700716300342.

[235] WH McAdams. Heat transmission, mcgraw-hill. New York, pages 252–262, 1954.

[236] Valentin Guichet and Hussam Jouhara. Condensation, evaporation and boiling of falling films in wickless heat pipes (two-phase closed thermosyphons): A critical review of correlations. International Journal of Thermofluids, 1:100001, 2020.

[237] Piotr Leonidovich Kapitza. Wave flow of thin layers of viscous liquids. ii. flow in a contact with a gase flux and heat transfer. Zhurnal Eksperimentalnoi i Teoreticheskoi Fiziki, 18:19–28, 1948.

[238] W.M. Rohsenow, J.P. Hartnett, and Y.I. Cho. Handbook of Heat Transfer. McGraw-Hill, New York, 1998.

[239] Seol Ha Kim, Moo Hwan Kim, Dong Won Lee, and Chiwoong Choi. Code validation and development for MHD analysis of liquid metal flow in Korean TBM. Fusion Eng. Des., 87(7-8):951–955, 2012. ISSN 09203796. doi: 10.1016/j.fusengdes.2012.02.048. URL http://dx.doi.org/10.1016/j.fusengdes.2012.02.048.

[240] Lorenzo Melchiorri, Vincenzo Narcisi, Cristiano Ciurluini, F Giannetti, G Caruso, and A Tassone. Preliminary mhd pressure drop analysis for the prototypical wcll tbm with relap5/mod3. 3. Fusion Engineering and Design, 176:113048, 2022.

[241] TR Barrett, M Bamford, B Chuilon, T Deighan, P Efthymiou, L Fletcher, M Gorley, T Grant, T Hall, D Horsley, et al. The chimera facility development programme. Fusion Engineering and Design, 194:113689, 2023.

[242] M Eboli, A Ciampichetti, F Giannetti, N Forgione, and A Del Nevo. The lifus5 separate effect test facility experimental programme. Nuclear Engineering and Design, 411:112425, 2023.

[243] Marica Eboli, Pietro Arena, Nicolò Badodi, Antonio Cammi, Cristiano Ciurluini, Vittorio Cossu, Nicola Forgione, Francesco Galleni, Fabio Giannetti, Bruno Gonfiotti, Daniele Martelli, Lorenzo Melchiorri, Carmine Risi, Alessandro Tassone, and Alessandro Del Nevo. Pbli/water reaction: experimental campaign and modelling advancements in wpbb eurofusion project. Energies, 2023. Under review.

[244] Charles Newlin Kawczynski. A Numerical Investigation of Moderate Magnetic Reynolds Number Fusion Liquid Metal Magnetohydrodynamic Flows. University of California, Los Angeles, 2018.

Appendix A

```
      subroutine mhd2d(fmhd, kappa , gamma)
c
c  MHD 2D correlations for pressure drop coefficents
c
c  Cognizant engineer: ElPeligro
c
      implicit none
c
      include 'cons.h'
      include 'contrl.h'
      include 'fast.h'
      include 'stcblk.h'
      include 'voldat.h'
      include 'jundat.h'
c
c  local variables
c
      real*8 fmhd, kpHua, Hart, Reyn, btot, coave, fac1, fac2, kpTil
      real*8 kpTiTa, cs1, cs2, fac3
      integer kappa, gamma, index

      index = kappa + gamma
      btot = sqrt(bfield(index)**2 + bftwo(index)**2)
      Hart=alnght(index)*btot*sqrt(elconf(index)/viscf(index))
      Reyn=rhof(index)*abs(velf(index))*alnght(index)/viscf(index)

      cratio(index) = (thickw(index)*elconw(index))/(elconf(index)*
     alnght(index))
      copt1(index) = (twsl1(index)*elconw(index))/(elconf(index)*
```

```
    alnght(index))
      copt2(index) = (twsl2(index)*elconw(index))/(elconf(index)*
    alnght(index))
      deltar(index) = alnght(index)/(blnght(index)*3)
      if (blnght(index) .eq. 0.0d0)then
          deltar(index) = 0.0d0
      endif

      kpHua = +((1/(1+(1/cratio(index))+(deltar(index)/2)*((1/copt1(
    index))+(1/copt2(index))))))
      coave = (copt1(index) + copt2(index)) * 0.5
      fac1 = (Hart**0.5)/(1 + coave * Hart**0.5)
      fac2 = (cratio(index) + 1)/(cratio(index) + Hart**(-1))
      kpTil = 1/(deltar(index)*fac1 + fac2)
      fac3 = 1/fac2
      cs1 = 0.5/(Hart**-0.5 + copt1(index))
      cs2 = 0.5/(Hart**-0.5 + copt2(index))
      kpTiTa = fac3/(1+deltar(index)*(fac3*(cs1+cs2)))
      fmhd = kpTiTa*elconf(index)*bfield(index)**2

      return
      end
```

Listing A.1: REDMaHD MHD 2D factors subroutines

```
      subroutine mhd3d(hydrol, li , ri, ni)
c     MHD 3D correlations for pressure drop coefficents
c     Cognizant engineer: ElPeligro
      implicit none

      include 'cons.h'
      include 'contrl.h'
      include 'fast.h'
      include 'stcblk.h'
      include 'voldat.h'
      include 'jundat.h'

c     local variables
      real*8 hydrol, Hart, Reyn, dp3d, scf, kcross, khoriz,
     &       kvert, erat, q1, q2, q3, q4, kdoom, eratc, kdoomB,
     &       btot, kfci, bleft, bright
```

```
      integer ri, li, ni
      logical bflag, isgap
      parameter (q1 = 0.1d0, q2 = 0.99d0, q3 = 1.01d0, q4 = 10.d0,
     &           kdoom = 1.0d0, kdoomB = 1.5d0)

      bflag = .FALSE.
      bleft = sqrt(bfield(li)**2 + bftwo(li)**2)
      bright = sqrt(bfield(ri)**2 + bftwo(ri)**2)
      btot = max(bleft,bright)
      Hart = alnght(ri)*btot*sqrt(elconf(ri)/viscf(ri))
      Reyn = rhof(ri)*abs(velf(ri))*alnght(ri)/viscf(ri)

c     EXPANSION/CONTRACTION ratio
      if (velf(li) .gt. 0.0d0) then
          erat = avol(ri)/avol(li)
      else
          erat = avol(li)/avol(ri)
      endif
      eratc = 1.0d0/erat

c     Bhuler Correlation for Expansion
      dp3d = 0.315+4.76*(1/sqrt(Hart))+(8.2)*Reyn**(0.33)*(0.001)

c     Scaling factor
      if (abs(velf(ri)) .lt. 10.0**(-6) .or. abs(velf(li)) .lt.
   10.0**(-6)) then
          scf = 0.0
      else
          scf = (2*elconf(ri)*min(alnght(ri),alnght(li))*btot**2) /
     &          (rhof(ri)*abs(velfjo(ni)))
      endif
      if (bflag) go to 200
c     Correlations
c     Expansion/contraction
c     Range of Buhler correlation (for c = 0.028)
      if (avol(li) .ne. avol(ri)) then
          if (fiang2(li) .eq. 0.0d0 .or. fiang2(ri) .eq. 0.0d0) then
              if (Hart .lt. 10.d0 .or. Reyn .gt. 300000.d0) then
                  kcross = kdoomB*scf
              else
```

```
200            if (erat .lt. q1 .and. erat .ge. 0.0d0) then
                     kcross = kdoom*scf
                 elseif (erat .ge. q1 .and. erat .lt. q2) then
                     kcross = (0.00212*eratc**3 -0.0551*eratc**2 + 0.482145*eratc -0.43296432)*scf
                 elseif (erat .ge. q2 .and. erat .le. q3) then
                     kcross = 0.0d0
                 elseif (erat .eq. 4.d0) then
                     kcross = dp3d*scf
                 elseif (erat .gt. q3 .and. erat .lt. q4) then
                     kcross = (0.00212*erat**3 -0.0551*erat**2 + 0.482145*erat -0.43296432)*scf
                 elseif (erat .ge. q4) then
                     kcross = kdoom*scf
                 endif
             if (bflag) go to 300
             endif
         else
             if (bftwo(li) .ne. 0.0d0 .or. bftwo(ri) .ne. 0.0d0) then
                 bflag = .TRUE.
                 btot = bftwo(ri)
                 go to 100
             else
                 bflag = .TRUE.
                 btot  = bfield(ri)/4.0d0
                 go to 100
             endif
         endif
     else
         kcross = 0.0d0
     endif

     btot = sqrt(bfield(ri)**2+bftwo(ri)**2)
     if (abs(velf(ri)) .lt. 10.0**(-6) .or. abs(velf(li)) .lt. 10.0**(-6)) then
         scf = 0.0
     else
         scf = (2*elconf(ri)*min(alnght(ri),alnght(li))*btot**2) / ( rhof(ri)*velfjo(ni))
     endif
```

```
c HORIZONTAL bend
 300   btot = sqrt(bfield(ri)**2 + bftwo(ri)**2)
       if (abs(velf(ri)) .lt. 10.0**(-6) .or. abs(velf(li)) .lt. 10.0**(-6)) then
           scf = 0.0
       else
           scf = (2*elconf(ri)*min(alnght(ri), alnght(li))*btot**2) / (rhof(ri)*velfjo(ni))
       endif

       if (dilde(li) .ne. dilde(ri)) then
           if (deltar(li) .ne. 0.0d0) then
               if (fiangl(li) .eq. 0.0d0) then
                   khoriz = (1.063d0*cratio(li)/(4.0d0/3.0d0 + cratio(li))) * (max(abs(dilde(li)), abs(dilde(ri))) / 90.0d0) * scf / 2.0d0
               else
                   khoriz = (1.063d0*cratio(li)/(4.0d0/3.0d0 + cratio(li))) * (max(abs(dilde(li)), abs(dilde(ri))) / 90.0d0) * scf / 6.0d0
               endif
           else
               if (fiangl(li) .eq. 0.0d0) then
                   khoriz = 0.125 * scf / 2.0d0
               else
                   khoriz = 0.125 * scf / 6.0d0
               endif
           endif
       else
           khoriz = 0.0d0
       endif

c VERTICAL bend
       if (abs(sinb(li)/sinb(ri)) .lt. 0.8d0 .or. abs(sinb(li)/sinb(ri)) .gt. 1.25d0) then
           if (deltar(li) .ne. 0.0d0) then
               if (fiangl(li) .eq. 0.0d0) then
                   kvert = (1.063d0*cratio(li)/(4.0d0/3.0d0 + cratio(li))) * (asin(max(abs(sinb(li)), abs(sinb(ri)))) / piovr2) * scf / 2.0d0
```

```
                else
                    kvert = (1.063d0*cratio(li)/(4.0d0/3.0d0 + cratio(li))) * (asin(max(abs(sinb(li)), abs(sinb(ri)))) / piovr2) * scf / 6.0d0
                endif
            else
                if (fiangl(li) .eq. 0.0d0) then
                    kvert = 0.125 * scf / 2.0d0
                else
                    kvert = 0.125 * scf / 6.0d0
                endif
            endif
        else
            kvert = 0.0d0
        endif
c Start block for FCI pressure drop
        if (fcflag(1,ri) .eq. 2) then
            if (cratio(li)/cratio(ri) .gt. 1.3d0 .or. cratio(li)/cratio(ri) .lt. 0.77d0) then
                if (isgap) goto 69

                c GAP
                if (cratio(li) .eq. cratio(ri+ri-li) .and. cratio(li) .ne. cratio(ri) .and. cratio(ri) .ne. cratio(ri+ri-li)) then
                    kfci = (0.12d0 - dl(ri)/alnght(ri) * (1 / (1 + (1 / cratio(ri)) + (deltar(ri) / 2) * ((1 / copt1(ri)) + (1 / copt2(ri)))))) * scf
                    isgap = .TRUE.
                endif

                c Entrata/Uscita
                if (cratio(li) .ne. cratio(ri) .and. cratio(ri) .eq. cratio(ri+ri-li) .and. cratio(li) .ne. cratio(ri+ri-li)) then
                    kfci = 0.02032d0 * scf
                    isgap = .FALSE.
                endif
            else
69              kfci = 0.0d0
                isgap = .FALSE.
            endif
```

```
      else
          kfci = 0.0d0
      endif

c Total K for MHD 3D loss
      hydrol = khoriz + kvert + kcross + kfci
      return
      end
```

Listing A.2: REDMaHD MHD 3D factors subroutines

```
tic
hindex = 0.0;
Results_vec = {zeros};
Results_vec_vol = {zeros};
cw_v = zeros;
HaAx = zeros;
w = 400;
for hn = [0.1 0.11111 0.125 0.143 0.1666 0.2 0.25 0.3333 0.5 1 2 3 4 5
     6 7 8 9 10]
    hindex = hindex + 1;
    Results = zeros;
    ResultsVol = zeros;
    lindex = 0.0;
l = (hn+1)/2;% total length tor [m]
h = l/hn;
dh = 2*(l*h)/(l+h); % Hyraulic Diameter [m]
a = l/(2*dh);
b = h/(2*dh);
aspect_ratio = a/b;

    if aspect_ratio >= 1
        armoniche = 200;
    elseif aspect_ratio < 1 && aspect_ratio >= 0.2
       armoniche = 900;
    elseif aspect_ratio < 0.2 && aspect_ratio >= 0.125
        armoniche = 1500;
    else
       armoniche = 6000;
    end
for tRat =  [0.0001 0.001 0.005 0.01 0.05 0.1 0.5 1 5 10]
```

```
    lindex = lindex + 1;
    cw_v (1,lindex) = tRat;
    index = 0.0;
for tommaso = -1:0.1:6
Ha = 10^tommaso;
sigma_Eurofer_600K = 1144793.48;
sigma_PbLi_600K = 874676.37;
sigRat = sigma_Eurofer_600K/sigma_PbLi_600K;
%tRat = 0.01;
cw = sigRat*tRat;
% Grid
leftbndHa = -a;
rightbndHa = a;
leftbndS = -b;
rightbndS = b;
chebychevgrid=@(leftbnd,rightbnd,w)leftbnd+((rightbnd-leftbnd)/2)*(cos
    (linspace(pi,0,w))+1);
% F = linspace(-a,a,w);
% Y = linspace(-b,b,w); % Governa le colonne
Y = chebychevgrid(leftbndS,rightbndS,w);
F = chebychevgrid(leftbndHa,rightbndHa,w);
X = F'; % Governa le righe
[x,y] = meshgrid(X,Y);
% Inizializzazione
Ush = 0.0;

Ulh = 0.0;

Urh = 0.0;

Un = 0.0;

UshD = 0.0;

Ulhd = 0.0;

Urhd = 0.0;

UmSH = 0.0;

```

```
Umh = 0.0;

U17 = 0.0;

UhA = 0.0;

UmSHd = 0.0;

SumG = 0.0;

UnH = 0.0;

UhnTot = 0.0;

UhTot = 0.0;

Nvol = 0.0;

for n = 1:armoniche

lambda = Ha/2;

lambdaN = (n-1/2)*(pi/b);

pn1 = ( lambda - ((lambda^2) + (lambdaN^2))^(1/2) );

pn2 = ( lambda + ((lambda^2) + (lambdaN^2))^(1/2) );

kn = ( 2 * sin( lambdaN * b) )/( lambdaN );

eta = sqrt(lambdaN^2 + lambda^2);

Gamma =  cos( lambdaN * y );

% Semplificazione bN %%%%%%%%%%%%%%%%%%%%

if abs(2*lambda*a) <= 701 && abs(2*eta*a) <= 701

bN = eta * cosh( 2 * lambda * a) / ( cosh( 2 * eta * a ) );

```

```
elseif abs(2*lambda*a) > 701 && abs(2*eta*a) > 701

logbns = log(eta) + (2*lambda*a) - (2*eta*a);

bN = exp(logbns); % bN = eta*exp(2*a(lambda-eta))

elseif abs(2*lambda*a) <= 701 && abs(2*eta*a) > 701

bN = exp(log(2) + log(eta) + log(cosh(2*lambda*a)) - 2* eta*a);

elseif abs(2*lambda*a) > 701 && abs(2*eta*a) <= 701

bN = exp(log(0.5) - log(cosh(2*eta*a)) + 2*lambda*a + log(eta));

end
%%%%%%%%%%%%%%%%%%%%%%%%%%%%%%%%%%%%%%%%%

% Shercliff Solution - Semplificazione

if 2* eta*a <= 701

Un = (kn / (lambdaN^2*b)) * ( 1 - ( sinh( pn2*a ) * cosh( pn1 * x ) - sinh( pn1*a ) * cosh( pn2 * x ) ) / ( sinh( 2* eta*a )));

elseif 2* eta*a > 701

i1 =  pn1*(a+x);
I = (abs(i1) <= 701) .* (exp(i1)) + (abs(i1) > 701) .* (exp(-701));

h1 =  pn1*(a-x);
H = (abs(h1) <= 701) .* (exp(h1)) + (abs(h1) > 701) .* (exp(-701));

ii1 =  pn1*(a+x) - 2*pn2*a;
II = (abs(ii1) <= 701) .* (exp(ii1)) + (abs(ii1) > 701) .* (exp(-701));

hh1 =  pn1*(a-x) - 2*pn2*a;
HH = (abs(hh1) <= 701) .* (exp(hh1)) + (abs(hh1) > 701) .* (exp(-701));

```

```
l1 =  pn2*(x-a) + 2*pn1*a;
L = (abs(l1) <= 701) .* (exp(l1)) + (abs(l1) > 701) .* (exp(-701));

m1 =  -pn2*(x+a) + 2*pn1*a;
M = (abs(m1) <= 701) .* (exp(m1)) + (abs(m1) > 701) .* (exp(-701));

n1 =  pn2*(x-a);
N = (abs(n1) <= 701) .* (exp(n1)) + (abs(n1) > 701) .* (exp(-701));

o1 =  -pn2*(x+a);
O = (abs(o1) <= 701) .* (exp(o1)) + (abs(o1) > 701) .* (exp(-701));

Un = (kn / (lambdaN^2*b)) * ( 1 - (0.5) *( I + H - L - M + N + O - II - HH) );

end

Ush = Gamma.*Un   + Ush ;

% Semplificazione DNsh

if ( 2 * eta*a ) <= 701

DNsh = (kn/(lambdaN^2*b)) *  (( pn2 * sinh( pn1*a ) * cosh( pn2*a ) - pn1 * sinh( pn2*a ) * cosh( pn1*a) ) /  sinh( 2 * eta*a ) );

elseif  ( 2 * eta*a ) > 701

aaa =  2*pn1*a;
AAA = (abs(aaa) <= 701) .* (exp(aaa)) + (abs(aaa) > 701) .* (exp(-701));

bbb =  2*pn1*a - 2*pn2*a;
BBB = (abs(bbb) <= 701) .* (exp(bbb)) + (abs(bbb) > 701) .* (exp(-701));

ccc =  -2*pn2*a;
CCC = (abs(ccc) <= 701) .* (exp(ccc)) + (abs(ccc) > 701) .* (exp(-701));

```

```
DNsh = 0.5*(kn/(lambdaN^2*b))*(pn2*(AAA + BBB -1 - CCC )-pn1*(AAA + 1
    - BBB - CCC));

end
%%%%%%%%%%%%%%%%%%%%%%%%%%%%%%%%%%%%%%%%

aN = eta + lambdaN*(sigRat^-1)*tanh( 2 * eta *a)*coth(lambdaN*tRat);

%%%%%%%%%%%%%%%%%%%%%%%%%%%%%%%%%%%%%%%%
% Per Nu di Hunt
 PnL = DNsh / (aN + bN) ;
% Per Nu di Shercliff
% PnL = 0.0 ;

PnR = - (DNsh / (aN + bN) );

% Hunt alone solution
if (2*eta*a) <= 701

UhnTot = (1/cosh(2*eta*a))*(cosh(pn2*a)*cosh(pn1*x)-cosh(pn1*a)*cosh(
    pn2*x));

else

lll =  pn1*(a+x);
LLL = (abs(lll) <= 701) .* (exp(lll)) + (abs(lll) > 701) .* (exp(-701)
    );

mmm =  pn1*(a-x);
MMM = (abs(mmm) <= 701) .* (exp(mmm)) + (abs(mmm) > 701) .* (exp(-701)
    );

nnn =  pn1*(a+x) - 2*pn2*a;
NNN = (abs(nnn) <= 701) .* (exp(nnn)) + (abs(nnn) > 701) .* (exp(-701)
    );

ooo =  pn1*(a-x) - 2*pn2*a;
OOO = (abs(ooo) <= 701) .* (exp(ooo)) + (abs(ooo) > 701) .* (exp(-701)
    );

```

```
ppp =  pn2*(x - a) + 2*pn1*a;
PPP = (abs(ppp) <= 701) .* (exp(ppp)) + (abs(ppp) > 701) .* (exp(-701)
    );

qqq =  -pn2*(x + a) + 2*pn1*a;
QQQ = (abs(qqq) <= 701) .* (exp(qqq)) + (abs(qqq) > 701) .* (exp(-701)
    );

rrr =  pn2*(x - a);
RRR = (abs(rrr) <= 701) .* (exp(rrr)) + (abs(rrr) > 701) .* (exp(-701)
    );

sss =  -pn2*(x + a);
SSS = (abs(sss) <= 701) .* (exp(sss)) + (abs(sss) > 701) .* (exp(-701)
    );

UhnTot =(1/2)*(LLL + MMM + NNN + OOO - PPP - QQQ - RRR - SSS);
end

UhTot = UhTot + PnL*Gamma.*UhnTot;

% Semplificazione per Nusselt %%%%%%%%%%%%%%%%%%%%
primo = kn/(lambdaN^2*b);

secondo = -1/lambdaN^2;

terzo = -(sinh(pn2*a)*cosh(pn1*x))/(sinh(2*eta*a)*(pn1^2-lambdaN^2));

quarto = (sinh(pn1*a)*cosh(pn2*x))/(sinh(2*eta*a)*(pn2^2-lambdaN^2));

secondo2 = (cosh(pn2*a)*cosh(pn1*x))/(cosh(2*eta*a)*(pn1^2-lambdaN^2))
    ;

terzo2 = -(cosh(pn1*a)*cosh(pn2*x))/(cosh(2*eta*a)*(pn2^2-lambdaN^2));

if (2*eta*a) <= 701

FnSH = primo * (secondo + terzo + quarto);
FnH = PnL*(secondo2 + terzo2);

```

```
elseif (2*eta*a) > 701
%%% Per termine c4 in FnSH
s1 = pn1*(a+x);
S = (abs(s1) <= 701) .* (exp(s1)) + (abs(s1) > 701) .* (exp(-701));

t1 = pn1*(a-x);
T = (abs(t1) <= 701) .* (exp(t1)) + (abs(t1) > 701) .* (exp(-701));

v1 = pn1*(x+a)- 2*pn2*a;
V = (abs(v1) <= 701) .* (exp(v1)) + (abs(v1) > 701) .* (exp(-701));

z1 = pn1*(a-x)- 2*pn2*a;
Z = (abs(z1) <= 701) .* (exp(z1)) + (abs(z1) > 701) .* (exp(-701));
%%%%%
%%% Per termine d4 in FnSH
ss1 = pn2*(x-a) + 2*pn1*a;
Ss = (abs(ss1) <= 701) .* (exp(ss1)) + (abs(ss1) > 701) .* (exp(-701))
    ;

tt1 = -pn2*(x+a) + 2*pn1*a;
Tt = (abs(tt1) <= 701) .* (exp(tt1)) + (abs(tt1) > 701) .* (exp(-701))
    ;

vv1 = pn2*(x-a);
Vv = (abs(vv1) <= 701) .* (exp(vv1)) + (abs(vv1) > 701) .* (exp(-701))
    ;

zz1 = -pn2*(a+x);
Zz = (abs(zz1) <= 701) .* (exp(zz1)) + (abs(zz1) > 701) .* (exp(-701))
    ;
%%%%

FnSH = primo*(secondo-(0.5*(S+T-V-Z)/(pn1^2-lambdaN^2)) + (0.5*(Ss+Tt-
    Vv-Zz)/(pn2^2-lambdaN^2)));

FnH = PnL*((0.5*(S+T+V+Z)/(pn1^2-lambdaN^2)) - (0.5*(Ss+Tt+Vv+Zz)/(pn2
    ^2-lambdaN^2)));

end
```

```
%%%%% Semplificazione Fattori sinh(lambdaN) %%%%%%%%%%%%%%

if 2*lambdaN*a <= 701

F1 = sinh(lambdaN*(x-a))/sinh(2*lambdaN*a);
F2 = sinh(lambdaN*(x+a))/sinh(2*lambdaN*a);

elseif 2*lambdaN*a > 701

af = lambdaN*(x-3*a);
AF = (abs(af) <= 701) .* (exp(af)) + (abs(af) > 701) .* (exp(-701));

bf = -lambdaN*(x+a);
BF = (abs(bf) <= 701) .* (exp(bf)) + (abs(bf) > 701) .* (exp(-701));

cf = lambdaN*(x-a);
CF = (abs(cf) <= 701) .* (exp(cf)) + (abs(cf) > 701) .* (exp(-701));

df = -lambdaN*(x+3*a);
DF = (abs(df) <= 701) .* (exp(df)) + (abs(df) > 701) .* (exp(-701));

F1 = AF - BF;
F2 = CF - DF;

end

gn = FnSH + FnH + ( FnSH(1,1) + FnH(1,1))*F1 - (FnSH(1,w) + FnH(1,w))*
    F2;

SumG = SumG + gn.*Gamma;

if lambdaN*a <= 701

Nvols = (((-1)^n)*cosh(lambdaN*x))/((lambdaN^3)*((cosh(lambdaN*a))));

else
tooc = lambdaN*(x-a);
TOOC = (abs(tooc) <= 701) .* (exp(tooc)) + (abs(tooc) > 701) .* (exp
    (-701));

```

```
tac = -lambdaN*(x+a);
TAC = (abs(tac) <= 701) .* (exp(tac)) + (abs(tac) > 701) .* (exp(-701)
    );

Nvols = (((-1)^n)*(TAC+TOOC))/(lambdaN^3);
end

Nvol = Nvol + Nvols.*Gamma;

end %%%%%

U = (UhTot + Ush);
% first iteration
UMF = trapz(X,trapz(Y,U,2))/(4*a*b);
Unon = U/UMF;
% % second iteration
% UMF1 = trapz(X,trapz(Y,Unon,2))/(4*a*b);
% Unon1 = Unon/UMF1;
% %
Uc = Unon(w/2,w/2);
UnonC = Unon/Uc;

BB = Unon.*SumG;

BBT = trapz(X,trapz(Y,BB,2));

MM = trapz(X,trapz(Y,U,2));

NuMedio = -1*0.25*(MM/BBT);

NVI1 = (b^2 - y.^2).*Unon;
NVI2 = (4*Nvol/b).*Unon;
NVI = NVI1 + NVI2;
NVIS = trapz(X,trapz(Y,NVI,2));

NuVolMedio = (1/(4*NuMedio) + (NVIS)/(8*a*b))^-1;

Umax = max(Unon,[],'all');

index = index + 1;
```

```
Results(index,lindex) = NuMedio;

ResultsVol(index,lindex) = NuVolMedio;

HaAx(index,1) = Ha;
end

end
Results_vec{1,hindex} = Results;
Results_vec_vol{1,hindex} = ResultsVol;
end
toc
%%
% % grid off
% figure
% % % surf(x,y,U, 'EdgeColor','flat')
% UnonHa = Unon(w/2,:);
% UnonS = Unon(:,w/2);
% % % UC1 = UhTot(:,w/2);
% % % UC2 = Ush(:,w/2);
% % UC3 = U(:,w/2);
% % % UC4 = UnonC(:,w/2);
% % figure
% % grid on
% plot (X, UnonHa, 'LineWidth',1.5, 'LineStyle','-')
% figure
% % % hold on
% plot (Y,UnonS, 'LineWidth',1.5, 'LineStyle','-')
% % % figure
% % % plot (X,UC1, 'LineWidth',1.5, 'LineStyle','-.')
% % % hold on
% % % plot (X,UC2, 'LineWidth',1.5, 'LineStyle','--')
% % % figure
% % figure
% % plot (Y,UC3, 'LineWidth',1.5, 'LineStyle','-.')
% % % hold on
% % % plot (Y,UC4, 'LineWidth',1.5, 'LineStyle',':')
% % %
%
```

```
% % figure
% % for op = 1:1:lindex
% % hold on
% % txt = ['Sigma Ratio =', num2str(cw_v(op))];
% % plot (HaAx,Results(:,op), 'LineWidth',3, 'LineStyle','-','
    DisplayName',txt)
% % end
% % xlabel ('Hartmann')
% % ylabel ('Nusselt')
% % title ('Sigma Ratio = 1.3')
% % grid on
% % set(gca, 'XScale', 'log')
% % lgd = legend;
% % lgd.FontSize = 30;
%
% % figure
% % for op = 1:1:lindex
% % hold on
% % plot (HaAx,ResultsVol(:,op), 'LineWidth',3, 'LineStyle','--')
% % end
% % grid on
% % set(gca, 'XScale', 'log')
% % figure
% % hold on;
% % plot (x,y,'k')
% % plot (x.',y.','k')
%
%
%
%
%
%
%
```

Listing A.3: MatLab Script for Bluck's solution